Nonlinear global modes and sound generation in hot jets.

Lutz Lesshafft

Lutz Lesshafft

Nonlinear global modes and sound generation in hot jets

Thèse de doctorat
École Polytechnique
2006

Il était un dimanche matin,

sous un grand ciel bleu de janvier : la valise à la main, je sortais du métro St. Paul, près de l'hôtel que Patrick avait choisi pour moi. J'ai tout de suite su, avant même de connaître le sujet de thèse qu'on allait me proposer, où je voulais passer les prochaines années. Ce furent des années extraordinaires — très laborieuses aussi, mais Paris vaut bien un stress. Mon travail de thèse doit son succès, et mon séjour son glamour, au soutien et à la présence d'un grand nombre de personnes :

Merci Patrick, pour ton soutien inconditionel. Je suis admiratif et très reconnaissant devant ta compréhension profonde de la science aussi bien que de l'âme du jeune chercheur. Merci pour les week-ends que tu m'as consacrés, pour ton enthousiasme quand ça marchait, ton optimisme quand ça ne marchait pas du tout. Merci Pierre, pour ton pilotage sûr dans les marais du numérique, pour la confiance que tu as eue en moi, ainsi qu'en mes conditions aux limites, et pour ta disponibilité. Merci Marc, pour ton aide et ton accompagnement quand je chantais le Fortran blues.

Je remercie mon illustre jury, Sébastien Candel, Uwe Ehrenstein, Peter Monkewitz et Nigel Peake, de m'avoir fait le grand honneur d'évaluer ma thèse. Je remercie également mon ancien professeur Hans Fernholz de l'interêt continu qu'il a porté à mon chemin.

Mon travail a beneficié des contributions intellectuelles importantes de Jean-Marc, l'homme qui réfléchit plus vite que son ombre, et de Carlo, qui dispense toujours généreusement ses idées limpides autant que des mots d'encouragement. Merci au seleção de tous les autres chercheurs permanents – Paul le grand seigneur des choses trop compliquées, Paul l'asymptotique d'ordre élévé, Emmanuel le bel esprit ab imo pectore, Peter mon comexpat, mon ami "keep LadHyX weird" Charles, Pascal le voyageur extrème, Antoine le motard, et Sabine, qui ajoute le piment au café.

Merci à mes collègues à l'ONERA, à Ivan, François et tous les autres amis qui animent l'aile F! Et un grand merci à Lê, Brigitte et Ghislaine pour tous les efforts administratifs à mon égard et pour de bons moments conviviaux.

Merci aux autres doctorants du LadHyX : François, Matteo et Ramiro, qui ont donné l'exemple, Charlotte et Pantxika, mes co-novices de la première heure, Anne-Virginie, Cécile et Maher, et bien sûr Alan et Axel, avec qui on

a pu partager tous les états de la vie d'un thésard, de A comme angoisse à Z comme zen. Bon courage et zénitude aux prochains : Benoît, Cédric, Claire, Elena, Frédo, Grégory, Maria-Lu, Mathieu et Rémi! Merci Thérèse, Christiane et Sandrine pour avoir fait fonctionner la boutique. Merci Daniel pour ton talent à trouver des solutions pratiques et pour les bières à la Butte; grand merci Tonio pour ton aide et ta générosité pendant la fabrication de mes deux lampes tornades!

Merci Olivier et Olivier, mes amis et collocataires, de votre grand soutien et de votre tolérance pendant la rédaction de ce manuscrit; merci Anabel, pour ta belle âme. Et finalement, un merci très spécial à Dan, Florian, Friedrich, Kilian et Sascha, mes amis lointains qui sont toujours restés si proches.

Contents

Chapter 1

Introduction

Scientific exploration of jet instability phenomena was initially inspired by their visual beauty. In 1858, Le Conte [75] discovered during a lamp-lit classical concert that music stimulated rhythmic flickering in a gas flame:

> "Soon after the music began, I observed that the flame exhibited pulsations that were exactly synchronous with the audible beats. This (...) phenomenon was very striking, [especially] when the strong notes of the cello came in. It was exceedingly interesting (...) how perfectly even the trills (...) were reflected on the sheet of flame."

Tyndall, in 1867, explored the sensitivity of a flame to the poetry of Edmund Spenser [104]:

> Sweet words like dropping honny she did shed,
> And twixt the perles and rubins softly brake
> A silver sound, which heavenly musicke seemed to make.

Sketches of the flame response to these verses are shown in figure 1.1, a full account is given in the chapter "Sensitive naked flames" of Tyndall's notes on lectures held at the Royal Institution in London [109]. In similar experiments conducted during these lectures, Tyndall also observed that non-reacting hot jets are receptive to musical excitation[1]. Instability phenomena in non-reacting jets are the subject of my dissertation.

[1] Accounts on the discoveries by Le Conte and Tyndall are due to Lienhard [70].

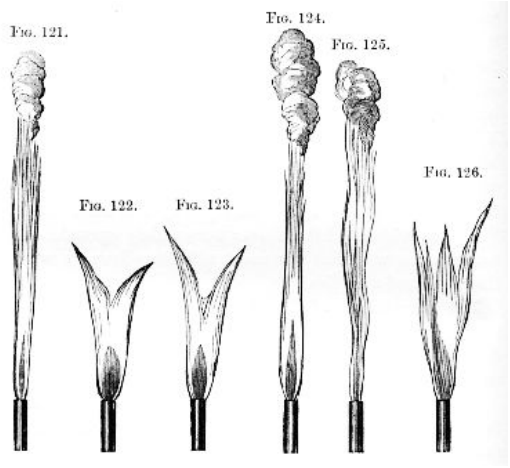

Figure 1.1: Poetry response of a gas flame in various régimes, taken from Tyndall [109]

On the basis of Lord Kelvin's description of the Kelvin–Helmholtz instability mechanism in plane shear layers, Lord Rayleigh [98] was the first to attempt a theoretical investigation of the instability of an inviscid cylindrical vortex sheet in 1879. His analysis revealed that round jets are unstable to axisymmetric disturbances.

In the twentieth century, purely æsthetic fascination has given way to more practical considerations. Industrial interest in hot jet dynamics, especially with regard to laminar-turbulent transition, has been primarily motivated by aircraft propulsion and combustion applications. In recent years, the reduction of jet noise has become the object of intensive research. Sound may emanate both from large-scale instability structures, as well as from small-scale turbulence. Jet noise today accounts in large measure for the acoustic nuisance of aircraft traffic. In internal combustion applications, it may cause resonant vibrations of the surrounding structure, among other undesirable effects.

1.1 Amplifiers and oscillators

All flows may be divided into three categories: in response to perturbations, they may be *stable*, or otherwise act as *amplifiers* or *oscillators*. In *stable* flows, any external disturbance is temporally damped. If, for instance, music had played while Spenser [104] contemplated an actual stream of honey flow-

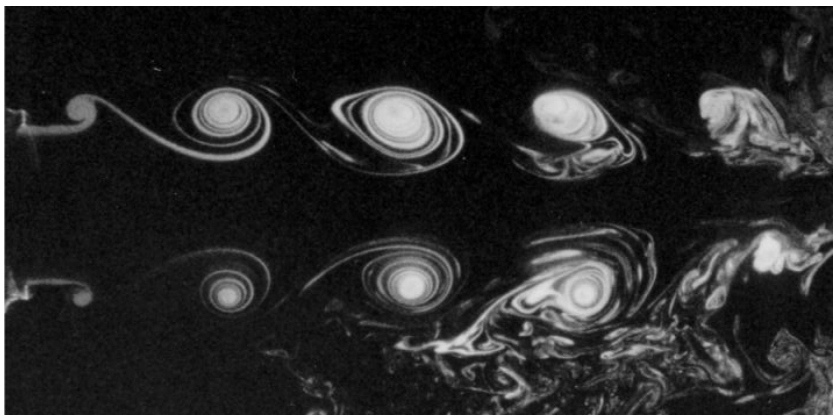

Figure 1.2: Vortical ring structure in an unheated round air jet at Reynolds number $\mathrm{Re}_D = 10^4$, axisymmetrically forced at Strouhal number $\mathrm{St} = 0.55$ (Re_D and St based on jet diameter and exit velocity). Taken from Parekh *et al.*[91]

ing from his muse's mouth, he would not have observed it pulsate in tune to cello notes. By contrast, the ripples that Le Conte [75] noticed in a gas flame in response to flute trills characterize the flame as an *amplifier* of external noise, or indeed music. A flow that acts as an amplifier displays instabilities driven by external excitation: perturbations introduced upstream experience growth as they travel downstream. In perfectly quiet surroundings, an amplifier-type flow remains unperturbed.

Jets display amplifier-type behavior over a large commonly observed parameter range. Amplification of controlled harmonic perturbations in a typical round laboratory jet is visualized in figure 1.2. In this photograph, a laser sheet illuminates the meridional plane of the jet during 25 ns, thereby giving an instantaneous picture of the flow, which is seeded with cigar smoke in the shear layer. Low-amplitude flow forcing at the nozzle exit engenders rapidly growing disturbances, resulting in a regular roll-up of the shear layer into vortex rings. The passage frequency of these convected vortex rings corresponds to the frequency of the upstream forcing.

Oscillator flows display self-excited behavior: starting from a steady state, such a flow develops persisting oscillations in response to an initial perturbation, and it never returns to the unperturbed state. The long-time dynamics of an oscillator are *intrinsic* to the flow system.

The best-known archetype of an oscillator-type flow is the wake of a circular cylinder, which may serve as an illustration. At Reynolds numbers

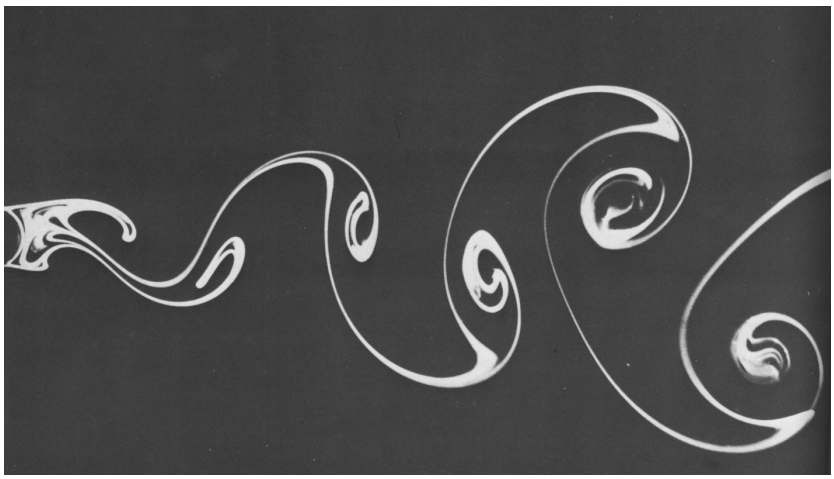

Figure 1.3: Bénard–Kármán vortex street in the wake of a circular cylinder at Reynolds number $\mathrm{Re}_D = 140$. Photograph by Sadatoshi Taneda, taken from van Dyke [110].

between 48.5 and 180, the instability of the wake gives rise to a periodic shedding of counter-rotating vortices that form the Bénard–Kármán vortex street, pictured in figure 1.3. The steady wake flow, as observed for $\mathrm{Re} < 48.5$, is still a solution to the Navier–Stokes equations, but this solution is unstable: subjected to an arbitrary perturbation, the steady flow bifurcates to a synchronized oscillating state of the form

$$\boldsymbol{q}(\boldsymbol{x}, t) = \boldsymbol{Q}(\boldsymbol{x})\, e^{-i\omega_g t}\,, \tag{1.1}$$

where the vectors $\boldsymbol{q}$, $\boldsymbol{Q}$ contain all flow variables, and ω_g is the *global frequency*. A time-harmonic solution (1.1) to the unforced Navier–Stokes equations is referred to as a *nonlinear global mode*. A steady flow that bifurcates to a global mode is characterized as being *globally unstable*.

The term *global* emphasizes that the oscillating solution encompasses the entire flow field. Nonlinear effects cause the fluctuation amplitudes to saturate at finite levels, thus limiting the temporal as well as spatial growth of the instability to an asymptotic state (1.1) with *real* global frequency ω_g.

Intrinsic oscillations in the cylinder wake were first observed and described by Bénard [6] in 1908. Some eighty years later, it has been found that hot jets may display a similar behavior.

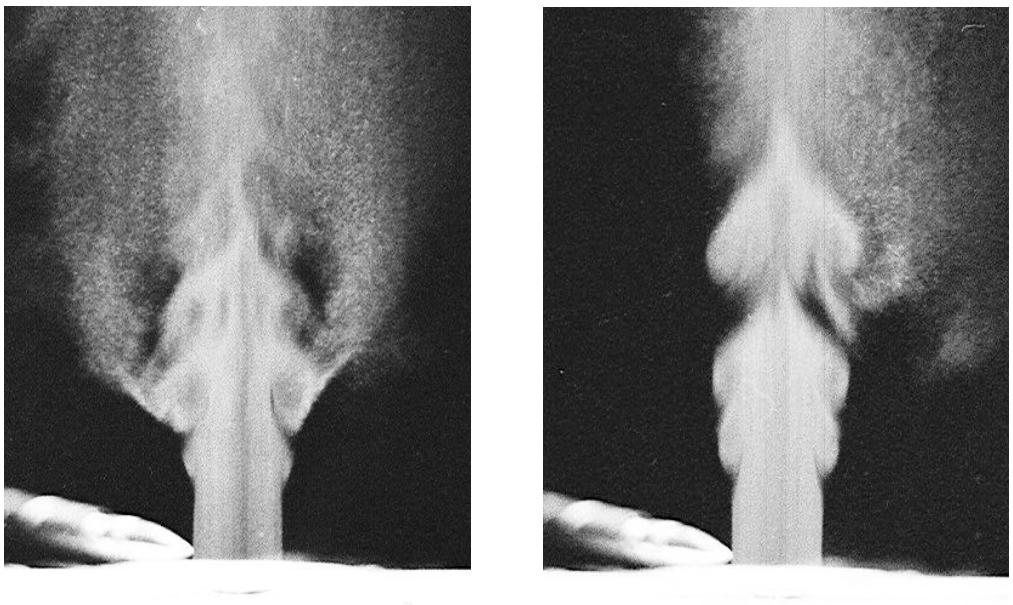

(a) (b)

Figure 1.4: Synchronized oscillations visualized in a hot jet at $S = 0.47$ and $\mathrm{Re}_D = 10\,000$. Smoke illuminated by a strobed laser sheet through the jet axis, photograph shutter speed 1/30 s. (*a*) stroboscope frequency $f = 700\,\mathrm{Hz}$; (*b*) stroboscope frequency $f = 350\,\mathrm{Hz}$. Unpublished pictures from the experiments of Monkewitz *et al.* [82], courtesy Hermann-Föttinger-Institut, TU Berlin.

1.2 Self-sustained oscillations in hot jets

Monkewitz, Bechert, Barsikow & Lehmann [82] were the first to observe the spontaneous onset of self-sustained oscillations in hot jets under controlled experimental conditions. Over a large streamwise region downstream of the nozzle, these oscillations were highly synchronized to a common frequency. Flow visualizations showed that the synchronized oscillations were associated with a street of regularly spaced axisymmetric ring vortices extending well into the downstream turbulent jet region. These ring vortices typically underwent one stage of vortex pairing, or "leap-frogging", at a fixed streamwise station.

The spatial structure of such a vortex street is pictured in figure 1.4, which presents two flow visualizations from the experiments of Monkewitz *et al.* [82]. The Reynolds number, based on jet diameter, is given as 10^4, and the jet temperature is 626 K. Both pictures are phase-averaged photographs

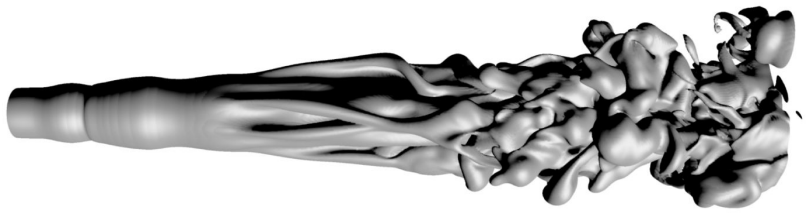

Figure 1.5: Snapshot of synchronized oscillations in a direct numerical simulation of a low-density jet at $S = 0.25$ and $Re_D = 1000$. Isosurface of a passive scalar, taken from Nichols [86].

of the same jet configuration, illuminated by a laser sheet strobed at the fundamental frequency $f = 700$ Hz in figure 1.4*a*, and at the subharmonic frequency $f = 350$ Hz in figure 1.4*b*. Four equidistant ring vortices may be distinguished in figure 1.4*a*. In figure 1.4*b*, a distinctive doubling of the vortex spacing is observed about three jet diameters downstream of the nozzle, where the regular structure in figure 1.4*a* vanishes as a result of vortex pairing.

The experiments of Monkewitz *et al.* [82] have shown that self-sustained oscillations set in as the ambient-to-jet temperature ratio $S = T_\infty/T_c$ falls below a critical value $S = 0.73$. The typical Strouhal number St, based on jet diameter and exit velocity, is given as St ~ 0.35 for the "mode I" state observed over the range of temperature ratios $0.63 \leq S \leq 0.73$. Below a second threshold value $S = 0.63$, a distinct new oscillating "mode II" state is reported to be dominant, with a new typical Strouhal number around 0.45. The pictures in figure 1.4 display the "mode II" state at temperature ratio $S = 0.47$; the fundamental Strouhal number may be estimated as St ~ 0.48.

Around the time of the Monkewitz *et al.* [82] experiments, Sreenivasan *et al.* [105] made similar observations in helium jets: these authors report the occurrence of intense self-sustained oscillations, also in the form of axisymmetric vortex rings, in jets with a jet-to-ambient density ratio below 0.6. A variable density ratio in these experiments was controlled by the mixing of helium and air in a jet emerging into pure air. Under the perfect gas assumption, the control parameter $S = T_\infty/T_c$ ([82]) may be equivalently defined as the jet-to-ambient density ratio $S = \rho_c/\rho_\infty$ ([105]). Only one oscillating state was observed by Sreenivasan *et al.* [105], with typical frequencies in good agreement with the "mode II" state of Monkewitz *et al.* [82].

Self-sustained oscillations in a jet with density ratio $S = 0.25$ have also been observed in recent direct numerical simulations by Nichols, Schmid & Riley [88]. A snapshot of a passive scalar field from these calculations is reproduced in figure 1.5. Unlike in the experiments [82, 105], no vortex pairing is observed by Nichols *et al.* [88], probably due to the choice of a low Reynolds number and a rather thick initial shear layer in comparison to the experimental settings. Instead, figure 1.5 demonstrates strong helical deformations of the initially axisymmetric ring vortices, setting in approximately five diameters downstream on the inlet.

1.3 Absolute instability in hot jets

The experiments of Monkewitz *et al.* [82] were theoretically motivated by the discovery that axisymmetric jets may undergo a transition from *convective* to *absolute* instability, if the jet is sufficiently heated with respect to the ambient air (Monkewitz & Sohn [85]). The concept of convective versus absolute instability has originally been formulated by Briggs [14] and Bers [7] for instability problems related to plasma physics. In the context of open shear flows, such as jets, absolute instability implies that an arbitrary initial perturbation in an infinite parallel flow gives rise to a wave packet which spreads simultaneously in the upstream and downstream directions, according to the linear equations of motion. The spatio-temporal spreading of the instability wave packet withstands the downstream advection, and hence contaminates the entire flow domain as $t \to \infty$. By contrast, in a convectively unstable setting, the downstream advection dominates over the upstream spreading of the instability, and the entire wave packet is convected away from the initial perturbation location. A precise definition of convective versus absolute instability in parallel open flows is given by Huerre & Monkewitz [54], together with the mathematical Briggs–Bers criterion used to discriminate between these two situations.

The linear instability analysis of Monkewitz & Sohn [85] revealed that absolute instability in hot round jets in the inviscid, zero-Mach-number limit first sets in for axisymmetric disturbances, at a temperature ratio $S = 0.72$. This critical upper limit is found for a velocity profile of finite vorticity thickness, given as $\theta_\omega = 0.087D$ in terms of the jet diameter D. The absolute instability threshold in a cylindrical vortex sheet has been determined as $S = 0.66$. Figure 1.6 is taken from Monkewitz & Sohn [85]. It displays the critical temperature ratios for the axisymmetric and first helical modes in a cylindrical vortex sheet as a function of Mach number: the transition to ab-

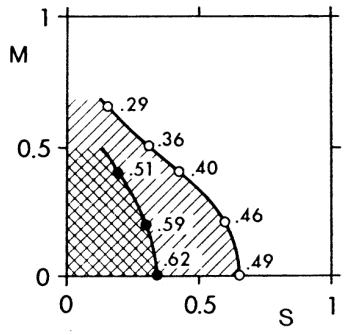

Figure 1.6: Absolute instability boundaries for the axisymmetric mode (○) and the first helical mode (●), in a cylindrical vortex sheet without counterflow. The hatched areas are the absolutely unstable regions, labels indicate the Strouhal number. Taken from Monkewitz & Sohn [85].

solute instability first sets in for axisymmetric disturbances, and the required heating increases with the Mach number.

1.4 From absolute to global instability

The distinction between convective and absolute instability in parallel flows can be related to the amplifier and oscillator behavior of non-parallel flows. This connection will be further elucidated in section 4.1; for introductory purposes, a heuristic argument may suffice to convey the principal idea.

If the streamwise development of the baseflow is slow over an instability wavelength, it may be assumed that perturbations at any streamwise station develop as if the baseflow was *locally* parallel. A baseflow that is only convectively unstable everywhere may amplify external perturbations, but in the absence of continuous forcing, the flow will ultimately return to a steady state. Intrinsic global oscillations can only be sustained in the presence of an absolutely unstable flow region, where initial perturbations may grow *in situ*. In the long-time limit, energy is continuously extracted from the baseflow within this region and transferred to perturbations that may drive a downstream global mode.

On the basis of this simple model, the local instability analysis of Monkewitz & Sohn [85] provides a convincing explanation for the observed global instability of low-density jets. Particularly striking is the agreement between the predicted critical temperature ratio $S = 0.72$ for the onset of absolute

instability and the experimental threshold value $S = 0.73$ for global instability, although no plausible argument for the occurrence of two distinct global modes has been proposed so far.

At the time of the Monkewitz *et al.* [82] experiments, global mode concepts were not yet sufficiently advanced to allow for further examination of the relationship between the observed oscillating states and local instability characteristics. It is precisely the goal of the present dissertation to ascertain whether recent developments in nonlinear global mode theory may predict the main features of synchronized oscillations in hot jets. A first result in this direction, for one parameter setting, is given by Nichols *et al.* [88], who report that the numerically observed global frequency in the low-density jet shown in figure 1.5 matches the absolute frequency of the inlet profile within 13.5%.

1.5 Acoustic field of instability wave packets

Linear perturbations of a parallel baseflow can be represented in the form of normal modes evolving independently in time and space. Acoustic and instability-related waves in a linear parallel system are decoupled, and at low Mach numbers may be distinguished with regard to their phase velocity. In non-parallel situations, or via nonlinear effects, acoustic and instability perturbations are coupled: an instability wave packet therefore radiates sound.

The starting point of modern aeroacoustics has been marked by the seminal work of Lighthill [71], who cast the equations of fluid motion in the form of a free-space wave operator for acoustic fluctuations, separated from nominal aeroacoustic source terms. Even though this separation is physically meaningful only when the ambient medium is at rest, Lighthill's theory has paved the way for most of the progress made in aeroacoustic sound prediction ever since.

Whereas Lighthill conceived a jet as made up of uncorrelated convecting quadrupoles associated with turbulent eddies, Huerre & Crighton [52], following the work of Tam *et al.* [107], envisioned the jet dynamics as resulting from deterministic instability waves superposed on an appropriate baseflow. On this basis, Huerre & Crighton [52] analysed the acoustic field emitted by an instability wave packet in a spatially developing round jet. Their theoretical study was motivated by experimental investigations of sound radiation due to vortex pairing in a forced isothermal jet, conducted by Laufer & Yen

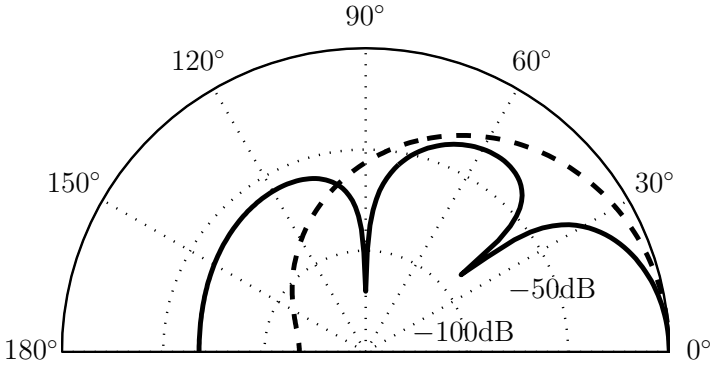

Figure 1.7: Polar diagram of superdirective sound radiation. Dashed line: expression (1.2), given by Laufer & Yen [65]; solid line: Lighthill solution derived by Huerre & Crighton, quadrupole pattern with superdirective antenna factor.

[65]. These measurements displayed a decay of far-field acoustic intensity I as a function of the observation angle ϑ, taken with respect to the downstream jet axis, in the form

$$I(\vartheta) \propto \exp\left[-A(1 - \mathrm{Ma}\,\cos\vartheta)^2\right] , \quad A = 45. \tag{1.2}$$

Acoustic fields exhibiting such an exponential decay in their directivity pattern have been named *superdirective* [32]. Expression (1.2) is plotted in figure 1.7 as a dashed line. The streamwise variation of the vortex pairing amplitude, in the experiments of Laufer & Yen [65], displayed the shape of a Gauß distribution, with a half-width of only one tenth of the acoustic wavelength. Superdirective radiation from such a compact source appeared to contradict usual aeroacoustic assumptions.

Huerre & Crighton [52] demonstrated that evaluation of Lighthill's equation for a Gaussian shaped near-field source distribution indeed yields an *antenna factor* of the general form (1.2), although their analysis predicted a factor $A = 26$ for the source envelope width measured by Laufer & Yen [65]. However, in the theoretical description this antenna factor only provides a modulation of the underlying classical quadrupole directivity that Lighthill's theory predicts for vortex sound, resulting in a pattern of several acoustic lobes, separated by angles where the intensity is zero (solid line in figure 1.7). No such lobe structure was detected by Laufer & Yen [65]. In a following study, Crighton & Huerre [32] examined a "wavy wall" model problem for acoustic radiation caused by amplitude-modulated near-field pressure fluctuations, neglecting the quadrupole character of the dominant Lighthill source

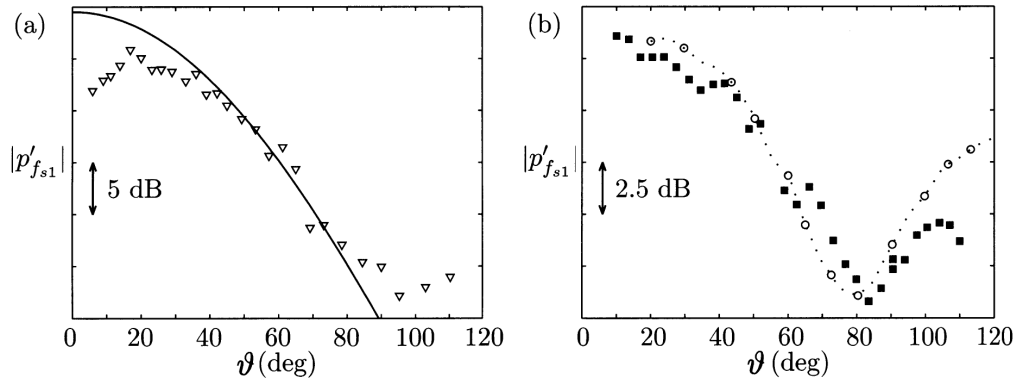

Figure 1.8: Vortex pairing sound measurements. (*a*) Superdirectivity measured by Fleury *et al.* [40] (▽), and according to expression (1.2), where $I \propto |p'_{s1}|^2$ (—). (*b*) Two-lobe directivity pattern measured by Fleury *et al.* [40] (■) and by Bridges & Hussain [13] ($\cdot \circ \cdot$). Both figures taken from Fleury *et al.* [40].

terms. It was demonstrated that the form of the antenna factor due to near-field amplitude modulations depends crucially on the precise spatial envelope shape, not only in the streamwise region of strong oscillations, but also in the very low-amplitude wings of the wave packet. Only a generalized Gaussian envelope shape of near-field oscillations $|p'| \propto \exp[-(x/\sigma)^n]$ was found to produce a superdirective radiation pattern (1.2).

Experimental evidence for superdirective acoustic radiation is scarce. The observations of Laufer & Yen [65] have been confirmed only in one instance by Fleury *et al.* [40, 41]: a superdirective pattern of the form (1.2) is reported in one particular flow configuration, where the jet shear layer at the nozzle is transitional (figure 1.8*a*). In a jet with a laminar exit profile, Fleury *et al.* [40] measure instead a two-lobe directivity pattern, in good agreement with the experiments of Bridges & Hussain [13](figure 1.8*b*). The two-lobe pattern is well described by an analytical expression derived by Fleury *et al.* [41] from an axisymmetric "wavy wall" approach.

The theoretical analyses [52, 32] make no assumptions explicitly connected to vortex pairing; any amplitude-modulated wave packet may be considered as aeroacoustic source. In chapter 5, the approach of Huerre & Crighton [52] will be pursued in order to investigate the acoustic field associated with a nonlinear global mode in a hot jet.

1.6 Objectives

Since the experimental discovery of self-sustained oscillations in hot jets, considerable progress has been made in the theoretical description of nonlinear global modes. Specifically, model analyses of Couairon *et al.* [24, 25, 26, 27] and Pier *et al.* [94, 95, 96] have led to new insights into the frequency selection process in fully nonlinear globally unstable systems. These models have been developed from arguments based on front dynamics, in the context of Ginzburg–Landau model equations. Fundamental criteria derived from the Ginzburg–Landau model, concerning the global frequency selection as well as the spatial structure of global modes, have since been verified to hold true in real flow situations for wakes (Zielinska & Wesfreid [117], Couairon & Chomaz [27], Pier & Huerre [94], Chomaz [18], Pier [93]) and for swirling jets (Gallaire *et al.* [44]). The main objective of this dissertation is to examine whether the intrinsic dynamics of hot jets bear the characteristics of front-dominated nonlinear global modes, and whether their frequency can be accurately predicted from the theoretical model described in section 4.1.

Such comparison between physical flow behavior and model predictions demands highly controlled flow conditions, as well as the liberty to study idealized flow situations, wherever this may be necessary in order to approach the assumptions of the theoretical model. The dynamics of physical jets are therefore studied via direct numerical simulations. Based on experimental evidence, and in agreement with theoretical predictions derived from the linear instability analysis of Monkewitz & Sohn [85], the relevant flow dynamics are assumed to be axisymmetric. The numerical code is therefore developed for an axisymmetric geometry.

The spatial structure of a global mode takes the form of an extended wave packet, modulated in amplitude and phase along the streamwise direction of the jet. The second objective of this dissertation is to compute the sound field associated with this structure, and to compare the numerical results to a prediction based on Lighthill's equation. The theory of Crighton & Huerre [32] predicts that an extended wave packet, under certain conditions, may emit a superdirective acoustic far field. The analysis of Huerre & Crighton [52] will be adapted to the hot jet configuration, and predictions will be compared to the acoustic field computed directly from the Navier–Stokes equations. The direct numerical simulation is therefore implemented for the compressible equations of motion, and the numerical domain is chosen large enough to extend into the acoustic far field. Simulations of this genre are also referred to as *direct noise computations* (DNC).

1.7 Outline

The body of this dissertation is composed of four chapters:

Linear local instability properties of hot jets are analysed in chapter 2. New results with regard to the existing literature have been compiled into a self-contained article, which alone forms this chapter. The spatio-temporal instability characteristics of parallel jets are retrieved from the *linear impulse response* wave packet, obtained numerically by solving the compressible dispersion relation. It is demonstrated that the action of the *baroclinic torque* is alone responsible for the transition from convective to absolute instability in hot jets. The competition between *jet column* and *shear layer* modes is investigated for parallel jets. An appendix to the article of chapter 2 describes in detail the numerical method used for the linear instability analysis. The results of this chapter form the basis for the later global instability studies.

Direct numerical simulation is used as a means to investigate physical jet dynamics. The numerical method is exposed in chapter 3. Spatially developing baseflows are computed according to the boundary layer equations prior to the direct simulation of perturbations according to the unsteady compressible equations of motion. Spatial and temporal schemes of the flow solver are documented in full detail. The greatest numerical difficulty lies in the numerical boundary treatment, which receives due attention in this chapter. Validation tests demonstrate the accuracy of baseflow and perturbation computations as well as the performance of the numerical boundary conditions.

Nonlinear global instability of hot jets is investigated in chapter 4. First, the existing theoretical model for the description of global modes is introduced. Theoretical predictions about the onset of global instability and about the global frequency are then compared to DNS results. These studies are presented in the form of two publications. The first, section 4.2, establishes the validity of the theoretical model for a family of jets with rather *thick* shear layers. The second article, section 4.3, extends the investigation to the numerically less benign case of jets with *thin* shear layers in order to approach the experimental conditions of Monkewitz *et al.* [82].

Sound generation by a nonlinear global mode is the topic of chapter 5. Explicit solutions of the Lighthill equation are derived for axisymmetric jets, thereby providing a prediction of the acoustic far field associated with a

given instability wave packet. These predictions are compared to the directly computed sound field. The Lighthill formulation allows to examine the contribution of individual source terms to the total acoustic field. The procedure is validated for the case of a forced isothermal jet, then applied to a typical global mode in a hot jet.

Chapter 2

Linear impulse response in hot round jets

Lutz Lesshafft and Patrick Huerre
Laboratoire d'Hydrodynamique (LadHyX), CNRS – École Polytechnique,
91128 Palaiseau, France

published in *Physics of Fluids*, volume 19, issue 2

Abstract

The linear impulse response of axisymmetric jets is examined for a family of variable-temperature profiles typical of the potential core. The influence of jet heating, shear layer thickness, Reynolds and Mach number on the spatio-temporal stability of both axisymmetric and helical modes is investigated. The linear impulse response is retrieved from a numerical solution of the spatial eigenvalue problem, which is derived from the fully compressible equations of motion. Changes in the spatio-temporal stability of heated versus isothermal jets are shown to arise solely from the effect of the baroclinic torque. By considering the full linear impulse response, the competition between jet column modes and shear layer modes is characterized. Jet column modes are only found to occur for axisymmetric disturbances. In *thin* shear layer jets, the jet column mode is shown to prevail at low group velocities, whereas axisymmetric and helical shear layer modes dominate at high group velocities. The absolute mode of zero group velocity is found to always be of the jet column type. Although only convectively unstable, the maximum growth rates of the shear layer modes greatly exceed those of the jet column modes in thin shear layer jets. In *thick* shear layer jets, axisymmetric modes of mixed jet column / shear layer type arise. The weakened maximum growth rate of mixed modes accounts for the dominance of helical modes in temporal stability studies of thick shear layer jets.

2.1 Introduction

The theoretical and experimental studies of Monkewitz & Sohn [85] and Monkewitz, Bechert, Barsikow & Lehmann [82] have provided strong evidence that the occurrence of self-sustained oscillations in sufficiently heated jets is connected to a transition from convective to absolute instability of the unperturbed flow state. The objective of the present investigation is to fully characterize the linear instability modes that are observed in hot jets, as a function of their group velocity. Such instability modes precisely constitute the ingredients of the linear impulse response. A family of parallel velocity and temperature profiles typical of the potential core region in spatially developing jets is considered, and their spatio-temporal stability characteristics are determined from the full linear impulse response wave packet. An analysis of the dispersion relation allows to identify the physical mechanism by which hot jets become absolutely unstable. It should be understood that all results obtained for hot jets equally pertain to cases where density variations are due to the mixing of nonhomogeneous fluids, as for instance Helium jets in air [105, 11, 116].

The effect of temperature variations on the spatial instability of axisymmetric jets has been studied theoretically by Michalke [77, 78]. In agreement with earlier predictions drawn from the analysis of plane shear layers (Blumen [8]), heating of the jet with respect to the surrounding fluid was shown to promote the spatial growth of externally forced perturbations. Michalke identified a "regular" and an "irregular" unstable axisymmetric mode. Unexplained at the time, the eigenvalues of these two modes seemed to interchange as the ambient-to-jet temperature ratio fell below 0.7. Once the concepts of absolute and convective instability [14, 7] had been introduced to fluid mechanics, Huerre & Monkewitz [53] later interpreted the "irregular" mode as an upstream-travelling k^--branch, and the apparent mode interchange as a result of the onset of absolute instability.

The occurrence of absolute instability in hot round jets without counterflow has been firmly established by Monkewitz & Sohn [85]. These authors investigated the transition from convective to absolute instability in terms of the temperature ratio, the Mach number, and the shear layer thickness relative to the jet radius. Absolute instability was found to first set in for axisymmetric perturbations, at a critical temperature ratio of 0.72 and finite shear layer thickness. In contrast, Pavithran & Redekopp [92] demonstrated that nonhomogeneous plane shear layers only display absolute instability in the presence of counterflow.

Jendoubi & Strykowski [56] extended the analysis of Monkewitz & Sohn [85] to jets with ambient co- and counterflow. Their study remains the most comprehensive spatio-temporal analysis of axisymmetric jets to this day. Restricted to axisymmetric disturbances, their investigation revealed the presence of two distinct instability modes. In a thin shear layer jet, the first of these axisymmetric modes was shown to be closely related to the plane shear layer instability described by Pavithran & Redekopp [92]: All perturbations are concentrated within the jet shear layer region, and absolute instability only occurs in the presence of sufficiently strong counterflow. This mode will be denoted as the *shear layer mode* throughout this paper. The second mode was shown to be identical with the absolute instability mode discovered by Monkewitz & Sohn [85]. Its pressure eigenfunction peaks on the jet axis. Henceforth, this mode will be denoted as the *jet column mode*.

While the study of Jendoubi & Strykowski [56] clearly identifies the convective/absolute transition of the shear layer and jet column modes as a function of temperature ratio and external flow, the respective roles of these two competing modes in a given base flow cannot be understood by considering the absolute instability mode of zero group velocity alone. Arbitrary perturbations in real flows will always create non-zero group velocity modes, that may experience strong temporal amplification. The aim of the present paper is to provide a spatio-temporal instability analysis in terms of the full linear impulse response. The whole wave packet evolving from an initial Dirac-type perturbation according to the linear equations of motion is considered. This wave packet is composed of a continuous spectrum of jet column and shear layer modes, each one traveling in the axial direction at a distinct group velocity v_g. The simultaneous growth of jet column and shear layer modes can therefore be characterized as a function of their group velocity. For a review of spatio-temporal instability theory, the reader is referred to Huerre [51]. Unlike Ref. [56], axisymmetric as well as *helical* modes are considered. The inviscid results of Monkewitz & Sohn [85] and Jendoubi & Strykowski [56] are further complemented by parameter studies of the convective/absolute instability boundary at finite Reynolds and Mach numbers and for thin and thick shear layers. The analysis is restricted to situations with zero external flow without loss of generality, as the effect of co- or counterflow on the linear impulse response wave packet in parallel jet profiles can be obtained by a simple transformation provided in section 2.2.

The paper is organized as follows: The formulation of the base flow and the mathematical model for the linear instability analysis are defined in section 2.2. The numerical solution of the dispersion relation is briefly outlined in section 2.3. The eigenvalue problem representing the compressible viscous

dispersion relation is documented in the appendix, together with further details of its numerical discretization. The linear impulse response of an isothermal *thin* shear layer jet is examined in section 2.4.1 and compared to corresponding results obtained for a hot jet in section 2.4.2. Modifications of the dispersion relation lead to identify the physical mechanism responsible for the occurrence of absolute instability in hot jets. The linear impulse response of a *thick* shear layer jet as well as the influence of the Reynolds and Mach number on the onset of absolute instability are examined in section 2.4.3. The paper concludes with a summary of the main results.

2.2 Problem formulation

The linear impulse response is determined for an axisymmetric compressible jet base flow of density ρ_b, temperature T_b, pressure p_b and axial velocity u_b. The base flow is considered to be parallel in the axial direction and swirl-free, the radial and azimuthal velocity components v_b and w_b therefore are zero. The flow geometry is formulated in cylindrical coordinates (x, r, ϕ). All flow variables are given in non-dimensional form, scaled with respect to the jet radius R and the jet centerline values U_c, ρ_c and T_c. An analytical expression for base flow velocity profiles, typical of the potential core region in laboratory jets, is taken from Michalke [77]:

$$u_b(r) = \frac{1}{2} + \frac{1}{2}\tanh\left[\frac{R}{4\theta}\left(\frac{1}{r} - r\right)\right]. \tag{2.1}$$

The velocity profile is characterized by the parameter R/θ, where θ denotes the momentum thickness of the shear layer. The radial temperature variation for a given ambient-to-jet temperature ratio $S = T_\infty/T_c$ is linked to the velocity profile via the Crocco–Busemann relation [78]

$$T_b(r) = S + (1 - S)u_b(r) + \frac{\gamma - 1}{2}\mathrm{Ma}^2\left[1 - u_b(r)\right]u_b(r). \tag{2.2}$$

The Mach number is defined as $Ma = U_c/c_c$, with c_c the speed of sound on the jet centerline, and the ratio of specific heats γ is chosen as 1.4 throughout this study. The pressure p_b in the unperturbed jet is constant and can be obtained from the equation of state for a perfect gas

$$p = \frac{1}{\gamma \mathrm{Ma}^2}\rho T. \tag{2.3}$$

On the centreline, where ρ_b and T_b are unity, one finds

$$p_b = \frac{1}{\gamma \mathrm{Ma}^2}. \tag{2.4}$$

The density profile is then given as

$$\rho_b(r) = T_b(r)^{-1}. \tag{2.5}$$

The flow is assumed to be governed by the compressible equations of continuity, momentum and energy, written in total flow quantities as

$$\begin{aligned}
\frac{d\rho}{dt} &= -\rho \mathrm{div}\ \mathbf{u} && (2.6)\\
\rho \frac{d\mathbf{u}}{dt} &= -\mathrm{grad}\ p + \mathrm{div}\ \boldsymbol{\tau} && (2.7)\\
\rho \frac{d}{dt}\left(\frac{p}{\rho}\right) &= -(\gamma-1)p\ \mathrm{div}\ \mathbf{u} && (2.8)\\
&\quad + (\gamma-1)\boldsymbol{\tau} : \boldsymbol{\varepsilon} + \frac{\gamma}{Re\ Pr}\ \Delta\left(\frac{p}{\rho}\right),
\end{aligned}$$

with the Reynolds and Prandtl numbers defined as

$$Re = \frac{\rho_c R U_c}{\mu}, \quad Pr = c_p \frac{\mu}{\kappa}. \tag{2.9}$$

The viscous stress tensor $\boldsymbol{\tau}$ and the rate of strain tensor $\boldsymbol{\varepsilon}$ are given by

$$\begin{aligned}
\boldsymbol{\tau} &= -\frac{2}{3Re}(\mathrm{div}\ \mathbf{u})\mathbf{I} + \frac{2}{Re}\boldsymbol{\varepsilon} && (2.10)\\
\boldsymbol{\varepsilon} &= \frac{1}{2}\left(\mathrm{grad}\ \mathbf{u} + \mathrm{grad}^T\ \mathbf{u}\right). && (2.11)
\end{aligned}$$

The dynamical viscosity μ and thermal conductivity κ are taken to be constant throughout the flow and related by a Prandtl number of unity.

Small perturbations (ρ', u', v', w', p') to the base flow, where (u', v', w') denote the (x, r, ϕ) components of the perturbation velocity, are now expressed as normal modes of complex axial wave number k, integer azimuthal wave number m and complex angular frequency ω according to:

$$\begin{bmatrix} \rho' \\ u' \\ v' \\ w' \\ p' \end{bmatrix} (x, r, \phi, t) = \begin{bmatrix} D(r) \\ H(r) \\ iF(r) \\ G(r) \\ P(r) \end{bmatrix} e^{i(kx + m\phi - \omega t)} + \text{c.c.} \tag{2.12}$$

The notation (H, F, G, P) in equation (2.12) has been chosen to correspond to the incompressible problem formulation of Khorrami *et al.* [57]. Substitution of (2.12) into the equations of motion (2.6–2.8), linearized about the base flow, yields a linear system of ordinary differential equations. In the same manner as in Ref. [57], this system is cast in the form of a generalized eigenvalue problem which, for prescribed values of the frequency ω, admits spatial eigenvalues k and corresponding complex eigenfunctions (D, H, F, G, P). The compressible spatial eigenvalue problem is stated explicitly in the appendix.

At large times t, the linear impulse response along each spatio-temporal ray $x/t = const$ is dominated by the absolute instability mode in the reference frame moving at $v = x/t$ with respect to the laboratory frame (see Ref. [55]). In order to construct numerically the linear impulse response, values of $\omega(v_g)$, $k(v_g)$ for a given group velocity v_g can therefore be computed as the absolute instability modes in the co-moving reference frame $(\tilde{r}, \tilde{x}) = (r, x - v_g t)$, where the axial base flow velocity profile becomes $\tilde{u}_b(r) = u_b(r) - v_g$. The resulting values $\tilde{\omega}_0, \tilde{k}_0$ are then transformed back into the laboratory reference frame according to the relations $\omega(v_g) = \tilde{\omega}_0 + \tilde{k}_0 v_g$ and $k(v_g) = \tilde{k}_0$. For each azimuthal wave number m, results are presented in the laboratory frame in terms of real frequency $\omega_r(v_g)$ and spatio-temporal growth rate $\sigma(v_g) = \omega_i(v_g) - k_i(v_g)v_g = \tilde{\omega}_{0,i}$ along each ray $x/t = v_g$.

By construction, it is clear that the effect of external co- or counterflow on the linear impulse response merely results in an offset of v_g and a Doppler shift of the real frequency [35]. From the distributions $\omega_r(v_g)$, $\sigma(v_g)$, $k_r(v_g)$, $k_i(v_g)$ in a situation with zero external flow, the corresponding distributions $\tilde{\omega}_r(v_g)$, $\tilde{\sigma}(v_g)$, $\tilde{k}_r(v_g)$, $\tilde{k}_i(v_g)$ in a situation with external flow $\tilde{u}_b = u_b + u_e$ are obtained as

$$\begin{aligned} \tilde{\omega}_r(v_g) &= \omega_r(v_g - u_e) - u_e k_r(v_g - u_e) \\ \tilde{\sigma}(v_g) &= \sigma(v_g - u_e) \\ \tilde{k}_r(v_g) &= k_r(v_g - u_e) \\ \tilde{k}_i(v_g) &= k_i(v_g - u_e)\,. \end{aligned} \tag{2.13}$$

2.3 Numerical method

In order to compute values of the absolute frequency and wavenumber, Monkewitz & Sohn [85] as well as Jendoubi & Strykowski [56] used a shooting method to numerically solve the dispersion relation in the form of a single-variable ordinary differential equation [77]. The numerical procedure used in the present study closely follows the Chebyshev collocation method described by Ash & Khorrami [2], which only had to be extended to include

compressible effects. For a given set of parameters $(m, v_g, R/\theta, S, Re, \mathrm{Ma})$, the eigenvalue problem (2.20–2.24) is discretized and solved numerically for the spatial branches $k(\omega)$. A code provided by Olendraru & Sellier [89] has been adapted to the compressible jet problem. The complex pair (k_0, ω_0) is then determined by tracking the point where a k^+ and a k^- branch pinch in the complex k-plane[14, 8]. For this purpose, the iterative search algorithm described in Ref. [85] was found to be reliable and very time-efficient. The transformation used for an appropriate distribution of collocation points for thin shear layer jet profiles is given in the appendix. A validation of the numerical procedure has been presented in Ref. [69] by comparing the $\sigma(v_g)$ distribution computed from the dispersion relation for $m = 0$ to the results of a direct numerical simulation of the axisymmetric linear Navier–Stokes equations.

2.4 Results

2.4.1 Incompressible inviscid jet

We first consider the linear impulse response of an isothermal jet ($S = 1$) in the inviscid, zero-Mach-number limit. The velocity profile parameter for this *thin shear layer* example is chosen as $R/\theta = 20$. While such a profile may not be considered 'thin' by some readers, comparison with the results discussed in section 2.4.3 will show that the separation of scales between jet radius and shear layer thickness is sufficient to allow a discussion of the spatio-temporal characteristics of arbitrarily thin shear layer jets. The spatio-temporal growth rate σ, real frequency ω_r, real wavenumber k_r and spatial growth rate $-k_i$ of the axisymmetric ($m = 0$) component are presented in figure 2.1 (thin lines) as functions of their group velocity v_g.

A discontinuity in the spectrum at $v_g = 0.182$ divides the wave packet into two regions, each composed of a distinct class of instability modes. The low group velocity modes correspond to absolute instability modes in jets with zero or moderate counterflow. According to Jendoubi & Strykowski [56], these modes are of the *jet column* type. Modes travelling at group velocities $v_g > 0.182$ correspond to absolute instability modes in jets with strong counterflow, characterized as being of the *shear layer* type[56]. This distinct jet column / shear layer character is confirmed in figure 2.2: For two profile parameters $R/\theta = 20$ (thin line, same as in figure 2.1) and $R/\theta = 40$ (thick line), the $\sigma(v_g)$ distributions are compared when scaled with respect to the jet radius R (figure 2.2a) and the shear layer momentum thickness θ

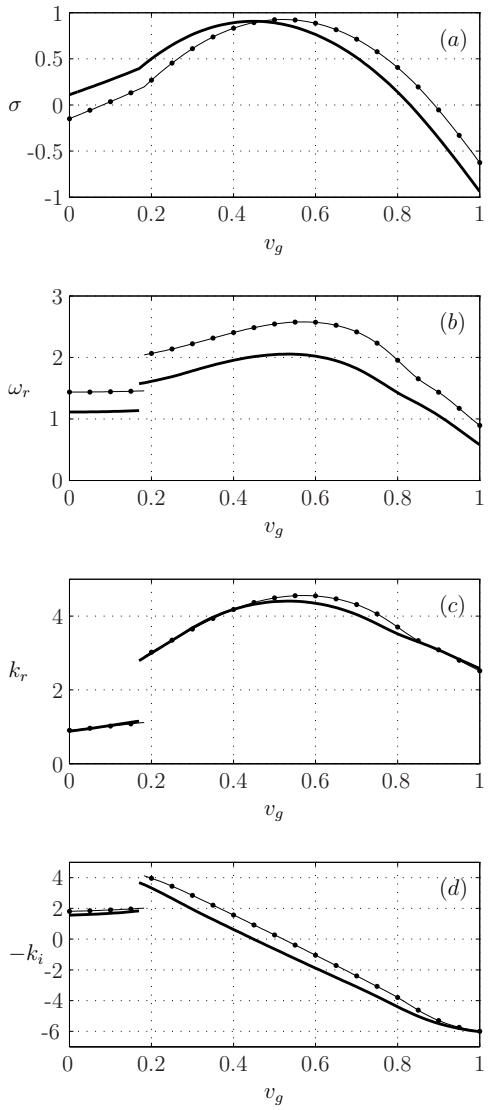

Figure 2.1: Axisymmetric linear impulse response for flow parameters $R/\theta = 20$, $Re = \infty$, Ma $= 0$. Isothermal case $S = 1$ (thin line); heated case $S = 0.5$ (thick line); heated case $S = 0.5$ in the absence of baroclinic torque (•). (a) Spatio-temporal growth rate; (b) real frequency; (c) real wavenumber; (d) spatial growth rate, all as functions of group velocity v_g.

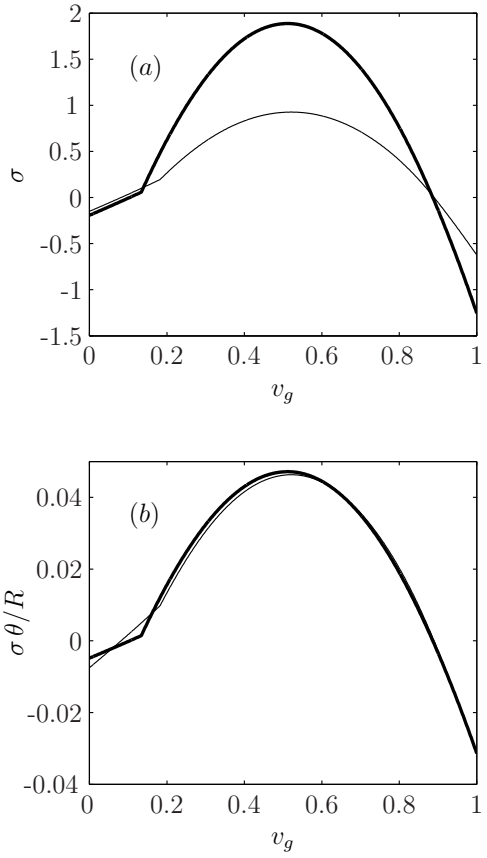

Figure 2.2: Comparison of the spatio-temporal growth rates σ in jets for $R/\theta = 20$ (thin line) and $R/\theta = 40$ (thick line); $m = 0$, $S = 1$, $Re = \infty$, Ma $= 0$. (a) σ scaled with jet radius R; (b) σ scaled with shear layer thickness θ.

(figure 2.2b), respectively. The growth rate is found to scale with R for the low group velocity modes and with θ for the high group velocity modes.

Jendoubi & Strykowski [56] have shown that the absolute instability mode in jets with variable external flow arises from pinching events involving the same unstable k^+ branch, but two distinct k^- branches for the shear layer and jet column modes. It should be pointed out that only one of these two pinching events, i.e. the one occurring at a higher value of σ, is to be regarded as physically relevant [54]. The interaction of a unique k^+ branch with one out of several k^- branches has also been reported by Loiseleux, Chomaz & Huerre [72] to produce distinct absolute instability modes in swirling jets with counterflow. The pinching between branches in the complex k-plane is presented in figure 2.3 for the case considered here, for two group velocities

$v_g = 0$ and $v_g = 0.3$. The displayed branches are obtained as solutions of the dispersion relation for given values $\omega = \omega_r + i\omega_i$, where ω_r is continuously varied for three fixed values of ω_i. Consistent with the notation of Ref. [72], let k_1^- denote the spatial branch in our problem which upon pinching with the k^+ branch gives rise to a jet column mode, and k_2^- its counterpart for the shear layer mode. At $v_g = 0$ (figure 2.3a), the k^+,k_1^-,k_2^- branches are well separated for $\omega_i = 0$ (thin solid lines). With $\omega_i = \omega_{0,i} = -0.150$ (thick lines), the k^+ and k_1^- branches pinch at the saddle point $k_0 = 0.901 - 1.808i$ for a real frequency $\omega_{0,r} = 1.436$. These values correspond to those plotted in figure 2.1 at $v_g = 0$. If ω_i is lowered further, a second saddle point is eventually formed by the merged k^+/k_1^- branch and the k_2^- branch (dashed lines). However, formal solutions of the dispersion relation for $\omega_i < \omega_{0,i}$ are non-causal [51], and therefore do not correspond to physical situations. Only the pinching events between k^+ and k^- branches occurring at the highest value of ω_i are taken into account in this study.

Corresponding k branch diagrams in figure 2.3b display that the relevant saddle point for $v_g = 0.3$ is formed between the k^+ and k_2^- branches; the associated instability mode is of the shear layer type, as for all group velocities $v_g > 0.182$. A different scenario is observed in *thick shear layer* jets, as discussed in section 2.4.3.

According to figure 2.1, a real wavenumber $k \sim 1$ is found to be typical of the jet column modes. This value corresponds to a wavelength $\lambda \sim 2\pi$, large when compared to the shear layer mode wavelengths, and a real phase velocity ω_r/k_r larger than the jet centreline velocity. The parabola-shaped variation of $\sigma(v_g)$ at group velocities $v_g > 0.182$ is typical of the Kelvin–Helmholtz instability for a plane shear layer. The mode of maximum spatio-temporal growth, which corresponds to the most unstable temporal mode with $\omega_{i,max} = \sigma_{max}$ and $k_i = 0$ (see for instance Huerre [51]), is of the shear layer type. Since $\sigma(0) < 0$ and $\sigma_{max} > 0$, the isothermal jet is convectively unstable, in agreement with Monkewitz & Sohn [85].

The growth rates of the first four azimuthal modes ($m = 1, 2, 3, 4$) are compared to the $m = 0$ mode in figure 2.4. The maximum values σ_{max} of each individual curve are seen to slowly diminish with increasing azimuthal wave number m. However, the growth rates of the $m = 0$ shear layer modes and the $m = 1$ modes are nearly identical. All modes $m \geq 1$ are of the shear layer type, whatever the value of v_g. At low group velocities, and in particular at $v_g = 0$, the linear impulse response is clearly dominated by the axisymmetric jet column mode.

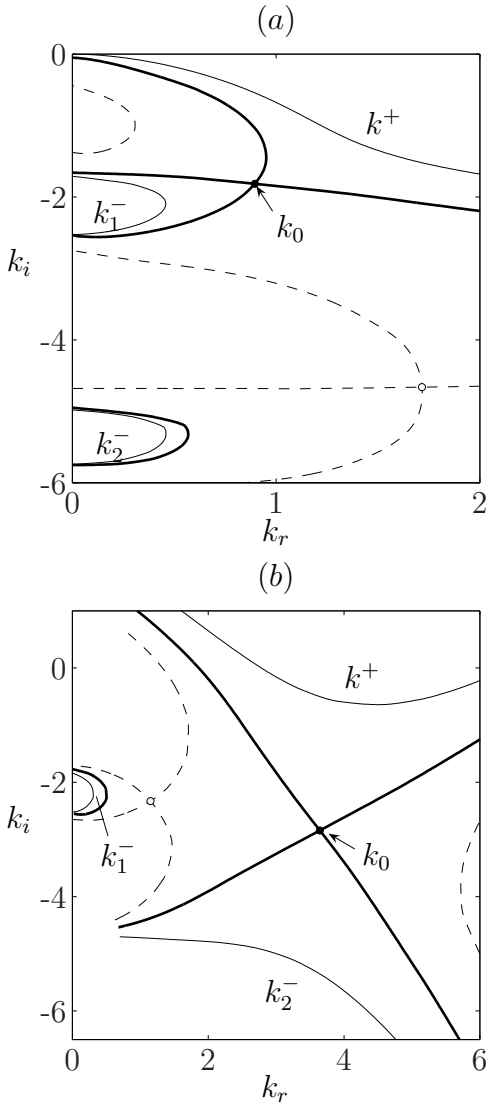

Figure 2.3: Branches in the complex k-plane for $R/\theta = 20$, $S = 1$, $Re = \infty$ and $Ma = 0$.
a) $v_g = 0$, three constant values of ω_i: 0 (—), 0.15 (—), 0.63 (---); b) $v_g = 0.3$, three constant values of ω_i: 0.8 (—), 0.61 (—), 0.45 (---).

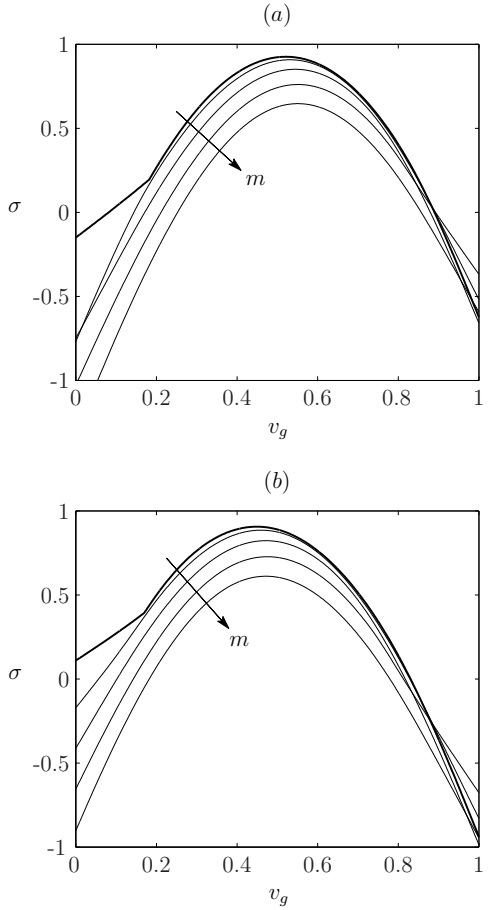

Figure 2.4: Growth rates σ of the axisymmetric $m = 0$ mode (thick line) and azimuthal modes $m = 1, 2, 3, 4$ in a thin shear layer jet; $R/\theta = 20$, $Re = \infty$, $Ma = 0$. (a) $S = 1$; (b) $S = 0.5$.

2.4.2 Influence of the temperature ratio S: Baroclinic torque

The effect of a non-uniform temperature profile on the spatio-temporal instability of a jet is demonstrated for a temperature ratio $S = 0.5$, with all other parameters identical to the isothermal case described in the previous section.

The axisymmetric linear impulse response of the heated jet is given in figure 1 (thick lines) for comparison with the isothermal case. For the jet column mode ($v_g < 0.170$), the heating is seen to give rise to an overall increase of the growth rate σ, while the real frequency takes on lower values. In agreement with the analysis of Monkewitz & Sohn [85], the $S = 0.5$ case is found to be absolutely unstable ($\sigma(0) > 0$). The complex wavenumbers of the jet column modes are hardly affected by the temperature ratio. The parabola-shaped σ distribution of the shear layer modes is shifted towards lower group velocities as compared to the isothermal case, but the maximum growth rate σ_{max} remains approximately the same. The growth rates of the azimuthal modes of the heated jet, displayed in figure 2.4b, are found to display the same trend. As in isothermal jets, the axisymmetric and first azimuthal modes are in close competition for high group velocities. All azimuthal modes are convectively unstable at $S = 0.5$.

It has been suggested by Soteriou & Ghoniem [103] that differences in the instability characteristics of homogeneous and non-homogeneous shear layers may be ascribed to the action of the baroclinic torque. According to these authors, the presence of a baroclinic vorticity dipole within a rolled-up eddy may explain the lateral displacement of the eddy core into the low-density stream as well as the bias of its convection speed towards the velocity of the high-density stream. Both of these features are in qualitative agreement with numerical observations [103].

Following this idea, the role of baroclinic effects in the linear impulse response of a heated jet is quantitatively assessed by solving a modified dispersion relation, in which the baroclinic torque term is counterbalanced by appropriate forcing. Only the axisymmetric case is considered here. In the presence of source terms denoted as S_x and S_r, the linear inviscid momentum equations become

$$\frac{\partial u'}{\partial t} = -v'\frac{\partial u_b}{\partial r} - u_b\frac{\partial u'}{\partial x} - \frac{1}{\rho_b}\frac{\partial p'}{\partial x} + S_x \tag{2.14a}$$

$$\frac{\partial v'}{\partial t} = -u_b\frac{\partial v'}{\partial x} - \frac{1}{\rho_b}\frac{\partial p'}{\partial r} + S_r, \tag{2.14b}$$

and the azimuthal perturbation vorticity $\Omega'_\theta = \text{curl}\ \mathbf{u}'$ is found to evolve as

$$\begin{aligned}\frac{\partial \Omega'_\theta}{\partial t} &= v'\frac{\partial^2 u_b}{\partial r^2} + u_b\frac{\partial^2 u'}{\partial x \partial r} - u_b\frac{\partial^2 v'}{\partial x^2} \\ &\quad + \frac{\partial u_b}{\partial r}\left(\frac{\partial u'}{\partial x} + \frac{\partial v'}{\partial r}\right) \\ &\quad - \frac{1}{\rho_b^2}\frac{\partial \rho_b}{\partial r}\frac{\partial p'}{\partial x} + \frac{\partial S_r}{\partial x} - \frac{\partial S_x}{\partial r}. \end{aligned} \tag{2.15}$$

In order to eliminate the effect of the baroclinic torque $(\nabla\rho \times \nabla p)/\rho^2$, the source terms S_x and S_r are selected so as to satisfy the constraint

$$\frac{\partial S_r}{\partial x} - \frac{\partial S_x}{\partial r} = \frac{1}{\rho_b^2}\frac{\partial \rho_b}{\partial r}\frac{\partial p'}{\partial x} \tag{2.16}$$

without introducing mass sources in the continuity equation, i.e.

$$\frac{1}{r}\frac{\partial}{\partial r}\left(r\rho_b S_r\right) + \frac{\partial}{\partial x}\left(\rho_b S_x\right) = 0. \tag{2.17}$$

A modified dispersion relation is now constructed from the forced momentum equations (2.14) and the unforced continuity and energy equations, together with the forcing conditions (2.16,2.17). The source terms S_x and S_r are considered as new additional variables of the generalized eigenvalue problem.

The resulting linear impulse response is included in figure 2.1 for $S = 0.5$ (bullet symbols). Without the action of the baroclinic torque, all curves for $S = 0.5$ and $S = 1$ are found to be identical within the accuracy of the calculations, which we believe to be exact to at least four significant digits in ω_0. It may therefore be concluded that the baroclinic torque is responsible for the onset of absolute instability in heated jets, whereas other terms involving S in the continuity and energy equations are negligible. Note that the role of gravity has been neglected in these calculations, and that the baroclinic torque arises only from the base flow temperature gradient and the pressure eigenfunction.

A physical interpretation of how the baroclinic torque contributes to the destabilization of the absolute mode can be deduced from an inspection of the eigenfunction. In figure 2.5, the spatial distribution of the baroclinic torque Γ_{bc} is superposed with the total displacement η of the shear layer at $r = 1$, both computed for the absolute mode of the $R/\theta = 20$, $S = 0.5$ jet. The displacement follows from the radial perturbation velocity according to $\partial_t\eta + u_b\partial_x\eta = v'$. For a better visualization, the spatial amplitude growth $-k_{0,i}$

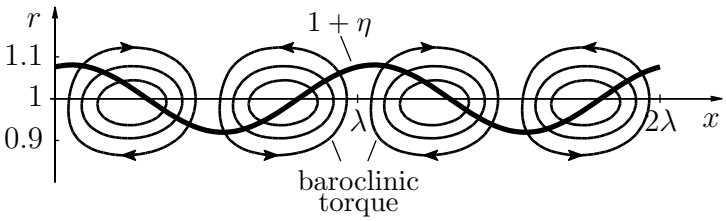

Figure 2.5: Absolute mode eigenfunction of the displacement $\eta(x, r = 1)$ and of the baroclinic torque $\Gamma_{bc}(x, r)$, according to equations (2.18,2.19), for the $R/\theta = 20$, $S = 0.5$ jet.

has been neglected in figure 2.5. At a given time t_0, the spatial distributions are then obtained with equation (2.12) as

$$\eta(x, r) = \frac{F(r)}{k_0\, u_b - \omega_0}\, e^{i(k_{0,r}x - \omega_0 t_0)}\,, \tag{2.18}$$

$$\Gamma_{bc}(x, r) = \frac{ik_0\, P(r)}{\rho_b^2}\frac{\partial \rho_b}{\partial r}\, e^{i(k_{0,r}x - \omega_0 t_0)}\,. \tag{2.19}$$

Both $F(r)$ and $P(r)$ have been scaled with the same arbitrary factor in figure 2.5. Equispaced isocontours of $\Gamma_{bc}(x, r)$ are shown together with the displacement of the center of the shear layer $1 + \eta(r = 1)$. The orientation of Γ_{bc} is indicated by arrows. It is found that the baroclinic torque is concentrated in regions of alternating sign within the shear layer. The center of rotation of each such region, where the maximum absolute value occurs, approximately coincides with a point where the displacement is zero. The baroclinic torque arises from the shear layer undulation, and in turn it induces a further deformation that is in phase with the total shear layer displacement. Thus the temporal growth of the absolute instability mode is increased by the action of the baroclinic torque.

2.4.3 Influence of the shear layer thickness, Reynolds number and Mach number

The distinction between jet column and shear layer modes implies a separation of scales between the jet radius R and the momentum shear layer thickness θ. For low values of R/θ, towards the end of the potential core in a spatially developing jet, this assumption is no longer valid. The effect of R/θ on the transition from convective to absolute instability in hot jets is explored in figure 2.6. Contours of marginal absolute instability ($\omega_{0,i} = 0$) are

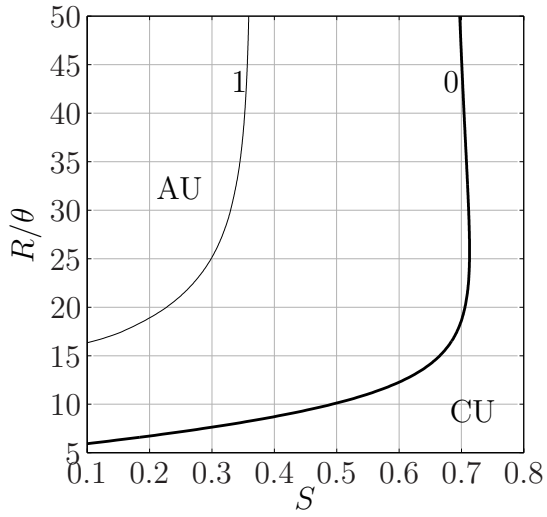

Figure 2.6: Convective/absolute instability boundaries in the S–R/θ plane for $m = 0$ and $m = 1$. $Re = \infty$, Ma $= 0$.

displayed in the S–R/θ plane for the axisymmetric and the first azimuthal mode. The absolute/convective boundary of the axisymmetric mode is identical with figure 8 of Ref. [56] and also in excellent agreement with the results given in Ref. [85]. Absolute instability is found to first occur for the axisymmetric jet column mode at a critical temperature ratio $S = 0.713$ for $R/\theta = 26$. Higher values of R/θ have a slight stabilizing effect. Below $R/\theta \sim 15$ the critical value of S decreases sharply. Monkewitz & Sohn [85] have shown that absolute instability of the $m = 1$ mode in a top-hat jet profile requires much stronger heating than is necessary for the $m = 0$ mode. However, in temporal [4, 43] as well as in spatial [78] jet instability studies, the $m = 1$ mode has been found to display larger growth rates than its axisymmetric counterpart at very low R/θ. The $m = 1$ absolute instability boundary in the S–R/θ plane has therefore been included in figure 2.6. It is confirmed that absolute instability always occurs first for the axisymmetric mode, even at values of R/θ as low as 6.

Growth rates of the full linear impulse response in a thick shear layer jet with $R/\theta = 5$, $S = 1$, Ma $= 0$ and Re $= \infty$ are displayed in figure 2.7 for azimuthal wave numbers $m \leq 2$. Higher-order azimuthal modes are stable everywhere. The $\sigma(v_g)$ distributions should be compared to the thin shear layer case $R/\theta = 20$ of figure 2.4. Note that the discontinuity that separates the axisymmetric jet column and shear layer modes in the $R/\theta = 20$ jet is not observed in figure 2.7. A detailed inspection of the spatial branches reveals that the axisymmetric absolute instability mode ($v_g = 0$) still arises

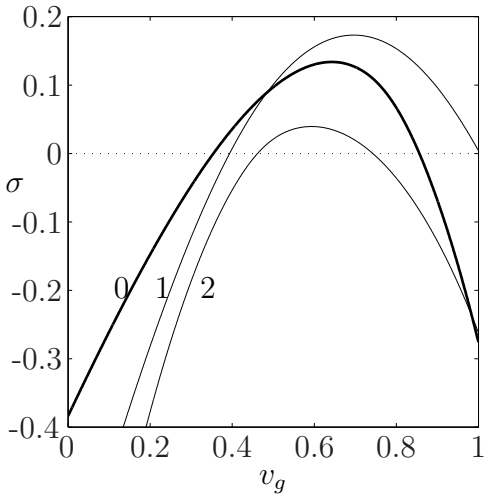

Figure 2.7: Spatio-temporal growth rates in an isothermal R/θ=5 thick shear layer jet for azimuthal wave numbers $m = 0, 1, 2$. $Re = \infty$, Ma = 0.

from the pinching of the k^+- and k_1^--branches, as defined in section 2.4.1. However, at higher group velocities, both k^--branches first merge with each other, and the pinching at $\sigma(v_g)$ then takes place between the k^+- and a combined $k_{1/2}^-$-branch. This behavior is illustrated in figure 2.8 for a profile with $R/\theta = 10$, $S = 1$ and a group velocity $v_g = 0.3$. Note that the k_1^- and k_2^- branches are no longer distinct for $\omega_i < 0.487$, whereas pinching with the k^+ branch occurs for $\omega_i = 0.259$. The resulting spatio-temporal modes cannot be categorized as being distinctly of the jet column or shear layer type, but rather of mixed character. These mixed axisymmetric modes display lower growth rates than the formerly distinct shear layer modes. In the $R/\theta = 5$ case of figure 2.7, the maximum axisymmetric temporal growth rate has now fallen below the σ_{max} of the first helical mode. The merging of the k_1^- and k_2^- branches therefore explains the dominance of the $m = 1$ over the $m = 0$ mode observed in temporal stability studies of thick shear layer jets [4, 43].

The action of viscosity has been neglected in all instability calculations presented so far. If the Reynolds number takes on finite values, the inviscid instability modes described above are affected by viscous damping. The effect of viscosity on the absolute instability of the axisymmetric mode is exhibited in figure 2.9. As the Reynolds number decreases, the absolute/convective transition is delayed towards lower values of S. At high Reynolds numbers, viscosity first affects the critical temperature ratio at high values of R/θ. The slight stabilizing effect of $R/\theta \rightarrow \infty$ observed in the inviscid limit becomes more pronounced in viscous jets.

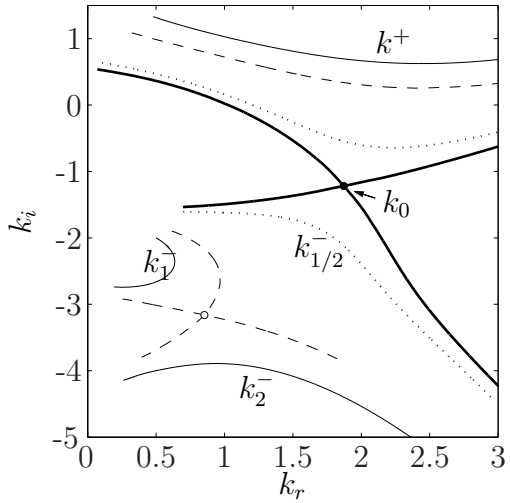

Figure 2.8: Branches in the complex k-plane for $v_g = 0.3$, $R/\theta = 10$, $S = 1$, $Re = \infty$ and $Ma = 0$. Four constant values of ω_i: 0.6 (—), 0.487 (---), 0.3 ($\cdots$), 0.259 (—·—).

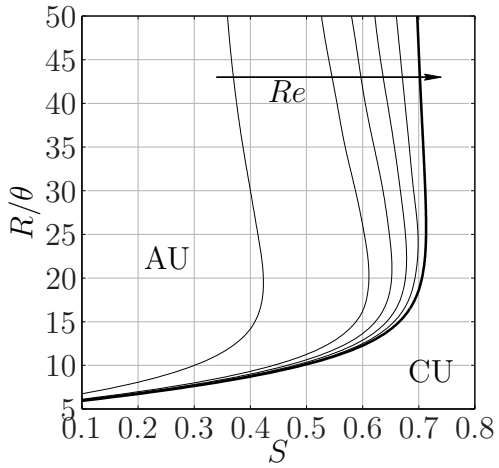

Figure 2.9: Convective/absolute instability boundaries in the S–R/θ plane for Ma = 0. Re = 100, 500, 1000, 2000, 5000 (thin lines), $Re = \infty$ (thick line).

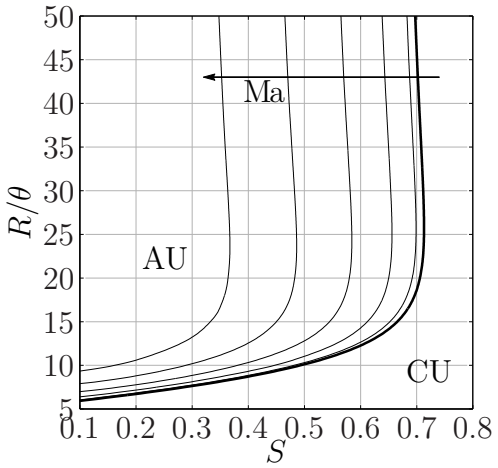

Figure 2.10: Convective/absolute instability boundaries in the S–R/θ plane for $Re = \infty$. Ma = 0 (thick line), Ma = 0.1, 0.2, 0.3, 0.4, 0.5 (thin lines).

Corresponding curves of the absolute instability boundary for various Mach numbers at $Re = \infty$ are presented in figure 2.10. In agreement with earlier studies[85, 56], the stabilization of the jet column mode is quite significant already at moderate Mach numbers. The offset ΔS of the convective / absolute transition that is induced by a given Mach number over the interval $0 \leq \mathrm{Ma} \leq 0.5$ is found to be uniform for all R/θ, and can be well approximated as $\Delta S = -1.4\mathrm{Ma}^2$.

2.5 Conclusions

The linear impulse response of isothermal and heated round jets has been investigated for axisymmetric and higher-order azimuthal modes. A fully compressible formulation of the spatial instability problem has been developped, and results for the linear impulse response have been presented in terms of complex frequency and wavenumber as functions of the group velocity. In agreement with Jendoubi & Strykowski [56], the absolute mode ($v_g = 0$) in jets without counterflow has been found to always be of the axisymmetric *jet column* type. However, *shear layer* modes have been shown to dominate the linear impulse response for high group velocities in thin shear layer jets. Axisymmetric and helical modes are in close competition throughout this portion of the wave packet. The most amplified spatio-temporal mode in thin shear layer jets is of the shear layer type. Jet column type solutions are only admitted for axisymmetric perturbations, and their prevalence over shear layer modes is restricted to a small range of low group velocities.

In the presence of sufficiently strong heating, the jet column mode becomes absolutely unstable. In excellent agreement with Refs. [85, 56], the critical temperature ratio for this transition has been determined as $S_c = 0.713$ for a shear layer thickness given by R/θ=26. The onset of absolute instability in heated jets has been demonstrated to arise from the action of the baroclinic torque, and a physical interpretation has been proposed. An inspection of the absolute mode eigenfunction has shown that the additional deformation induced by the baroclinic torque is in phase with the total shear layer deformation. If the baroclinic torque is eliminated from the dispersion relation, the linear impulse responses of heated and isothermal jets in the inviscid, zero-Mach-number limit are identical.

The clear cut duality of jet column versus shear layer modes is lost as the shear layer thickness approaches the jet radius. The axisymmetric linear impulse response of a R/θ=5 jet profile displays a smooth transition between

the formerly clearly divided jet column/shear layer dominated regions of the wave packet. It has been found from examination of the complex k-branches that in thick shear layer jets, modes of a mixed character arise from the merging of jet column and shear layer type k^--branches prior to the pinching with the k^+-branch. This mixed character accounts for a lowered maximum temporal growth rate of axisymmetric disturbances relative to their helical counterparts, as it has been observed in temporal instability studies of thick shear layer jets[4, 43].

The influence of viscosity on the absolute/convective transition has been analysed by tracking the critical temperature ratio as a function of R/θ for Reynolds numbers between 100 and infinity. As may have been expected, viscosity has a purely stabilizing effect, but its influence lessens for low values of R/θ. In contrast, a finite Mach number delays the critical temperature ratio by a constant offset for all R/θ.

Acknowledgments

The authors are grateful to C. Olendraru and A. Sellier for their help in the development of the instability code. Fruitful comments from C. Cossu and J.-M. Chomaz have also contributed to the present study. The friendly Ladhyx work environment is warmly appreciated.

Appendix: the compressible spatial eigenvalue problem

If the equations of motion (2.6–2.8) are linearized about the base flow defined in section 2.2, and all perturbation quantities are expressed in normal mode form (2.12), the following system of equations is obtained:

continuity:

$$r\omega D + (\rho_b + r\rho_b')F + r\rho_b F' + m\rho_b G = -ru_b kD - r\rho_b kH \tag{2.20}$$

x-momentum:

$$\left(ir^2\rho_b\omega - \frac{m^2}{Re}\right)H + \frac{r}{Re}H' + \frac{r^2}{Re}H'' - ir^2\rho_b u_b' F \tag{2.21}$$
$$= ir^2\rho_b u_b kH + \frac{r}{3Re}kF + \frac{r^2}{3Re}kF' + \frac{mr}{3Re}kG + ir^2 kP + \frac{4r^2}{3Re}k^2 H$$

r-momentum:

$$\left(ir^2\rho_b\omega - \frac{4+3m^2}{3Re}\right)F + \frac{4r}{3Re}F' + \frac{4r^2}{3Re}F'' - \frac{7m}{3Re}G + \frac{mr}{3Re}G' + ir^2P \tag{2.22}$$
$$= -\frac{r^2}{3Re}kH' + ir^2\rho_b u_b kF + \frac{r^2}{Re}k^2F$$

ϕ-momentum:

$$\frac{7m}{3Re}F + \frac{mr}{3Re}F' + \left(-ir^2\rho_b\omega + \frac{3+4m^2}{3Re}\right)G - \frac{r}{Re}G' - \frac{r^2}{Re}G'' + imrP \tag{2.23}$$
$$= -\frac{mr}{3Re}kH - ir^2\rho_b u_b kG - \frac{r^2}{Re}k^2G$$

energy:

$$\begin{aligned}
&\frac{1}{\gamma-1}\left[\frac{i\omega r^2}{\rho_b} - \frac{\gamma}{\rho_b^2 RePr}\left(m^2 - 6r^2\frac{\rho_b'^2}{\rho_b^2} + 2r\frac{\rho_b'}{\rho_b} + 2r^2\frac{\rho_b''}{\rho_b}\right)\right]D \\
&+\frac{\gamma^2\mathrm{Ma}^2r^2}{(\gamma-1)\rho_b^2RePr}\left(1 - 4r\frac{\rho_b'}{\rho_b}\right)D' + \frac{\gamma r^2}{(\gamma-1)\rho_b^2RePr}D'' - \frac{2\gamma\mathrm{Ma}^2}{Re}r^2u_b'H' \\
&+\left[ir - \frac{ir^2\rho_b'}{(\gamma-1)\rho_b}\right]F + ir^2F' + imrG \\
&+\frac{\gamma\mathrm{Ma}^2}{\gamma-1}\left[-ir^2\omega - \frac{\gamma}{\rho_b RePr}\left(2\frac{r^2\rho_b'^2}{\rho_b^2} - \frac{r^2\rho_b''}{\rho_b} - \frac{r\rho_b'}{\rho_b} - m^2\right)\right]P \qquad (2.24) \\
&+\frac{\gamma^2\mathrm{Ma}^2r}{(\gamma-1)\rho_b RePr}\left(2r\frac{\rho_b'}{\rho_b} - 1\right)P' - \frac{\gamma^2\mathrm{Ma}^2r^2}{(\gamma-1)\rho_b RePr}P'' \\
= \;& i\frac{r^2u_b}{(\gamma-1)\rho_b}kD - ir^2kH - \frac{2}{Re}\gamma\mathrm{Ma}^2r^2u_b'kF - i\frac{\gamma\mathrm{Ma}^2}{\gamma-1}r^2u_bkP \\
&+\frac{\gamma r^2}{(\gamma-1)\rho_b^2RePr}k^2D - \frac{\gamma^2\mathrm{Ma}^2r^2}{(\gamma-1)\rho_b RePr}k^2P.
\end{aligned}$$

Primes in the above equations denote radial derivatives. In the incompressible limit $\mathrm{Ma} = 0$, $\rho_b' \equiv 0$, $D \equiv 0$, the continuity and energy equations (2.20,2.24) are identical, and equations (2.20-2.23) are equivalent to the incompressible formulation given by Ash & Khorrami [2].

The system (2.20-2.24) may now be written in the form of a generalized eigenvalue problem

$$\mathbf{A}\boldsymbol{X} = k\mathbf{B}\boldsymbol{X} \tag{2.25}$$

involving the eigenvector $X = (D, H, F, G, P, kD, kH, kF, kG, kP)$ and two linear operators $\mathbf{A}$ and $\mathbf{B}$.

Boundary conditions

In the coordinate singularity at $r = 0$, compatibility conditions [4] must be imposed so as to ensure bounded solutions for all perturbations. Khorrami *et al.* [57] obtained these conditions for H, F, G, P in a formal way by requiring the azimuthal derivatives of velocity and pressure perturbations to vanish as $r \to 0$. Accordingly, density variations ρ' must obey

$$\lim_{r\to 0} \frac{\partial \rho'}{\partial \phi} = imD(0) = 0. \tag{2.26}$$

Together, these requirements impose (see Ref. [2]):

$$\left.\begin{array}{r} F(0) = G(0) = 0 \\ D(0),\ H(0) \text{ and } P(0) \text{ finite} \end{array}\right\} \quad \text{for } m = 0$$

$$\left.\begin{array}{r} F(0) \pm G(0) = 0,\ F'(0) = 0 \\ D(0) = H(0) = P(0) = 0 \end{array}\right\} \quad \text{for } m = \pm 1$$

$$\left.\begin{array}{r} D(0) = H(0) = F(0) \\ = G(0) = P(0) = 0 \end{array}\right\} \quad \text{for } |m| > 1.$$

Explicit expressions for $D(0)$, $H(0)$ and $P(0)$ in the $m = 0$ case are further deduced from Taylor expansions of equations (2.21,2.22,2.24) around the jet centerline. In the limit $r \to 0$, these equations admit

$$H'(0) = 0 \tag{2.27}$$

$$P'(0) = i\frac{2}{Re}F''(0) \tag{2.28}$$

$$D'(0) = \gamma \mathrm{Ma}^2 P'(0). \tag{2.29}$$

According to Ash & Khorrami [2], all eigenfunctions decay exponentially as $r \to \infty$. The far field conditions to the spatial eigenvalue problem for all m are simply

$$D(\infty) = H(\infty) = F(\infty) = G(\infty) = P(\infty) = 0. \tag{2.30}$$

Chebyshev collocation

Following Ref. [57], the eigenfunctions (D, H, F, G, P) are mapped from the physical domain $0 \le r \le r_{max}$ onto the Chebyshev interval $-1 \le \xi \le 1$, where they are discretized in N collocation points

$$\xi_j = \cos\left(\frac{j\pi}{N-1}\right), \quad j = 0, \ldots, N-1. \tag{2.31}$$

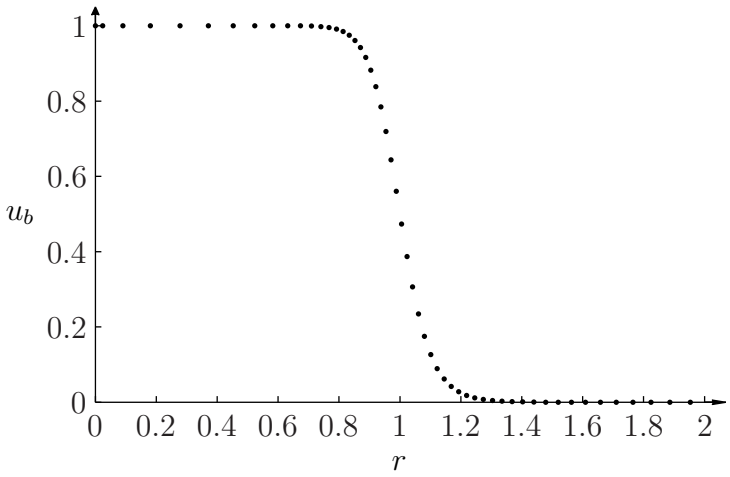

Figure 2.11: Discrete resolution of a $R/\theta = 20$ velocity profile as obtained from transformation (2.32) with $r_c = 1.8$, $r_{max} = 100$, $N = 100$.

For the problem at hand, a suitable mapping function $\xi(r)$ had to be conceived to concentrate most collocation points within the shear layer region of the physical domain. With the two-parameter transformation

$$\xi(r) = \frac{r_c}{2r} - \sqrt{1 + \frac{r_c^2}{4r^2} + \frac{2r_c}{r_{max}} - \frac{r_c}{r}} \tag{2.32a}$$

$$r(\xi) = r_c \frac{1-\xi}{1-\xi^2 + 2r_c/r_{max}}, \tag{2.32b}$$

approximately half of the points $r_j = r(\xi_j)$ are placed in the interval $0 \leq r \leq r_c$, concentrated around $r = r_c/2$. The far field conditions (2.30) are imposed at $r_{max} \gg 1$. Values of $r_c = 1.8$ and $r_{max} = 100$ have been used in all calculations. The discretization of a R/θ=20 velocity profile obtained with these settings and with a typical resolution $N = 100$ is shown in figure 2.11.

Chapter 3

Direct numerical simulation method

3.1 Introduction

The code AJAX (*Aéroacoustique des Jets AXisymétriques*) has been designed for the investigation of instability characteristics of subsonic axisymmetric jets, and of the aeroacoustic sound field that emanates from the instability structures. This is done by directly resolving the Navier-Stokes equations. No modelling is used, neither for the small flow scales nor for the sound field. The acoustic far field is included in the computational domain of the DNS. This approach has become known as *Direct Noise Calculation* (DNC). It marks the advent of the "Second Golden Age of Aeroacoustics", based on modern computational capacities, that Lighthill prophecied in the early 1990s.

This code is conceived to handle an axisymmetric geometry. The calculations may therefore be carried out in two dimensions – the polar coordinates r and x – for flow quantities that do not depend on the azimuthal coordinate φ. The restriction to axisymmetric disturbances is justified by the experimental observations of Monkewitz *et al.* [82] and Kyle & Sreenivasan [62], who report that self-sustained oscillations in globally unstable jets always appear in the form of axisymmetric ring vortices.

The aim of the simulations is not to predict or reproduce the flow behavior in a highly specific experimental configuration, but to explore the validity of recent theoretical models for nonlinear global instability in open flows when applied to heated round jets. The nozzle and duct delivery system

in an experimental setting are therefore replaced by generic inflow boundary conditions. These must be designed to match as closely as possible the assumptions made about the inflow conditions in the theoretical model described in chapter 4. The choice of appropriate boundary conditions is one key issue in the code design and will receive special attention in section 3.5.

The theoretical predictions that the simulation results will be compared to are further based on the instability properties of the unperturbed steady *base flow* for a given set of flow parameters. For a rigorous analysis, this base flow must be known *a priori*. The governing equations are therefore formulated so as to allow the simulation of *perturbations* temporally evolving in a prescribed base flow. For the purpose of the present investigation, it is essential that base flow and perturbation quantities be resolved independently, *i.e.* that their amplitude ratio not be limited by the numerical mantissa length. The accurate resolution of very low-amplitude instability perturbations presents a much more demanding requirement in terms of numerical precision than the resolution of acoustic wave amplitudes in the far field.

This chapter is organized in the following way: The mathematical model and the governing equations are developed in section 3.2. Section 3.3 presents the numerical procedure that is used to construct the base flow. The algorithm is validated against a self-similar solution of spatially developing compressible round jets. The numerical method used in the direct numerical simulation is detailed in section 3.4, while section 3.5 is dedicated to the boundary treatment. Test computations are also presented in section 3.5 to characterize the performance of the employed inlet boundary conditions. The numerical precision of the flow solver is demonstrated in a validation test in section 3.6.

3.2 Flow model

3.2.1 Flow Variables

The governing equations are formulated in terms of the conservative variables $(\rho, \rho u, \rho v, \rho E)$, where ρ denotes density, u and v are the axial and radial components of the flow velocity $\boldsymbol{u}$, and the total energy E is defined with pressure p as

$$E = \frac{p}{\rho(\gamma - 1)} + \frac{1}{2}|\boldsymbol{u}|^2 \,. \tag{3.1}$$

The generic symbol q will be used to denote any of the conservative variables, or $\boldsymbol{q}$ for their ensemble. Each total variable $q(x,r,t)$ is expressed as the sum of a steady base flow $q_b(x,r)$ and a time-dependent perturbation component $q'(x,r,t)$:

$$q(x,r,t) = q_b(x,r) + q'(x,r,t)\ . \tag{3.2}$$

The following notation will be used for the conservative variables:

$$\begin{aligned} & \rho u = \rho_b u_b + (\rho u)' \\ \text{where} \quad & (\rho u)' = \rho_b u' + \rho' u_b + \rho' u' \\ \text{and accordingly:} \quad & (\rho v)' = \rho_b v' + \rho' v_b + \rho' v' \\ & (\rho E)' = \rho_b E' + \rho' E_b + \rho' E'\ . \end{aligned} \tag{3.3}$$

All expressions will be given in non-dimensional form throughout this chapter. The reference quantities used are

R	-	jet radius (where the inlet velocity is $u_b = 0.5$)
U_c	-	centerline velocity at the inlet
ρ_c	-	centerline density at the inlet
T_c	-	centerline temperature at the inlet.

3.2.2 Perturbation equations

The governing equations for a compressible, viscous, non-isothermal flow are the continuity, momentum and energy equations, closed by an equation of state. In terms of the total conservative variables, these can be written as follows.

Continuity:

$$\frac{\partial \rho}{\partial t} = -\mathrm{div}\,(\rho \boldsymbol{u}) \tag{3.4}$$

Momentum:

$$\frac{\partial}{\partial t}(\rho \boldsymbol{u}) = -\mathrm{div}\,(\rho \boldsymbol{u} \otimes \boldsymbol{u}) - \mathrm{grad}\ p + \mathrm{div}\ \underline{\underline{\tau}} \tag{3.5}$$

Energy:

$$\frac{\partial}{\partial t}(\rho E) = \mathrm{div}\left[-(\rho E + p)\boldsymbol{u} + \underline{\underline{\tau}} \cdot \boldsymbol{u} + \frac{\mathrm{grad}\ T}{(\gamma - 1)\mathrm{Ma}^2 \mathrm{RePr}}\right] \tag{3.6}$$

Equation of state for a thermally and calorically perfect gas:

$$p = \frac{1}{\gamma \mathrm{Ma}^2} \rho T \tag{3.7}$$

In these equations, $\underline{\underline{\tau}}$ is the viscous stress tensor, and the symbol '$\otimes$' denotes the tensor product $(\boldsymbol{a} \otimes \boldsymbol{b})_{ij} = a_i b_j$. The Reynolds, Prandtl and Mach numbers are defined as

$$\mathrm{Re} = \frac{\rho_c U_c R}{\mu}\,, \qquad \mathrm{Pr} = \frac{\mu c_p}{\kappa}\,, \qquad \mathrm{Ma} = \frac{U_c}{c_c}\,, \tag{3.8}$$

where the viscosity μ, the thermal conductivity κ and the specific heat c_p are assumed to be constant throughout the flow, and c_c is the speed of sound on the centerline at the inlet. The ratio of specific heats $\gamma = c_p/c_v$ is taken as 1.4 in all computations.

The equations that govern the temporal evolution of perturbations $\boldsymbol{q}'$ in a prescribed base flow $\boldsymbol{q}_b$ are obtained by subtracting equations (3.4–3.7) written in terms of $\boldsymbol{q}_b$ from the same equations written in terms of the total flow variables. In order to arrive at the axisymmetric perturbation equations, the resulting expressions must first be written out in cylindrical coordinates (x, r, φ), then all terms containing azimuthal derivatives or velocities may be eliminated. The cylindrical components of the viscous stress tensor for an axisymmetric velocity field $\boldsymbol{u} = u\mathbf{e}_x + v\mathbf{e}_r$ are

$$\begin{aligned}
\tau_{rr}(\boldsymbol{u}) &= \frac{4}{3\mathrm{Re}}\frac{\partial v}{\partial r} - \frac{2}{3\mathrm{Re}}\left(\frac{v}{r} + \frac{\partial u}{\partial x}\right) \\
\tau_{\varphi\varphi}(\boldsymbol{u}) &= \frac{4}{3\mathrm{Re}}\frac{v}{r} - \frac{2}{3\mathrm{Re}}\left(\frac{\partial v}{\partial r} + \frac{\partial u}{\partial x}\right) \\
\tau_{xx}(\boldsymbol{u}) &= \frac{4}{3\mathrm{Re}}\frac{\partial u}{\partial x} - \frac{2}{3\mathrm{Re}}\left(\frac{\partial v}{\partial r} + \frac{v}{r}\right) \\
\tau_{rx}(\boldsymbol{u}) &= \tau_{xr}(\boldsymbol{u}) = \frac{1}{\mathrm{Re}}\left(\frac{\partial v}{\partial x} + \frac{\partial u}{\partial r}\right) \\
\tau_{r\varphi}(\boldsymbol{u}) &= \tau_{\varphi r}(\boldsymbol{u}) = \tau_{x\varphi}(\boldsymbol{u}) = \tau_{\varphi x}(\boldsymbol{u}) = 0\ .
\end{aligned} \tag{3.9}$$

Short notation $\tau_{ij}^b = \tau_{ij}(\boldsymbol{u}_b)$ and $\tau_{ij}' = \tau_{ij}(\boldsymbol{u}')$ will be used. Note that $\tau_{\varphi\varphi}$ is *not* automatically zero for an axisymmetric flow. This term does appear in the expansion of div $\underline{\underline{\tau}}$. The final perturbation equations (3.10–3.13) are given on the following page.

$$\frac{\partial}{\partial t}\rho' = -\frac{\partial}{\partial r}(\rho v)' - \frac{(\rho v)'}{r} - \frac{\partial}{\partial x}(\rho u)' \tag{3.10}$$

$$\begin{aligned}\frac{\partial}{\partial t}(\rho v)' = &-\frac{\partial}{\partial r}\left[p' + \rho_b v_b v' + (\rho v)' v_b + (\rho v)' v' - \tau'_{rr}\right] \\ &-\frac{1}{r}\left[\rho_b v_b v' + (\rho v)' v_b + (\rho v)' v' - \left(\tau'_{rr} - \tau'_{\varphi\varphi}\right)\right] \\ &-\frac{\partial}{\partial x}\left[\rho_b v_b u' + (\rho v)' u_b + (\rho v)' u' - \tau'_{rx}\right]\end{aligned} \tag{3.11}$$

$$\begin{aligned}\frac{\partial}{\partial t}(\rho u)' = &-\frac{\partial}{\partial r}\left[\rho_b u_b v' + (\rho u)' v_b + (\rho u)' v' - \tau'_{rx}\right] \\ &-\frac{1}{r}\left[\rho_b u_b v' + (\rho u)' v_b + (\rho u)' v' - \tau'_{rx}\right] \\ &-\frac{\partial}{\partial x}\left[p' + \rho_b u_b u' + (\rho u)' u_b + (\rho u)' u' - \tau'_{xx}\right]\end{aligned} \tag{3.12}$$

$$\begin{aligned}\frac{\partial}{\partial t}(\rho E)' = &-\frac{\partial}{\partial r}\left\{\left[\rho_b E_b + p_b\right] v' + \left[(\rho E)' + p'\right] v_b + \left[(\rho E)' + p'\right] v' - D_r\right\} \\ &-\frac{1}{r}\left\{\left[\rho_b E_b + p_b\right] v' + \left[(\rho E)' + p'\right] v_b + \left[(\rho E)' + p'\right] v' - D_r\right\} \\ &-\frac{\partial}{\partial x}\left\{\left[\rho_b E_b + p_b\right] u' + \left[(\rho E)' + p'\right] u_b + \left[(\rho E)' + p'\right] u' - D_x\right\}\end{aligned} \tag{3.13}$$

with
$$\begin{aligned}D_r = &\frac{1}{(\gamma-1)\mathrm{Ma}^2\mathrm{RePr}}\frac{\partial T'}{\partial r} + \tau^b_{rr} v' + \tau^b_{rx} u' \\ &+ \tau'_{rr} v_b + \tau'_{rx} u_b + \tau'_{rr} v' + \tau'_{rx} u'\end{aligned}$$

$$\begin{aligned}D_x = &\frac{1}{(\gamma-1)\mathrm{Ma}^2\mathrm{RePr}}\frac{\partial T'}{\partial x} + \tau^b_{rx} v' + \tau^b_{xx} u' \\ &+ \tau'_{rx} v_b + \tau'_{xx} u_b + \tau'_{rx} v' + \tau'_{xx} u'\end{aligned}$$

3.3 Baseflow

3.3.1 Boundary layer equations

As the base flow is assumed to slowly develop in the streamwise direction, it is sought as a solution of the steady compressible boundary layer equations. In non-dimensional form, these equations read

$$\frac{\partial}{\partial x}(\rho u) + \frac{1}{r}\frac{\partial}{\partial r}(r\rho v) = 0 \tag{3.14}$$

$$\rho u\frac{\partial u}{\partial x} + \rho v\frac{\partial u}{\partial r} = -\frac{\partial p}{\partial x} + \frac{1}{r\,\mathrm{Re}}\frac{\partial}{\partial r}\left(r\frac{\partial u}{\partial r}\right) \tag{3.15}$$

$$\rho u\frac{\partial T}{\partial x} + \rho v\frac{\partial T}{\partial r} = (\gamma-1)\mathrm{Ma}^2 u\frac{\partial p}{\partial x} + \frac{1}{r\mathrm{Re}\,\mathrm{Pr}}\frac{\partial u}{\partial r}\left(r\frac{\partial T}{\partial r}\right) + (\gamma-1)\frac{\mathrm{Ma}^2}{\mathrm{Re}}\left(\frac{\partial u}{\partial r}\right)^2, \tag{3.16}$$

with the equation of state

$$p = \frac{1}{\gamma\mathrm{Ma}^2}\rho T\,. \tag{3.17}$$

The procedure for a numerical solution of this system of equations has been implemented to allow for $\partial p/\partial x \neq 0$ and $\mathrm{Pr} \neq 1$. However, in practice, only base flows with zero pressure gradient and $\mathrm{Pr} = 1$ are used in the simulations. In this case, the energy equation (3.16) can be replaced by the Crocco–Busemann relation

$$T(r) = S + (1-S)u(r) + \frac{\gamma-1}{2}\mathrm{Ma}^2 u(r)\left[1-u(r)\right]. \tag{3.18}$$

The Reynolds number dependence in the momentum equation is dropped by introducing a slow streamwise coordinate $X = x/\mathrm{Re}$. With the substitution

$$\begin{array}{ll} \rho(r,x) \to \rho_0(r,X) & v(r,x) \to \mathrm{Re}^{-1}v_0(r,X) \\ u(r,x) \to u_0(r,X) & T(r,x) \to T_0(r,X) \end{array} \tag{3.19}$$

and with

$$p_0 = \frac{1}{\gamma\mathrm{Ma}^2}\,, \tag{3.20}$$

the boundary layer equations can be written as

$$\frac{\partial \rho_0 u_0}{\partial X} + \frac{1}{r}\frac{\partial}{\partial r}(r\rho_0 v_0) = 0 \tag{3.21}$$

$$\rho_0 u_0 \frac{\partial u_0}{\partial X} + \rho_0 v_0 \frac{\partial u_0}{\partial r} = \frac{1}{r}\,\frac{\partial}{\partial r}\left(r\frac{\partial u_0}{\partial r}\right) \tag{3.22}$$

$$T_0 = S + (1-S)u_0 + \frac{\gamma-1}{2}\mathrm{Ma}^2 u_0(1-u_0) \tag{3.23}$$

$$\rho_0 = T_0^{-1}\ . \tag{3.24}$$

The system (3.21–3.24) is parabolic, and therefore can be integrated numerically stepping forward in X.

3.3.2 Numerical method

The boundary layer equations (3.21–3.24) are discretized and solved at N equispaced radial points

$$\xi_i = \frac{i-1}{N-1} \qquad\qquad i = 1, \ldots, N\,. \tag{3.25}$$

The computational domain $0 \le \xi \le 1$ is mapped onto the physical domain $0 \le r \le r_{max}$ via an analytical mapping function. The resulting distribution $r_i = r(\xi_i)$ should at least be close to the radial grid point distribution used in the direct numerical simulation. In practice, the mapping function $r(\xi)$ has been defined as a piecewise 5^{th} order polynomial. The coefficients of this polynomial are computed by prescribing appropriate values of the grid spacing $\Delta r_i = r'(\xi_i)\Delta\xi$ at $r = 0$, $r = 1$ and $r = r_{max}$, and by requiring the distribution to be continuous in r, r' and r'' at the junction points. As the convergence order of the numerical scheme used in the baseflow computation is lower than the one used in the DNS (see section 3.4.2), the radial step size has usually been chosen as half the value of the DNS grid. The distribution $\Delta r = f(r)$ of the mapping function used to generate the base flows for the simulations presented in section 4.2.5 is shown in figure 3.1.

To perform the numerical integration, the boundary layer equations (3.21–3.24) are cast in the computational coordinates (X, ξ) and discretized at the collocation points (X_i, ξ_j). Radial derivatives are expressed as

$$\frac{\partial}{\partial r} = \frac{1}{r'(\xi)}\,\frac{\partial}{\partial \xi}\,. \tag{3.26}$$

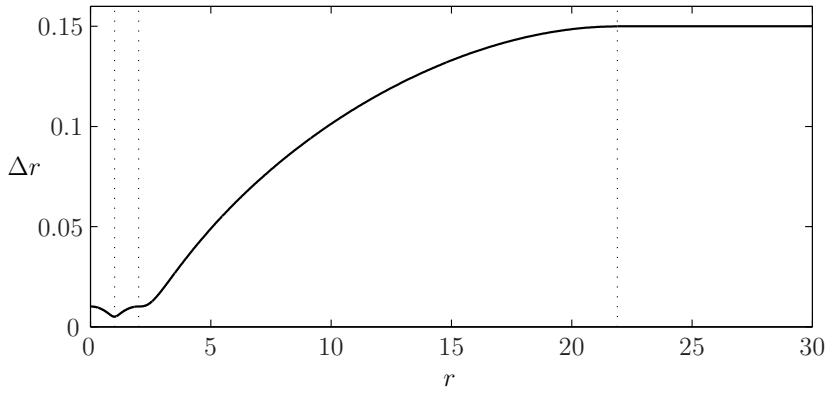

Figure 3.1: Radial grid spacing used for baseflow calculations in section 4.2.5. Junction points of the piecewise polynomial $r(\xi)$ are marked by dotted lines.

The numerical scheme is taken from Lu & Lele [74], who adapted an algorithm given by Anderson, Tannehill & Pletcher [1]. The subscript $()_0$ is dropped in the following expressions for better readability.

The continuity equation (3.21) is discretized around $(X_{i+1/2}, \xi_{j+1})$ via an implicit Euler scheme:

$$\frac{\rho_{j+1}^{i+1}u_{j+1}^{i+1} - \rho_{j+1}^{i}u_{j+1}^{i} + \rho_{j}^{i+1}u_{j}^{i+1} - \rho_{j}^{i}u_{j}^{i}}{2\Delta X} + \frac{r_{j+1}\rho_{j+1}^{i+1}v_{j+1}^{i+1} - r_j\rho_j^{i+1}v_j^{i+1}}{r_{j+1/2}r'_{j+1/2}\Delta\xi} = 0 \tag{3.27}$$

A Crank–Nicholson method is used for the momentum equation (3.22), expanded around $(X_{i+1/2}, \xi_j)$:

$$\begin{aligned} & \frac{(\rho_j^{i+1}u_j^{i+1} + \rho_j^i u_j^i)(u_j^{i+1} - u_j^i)}{2\Delta X} \\ & + \frac{(\rho_j^{i+1}v_j^{i+1} + \rho_j^i v_j^i)(u_{j+1}^{i+1} - u_{j-1}^{i+1} + u_{j+1}^i - u_{j-1}^i)}{8r'_j\Delta\xi} \\ = \; & \frac{1}{2r_j r'_j \Delta\xi^2}\left[\frac{r_{j+1/2}}{r'_{j+1/2}}\left(u_{j+1}^{i+1} - u_j^{i+1} + u_{j+1}^i - u_j^i\right)\right. \\ & \left. - \frac{r_{j-1/2}}{r'_{j-1/2}}\left(u_j^{i+1} - u_{j-1}^{i+1} + u_j^i - u_{j-1}^i\right)\right]. \end{aligned} \tag{3.28}$$

Application of the same Crank–Nicholson scheme to the energy equation (3.16) is straightforward, but leads to a lengthy expression. In the calculations presented in this study, the Crocco–Busemann law has been employed

instead:

$$T_j^{i+1} = S + (1-S)u_j^{i+1} + \frac{\gamma-1}{2}\mathrm{Ma}^2 u_j^{i+1}(1-u_j^{i+1})\,. \tag{3.29}$$

It has been verified that a numerical solution of the full energy equation yields identical results in zero-pressure-gradient situations with $\mathrm{Pr} = 1$. The discrete equation of state is simply

$$\rho_j^{i+1} = (T_j^{i+1})^{-1}\,. \tag{3.30}$$

The computation starts from an analytical jet velocity profile (Michalke [77])

$$u(r, X_0) = \frac{1}{2} + \frac{1}{2}\tanh\left[\frac{R}{4\theta}\left(\frac{1}{r} - r\right)\right]\,, \quad v(r, X_0) \equiv 0 \tag{3.31}$$

prescribed at X_0. Corresponding temperature and density profiles are obtained from equations (3.23,3.24). The velocity profile is characterized by the parameter R/θ, where θ is the shear layer momentum thickness

$$\theta = \int_0^\infty u(r)(1-u(r))\,\mathrm{d}r\,. \tag{3.32}$$

As equations (3.27–3.30) are coupled, radial profiles at X_{j+1} must be computed in an iterative process. Each iteration substep consists of the following procedure: The nonlinear term $(u_j^{i+1})^2$ in equation (3.28) is linearized as $(u_j^{i+1})^2 = 2\tilde{u}_j^{i+1}u_j^{i+1} - (\tilde{u}_j^{i+1})^2$, where $\tilde{u}_j^{i+1}$ denotes the value from the previous iteration substep. The axial velocity profile u^{i+1} is then obtained from equation (3.28) as the solution of a tridiagonal system, with all other variable values at X_{i+1} taken from the last iteration substep. Boundary conditions are imposed as

$$\frac{\partial u}{\partial r}(r=0) = 0 \quad \text{and} \quad u(r_{max}) = 0\,. \tag{3.33}$$

New values T^{i+1} and ρ^{i+1} follow directly from equations (3.29) and (3.30). The radial velocity v^{i+1} is then obtained explicitly from equation (3.27) in the form $v_{j+1}^{i+1} = f(v_j^{i+1})$, with $v(r=0) = 0$ as boundary condition. The next iteration substep is started by recalculating u^{i+1} with the updated values of v^{i+1}, T^{i+1} and ρ^{i+1}. The iteration at X_{i+1} is taken as converged when $\max_j(|u_j^{i+1} - \tilde{u}_j^{i+1}|) < 10^{-14}$. Starting values for the iteration procedure at the next streamwise station are extrapolated from previous results. A second-order extrapolation $q_j^{i+1} \sim f(q_j^i, q_j^{i-1}, q_j^{i-2})$ has been found to work best.

At the starting location X_0, the radial velocity profile (3.31) is prescribed to be zero for want of a better guess. This inconsistency of the initial profile

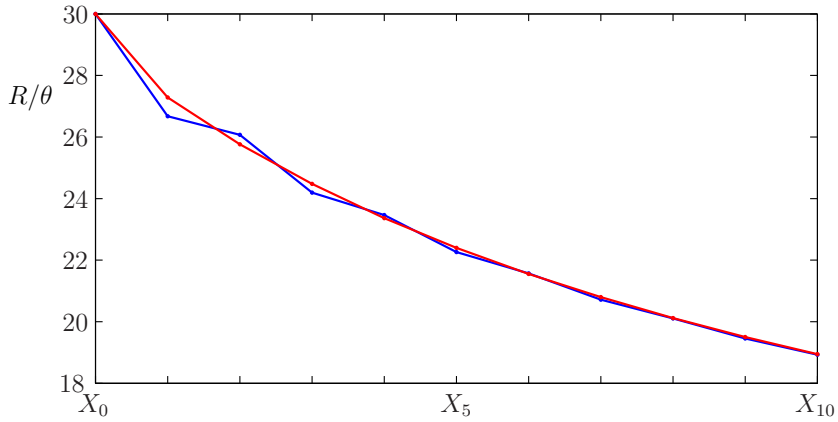

Figure 3.2: Streamwise development of R/θ from calculations without (blue) and with (red) averaging procedure at the first five X locations. The step size ΔX is untypically large in this example.

results in an over-adjustment of v in X_1 and leads to spurious oscillations further on along X that die out very slowly. The blue line in figure 3.2 shows the resulting development of R/θ. In order to quickly adjust the radial velocity profile to the natural spreading of the jet, an averaging technique proposed by Shin & Ferziger [102] has been employed: after a first estimation of the flow profiles at $X_1 = X_0 + \Delta X$, the calculation is restarted from the midway location $X_{1/2} = X_0 + 0.5\Delta X$ with the averaged solution $q(X_{1/2}, \xi) = 0.5[q(X_0, \xi) + q(X_1, \xi)]$ in order to obtain a new estimate at X_1. The solutions at $X_{1/2}$ and X_1 are again averaged, and $q(X_1, \xi)$ is again recalculated from the location $X_0 + 0.75\Delta X$. For the precision needed in the present simulations, five such averaging steps are performed to arrive at the final solution at X_1, and the same procedure is repeated for $X_2, \ldots, X_5$. Beyond X_5 the calculation is continued normally. Figure 3.2 demonstrates that this procedure efficiently eliminates spurious oscillations. The first five points in X are truncated before the baseflow is used in the direct numerical simulations. The initial profile parameter R/θ in equation (3.31) therefore must be chosen sufficiently larger than the value needed at $x = 0$ in the DNS.

The streamwise development of the local profile parameter R/θ in X is presented in figure 3.3 for two $\mathrm{Ma} = 0.1$ jets with temperature ratios $S = 1$ and $S = 0.5$. The first five computational points are not included in the diagram.

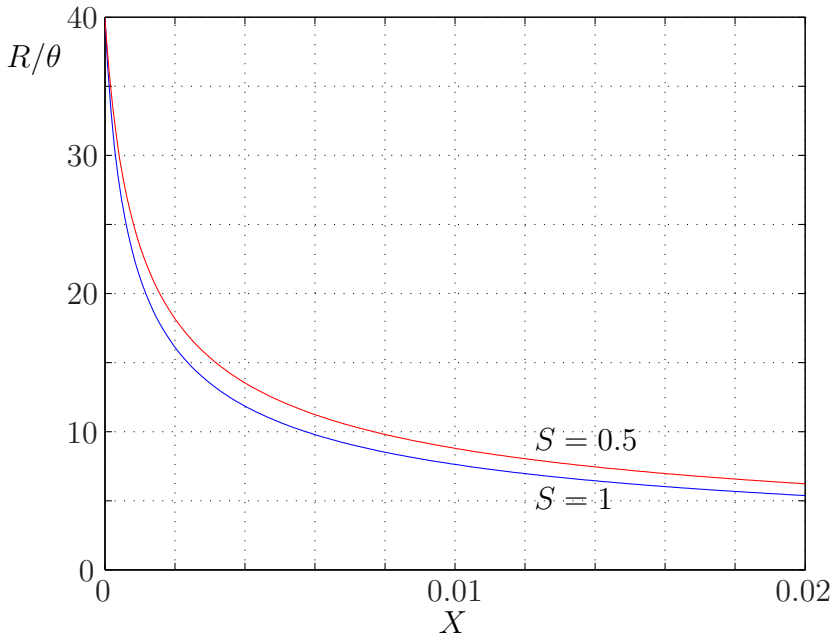

Figure 3.3: Streamwise development of the profile parameter R/θ at temperature ratios $S = 1$ (isothermal, blue line) and $S = 0.5$ (hot, red line), according to numerical integration of the boundary layer equations.

3.3.3 Validation

The numerical integration of the boundary layer equations is validated against an analytical self-similar solution for developing jet profiles downstream of the potential core. For an incompressible axisymmetric jet, a closed-form solution has been developed by Schlichting [101]. Pack [90] later extended the formalism to include compressibility effects for S=1, Pr=1 and Ma<1 and found an approximative solution in the form of a power series. Pack's formulation will be rewritten here in a notation analogous to that of Schlichting [101], adapted to the baseflow assumptions made in this study, and it will be demonstrated how the self-similar jet profiles can be retrieved without the necessity of a power expansion. For a detailed derivation of the formalism, the reader is referred to the original work [90].

The radial variations of the velocity and density profiles are expressed in terms of a scaling variable $\eta = \xi/X$, where ξ is defined at each streamwise station through

$$\rho_\infty \xi = 2 \int_0^r \rho(r')\, r'\, dr' \ . \tag{3.34}$$

Note that ξ is distinct from the quantity used in the previous section. For a numerical implementation, an explicit expression is needed for the transformation between r and ξ. With the approximation

$$\xi = \sqrt{\frac{\rho(r)}{\rho_\infty}}\, r \tag{3.35}$$

a stream function can be defined, which takes the same form as in the incompressible case (Schlichting [101]):

$$\psi(\eta) = X\, \frac{\gamma^2\eta^2}{(1+\frac{1}{4}\gamma^2\eta^2)^2}\ . \tag{3.36}$$

The velocities at a given streamwise station X are computed from the stream function as

$$u_0(\xi) = \frac{1}{\rho_\infty \xi}\, \frac{\partial\psi}{\partial\xi}\Big|_X \tag{3.37}$$

$$v_0(\xi) = \frac{1}{\rho(\xi) r(\xi)}\, \left[\frac{\partial\psi}{\partial X}\Big|_\xi + \frac{\partial\psi}{\partial\xi}\Big|_X \times \frac{\partial\xi}{\partial X}\Big|_r\right] \tag{3.38}$$

Pack [90] shows that even for a Mach number of 0.9 the error committed in u_0 by using the approximation made in equation (3.35) is not greater than 2%.

Using the jet radius R and the centerline values U_c, ρ_c and T_c as reference quantities, the velocities in nondimensional form become:

$$u_0(\eta) = \frac{1}{\rho_\infty X}\, \frac{2\gamma^2}{(1+\frac{1}{4}\gamma^2\eta^2)^2} \tag{3.39}$$

$$v_0(\eta) = \frac{1}{\rho(\eta) r}\left\{\frac{2\gamma^2\eta^2}{(1+\frac{1}{4}\gamma^2\eta^2)^2} - \frac{\gamma^2\eta^2}{1+\frac{1}{4}\gamma^2\eta^2} + \frac{2\gamma^2\eta}{(1+\frac{1}{4}\gamma^2\eta^2)^2}\left(\frac{\partial\xi}{\partial X}\right)_r\right\} \tag{3.40}$$

The streamwise derivative of ξ can only be determined numerically. The density profile $\rho(\eta)$, needed for the evaluation of equation (3.40), is found from the Crocco-Busemann law (3.23) together with the equation of state (3.24). The physical coordinate $r(\xi, X)$ can then be calculated from the transformation (3.35), and the radial velocity from equation (3.40).

The term $\partial\xi/\partial X$ in equation (3.40) can only be evaluated once $r(\xi, X)$ is known for the whole flow field. At each streamwise station X_j, the values of $\xi(r, X_{j-1})$ and $\xi(r, X_{j+1})$ are then interpolated onto the points $r_j = r(\xi, X_j)$, and the derivative $\partial\xi/\partial X$ at constant r is obtained as a second-order central

difference. However, the contribution of this metric term to v is negligible for small Mach numbers.

In order to obtain start profiles for a boundary layer calculation, the parameters γ and X_0 must be chosen appropriately, so that $u_0(r = 0, X_0) = 1$ and $u_0(r = 1, X_0) = 0.5$. With equation (3.35), $r = 1$ can be replaced with $\xi = (\rho_1/\rho_\infty)^{1/2}$. This leads to the parameter values

$$X_0 = (1 + \sqrt{2})\frac{\rho_1}{8} \qquad \gamma^2 = (1 + \sqrt{2})\frac{\rho_1\rho_\infty}{16}\,, \tag{3.41}$$

where $\rho_1 = \rho(u_0{=}0.5)$ and $\rho_\infty = \rho(u_0{=}0)$ are calculated from equations (3.23,3.24).

Results obtained from the numerical boundary layer integration are compared to the corresponding self-similar solutions for Ma=0.9 (figure 3.4a) and for Ma=0.1 (figure 3.4b–d). The initial profiles used in the boundary layer integration have been taken from equations (3.39,3.40), with X_0 and γ as given in equation (3.41). The agreement is excellent. Note that the radial velocity in figure 3.4c has been scaled with the Reynolds number according to equation (3.19).

3.4 Numerical solution of the perturbation equations

3.4.1 Time advancement

The time derivatives of the conservative flow variables $\boldsymbol{q}$ are given by equations (3.10–3.13) in the form

$$\frac{\partial \boldsymbol{q}}{\partial t} = F(\boldsymbol{q}) \tag{3.42}$$

and can be evaluated at each time step. $F(\boldsymbol{q})$ contains spatial derivatives that will be discretized by use of appropriate spatial schemes. From $\partial\boldsymbol{q}/\partial t$, the flow variables are advanced in time using a third order Runge-Kutta algorithm in the low-storage version of Lowery & Reynolds [73]. A new time

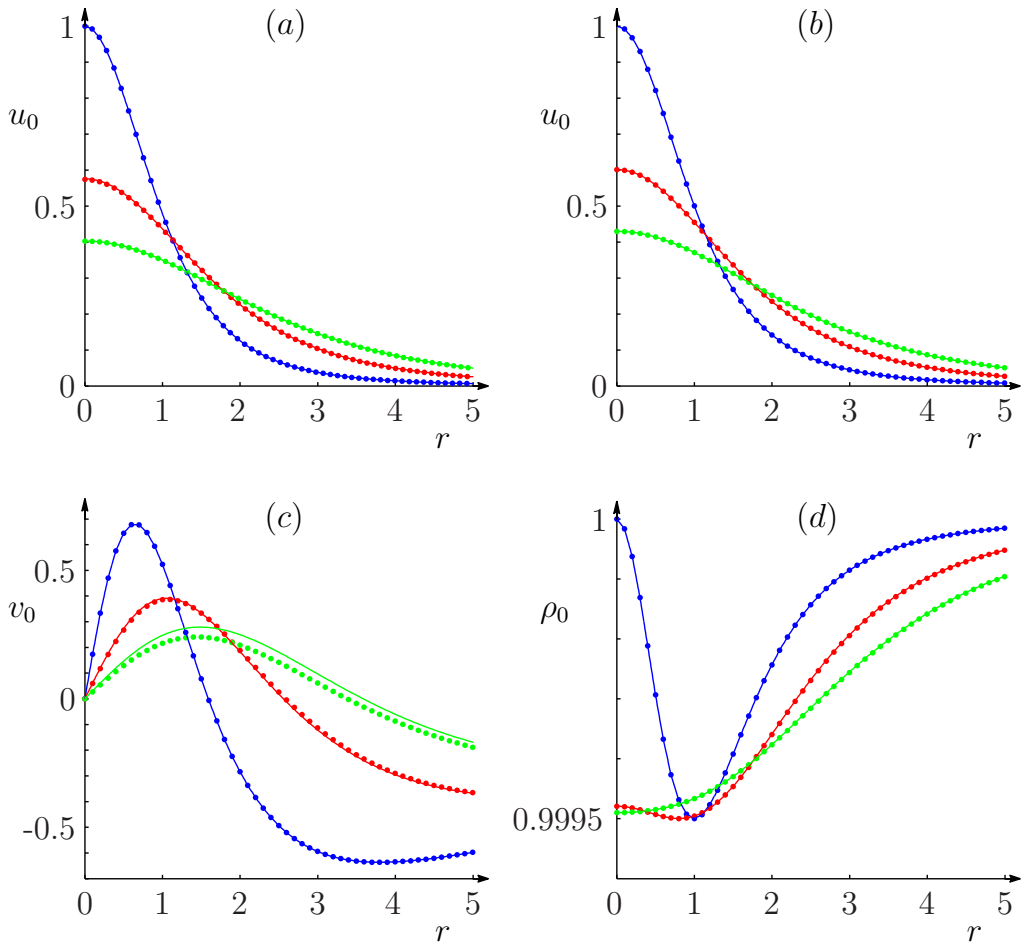

Figure 3.4: Radial jet profiles at $X = X_0$ (blue), $X = X_0 + 0.2$ (red), $X = X_0 + 0.4$ (green). Solid lines: boundary layer equation; dots: self-similar solution according to Pack [90]. a) Ma = 0.9, b)–d) Ma = 0.1.

step q^{n+1} is calculated from q^n in three substeps:

$$\begin{aligned} \Delta q_1 &= F(q^n) \\ q_1 &= q^n + \alpha_1 \Delta q_1 \Delta t \\ \Delta q_2 &= F(q_1) + \beta_1 \Delta q_1 \\ q_2 &= q_1 + \alpha_2 \Delta q_2 \Delta t \\ \Delta q_3 &= F(q_2) + \beta_2 \Delta q_2 \\ q^{n+1} &= q_2 + \alpha_3 \Delta q_3 \Delta t \end{aligned}$$

with the coefficients

$$\begin{aligned} \alpha_1 &= 0.5 & \beta_1 &= -0.6830127018922193 \\ \alpha_2 &= 0.9106836025229591 & \beta_2 &= -4/3 \\ \alpha_3 &= 0.3660254037844387 \end{aligned}$$

The scheme can be expected to be stable when the Courant-Friedrich-Levy (CFL) number is lower or equal to $\sqrt{3}$. With a CFL number of unity, no information is transported further than one computational cell within one time step. For convective transport, the criterion is

$$\Delta t_c = \frac{\min(\Delta r, \Delta x)}{1 + \mathrm{Ma}^{-1}}\,, \tag{3.43}$$

and for viscous transport:

$$\Delta t_v = \frac{\mathrm{Re}}{2\gamma} \min\{(\Delta r)^2, (\Delta x)^2\}\,. \tag{3.44}$$

The time step has to be chosen according to the more restrictive of the two criteria: $\Delta t = \mathrm{CFL}\ \min(\Delta t_c, \Delta t_v)$. In computations at moderate Reynolds and low Mach numbers, the time step is always dictated by the convective transport.

3.4.2 Spatial derivatives

Derivatives with respect to r and x in (3.10–3.13) are discretized via a classical sixth-order-accurate explicit centered finite difference scheme, which uses a seven point stencil (see Desquesnes *et al.* [36]):

$$\begin{aligned} \left.\frac{\partial q}{\partial r}\right|_{i,j} &= \frac{1}{m^r_{ij}} \sum_{k=1}^{3} a_k (q_{i+k,j} - q_{i-k,j}) \\ \left.\frac{\partial q}{\partial x}\right|_{i,j} &= \frac{1}{m^x_{ij}} \sum_{k=1}^{3} a_k (q_{i,j+k} - q_{i,j-k}) \end{aligned} \tag{3.45}$$

$$\text{with} \qquad a_1 = \frac{45}{60}\,, \quad a_2 = -\frac{9}{60}\,, \quad a_3 = \frac{1}{60}\,.$$

The subscripts i, j denote the grid point at location (r_i, x_j). The matrices m^r_{ij} and m^x_{ij} are metric terms that stem from the transformation between the grid in the physical domain (r, x), with nonuniform spacing, and a computational grid (ξ, η) where $\Delta\xi \equiv 1$ and $\Delta\eta \equiv 1$. The derivatives with respect to (ξ, η) and with respect to (r, x) are related as

$$\begin{aligned} \frac{\partial q}{\partial r}\Big|_{i,j} &= \left(\frac{\partial r}{\partial \xi}\right)^{-1}_{i,j} \frac{\partial q}{\partial \xi}\Big|_{i,j} \qquad \Rightarrow \quad m^r_{ij} = \frac{\partial r}{\partial \xi}\Big|_{i,j} \\ \frac{\partial q}{\partial x}\Big|_{i,j} &= \left(\frac{\partial x}{\partial \eta}\right)^{-1}_{i,j} \frac{\partial q}{\partial \eta}\Big|_{i,j} \qquad \Rightarrow \quad m^x_{ij} = \frac{\partial x}{\partial \eta}\Big|_{i,j} \end{aligned} \tag{3.46}$$

Near the boundaries of the domain, less than three points away from the last grid point, centered spatial schemes of lower order are employed. Decentered finite differences are diffusive, and should generally be avoided. Only on the outermost points, a decentered first order two-point stencil is applied for lack of alternatives. These points near the boundary, where low-order derivative and filtering schemes are used (see also section 3.4.3), will be referred to as *ghost points*. The quantities computed at these points are not regarded as being physically relevant. The reduction of the stencil sizes is sketched in figure 3.5.

The coefficients of the lower-order schemes are:

$$\begin{aligned} 4^{th} \text{ order:} \qquad & a_1 = \frac{2}{3} \qquad a_2 = -\frac{1}{12} \\ 2^{nd} \text{ order:} \qquad & a_1 = \frac{1}{2} \end{aligned}$$

Second derivatives $\frac{\partial^2}{\partial r^2}$ and $\frac{\partial^2}{\partial x^2}$ in the diffusion terms are approximated by successive application of the above finite difference schemes.

The efficiency and precision of the implemented spatial and temporal schemes for both aerodynamic and aeroacoustic applications has been demonstrated in recent studies by Desquesnes *et al.* [36] and by Terracol *et al.* [108].

3.4.3 Spatial filtering

Centered finite-difference schemes are non-diffusive and known to give rise to under-resolved spurious oscillations on the scale of the grid spacing. Such

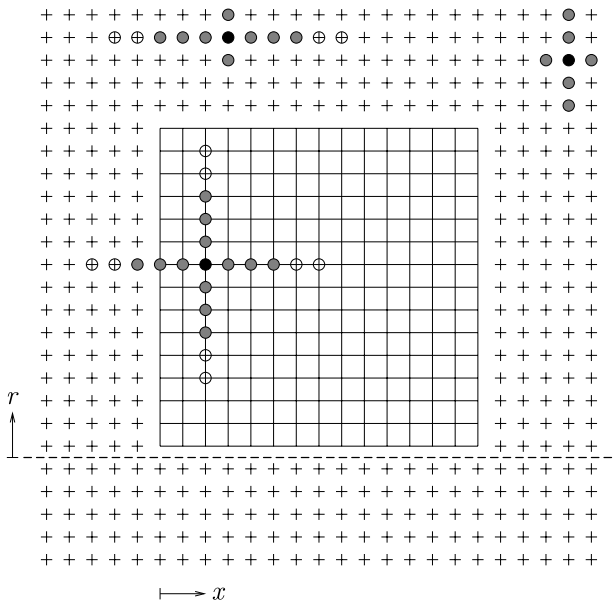

Figure 3.5: Stencil size for filter and derivative scheme; treatment near the boundaries. Interior domain (—), ghost points (+) and axis (---). The points marked ∘ are used for the filtering scheme, the grey points for the filter and the derivative.

oscillations especially arise from discontinuities in the numerical approximation, such as grid stretching or boundary treatment. As a result, unphysical waves can spread throughout the whole computational domain, pollute the solutions and give rise to numerical instabilities. It is therefore necessary to introduce a spatial filtering procedure that very selectively eliminates high, under-resolved frequencies.

In the present study, an explicit 10^{th} order filter scheme is implemented, as proposed by Lele [66] and further discussed by Visbal & Gaitonde [113]. For the 10^{th} order filter, an 11-point stencil is used to compute the value in one point with high frequency variations filtered out in one spatial direction. The filter is applied to all conservative variables at the end of each time step, first in the axial, then in the radial direction. On the ghost points, the stencil size is progressively reduced (see figure 3.5).

If $\tilde{q}_{ij}$ is the unfiltered result obtained from the Runge-Kutta algorithm, then the end result q_{ij} of the time step is

$$q_{ij} = f_r\left(f_x(\tilde{q}_{ij})\right),$$

computed as

$$f_x(q_{ij}) = \sum_{k=-n}^{n} b_k^x q_{i,j+k} \tag{3.47}$$

$$f_r(q_{ij}) = \sum_{k=-n}^{n} b_k^r q_{i+k,j}\,. \tag{3.48}$$

As the filter stencils are larger than those used for the spatial derivative schemes, the necessary number of ghost points is determined by the filtering scheme. For application of a 10^{th} order filter in the physical region of the computational domain, five layers of ghost points are needed.

Following a procedure proposed by Falissard [38], the coefficients $b_k^{[x,r]}$ are defined locally such that the 10^{th} order precision is preserved also on non-uniform computational grids. At each position x_j, the b_k^x are obtained as a solution of the linear system

$$\begin{pmatrix} 1 & 1 & 1 & 1 & 1 & \dots \\ 0 & \Delta x_1 & \Delta x_{-1} & \Delta x_2 & \Delta x_{-2} & \dots \\ 0 & \Delta x_1^2 & \Delta x_{-1}^2 & \Delta x_2^2 & \Delta x_{-2}^2 & \dots \\ \vdots & \vdots & \vdots & \vdots & \vdots & \\ \vdots & \vdots & \vdots & \vdots & \vdots & \\ 0 & \Delta x_1^{10} & \Delta x_{-1}^{10} & \Delta x_2^{10} & \Delta x_{-2}^{10} & \dots \end{pmatrix} \begin{pmatrix} b_0^x \\ b_1^x \\ b_{-1}^x \\ b_2^x \\ b_{-2}^x \\ \vdots \end{pmatrix} = \begin{pmatrix} 1 \\ 0 \\ \\ \vdots \\ \\ 0 \end{pmatrix}, \tag{3.49}$$

where Δx_k denotes $x_{j+k} - x_j$. The coefficients b_k^r are computed accordingly for each radial position r_i.

3.4.4 Computational grids

The grid point distributions used in the simulations presented in the following chapters are briefly documented here.

In section 4.2, two types of flow configurations are considered. Both are computed on the same radial grid point distribution (figures 3.6*a*,*c*). As only acoustic wave lengths $\lambda \sim 35$ need to be resolved in the far field, Δr can be chosen very large for $r \gtrsim 5$. However, the stretching rate from one radial point to the next is kept below 4% in the physical region, in order to minimize the generation of spurious waves. The radial grid distribution in figures 3.6*a*,*c* within the physical region $r < 46$ corresponds to the function $\Delta r = 2f(r)$, with $\Delta r = f(r)$ being the grid spacing that has been used in the

calculation of the baseflow (see figure 3.1). Thus the baseflow quantities are available directly at the grid points used in the DNS, without necessitating interpolation. The axial grid spacing (figure 3.6*b*) is kept constant throughout the physical region. In the computations of section 4.2.4, $\Delta x = 0.05$ was chosen in order to provide a high resolution of baseflow variations. The baseflows considered in section 4.2.5 vary very slowly, and a resolution $\Delta x = 0.1$ was found to be sufficient.

Since the computations of section 4.2 were the first published attempt to capture global modes in a direct numerical simulation, the construction of the grid was guided by great prudence. Later tests showed that in particular the radial resolution of the near field (figure 3.6*c*) is excessive, and that a bicubic interpolation, as implemented in MATLAB, of the baseflow onto a well-designed DNS grid yields highly accurate results. The computational grid used in the simulations presented in section 4.3 is conceived to allow more time-efficient simulations for a parametric study. The radial and axial grid point distributions are displayed in figure 3.7. The axial sponge region, not shown entirely in figure 3.7*b*, extends down to $x = 125$, where $\Delta x = 3.35$. Grid independence of the results has been demonstrated in test calculations with a $R/\theta = 25$, $S = 0.5$ baseflow profile on a finer grid, where Δr and Δx were decreased by a factor 1.5. Any influence of box effects (see Buell & Huerre [16]) on the simulation results has been excluded in tests on a larger computational domain, with a physical region $0 \leq x \leq 50$.

3.5 Boundary Conditions

The theoretical model assumes a flow domain that extends to infinity in the downstream and radial directions. Instability-related perturbations are supposed to be zero at the upstream boundary of the flow domain, whereas acoustic waves should propagate upstream as in an infinite medium. By contrast, the computational domain is inevitably finite in size. Boundary conditions must therefore be conceived that mimic a continuous infinite medium. Specifically, all radiated sound waves and all convected vorticity and entropy waves must be allowed to leave the computational domain without significant interaction or reflection at the boundaries, but upstream-propagating instability waves must be blocked at $x = 0$.

Each of the four boundaries in the implemented numerical method has distinct characteristics. The top boundary at $r = r_{max}$ has to be nonreflecting to acoustic waves. The outflow boundary must let acoustic, vorticity and

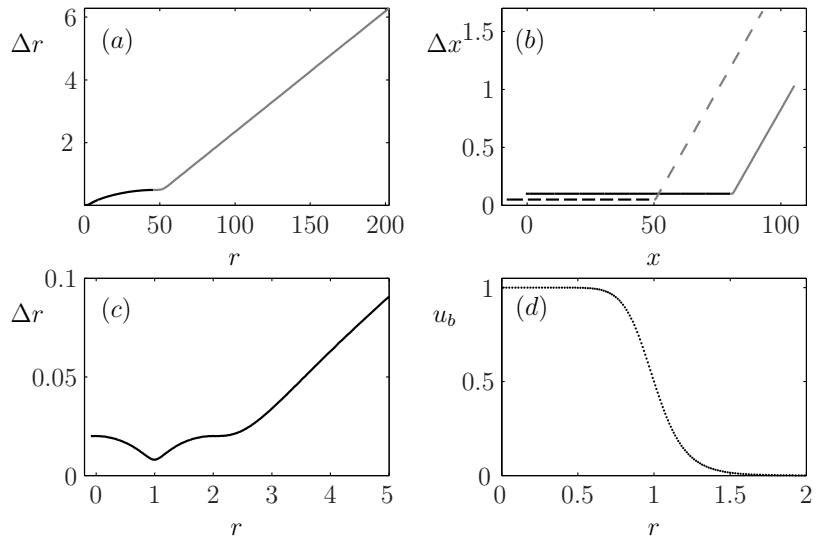

Figure 3.6: Computational grid used in the simulations of section 4.2. (a) Radial grid spacing, sponge zone in grey; (b) axial grid spacing, solid: section 4.2.5, dashed: section 4.2.4, sponge zones in grey; (c) radial grid spacing in the jet region; (d) radial resolution of a $R/\theta = 10$ velocity profile.

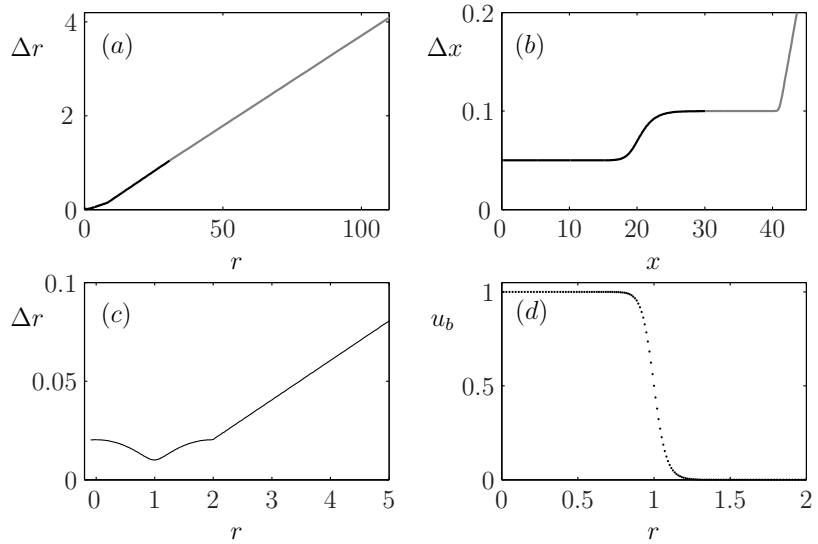

Figure 3.7: Computational grid used in the simulations of section 4.3. (a) Radial grid spacing, sponge zone in grey; (b) axial grid spacing, sponge zones in grey; (c) radial grid spacing in the jet region; (d) radial resolution of a $R/\theta = 25$ velocity profile.

entropy waves pass. The inflow boundary must be transparent for outgoing acoustic waves and impermeable for vorticity and entropy waves. Forcing will also be applied at the upstream boundary in some computations. Across the axis, all quantities must fulfill symmetry conditions.

The many existing numerical concepts for nonreflecting boundary conditions have been reviewed by Colonius [22]. None of these can claim to be conclusive. In practice, most CAA calculations rely on the use of "sponge zones" surrounding the interior domain, where all fluctuations are progressively damped to negligible levels through artificial dissipation, before they reach the boundary of the computational domain.

3.5.1 Symmetry conditions at the jet axis

Equations (3.10–3.13) are singular at $r = 0$, and therefore cannot be evaluated directly on the jet axis. The easiest and most obvious way to circumvent this problem is to place the first physical radial grid point at $r = \Delta r/2$, as sketched in figure 3.5. No problems have been encountered with this treatment of the coordinate singularity.

Of the conservative flow variables, density, axial momentum and total energy are symmetric with respect to $r = 0$, whereas the radial momentum is antisymmetric. The inverse is true for the respective radial derivatives. These conditions are enforced by placing ghost points on the negative side of the axis and by copying the values of the flow quantities from the corresponding points on the positive side of the axis after each calculation. The use of reduced-order schemes is not necessary for the calculation of radial derivatives near the axis, as the values of the derivatives that have been computed with a seven-point stencil on the physical side of the axis can be copied onto the ghost points.

3.5.2 Sponge zones

The treatment of the top and outflow boundaries does not involve any physical modelling. Reflection is prevented by attenuating all perturbations $\boldsymbol{q}$ within a *sponge zone*, where a damping term $-\lambda \boldsymbol{q}'$ is added to the right hand side of the perturbation equations (3.10–3.13). The computed values in these regions are not considered as physically meaningful. Within the exit sponge zone, the damping coefficient λ increases smoothly from 0 to λ_{max} over a

streamwise distance $x_1 < x < x_2$, according to the function

$$\lambda(x) = \lambda_{max} \left[1 + \exp\left(\frac{x_2 - x_1}{x - x_2} + \frac{x_2 - x_1}{x - x_1} \right) \right]. \tag{3.50}$$

Within the sponge zone at the top boundary, λ varies accordingly in r. In addition to the artificial damping, numerical dissipation in the sponge zones is increased by significant progressive grid stretching. For a discussion of the use of sponge zones, see the review by Colonius [22].

On the ghost points near r_{max} and x_{max}, the reduction of the filter stencil size (see section 3.4.3) provides another strong increase of numerical dissipation. On the outermost grid point, all disturbance quantities are set to zero. The properties of this boundary treatment have been extensively studied by Redonnet [99].

3.5.3 Inflow Conditions and Forcing

Unlike the top and outflow boundaries, the jet inflow conditions are to be specified at a precise streamwise location. The use of an upstream sponge zone is therefore prohibited. Conceptually, a characteristics method seems to be the best suited: It allows to specifically define all modes that are entering the domain. This procedure is particularly convenient if forcing is to be applied at the upstream boundary. However, the required decomposition of the flow variables into acoustic, vortical and entropy modes cannot be exact for the axisymmetric Navier–Stokes equations, and several approximate methods have been proposed (see Colonius [22]). Following the example of Mitchell *et al.* [79, 80], the conditions formulated by Giles [46] are used at the upstream numerical boundary.

In the increment calculation of each Runge-Kutta substep, the conservative variables $\boldsymbol{q}'$ at the ghost points are transformed first to primitive, then to characteristic variables $\boldsymbol{w}$. These are the characteristics of the one-dimensional Euler equation in the direction perpendicular to the inflow boundary, propagating at a velocity u_λ, which is positive for incoming characteristics and negative for outgoing characteristics:

$$\begin{array}{lll} w_1 = p' - c^2\rho' & \text{entropy} & u_\lambda = u_b \\ w_2 = \rho_b c v' & \text{vorticity} & u_\lambda = u_b \\ w_3 = p' + \rho_b c u' & \text{acoustic} & u_\lambda = u_b + c \\ w_4 = p' - \rho_b c u' & \text{acoustic} & u_\lambda = u_b - c \end{array} \tag{3.51}$$

$$\text{with } c = \sqrt{\gamma \frac{p_b}{\rho_b}}. \tag{3.52}$$

For a subsonic jet without counterflow, w_1, w_2, w_3 are incoming, whereas w_4 is an outgoing characteristic. The form of the characteristics in cylindrical coordinates given above has been derived by Mitchell *et al.* [79] from the three dimensional Cartesian form given by Giles [46].

For "zero-order" boundary conditions, perfectly suited for a one-dimensional flow, all w_i could directly be imposed and retransformed into conservative variables. For example, in order to prevent any perturbations from (re-)entering the computational domain, all incoming characteristics can be set to zero while leaving w_4 unchanged. However, this treatment performs poorly for waves hitting the boundary at oblique angles of incidence (see section 3.5.4). Giles [46] proposed conditions not for w_i, but for their time derivatives, which take into account oblique incidence at *first order*. Unless explicitly stated otherwise, these conditions are employed in all simulations presented.

The algorithm described by Giles eliminates reflections. In order to include the possibility of forcing, the characteristic variables are split into a "non-reflective" component $\tilde{w}_i$ and a forcing component w_i^f:

$$w_i = \tilde{w}_i + w_i^f \,. \tag{3.53}$$

Following the procedure outlined by Mitchell *et al.* [79], the non-reflective parts $\tilde{w}_2$ and $\tilde{w}_3$ are calculated according to the first order Giles conditions, while using zeroth order for $\tilde{w}_1$:

$$\begin{aligned}
\tilde{w}_1 &= 0 && (3.54)\\
\frac{\partial \tilde{w}_2}{\partial t} &= -v_b \frac{\partial \tilde{w}_2}{\partial r} - \frac{1}{2}(c+u_b)\frac{\partial \tilde{w}_3}{\partial r} - \frac{1}{2}(c-u_b)\frac{\partial \tilde{w}_4}{\partial r} && (3.55)\\
\frac{\partial \tilde{w}_3}{\partial t} &= -v_b \frac{\partial \tilde{w}_3}{\partial r} - \frac{1}{2}(c-u_b)\left(\frac{\partial \tilde{w}_2}{\partial r} + \frac{\tilde{w}_2}{r}\right) \,. && (3.56)
\end{aligned}$$

The outgoing characteristic $\tilde{w}_4$ is left unchanged. Its time derivative has to be computed by differentiation of equation (3.51):

$$\frac{\partial \tilde{w}_4}{\partial t} = \frac{\partial p'}{\partial t} - \rho_b c \frac{\partial u'}{\partial t} \,. \tag{3.57}$$

with

$$\begin{aligned}
\frac{\partial p'}{\partial t} &= (\gamma-1)\left\{\frac{\partial(\rho E)'}{\partial t} - \frac{1}{2}\frac{\partial \rho'}{\partial t}\left[(v_b+v')^2+(u_b+u')^2\right]\right. \\
&\quad \left. -(\rho_b+\rho')\left[(v_b+v')\frac{\partial v'}{\partial t}+(u_b+u')\frac{\partial u'}{\partial t}\right]\right\} \\
\frac{\partial v'}{\partial t} &= \frac{1}{\rho_b+\rho'}\left[\frac{\partial(\rho v)'}{\partial t} - (v_b+v')\frac{\partial \rho'}{\partial t}\right] \\
\frac{\partial u'}{\partial t} &= \frac{1}{\rho_b+\rho'}\left[\frac{\partial(\rho u)'}{\partial t} - (u_b+u')\frac{\partial \rho'}{\partial t}\right] .
\end{aligned}$$

The inflow forcing is first specified in terms of the primitive variables (ρ^f, u^f, v^f, p^f) and then transformed through equations (3.51) into their corresponding characteristic forms $(w_1^f, w_2^f, w_3^f, w_4^f)$. No forcing is imposed on the outgoing characteristic.

Implementation. The inflow boundary conditions are imposed at each Runge-Kutta substep in the following manner: First, the time derivatives of the conservative variables are computed for the entire computational domain including all ghost points. Next, the characteristic variables w_i are computed on the ghost points of the inflow boundary according to equations 3.51. The forcing terms w_i^f are computed and subtracted from the w_i to obtain the non-reflective parts $\tilde{w}_i$. Then the time derivatives (3.55–3.57) are imposed. After the whole flow field has been time advanced – characteristic variables on the inflow ghost points, conservative variables everywhere else – the 0^{th} order condition (3.54) is applied to $\tilde{w}_1$ and the forcing terms w_i^f are added to $\tilde{w}_i$. Finally, the conservative variables are recovered from the characteristics.

Note that when adding and subtracting the forcing components of the characteristics, they must be evaluated at the appropriate time step. In the compact, three-step Runge-Kutta algorithm described in section 3.4.1, the effective time at the three substeps is to be taken as follows:

First substep:

$\Delta q_1(t_n) = F(q(t_n))$	conservative increment
$\Delta\tilde{w}(t_n) \leftarrow w(t_n) - w^f(t_n)$	subtract $w^f(t_n)$
$q(t_n+\delta_1\Delta t) = q(t_n) + \alpha_1\Delta q_1\Delta t$	time advancement
$w(t_n+\delta_1\Delta t) = \tilde{w}(t_n+\delta_1\Delta t) + w^f(t_n+\delta_1\Delta t)$	add $w^f(t_n+\delta_1\Delta t)$

Second substep:

$\Delta q_2(t_n + \delta_1 \Delta t) = F(q(t_n + \delta_1 \Delta t)) + \beta_1 \Delta q_1$	conservative increment
$\Delta \tilde{w}(t_n + \delta_1 \Delta t) \leftarrow w(t_n + \delta_1 \Delta t) - w^f(t_n + \delta_1 \Delta t)$	subtract $w^f(t_n + \delta_1 \Delta t)$
$q(t_n + \delta_2 \Delta t) = q(t_n + \delta_1 \Delta t) + \alpha_2 \Delta q_2 \Delta t$	time advancement
$w(t_n + \delta_2 \Delta t) = \tilde{w}(t_n + \delta_2 \Delta t) + w^f(t_n + \delta_2 \Delta t)$	add $w^f(t_n + \delta_2 \Delta t)$

Third substep:

$\Delta q_3(t_n + \delta_2 \Delta t) = F(q(t_n + \delta_2 \Delta t)) + \beta_2 \Delta q_2$	conservative increment
$\Delta \tilde{w}(t_n + \delta_2 \Delta t) \leftarrow w(t_n + \delta_2 \Delta t) - w^f(t_n + \delta_2 \Delta t)$	subtract $w^f(t_n + \delta_2 \Delta t)$
$q(t_n + \delta_3 \Delta t) = q(t_n + \delta_2 \Delta t) + \alpha_3 \Delta q_3 \Delta t$	time advancement
$w(t_n + \delta_3 \Delta t) = \tilde{w}(t_n + \delta_3 \Delta t) + w^f(t_n + \delta_3 \Delta t)$	add $w^f(t_n + \delta_3 \Delta t)$

where

$$\begin{aligned} \delta_1 &= \alpha_1 = 0.5 \\ \delta_2 &= \alpha_1 + \alpha_2(1 + \beta_1) = 0.7887 \\ \delta_3 &= \alpha_1 + \alpha_2(1 + \beta_1) + \alpha_3(1 + \beta_2 + \beta_1\beta_2) = 1. \end{aligned}$$

3.5.4 Tests of the inflow boundary conditions

The performance of the numerical inflow boundary conditions has a strong impact on the simulation results. The following tests are presented to assess the non-reflecting properties and the quality of the upstream condition provided by the inflow boundary treatment.

Acoustic reflections

The reflection of acoustic waves is compared for three types of boundary conditions:

- Dirichlet boundary conditions for the conservative perturbation variables $\boldsymbol{q}' = 0$ at the outermost ghost point. These are employed at the lateral and the downstream boundary of the computational domain, behind the sponge zones, in the simulations presented in chapter 4. No sponge zone is added in these tests.
- Zero-order characteristic boundary conditions: $(w_1, w_2, w_3) = 0$.
- First-order characteristic boundary conditions as described in section 3.5.3.

The reflections of a plane wave parallel to the boundary and of a spherical wave are examined.

Plane wave. An upstream travelling acoustic pulse parallel to the inflow boundary in an inviscid homogeneous fluid at rest is created as

$$p'(x) = 0.001 \exp\left[\frac{(x-x_0)^2}{0.3^2}\right] \qquad \rho'(x) = \frac{p'(x)}{c^2} \qquad u'(x) = -\frac{p'(x)}{c}\ , \tag{3.58}$$

All flow variables are invariant in r. A Neumann condition $\partial \boldsymbol{q}'/\partial r = 0$ at r_{max} guarantees a one-dimensional flow field at all times. As the flow is inviscid and one-dimensional, the shape and amplitude of acoustic signals remains unchanged as they propagate through the interior of the computational domain. The pressure signal of the original pulse is shown in figure 3.8*a* before it reaches the boundary at $x = 0$, and the downstream travelling reflected pressure waves some time later are compared in figures 3.8*b*–*d* for the three different boundary conditions. Ideally, the reflected signal would be zero. The ratio of the peak-to-peak amplitudes of the reflected waves and the original pulse defines a reflection coefficient of 2.0×10^{-4} for the Dirichlet condition, and of 3.5×10^{-6} for both characteristic boundary schemes. Indeed the zero- and first-order characteristic boundary conditions perform almost identically well for an incident plane acoustic wave parallel to the boundary.

Spherical wave. A spherical acoustic wave in an inviscid homogeneous fluid at rest emerges from an initial pulse at $(x, r) = (10, 0)$ of the form

$$p'(x,r) = 0.001 \exp\left[\frac{(x-x_0)^2 + r^2}{0.3^2}\right] \qquad T'(x,r) = \frac{p'(x,r)}{p_b} \qquad \rho' = \boldsymbol{u'} = 0\,. \tag{3.59}$$

The speed of sound is chosen to be $c = 10$, and the ambient pressure is given by $p_b = c^2/\gamma$. The computation is performed on an equidistant grid with spacing $\Delta x = \Delta r = 0.05$.

The pressure field at $t = 2$ is displayed in figure 3.9 for all three numerical boundary conditions. Only the relevant part of the domain is shown, including the upstream 'ghost points' at $x < 0$. The acoustic wave has not yet reached the lateral and downstream boundaries. Isocontours are plotted for values $-10^{-6} \le p' \le 10^{-6}$ in order to visualize the reflections, whereas the amplitude of the original pressure wave at $t = 2$ is $\pm 3.4 \times 10^{-6}$.

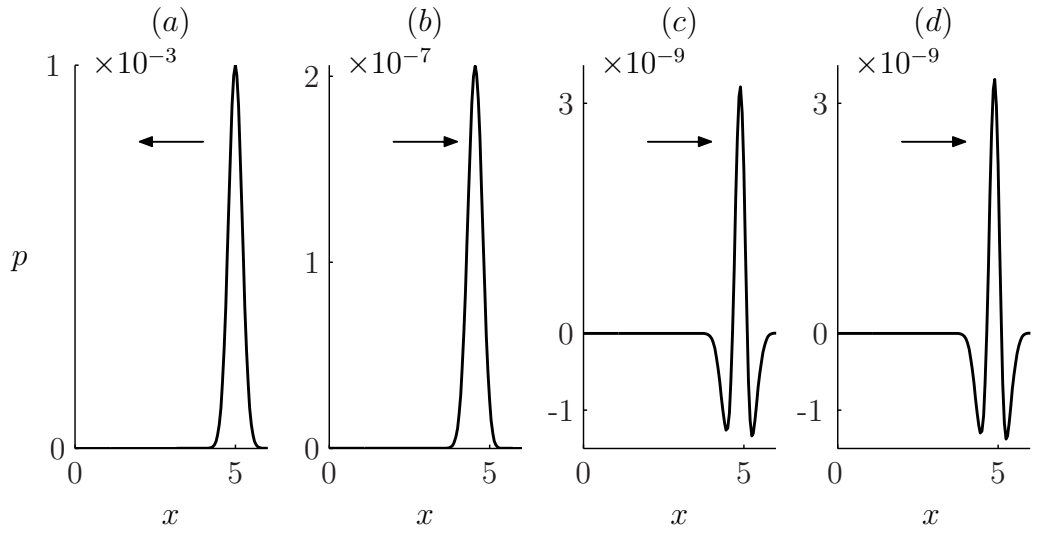

Figure 3.8: Reflection of a plane acoustic wave at $x = 0$, pressure signals. a) Upstream travelling acoustic pulse; b) reflected pulse from the Dirichlet condition; c) reflected pulse from the zero-order characteristic boundary condition; d) reflected pulse from the first-order characteristic boundary condition.

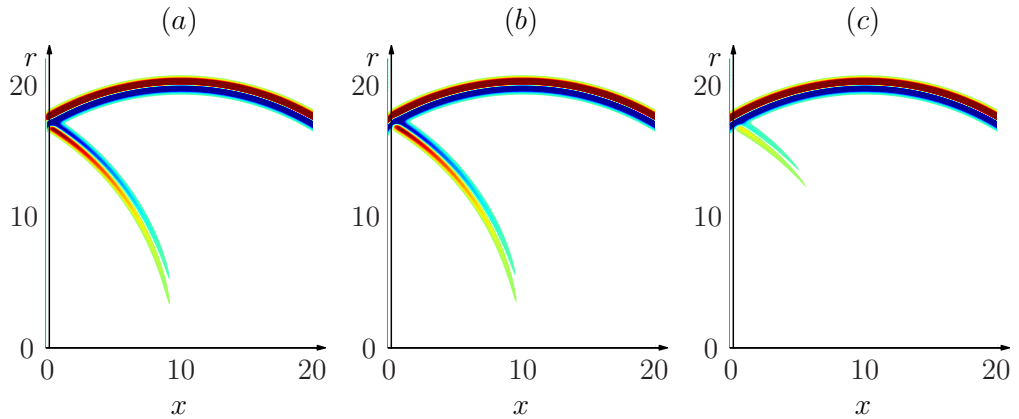

Figure 3.9: Reflection of a spherical acoustic wave at $x = 0$. Pressure perturbations at $t = 2$; red is positive, blue is negative. a)Dirichlet condition; b) zero-order charateristic condition; c) first-order characteristic condition.

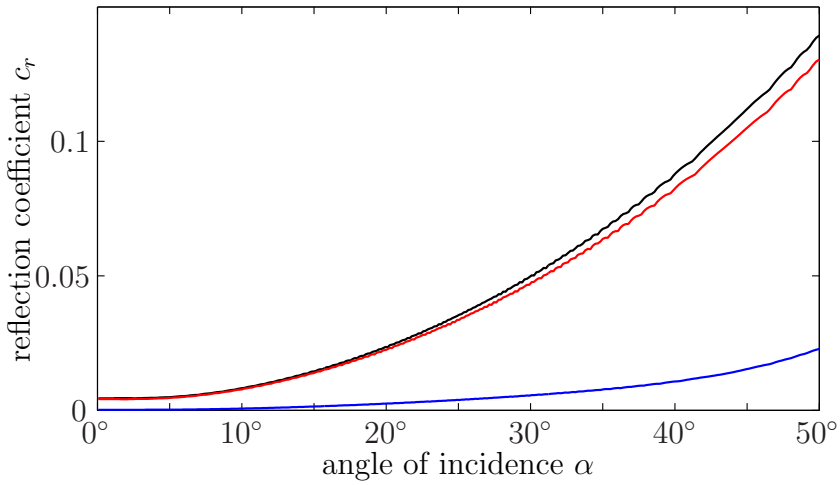

Figure 3.10: Reflection coefficients as functions of the angle of incidence for a spherical pulse. Black: Dirichlet conditions, red: zero-order characteristic conditions, blue: first-order characteristic conditions.

The amplitude ratio of the reflected waves in figure 3.9 and the unreflected wave can be examined as a function of the angle α, formed between the propagation direction and the axis $r = 0$, which corresponds to the angle of incidence at the upstream boundary when the reflection was formed. The resulting curves are given in figure 3.10. Interestingly, it is found that the Dirichlet and zero-order characteristic conditions reflect a spherical wave almost identically. The first-order correction of the characteristic boundary condition is seen to yield a significant improvement, not only for large angles of incidence, but also for $\alpha = 0$ in the case of a curved wave front.

Impermeability of the upstream boundary to instability waves

The theoretical model of nonlinear global modes discussed in chapter 4 is based on the assumption that all upstream propagating instability waves are blocked at the upstream boundary, *i.e.* that the fluctuation amplitudes associated with vortical instability modes are forced to zero. This impermeability requirement is tested for the zero- and first-order characteristic boundary conditions.

The base flow chosen for this test is an absolutely unstable parallel jet profile with the parameters $R/\theta = 14.8$ and $S = 0.5$. Direct numerical simulations of nonlinear perturbations in this base flow are carried out at $\mathrm{Re} = 3750$ and $\mathrm{Ma} = 0.1$. The computations start from an initial pulse at

$(x, r) = (2, 1)$ in the form of a ring vortex (Bogey, Bailly & Juvé [10])

$$\begin{pmatrix} u' \\ v' \end{pmatrix} = 0.1 \begin{pmatrix} 1-r \\ x-2 \end{pmatrix} \frac{1}{0.2\ r} \exp\left[-\ln 2 \frac{(x-2)^2 + (r-1)^2}{0.2^2} \right] . \qquad (3.60)$$

This strong perturbation gives rise to a roll-up of discrete vortices downstream and excites the linear absolute instability mode upstream near $x = 0$. For sufficiently long time, the flow settles into a periodic oscillating *global mode* state. A detailed investigation of such flow states is postponed to chapter 4. The aim of the present test computations is to qualitatively demonstrate the influence of the upstream boundary conditions on the spatial envelope of the oscillation amplitude.

Once the asymptotic flow state of periodic oscillations is reached, the temporal rms values of radial velocity fluctuations are computed over one oscillation cycle at $r = 1$ and over the interval $0 \leq x \leq 5$. The resulting distributions $v'_{rms}(x)$ are displayed in figure 3.11 for the computations with zero-order (red) and with first-order (blue) characteristic boundary conditions. In both cases, v'_{rms} is strictly zero at the ghost points $x < 0$. Yet, the downstream development of the instability wave packet is not identical. The zero-order condition results in larger oscillation amplitudes near the boundary, and as a consequence, the nonlinear amplitude saturation sets in closer to the inlet as compared to the computations with first-order boundary conditions. The difference in the spatial structure of the upstream wave front is associated with different oscillation frequencies: With zero-order conditions, the global frequency is found to be $\omega_g = 1.206$, whereas the simulation with first order conditions yields $\omega_g = 1.144$. The linear absolute frequency of the base flow is $\omega_0 = 1.019$. The radial velocity has been chosen over the perturbation vorticity as a measure of the instability wave amplitude, because evaluation of the vorticity involves a numerical axial derivation of v', which is necessarily inaccurate near $x = 0$ with $v' \equiv 0$ in the ghost point region.

Buell & Huerre [16] observed self-sustained global oscillations in numerical simulations of convectively unstable shear layers. These oscillations have been shown to be the result of an acoustic feedback mechanism, involving spurious acoustic waves radiated from the downstream numerical boundary. No such states have been found to arise in simulations with the numerical method described here. But even in the absence of acoustic feedback, the tests presented in this section demonstrate how sensitive the dynamics of a globally unstable flow observed in direct numerical simulations may be to the choice of appropriate boundary conditions. Although the first order characteristic boundary conditions seem to display the most desirable properties for the purpose of the present investigation, it must be expected that the

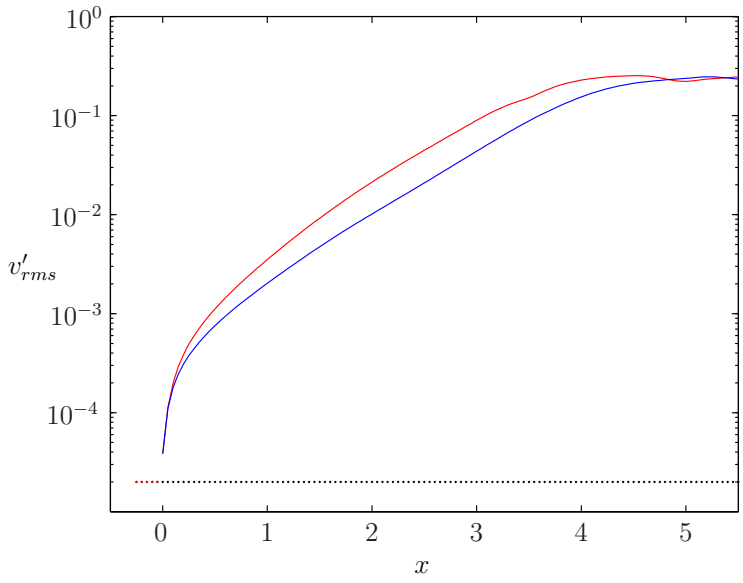

Figure 3.11: Instability wave amplitudes near the inlet: radial velocity fluctuations v'_{rms} at $r = 1$ as a function of x. Red: zero order characteristic boundary conditions, blue: first order characteristic boundary conditions. Axial grid point distribution: ghost points are shown in red.

results of the direct numerical simulations are affected to some extent by the imperfections of this particular boundary treatment.

3.6 Validation: Linear impulse response

The accuracy of the numerical method described in the previous section with respect to the evolution of instability waves is assessed by computing the linear impulse response of a parallel jet profile. Nonlinear terms in the perturbation equations (3.10–3.13) are switched off for this test calculation. The results of the linear direct numerical simulation can then be compared to a spatio-temporal instability analysis, obtained from the numerical procedure that has been outlined in chapter 2.

A parallel base flow with the parameters $R/\theta = 20$ and $S = 0.57$ is considered. The temporal evolution of an impulse perturbation

$$u'(x,r) = A \exp\left(-\frac{x^2 + (r-1)^2}{0.3^2}\right) \quad \text{with } A = 10^{-30}\ , \tag{3.61}$$

introduced at a time $t_0 > 0$, is computed at $\mathrm{Re} = 500$ and $\mathrm{Ma} = 0.1$. The

computational domain extends over $0 < r \leq 50$, $-50 \leq x \leq 50$, resolved with 900×4000 grid points. Periodic boundary conditions are imposed at $x = \pm 50$ in order to simulate an infinite domain in the axial direction.

The first validation result is that with an initial condition $\boldsymbol{q}' = 0$, the perturbation quantities stay *strictly* zero at all times, *i.e.* the numerical method does not introduce any spurious noise in the absence of explicit external forcing. The same behavior is observed in situations with non-parallel base flows and non-periodic boundary conditions.

At $t = t_0$, the impulse perturbation (3.61) gives rise to an exponentially growing wave packet. As demonstrated by Delbende, Chomaz & Huerre [35], the temporal growth rate σ can be constructed as a function of group velocity v_g (see section 2.2) by comparing the linear impulse response wave packet at two times $t_1,\ t_2$. Let the perturbation amplitude $A(x,t)$ along x at a given time t be defined as

$$A(x,t) = \left(\int_0^\infty |\tilde{u}(r,x,t)|^2 \, r \, \mathrm{d}r \right)^{1/2} , \tag{3.62}$$

where $\tilde{u}(r,x,t)$ is the Hilbert transform of $u'(r,x,t)$ as given in Delbende *et al.* [35].

If the wave packet emanated from an inital pulse at (x_0, t_0), the amplitude envelope (3.62) is readily expressed as a function $A(v_g, t)$ of the group velocity $v_g = (x - x_0)/(t - t_0)$. During the time interval $t_1 \leq t \leq t_2$, the wave packet experiences an exponential growth

$$A(v_g, t_2) = A(v_g, t_1) \; e^{\sigma(v_g)\,(t_2 - t_1)} \tag{3.63}$$

along each ray $x/t = v_g$. The growth rate distribution is therefore recovered as

$$\sigma(v_g) = \frac{\ln A(v_g, t_2) - \ln A(v_g, t_1)}{t_2 - t_1} \, . \tag{3.64}$$

Two curves obtained for $\sigma(v_g)$ in the present simulation are presented in figure 3.12. The blue line is computed from the amplitude envelope at $t_1 = 28$ and $t_2 = 35$, the red line from $t_2 = 35$ and $t_3 = 42$. The growth rates are well converged over the unstable range of group velocities $0 \leq v_g \leq 0.8$. Corresponding results obtained from the numerical solution of the dispersion relation (see chapter 2), displayed as black symbols in figure 3.12, show excellent agreement.

The real part of the absolute frequency as found in the DNS can be determined from the temporal pressure signal at $x = 0$, $r = 1$, displayed

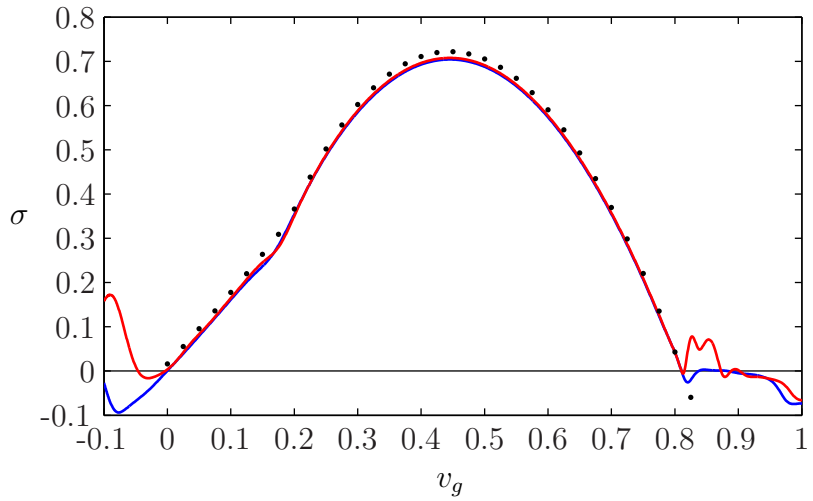

Figure 3.12: Temporal growth rate σ as a function of group velocity v_g. (—) according to DNS over $28 \leq t \leq 35$; (—) according to DNS over $35 \leq t \leq 42$; $(\cdot)$ according to dispersion relation (see chapter 2).

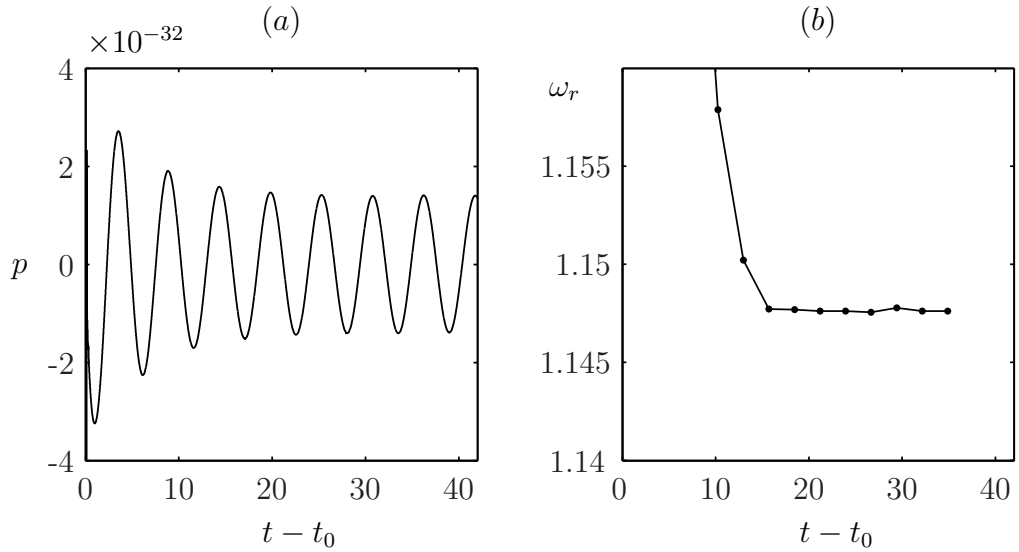

Figure 3.13: Temporal development of the absolute mode in the linear impulse response calculation. (a) Pressure signal $p'(t)$ at $x = 0$, $r = 1$. (b) Instantaneous frequency measured from the same signal.

in figure 3.13*a*. The temporal development of $\omega_r = 2\pi/\Delta t_i$, with $\Delta t_i = t_{i+1} - t_{i-1}$ such that $p(t_i) = 0 \; \forall \, i$, is given in figure 3.13*b*: the real absolute frequency in the DNS converges to

$$\omega_r = 1.1476\,,$$

to be compared to the theoretical result

$$\omega_{0,r} = 1.1475\,.$$

This validation test has demonstrated that the implemented numerical method for the direct numerical simulation captures the linear instability characteristics of the base flow with great accuracy. The results also demonstrate that the separation into base flow and perturbation quantities has been rigorously preserved in the implementation: the difference of approximately 30 orders of magnitude between base flow and perturbation amplitudes does not compromise the precision of the calculations. These properties are essential for the direct numerical simulation of the aerodynamic near field of globally unstable jets. A validation of the acoustic field computed in the DNS has to be postponed to chapter 5, where the computational results will be compared to solutions of the Lighthill equation.

Chapter 4

Nonlinear global instability

The *linear* impulse response of a *parallel* baseflow in an *infinite* domain has been examined in chapter 2. It will now be investigated how this information may be useful to describe the *nonlinear* dynamics of a *spatially developing* jet, in a domain that is *bounded* upstream at the location of an imaginary nozzle. Theoretical predictions about the onset of nonlinear global instability and about the frequency selection in globally unstable situations, inferred from the local linear instability properties of the baseflow, are to be compared to results obtained from direct numerical simulations of nonlinear perturbations in spatially developing jets.

The theoretical framework has been established by Arnaud Couairon, Benoît Pier and their respective coworkers [25, 26, 27, 93, 94, 95, 96]. Their analyses in turn rely in large measure on the front dynamics studies by Kolmogorov *et al.* [61], Dee & Langer [34] and van Saarlos [111, 112], among others, and on the global instability concepts introduced by Huerre & Monkewitz [54] and Chomaz [19]. A short survey of the literature on nonlinear global instability is provided in section 4.2.1.

The outline of the chapter is as follows: on the basis of the insight gleaned in chapter 2 concerning the linear impulse response, I first discuss the implications of nonlinearity, non-parallelism, and of the presence of an upstream boundary on the structure of global modes. The objective is neither to reproduce the methodology used in the development of the nonlinear global mode model, nor to establish a rigorous formalism for the present investigation. The purpose is rather to introduce the conceptual notions of nonlinear global mode theory in a tangible way, as needed for a physical interpretation of the numerical simulations. The occurrence of global modes in heated *thick shear layer* jets is presented and compared to theoretical predictions in sec-

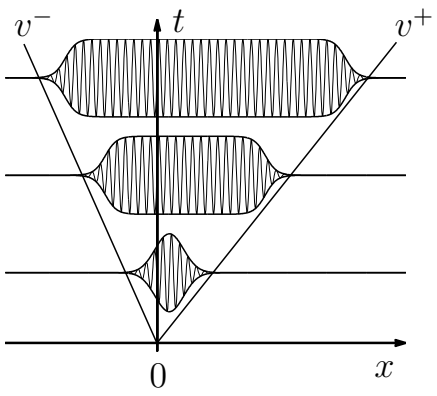

Figure 4.1: Schematics of a nonlinear wave packet evolving in an absolutely unstable flow. Nonlinear absolute instability follows from linear absolute instability. A *pulled* front propagates upstream at velocity v^-.

tion 4.2. Section 4.3 extends the investigated parameter range to *thin shear layer* jets, thereby approaching the conditions of the reference experiments of Monkewitz *et al.* [82].

4.1 Introduction to front dynamics

4.1.1 Nonlinear versus linear absolute instability

In order to examine the consequences of nonlinearity on the impulse response in an infinite parallel jet, consider the following Gedankenexperiment: from an infinitesimal small perturbation pulse, a linear wave packet forms according to the linear scenario studied in chapter 2. In an unstable setting, nonlinear saturation sets in as the fastest growing modes eventually reach amplitude levels of the same order as the baseflow. In physical terms, nonlinear amplitude saturation corresponds to the roll-up of the undulated shear layer into discrete vortices. The linear impulse response described in chapter 2 reveals that the strongest temporal growth occurs near the center of the wave packet, for modes of typical group velocity around $v_g = 0.5$. The extent of the saturated inner region of the wave packet increases in time, as illustrated schematically in figure 4.1.

The nonlinear wave packet is bounded in $x-t$ space by the rays $x/t = v^-$ and $x/t = v^+$, along which the temporal growth rate is zero. For large time, v^- and v^+ are the propagation velocities of *nonlinear wave fronts* that

separate the unperturbed base state from the bifurcated flow region. In analogy to the terminology of linear theory, the flow is said to be *nonlinearly absolutely unstable* if $v^- < 0$, and *nonlinearly convectively unstable* if $v^- > 0$ (see Chomaz [17]).

Two possible types of nonlinear absolute instability may typically arise: If the upstream front velocity v^- is identical with the group velocity of the upstream neutral mode of the *linear* impulse response, the effects of nonlinearity are confined to the interior of the wave packet. Nonlinear absolute instability in this case follows from linear absolute instability, and the leading edge of the nonlinear wave packet is formed by the linear mode of zero growth rate. Such an upstream traveling nonlinear wave front is referred to as a *pulled* front [112]. The real frequency and complex wave number of a pulled front, as well as its velocity v^-, are readily determined from a linear instability analysis.

In other flow configurations, it is possible that nonlinear modes evolve which propagate upstream faster than their neutral linear counterpart. These flows may be nonlinearly absolutely unstable although they remain linearly convectively unstable [17]. Since the front in this case advances due to mechanisms that do not act in the small-amplitude upstream tail, but from within the interior of the wave packet, such a front is referred to as a *pushed* front [112]. In the context of the Ginzburg–Landau equation, Couairon & Chomaz [25] have demonstrated that pushed fronts only occur over a very restricted range of control parameters. In the context of real flows, pushed fronts have not yet been observed. Henceforth, it is assumed that linear and nonlinear absolute instability in hot jets coincide, *i.e.* that both the velocity and the frequency of the upstream wave front are dictated by the linear instability properties of the baseflow.

4.1.2 Non-parallel baseflows

Many of the instability properties obtained for parallel profiles can be generalized to describe the evolution of perturbations in spatially developing baseflows, provided that their streamwise variations take place on a sufficiently large length scale when compared to an instability wavelength. Under this condition, instability modes at a given streamwise station can be expected to evolve as if the baseflow was *locally parallel*.

This condition is formally expressed as a decorrelation of two streamwise variables: instability oscillations take place on the scale of x, whereas the baseflow varies on the scale of a "slow" variable $X = \varepsilon x$ with $\varepsilon \ll 1$. The

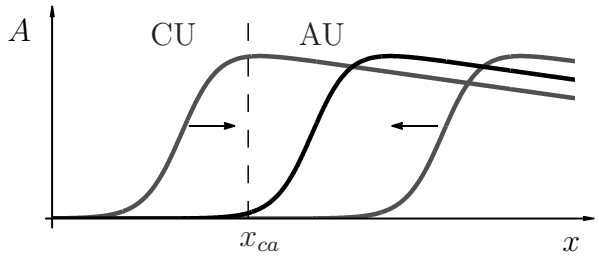

Figure 4.2: Schematics of nonlinear front propagation in a non-parallel baseflow with CU/AU transition at x_{ca}. The only stable position is around x_{ca}, indicated by a black curve.

slow variable has been introduced in section 3.3.1 as $X = x/\mathrm{Re}$ under the boundary layer assumptions. Under this assumption, the linear absolute frequency at any given streamwise station X in a weakly non-parallel baseflow may be expressed as

$$\omega_0 = \Omega[k_0(X); X] \tag{4.1}$$

$$\frac{\partial \Omega}{\partial k}[k_0(X); X] = 0\,. \tag{4.2}$$

In these expressions, $\Omega[k(X); X]$ is the frequency corresponding to $k(X)$, according to the linear dispersion relation of the locally parallel profile at X. The complex pair $\omega_0(X)$, $k_0(X)$ is then determined from an instability analysis of an infinite parallel flow, with radial profiles as in the spatially developing baseflow at the station X.

The spreading of a nonlinear wave packet in a slowly varying infinite baseflow thus depends on the local linear instability properties at the instantaneous location of the upstream front: if the baseflow is (locally) absolutely unstable everywhere, the wave packet spreads in the upstream and downstream directions. If the baseflow is convectively unstable everywhere, the whole wave packet is convected downstream, and at any streamwise station the flow will ultimately return to its unperturbed steady state.

In a setting where the baseflow is absolutely unstable downstream of a streamwise station x_{ca}, but convectively unstable upstream of x_{ca}, the long time response to an arbitrary perturbation is given by a nonlinear wave packet with a *stationary upstream front* located at the transition station x_{ca}. Such a situation is sketched in figure 4.2: a front originating from the absolutely unstable region propagates upstream, whereas within the convectively unstable region it would be convected downstream. Consequently, the transition station x_{ca} is a stable front position. Once the front is pinned at the transition

station, the low-amplitude oscillations at x_{ca} must correspond to the linear absolute instability mode at this location, characterized by a real frequency ω_0^{ca} and a spatial growth rate $-k_{0,i}^{ca} > 0$, as implied by the discussion of the previous section.

Such situations, *i.e.* a non-parallel basic state exhibiting a transition from upstream convective to downstream absolute instability in an infinite domain, have been studied by Pier *et al.*[96, 95]. From investigations of nonlinear Ginzburg–Landau model equations with varying coefficients, Pier *et al.*[95] have found that a stationary wave front at x_{ca} imparts its linearly selected frequency ω_0^{ca} on the entire downstream nonlinear wavetrain, thereby giving rise to an asymptotic state in the form of synchronized oscillations with a fixed spatial structure — a *nonlinear global mode*, as defined in equation (1.1), of global frequency

$$\omega_g = \omega_0^{ca} \,. \tag{4.3}$$

Pier & Huerre [94] have demonstrated that the conclusions drawn from the Ginzburg–Landau model can be generalized to real flow settings: the global frequency ω_g of the von Kármán vortex street, as observed in direct numerical simulations of a synthetic wake, matches the absolute frequency ω_0 at the transition station x_{ca} within 2%. The upstream front of the vortex street was found to be located at x_{ca}. In the naturally developing wake behind a circular cylinder, the frequency selection criterion (4.3) still provides a 10% accurate prediction over the range of Reynolds numbers $100 \leq \mathrm{Re} \leq 180$ [93].

In analogy to the study of Pier & Huerre [94], the validity of criterion (4.3) is investigated in section 4.2.4 for a spatially developing jet.

4.1.3 Semi-infinite flows with upstream boundary

While the typical streamwise development of wakes is appropriately modelled in an infinite domain with uniform, stable flow conditions upstream of the obstacle, a jet necessarily emerges from a nozzle, or orifice, that marks a hard upstream boundary for the development of instability waves in the free shear layer. Furthermore, the linear analysis of chapter 2 has shown that a transition from upstream convective to downstream absolute instability is untypical for a naturally spreading jet (see for instance figure 2.6).

The evolution of a nonlinear wave packet according to the Ginzburg–Landau equation in a *semi-infinite* domain, bounded upstream at $x = 0$, has been described by Couairon & Chomaz [26, 27]. The perturbation amplitude at $x = 0$ is assumed to be zero in their model. In purely convectively unsta-

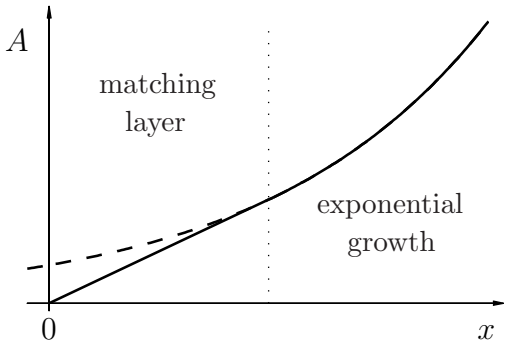

Figure 4.3: Schematics of a wave front (—) bent to $A = 0$ at the upstream boundary in an AU medium. In the absence of a boundary, the upstream development would be exponential (- - -).

ble surroundings, or if absolute instability only sets in at some downstream location $x > 0$, the presence of the boundary is irrelevant with regard to the long-time dynamics. By contrast, if an absolutely unstable region extends up to $x = 0$, a nonlinear wave packet within this region spreads in the upstream direction, until the advancement of its upstream front is blocked by the boundary. An impermeable upstream boundary adjacent to an absolutely unstable baseflow region therefore constitutes another configuration in which a *nonlinear global mode* with a stationary upstream front may be generated.

In view of the spatial structure and the frequency selection, the essential difference between the global mode scenarios in infinite and semi-infinite domains lies in the fact that in the former instance, the perturbation amplitude envelope $A(x)$ can freely develop upstream of the front location according to its spatial growth rate, $A(x) \propto exp[-ik_i(\omega_g)x]$, whereas in the latter instance, the amplitude is forced to zero at the upstream boundary, as illustrated in figure 4.3. The implications of the resulting distortion of the spatial global mode structure for the frequency selection process have been rigorously examined in the Ginzburg–Landau model by Couairon & Chomaz, first under the assumption of a parallel basic state [26], then generalized to weakly non-parallel situations [27]. Their analysis assumes that a *matching layer* (see figure 4.3) provides the connection between the $A = 0$ condition at the boundary and a region of exponential amplitude growth. The amplitude variations within this layer are obtained explicitly from a matched asymptotic expansion approach [26, 27].

The model analysis of Couairon & Chomaz [26, 27] has shown that the

onset of global instability in *parallel* basic states coincides with the onset of absolute instability. In a weakly *non-parallel* basic state, provided that absolute instability first occurs at the upstream boundary, it may be concluded that nonlinear amplitude saturation within the absolutely unstable region is required before global instability sets in. In both parallel and non-parallel settings, the global frequency in the Ginzburg–Landau model is found to obey

$$\omega_g = \omega_{0,r} + \mathcal{O}(\epsilon)\,, \tag{4.4}$$

where $\omega_{0,r}$ is the real part of the absolute frequency at the upstream boundary, and ϵ is a supercriticality parameter that marks the departure from the global instability threshold. Thus, if the model can be generalized to describe the behavior of real flows, the global frequency is predicted to correspond to the absolute frequency at the upstream boundary in a *marginally* globally unstable flow. Far above the global instability threshold, this criterion only provides a leading-order prediction.

One of the principle objectives of the numerical simulations presented in this chapter is to assess the validity of the frequency selection criterion (4.4), derived from Ginzburg–Landau model equations, in the context of global modes in hot jets. A first example of such a global mode observed in an absolutely unstable parallel jet has already been presented in section 3.5.4 as a test case for the choice of numerical upstream boundary conditions. Figure 3.11 demonstrates that the spatial structure of the upstream wave front displays the same characteristics as described in the model analysis of Couairon & Chomaz: a matching layer region $0 \leq x \lesssim 0.5$ is clearly identified, connecting the zero-amplitude condition at $x = 0$ to a region of exponential growth. As has been noted in section 3.5.4, slight differences in the boundary condition formulation result in a variation of the matching layer length, and in noticeable differences in the observed frequencies: the global frequencies in this supercritical absolutely unstable baseflow differ from the absolute frequency by 18% and 12%, respectively. This behavior indeed complies with the nonlinear global mode model of Couairon & Chomaz[26]. In what follows, non-parallel jet profiles will be considered.

Section 4.2

Nonlinear global modes in hot jets

By LUTZ LESSHAFFT[1,2], PATRICK HUERRE[1], PIERRE SAGAUT[3], AND MARC TERRACOL[2]

[1]Laboratoire d'Hydrodynamique (LadHyX), CNRS – École Polytechnique, 91128 Palaiseau, France,
[2]ONERA, Department of CFD and Aeroacoustics, 29 av. de la Division Leclerc, 92322 Châtillon, France
[3]Laboratoire de Modélisation en Mécanique, Université Pierre et Marie Curie, Boite 162, 4 place Jussieu, 75252 Paris Cedex 05, France

published in *Journal of Fluid Mechanics* **554**, 50th anniversary volume, p. 393–409

Abstract

Since the experiments of Monkewitz *et al.* [82], sufficiently hot circular jets are known to give rise to self-sustained synchronized oscillations induced by a locally absolutely unstable region. In the present investigation, numerical simulations are carried out in order to determine if such synchronized states indeed correspond to a nonlinear global mode of the underlying base flow, as predicted in the framework of Ginzburg–Landau model equations. Two configurations of slowly developing base flows are considered: In the presence of a pocket of absolute instability embedded within a convectively unstable jet, global oscillations are shown to be generated by a steep nonlinear front located at the upstream station of marginal absolute instability. The global frequency is given, within 10% accuracy, by the absolute frequency at the front location and, as expected on theoretical grounds, the front displays the same slope as a k^--wave. For jet flows displaying absolutely unstable inlet conditions, global instability is observed to arise if the streamwise extent of the absolutely unstable region is sufficiently large: While local absolute instability sets in for ambient-to-jet temperature ratios $S \leq 0.453$, global modes only appear for $S \leq 0.3125$. In agreement with theoretical predictions, the selected frequency near the onset of global instability coincides with the absolute frequency at the inlet. For lower S settings, it gradually departs from this value.

4.2.1 Introduction

Since the landmark investigations of Crow & Champagne [33] and Brown & Roshko [15], it has been generally acknowledged that high Reynolds number free shear flows such as circular jets, wakes and mixing layers are dominated by large-scale structures. The observed spreading rates are due in large measure to the streamwise development and interactions of these vortices (Winant & Browand [115]). It has also been well established that the dynamics of free shear flows, including their spreading rate, may be manipulated or controlled by applying at the inlet low-level acoustic or mechanical excitations of appropriate frequency (see Ho & Huang [50] and the review by Ho & Huerre [48]).

From the point of view of instability theory, vortical structures may be regarded in Fourier space as a collection of instability waves of distinct frequency and streamwise wavenumber. The above experimental observations have very early on led theoreticians to adopt the so-called spatial stability approach, which consists in determining the complex wavenumber associated with each real frequency, as dictated by the linear stability properties of parallel flows (Michalke [76]). A detailed review of spatial stability applied to parallel compressible circular jets is given in Michalke [78]. Such formulations have been successful in predicting the phase velocity, spatial growth rate and cross-stream distribution of low-intensity perturbations induced by external forcing. The generalization of these concepts to weakly non-parallel flows, in the framework of the WKBJ approximation, was first introduced for the case of incompressible circular jets by [31], and for the case of turbulent shear layers by Gaster, Kit & Wygnanski [45]. These analyses provided a systematic methodology to estimate the streamwise linear response of shear flows to forcing. In this setting, each shear flow is regarded as an amplifier of external perturbations, thereby reflecting its sensitivity to noise.

The legitimacy of this approach may only be assessed if one resorts to the concepts of absolute versus convective instability, first introduced by plasma physicists (Briggs [14], Bers [7]). The application of these concepts to various configurations has led to distinguish between two main classes of shear flows: *noise amplifiers*, which are sensitive to external forcing, and *oscillators*, which beat at a specific intrinsic frequency. Flows that are convectively unstable at all streamwise stations have been shown to behave as noise amplifiers, whereas intrinsic oscillations only exist for flows displaying a region of absolute instability (see Huerre & Monkewitz [54] and Huerre [51] for comprehensive reviews). Co-flow mixing layers and constant-density jets belong to the former class, whereas the von Kármán vortex street behind a circular

cylinder exemplifies an oscillator-type behaviour (Provansal, Mathis & Boyer [97]). Jets of sufficiently low density constitute yet another striking instance of shear flows displaying a transition from convective to absolute instability, as established theoretically by Monkewitz & Sohn [85]. The experiments of Monkewitz *et al.* [82] demonstrated that self-sustained oscillations arise beyond the absolute instability onset in hot air jets. A similar behaviour was shown to occur in helium jets by Sreenivasan, Raghu & Kyle [105], as further confirmed by Boujemaa, Amielh & Chauve [11]. In order to predict the frequency and spatial distribution of such self-sustained oscillations, it has proven fruitful to represent them as a *global mode*[1] consisting of an extended wavepacket which beats at a specific frequency (Chomaz, Huerre & Redekopp [21] and Monkewitz, Huerre & Chomaz [83]). The objective of the present numerical study is precisely to demonstrate that the synchronized oscillations experimentally observed in hot jets may be ascribed to the presence of a nonlinear global mode induced by absolute instability.

The main findings of Monkewitz & Sohn [85] and Monkewitz *et al.* [82] may be summarized as follows: For a family of analytical velocity profiles which accurately represent experimentally measured mean flows in hot jets, absolute instabiliy arises when the ratio S of ambient-to-jet temperature falls below 0.72. For a top hat inlet velocity profile typical of zero Mach number laboratory jets, the axisymmetric mode first exhibits a transition to absolute instability near the nozzle exit, at approximately 0.4 diameters away from the inlet. Furthermore, the experiments of Monkewitz *et al.* [82] indicate that the critical value $S = 0.72$ very closely coincides with the appearance of synchronized oscillations. Two axisymmetric modes have been observed to arise with respective Strouhal numbers, based on jet diameter, $St = 0.3$ and $St = 0.45$.

The present investigation is largely motivated by recent advances which have been made in extending the theory of global modes to the fully nonlinear régime (see Chomaz 2005 for a review). The comprehensive analyses of Ginzburg-Landau evolution models by Chomaz [17] and Couairon & Chomaz [24, 25, 26, 27] have firmly established the intimate connection between nonlinear global modes and front velocity dynamics in systems giving rise to pattern formation. According to van Saarloos [111, 112], the velocity of the front separating the bifurcated state from the unperturbed basic state is governed by either linear or nonlinear mechanisms. In the former instance (Dee & Langer [34]), the front moves at a velocity such that, in the co-moving

[1]For clarity, we reserve the term *global mode* throughout this study to denote a wavepacket which is dominated by its upstream front dynamics, as opposed to self–sustained oscillations which may exist due to acoustic feedback.

frame, the basic state is marginally absolutely/convectively unstable. In the latter instance, it is determined through a detailed phase space analysis which must be carried out on a case-by-case basis. As in wake flows, it will be assumed for the present discussion that the front dynamics are governed by the linear selection criterion. In the context of Ginzburg-Landau equations on the *semi-infinite interval* $x > 0$, Couairon & Chomaz [24, 25, 26, 27] have shown that the nonlinear global mode is dominated by a stationary front pinned at the upstream boundary $x = 0$. If the parameters are constant in x, the threshold for the appearance of a global mode coincides with the onset of absolute instability, and explicit scaling laws may be derived for its spatial structure. At threshold, the global frequency is given by the absolute frequency at the upstream boundary. In the context of Ginzburg-Landau equations with variable coefficients displaying a finite pocket of absolute instability in an *infinite domain*, Pier *et al.* [96, 95] have demonstrated that the corresponding nonlinear global mode is also dominated by a stationary front, this time located at the upstream boundary of the absolutely unstable region. The global frequency is then given by the absolute frequency prevailing at this transition station.

Many of the results pertaining to Ginzburg-Landau models have been shown to also hold in real flow situations. Thus, the scaling law for the global spatial structure in *semi-infinite* media has been validated by Couairon & Chomaz [27] in the case of the von Kármán vortex street simulations of Zielinska & Wesfreid [117] and Wesfreid, Goujon-Durand & Zielinska [114]. The recent numerical simulations of synthetic parallel wakes in a semi-infinite domain by Chomaz [18] very accurately follow the frequency selection criterion and the scaling law derived from Ginzburg-Landau models. The WKBJ formulation of Pier *et al.* [96] in *infinite* media has been generalized to two-dimensional wakes by Pier & Huerre [94]. The vortex street frequency computed in a slowly varying *streamwise infinite* wake is effectively given, within 2% accuracy, by the absolute frequency at the convective/absolute instability station. More strikingly, this same criterion has been demonstrated by Pier [93] to predict within 10% accuracy the von Karman frequency behind a circular cylinder for a range of Reynolds numbers between 100 and 200.

The experiments of Monkewitz *et al.* [82] have shown that hot jets become self-excited as soon as absolute instability appears. However, it has not been hitherto demonstrated that the observed oscillations are due to the presence of a nonlinear global mode, associated with a front which imposes its absolute frequency on the entire jet. This issue constitutes the essential motivation for the present numerical investigation. Nichols, Schmid & Riley [87] have recently presented direct numerical simulations of low-density jets

in a low Mach number approximation, where acoustic waves are filtered out. The global frequency was shown to be close to typical absolute frequencies of the *mean* flow profiles in the presence of finite-amplitude fluctuations. The focus of our study is the nonlinear global mode structure of absolutely unstable heated jets as predicted by the local instability properties of the underlying *base* flow profiles. We wish to emphasize that our main concern is not to reproduce all the detailed dynamics of hot jets in laboratory experiments. In the same spirit as Pier & Huerre [94] and Chomaz [18], we first seek to isolate and characterize the nonlinear global mode structure in a "synthetic" hot jet configuration. As the studies of Monkewitz & Sohn [85] and Monkewitz *et al.* [82] indicate that absolute and global instability first sets in for axisymmetric perturbations, we restrict the analysis to a two-dimensional axisymmetric geometry, thereby avoiding the "contamination" by secondary, symmetry-breaking helical instabilities. Additionally, in order to compare our results to the previous WKBJ analyses of Couairon & Chomaz [24, 25, 26, 27], Pier *et al.* [96] and Pier & Huerre [94], we consider slowly-varying base flows satisfying the boundary layer equations.

The outline of the study is as follows. The main physical assumptions and the equations governing the base flow and its perturbations are specified in section 4.2.2, together with the linear instability concepts essential to the analysis. Section 4.2.3 presents the main features of the numerical methods used to obtain the base flow, to determine its linear instability properties, and to simulate the spatio-temporal evolution of perturbations. Self-excited oscillations are analysed and compared to nonlinear global mode theory in two distinct configurations. In section 4.2.4, we examine the case of a base flow displaying a pocket of absolute instability embedded within convectively unstable surroundings. In section 4.2.5, base flows with absolutely unstable inlet conditions are considered. These situations respectively correspond to the case of nonlinear global modes in infinite and semi-infinite media. The main results of the study are summarized and discussed in section 4.2.6.

4.2.2 Problem formulation

Consider a laminar, subsonic, heated round jet emerging into an ambient fluid at rest. Its fundamental dynamics are assumed to be axisymmetric, and the problem is formulated in two-dimensional cylindrical coordinates r and x. The evolution of the flow is governed by the compressible, viscous equations of continuity, momentum and energy, cast in nondimensional conservative flow variables $\mathbf{q} = (\rho, \rho u, \rho v, \rho E)$, where ρ and E denote density and total

energy, and u and v are the axial and radial components of flow velocity $\mathbf{u}$. Together with the equations of state for a thermally and calorically perfect gas, the system is written in compact form as

$$\begin{aligned}
\frac{\partial \rho}{\partial t} &= -\mathrm{div}\,(\rho \mathbf{u}) && (4.5)\\
\frac{\partial (\rho \mathbf{u})}{\partial t} &= -\mathrm{div}\,(\rho \mathbf{u} \otimes \mathbf{u}) - \mathrm{grad}\; p + \mathrm{div}\; \underline{\underline{\tau}} && (4.6)\\
\frac{\partial (\rho E)}{\partial t} &= \mathrm{div}\left[-(\rho E + p)\mathbf{u} + \underline{\underline{\tau}} \cdot \mathbf{u} + \frac{1}{\mathrm{RePr}} \frac{\mathrm{grad}\; T}{(\gamma - 1)\mathrm{Ma}^2} \right] && (4.7)
\end{aligned}$$

$$p = \frac{1}{\gamma \mathrm{Ma}^2} \rho T \;, \qquad E = \frac{T}{\gamma(\gamma - 1)\mathrm{Ma}^2} + \frac{|\mathbf{u}|^2}{2} \tag{4.8}$$

with

$$\underline{\underline{\tau}} = -\frac{2}{3\mathrm{Re}} (\mathrm{div}\; \mathbf{u}) \underline{\underline{I}} + \frac{1}{\mathrm{Re}} \left(\mathrm{grad}\; \mathbf{u} + \mathrm{grad}^T \mathbf{u} \right) \tag{4.9}$$

being the viscous stress tensor for a Newtonian fluid, and p, T denoting pressure and temperature.

All quantities have been made nondimensional with respect to the jet radius R, the centreline velocity U_c, density ρ_c and temperature T_c at the inlet. The viscosity μ and the thermal conductivity κ are assumed to be constant throughout the flow. The flow parameters defined in terms of dimensional quantities are: the Reynolds, Mach and Prandtl numbers $\mathrm{Re} = \rho_c U_c R/\mu$, $\mathrm{Ma} = U_c/c_c$ (with c_c the speed of sound on the centreline), $\mathrm{Pr} = \mu c_p/\kappa$ (with c_p the specific heat at constant pressure), the ratio of ambient-to-jet temperature $S = T_\infty/T_c$, defined at the inlet, and the ratio of specific heats $\gamma = c_p/c_v$. Values of $\mathrm{Re} = 1000$, $\mathrm{Ma} = 0.1$, $\mathrm{Pr} = 1$ and $\gamma = 1.4$ are retained for all cases presented.

The total flow variables are written as $\mathbf{q} = \mathbf{q}_b + \mathbf{q}'$, where the perturbation components $\mathbf{q}'(r, x, t)$ evolve within a steady base flow $\mathbf{q}_b(r, x)$. The base flow is assumed to slowly develop in the streamwise direction, as in the case of sufficiently large Reynolds numbers. As in Pier & Huerre [94], a family of base flow profiles is then sought in terms of primitive variables ρ_b, u_b, v_b and T_b, whose streamwise development depends on a slow coordinate $X = x/\mathrm{Re}$:

$$\begin{array}{llll}
\rho_b(r,x) \sim \rho_0(r,X), & & u_b(r,x) \sim u_0(r,X), & \\
T_b(r,x) \sim T_0(r,X), & & v_b(r,x) \sim \mathrm{Re}^{-1} v_0(r,X). &
\end{array} \tag{4.10}$$

The "$\sim$" symbol in (4.10) emphasizes the fact that such base states constitute a leading-order approximation for large Reynolds numbers $\mathrm{Re} \gg 1$, satisfying

the compressible boundary layer equations

$$\frac{\partial \rho_0 u_0}{\partial X} + \frac{1}{r}\frac{\partial}{\partial r}(r\rho_0 v_0) = 0 \tag{4.11}$$

$$\rho_0 u_0 \frac{\partial u_0}{\partial X} + \rho_0 v_0 \frac{\partial u_0}{\partial r} = \frac{1}{r}\frac{\partial}{\partial r}\left(r\frac{\partial u_0}{\partial r}\right) \tag{4.12}$$

$$T_0 = S + (1-S)u_0 + \frac{\gamma-1}{2}\mathrm{Ma}^2 u_0(1-u_0) \tag{4.13}$$

$$\rho_0 = T_0^{-1} \ . \tag{4.14}$$

For unit Prandtl number and constant pressure, the energy equation has been replaced by the Crocco-Busemann relation (4.13). This parabolic set of equations is integrated numerically, with X as the advancing variable. The boundary condition for the axial velocity at $X = X_0$ is given by the analytical profile of Michalke [78]

$$u_0(r, X_0) = \frac{1}{2} + \frac{1}{2}\tanh\left[\frac{R}{4\theta}\left(\frac{1}{r} - r\right)\right] \ , \tag{4.15}$$

with zero radial velocity, and with temperature and density profiles deduced from equations (4.13) and (4.14). The steepness of the profile is specified by the nondimensional parameter R/θ, where θ is its momentum thickness. The slow variable X has been introduced for formal reasons only. In the presentation of the results, the base flow profiles will always be rescaled to the physical coordinate x.

If the right-hand side of (4.5–4.7) is written in shorthand as the nonlinear operator $NL(\mathbf{q})$, the perturbation equations for $\mathbf{q}'$ are expressed as

$$\frac{\partial \mathbf{q}'}{\partial t} = NL(\mathbf{q}_b + \mathbf{q}') - NL(\mathbf{q}_b) \ . \tag{4.16}$$

This system is solved numerically without modelling assumptions. The only approximation made in the present study therefore arises from neglecting higher-order terms in Re^{-1} in the computation of the base flow. Under this assumption, the temporal evolution of $\mathbf{q}'$ is computed exactly. This formulation also allows for the investigation of perturbations evolving in parallel base flows, as in the validation case presented in section 3.

In order to determine the local instability properties of the base flow, the Navier-Stokes equations (4.5–4.7) are recast in terms of primitive variables $\mathbf{q}_p = (\rho, u, v, p)$ and linearized about the parallel flow $\mathbf{q}_b$ at a given frozen streamwise station X [31, 54]. Perturbations $\mathbf{q}'_p$ are then sought in the form of normal modes

$$\mathbf{q}'_p(r, x, t) = \mathbf{Q}(r)\exp\left[i(kx - \omega t)\right] + \text{c.c.} \ , \tag{4.17}$$

with complex axial wavenumber k and complex angular frequency ω. The linear dispersion relation is expressed as a generalized eigenvalue problem in k with eigenfunction $\mathbf{Q}(r)$, which is solved numerically as a function of ω, thereby leading to the determination of the spatial instability characteristics. As ω is allowed to be complex, this algorithm also serves to identify the complex absolute frequency ω_0 and wavenumber k_0, at which k^+- and k^--branches first pinch in the complex k-plane [7].

4.2.3 Numerical methods and validation

The numerical scheme used for the integration of the boundary layer equations (4.11) is adapted from an algorithm described by Lu & Lele [74]. Starting from the inlet condition (4.15), radial profiles are obtained at successive streamwise locations. The momentum equation (4.12) is discretized through a second-order Crank-Nicolson scheme, which yields a tridiagonal system in u_0. Boundary conditions $\partial u_0/\partial r = 0$ on the axis and $u_0 = 0$ at the outer boundary point are imposed. The Crocco-Busemann relation and the equation of state can then be evaluated directly. The radial velocity v_0 is obtained by integration of the continuity equation along r, using an implicit Euler scheme, with $v_0 = 0$ as starting value on the axis. Since the equations are coupled, this procedure has to be iterated at each streamwise station until the profiles are converged. The algorithm has been validated against a self-similar solution of a compressible jet, derived by Pack [90].

For the perturbation equations (4.16), spatial derivatives in both directions are evaluated with sixth-order-accurate centered, explicit finite differences. A third-order Runge-Kutta algorithm is used for time advancement. Centered finite difference schemes are known to promote the growth of spurious oscillations of under-resolved wavelength. At each time step, these oscillations are dissipated by a selective tenth-order explicit filter scheme (Visbal & Gaitonde [113]), applied in both spatial directions, which uses an eleven-point stencil. The coefficients of the filter are defined locally, in order to preserve its high-order accuracy also on nonuniform grids. The temporal and spatial schemes used in this study have been extensively tested in both aerodynamic and aeroacoustic applications by Terracol *et al.* (2005).

The perturbation equations are discretized on an orthogonal grid. Inside the "physical" region, the spacing of grid points is kept constant in the axial direction ($\Delta x = 0.05$ for the cases presented in section 4.2.4, $\Delta x = 0.1$ in section 4.2.5), whereas in the radial direction, grid points are concentrated in the shear layer region. The radial grid is the same for all cases presented,

with a minimum spacing of $\Delta r = 0.008$ at $r = 1$, thereby resolving a shear layer momentum thickness of $\theta = 0.1R$ by 12 grid points.

At the lateral and outflow boundaries, the physical domain is padded with sponge regions, where a damping term $-\lambda(x)\mathbf{q}'$ is added to the right-hand side of the flow equations (4.5–4.7) (Colonius 2004), and grid stretching is smoothly increased up to a rate of 4% from one point to the next. The purpose of these sponge regions is to minimize numerical box size effects by gradually attenuating all vortical and acoustic fluctuations before they reach the boundary of the computational domain. The damping coefficient $\lambda(x)$ increases smoothly from 0 to 1, according to the ramping function given by Chomaz (2003), over a distance $l_r = 150$ in the lateral sponge region and $l_x = 10$ in the outflow region. At the last five outermost points near the actual inlet, outlet and lateral boundaries, centered differentiation and filter schemes of decreasing stencil size are employed, and all fluctuations are set to zero at the lateral boundary and at the numerical outlet. Symmetry conditions $\partial(\rho, \rho u, \rho E)/\partial r = 0$, $\rho v = 0$ are imposed at $r = 0$ by mirroring the values of the flow variables onto five virtual points across the axis, whereby the stencil size of the high-order schemes can be retained. The coordinate singularity at $r = 0$ is avoided by placing the first radial grid point of the physical domain at half the local step size away from the axis.

At the inlet, non-reflecting characteristic boundary conditions developed by Giles [46], and further discussed by Colonius *et al.* [23], are applied. At the first five computational points, which are not considered to be part of the physical region, the conservative flow variables are transformed to characteristic variables that represent incoming vorticity, entropy and acoustic waves and an outgoing acoustic wave. The incoming characteristics are either set to zero ("zeroth-order approximation"), or they are computed according to the first-order corrected formulation of Giles [46], which takes into account oblique incidence of outgoing acoustic waves. This boundary treatment is not designed to specifically model nozzle effects, but to provide a Dirichlet condition for instability waves and prevent acoustic reflections. However, imperfections of the characteristic decomposition, which is based on the assumption of a uniform base flow normal to the boundary, may give rise to low-level vorticity perturbations that are provoked by outgoing acoustic waves. This effect may be regarded as qualitatively similar to that of a hard nozzle in an experimental setting. In the computations presented in section 4.2.4, such perturbations are attenuated within an additional sponge zone at the inlet, extending over the interval $-8 \leq x < 0$, where the damping factor $\lambda(x)$ decreases from 1 to 0 over $-6 < x < 0$, and zeroth order boundary conditions are imposed at $x = -8$. In the configurations studied in section 4.2.5,

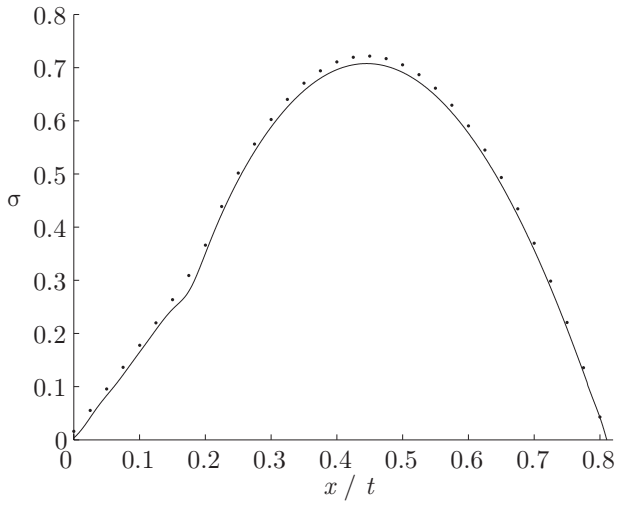

Figure 4.4: Comparison of the growth rate σ along spatio-temporal rays x/t as obtained from the numerical simulation (—) and from the dispersion relation ($\cdot$) of a parallel jet with the parameters $R/\theta = 20$, $S = 0.57$, $Re = 500$ and $M = 0.1$.

the need for an absolutely unstable and well-localised boundary precludes an inlet sponge zone. The first-order corrected boundary conditions are used in these cases.

For the numerical implementation of the linear instability analysis, a code developed by Olendraru & Sellier (2002) has been adapted to the heated jet case. The spatial eigenvalue problem is discretized via a Chebyshev collocation method, as elaborated by Khorrami, Malik & Ash (1989). An iterative search algorithm (Monkewitz & Sohn 1988) identifies the point k_0 in the complex k-plane where a k^+- and a k^--branch pinch. As a validation test, the results of Monkewitz & Sohn [85] for the inviscid, zero Mach number limit have been successfully reproduced.

The accuracy of the numerical method used for the perturbation equations (4.16) is assessed by computing the linear impulse response of a parallel base flow. Nonlinear terms in $\mathbf{q}'$ are temporarily discarded from (4.16) for this calculation. A concentrated initial pulse of the form

$$u'_x(r, x, t = 0) = A \ \exp\left(-\frac{x^2 + (r-1)^2}{0.3^2}\right), \quad A = 10^{-30}, \tag{4.18}$$

is introduced into the jet shear layer in order to trigger the linear impulse response. According to linear theory, the fluctuations along a spatio-temporal

ray x/t are then dominated for $t \to \infty$ by the most unstable linear mode with group velocity x/t and associated temporal growth rate σ (Huerre & Monkewitz 1990). Delbende, Chomaz & Huerre (1998) have proposed a method to evaluate $\sigma(x/t)$ from the numerically computed wavepacket at two distinct times. Results retrieved from the numerical simulation may then be compared to those obtained directly from the dispersion relation (Huerre & Rossi 1998), as displayed in figure 4.4. The numerical simulation is seen to accurately capture the linear instability properties of the base flow. In particular, the large disparity between the base flow and the perturbation amplitude (30 orders of magnitude) demonstrates that the formal separation into base flow and perturbation quantities has been rigorously preserved in the numerical implementation, so that perturbations are effectively resolved with full 64-bit machine precision. The slight offset between the two curves in figure 4.4 is attributed to the residual artificial dissipation introduced by the numerical method. Numerous tests have confirmed that this small underprediction of the absolute growth rate $\omega_{0,i}$ in the numerical simulation occurs systematically, whereas the real part $\omega_{0,r}$ of the absolute frequency is reproduced to even much higher precision.

The base flow chosen for this validation test is close to marginal absolute instability, with an absolute growth rate $\omega_{0,i} = \sigma(x/t = 0)$ near zero. Note that figure 1 displays a clear discontinuity at $x/t = 0.18$, for results computed both from the dispersion relation and from the linear impulse response. A detailed examination of the pinching process indeed confirms that the same k^+-branch but different k^--branches are involved above and below $x/t = 0.18$. The mode which is associated with the absolute growth rate $\omega_{0,i}$ is seen to be different from the one exhibiting the maximum temporal growth rate $\omega_{i,max} = \sigma_{max}$. The characteristics of these two modes have been discussed in detail by Jendoubi & Strykowski [56].

4.2.4 Nonlinear global mode in a jet with a pocket of absolute instability

In this section, we examine the properties of synchronized oscillations in a jet displaying a transition from convective instability at the inlet to absolute instability within a region of finite streamwise extent, in analogy with the synthetic wake of Pier & Huerre [94]. For this purpose, a base flow is conceived in which the streamwise development of the absolute growth rate $\omega_{0,i}$ is controlled by a prescribed variation of the ambient temperature $T_\infty(x)$ (figure 4.5*a*). The momentum thickness at the upstream boundary $x = 0$ of

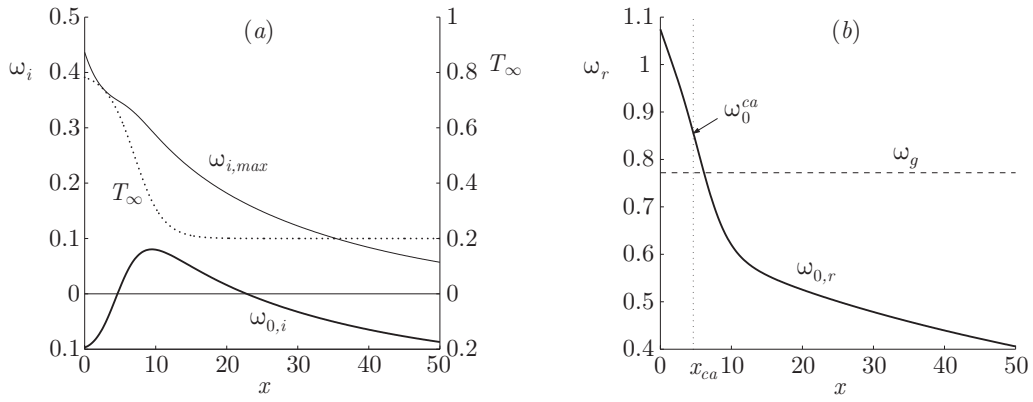

Figure 4.5: a) Local absolute and maximum growth rates $\omega_{0,i}$ (thick), $\omega_{i,max}$ (thin) and ambient temperature T_∞ (dotted) as a function of streamwise distance x. b) Comparison of the local absolute frequency $\omega_{0,r}(x)$ (solid) and the observed global frequency ω_g (dashed)

the physical region is taken to be such that $R/\theta = 11$. The computational grid consists of 430×1261 points in the radial and axial directions, with the physical region extending over $0 \leq r \leq 46$ and $0 \leq x \leq 50$. Tests on a grid of half the streamwise extent and without a lateral sponge zone have confirmed that the results presented here are not affected by the size of the computational box. We point out that in the presence of variations in the ambient temperature, the use of the Crocco-Busemann relation (4.13) has been stretched beyond its strict limit of validity. This proved to be necessary in order to obtain an absolutely unstable pocket with a sufficiently pronounced convective/absolute upstream transition. Note that the viscous spreading of the *base* flow preserves the potential core over a much larger streamwise distance than what is typical for *mean* profiles: In the present case, $u_0(0, x_{99}) = 0.99U_c$ is found at $x_{99} = 46$.

The streamwise variations of both $\omega_{0,i}$ and the maximum temporal growth rate $\omega_{i,max}$ are sketched in figure 4.5(a). The base flow is seen to be convectively unstable in an upstream region extending from the inlet to $x^{ca} = 4.63$. Due to the decreasing temperature ratio, absolute instability prevails in the central region $x^{ca} < x < x^{ac}$, with $x^{ac} = 22.81$. Downstream of x^{ac}, the spreading of the jet induces a decrease of $\omega_{0,i}$ to negative values, and thus the flow returns to convective instability. Corresponding variations of the absolute frequency $\omega_{0,r}$ as a function of downstream distance are displayed in figure 4.5(b).

An initial pulse of the form (4.18) with amplitude $A = 10^{-3}$, introduced

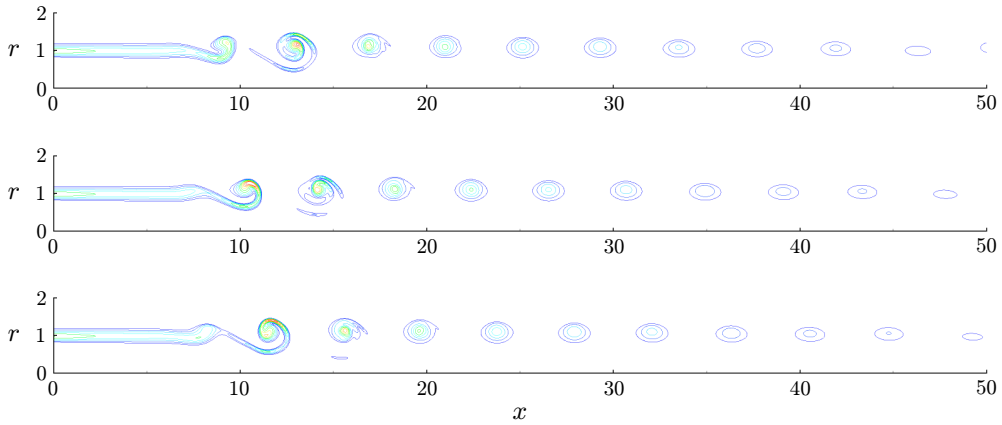

Figure 4.6: Total vorticity field $\omega_\theta(r, x)$ at three instants over one cycle in the periodic régime. Going from top to bottom, the snapshots are separated by one third of the cycle period.

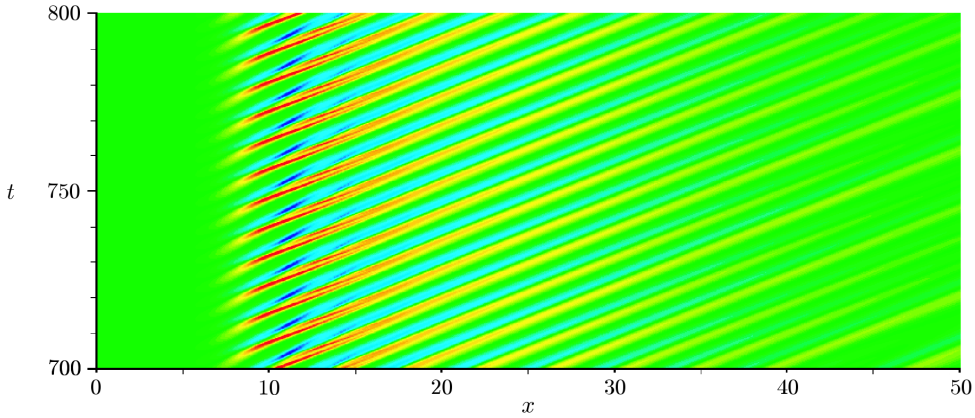

Figure 4.7: Spatio-temporal evolution of $v'(r = 1, x, t)$ in the periodic régime.

inside the absolutely unstable region at $x = 5$, gives rise, after a transient growth, to a synchronized periodic state at a global fundamental frequency ω_g. Figure 4.6 shows snapshots of the total azimuthal vorticity ω_θ over one cycle in the periodic régime. The flow is seen to be composed of regularly spaced ring vortices, which roll up at $x = 11$ and subsequently slowly decay further downstream. The diagram in figure 4.7 represents the synchronized oscillation of the radial velocity perturbation v' at the center of the shear layer ($r = 1$) as a function of time and streamwise distance. The periodicity of the converged oscillatory state is clearly exhibited, as well as the absence of pairing interactions. As presented in figure 4.5(b), the observed global frequency is $\omega_g = 0.772$, to be compared with the theoretical value $\omega_0^{ca} = 0.857$ predicted by the frequency selection criterion of Pier *et al.* (1998).

The nonlinear global mode nature of the observed synchronized oscillations may also be ascertained by inspecting its spatial structure. According to Pier & Huerre [94], the front that separates the bifurcated régime of saturated nonlinear oscillations from the unperturbed base state is located around the upstream point x^{ca} of marginal absolute instability. Upstream of x^{ca}, the tail of the global mode is then predicted to decay as a k^--wave.

In order to obtain a local measure of the amplitude at each streamwise station, the perturbation vorticity field $\omega'_\theta(r, x, t)$ is decomposed into the Fourier series

$$\omega'_\theta(r, x, t) = \sum_{n=-\infty}^{\infty} \Omega_n(r, x)\ e^{-in\omega_g t}, \tag{4.19}$$

and an amplitude function $\eta_n(x)$ for each harmonic component is defined as the square root of its enstrophy integrated over r:

$$\eta_n(x) = \left(\int_0^{r_{\max}} |\Omega_n(r, x)|^2\ r\ dr \right)^{1/2}. \tag{4.20}$$

The resulting amplitude function $\eta_1(x)$ of the fundamental frequency ω_g is displayed in figure 4.8(a). A sharp upstream front is seen to occur in the vicinity of x^{ca}, followed by a maximum at the vortex roll-up station $x = 11$ and a slowly decaying nonlinear wavetrain further downstream. The spatial structure of the upstream front can be observed in detail in the semi-logarithmic diagram of figure 4.8(b). A region of exponential growth $\eta_1(x) \propto \exp(-k_i x)$ is clearly exhibited over the interval $3.5 < x < 7$. For $x < 3.5$, the front shape is masked by residual low-level vorticity disturbances likely to be induced by the attenuation of upstream propagating acoustic waves within the numerical inlet sponge region. The spatial growth rates $-k_i^+(\omega_0^{ca})$ and

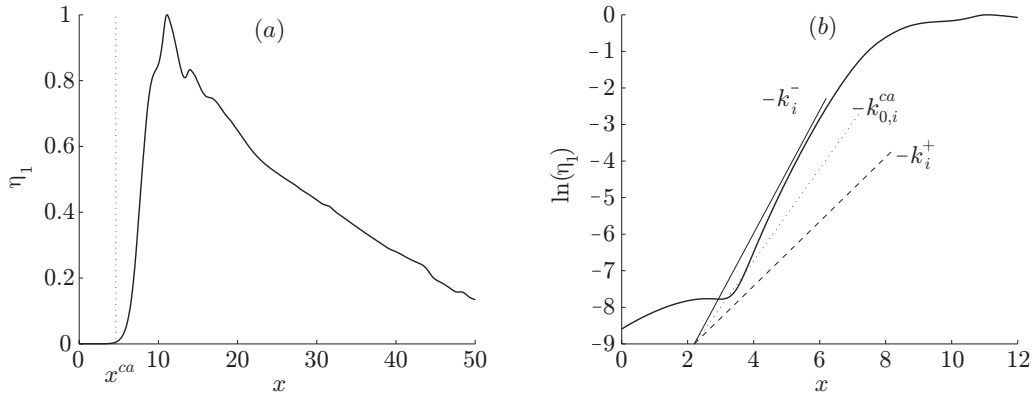

Figure 4.8: a) Oscillation amplitude η_1 as a function of streamwise distance. b) Semi-logarithmic plot of the upstream front region; comparison of the front slope with spatial growth rates $-k_{0,i}^{ca} = 1.26$, $-k_i^+(\omega_0^{ca}, x = 4) = 0.88$ and $-k_i^-(\omega_0^{ca}, x = 4) = 1.68$.

$-k_i^-(\omega_0^{ca})$ at a typical station $x = 4$ in the upstream tail are also sketched in figure 4.8(b), together with the absolute spatial growth rate $-k_{0,i}^{ca}$. In the context of the signalling problem, the complex wavenumbers k^+, k^- are associated with instability waves propagating in the downstream and upstream direction, respectively. In figure 4.8(b), the slope of the envelope in the convectively unstable region $x < x^{ca}$ is seen to compare favorably with the k^- spatial growth rate, and to be quite distinct from its k^+ counterpart. This observation strongly indicates that the global oscillation is generated by a "wave maker" within the flow, rather than by spurious forcing at the upstream boundary. The location of the front as well as its spatial structure correspond to the steep front scenario described by Pier & Huerre [94], thus confirming that the observed oscillations indeed arise from the presence of a nonlinear global mode triggered by the pocket of absolute instability.

The global frequency $\omega_g = 0.772$ agrees reasonably well with the predicted value $\omega_0^{ca} = 0.857$. The 10% discrepancy is of the same order of magnitude as in Pier [93] for the cylinder wake. It is markedly narrower than the total variation in $\omega_{0,r}$ over the entire physical domain (figure 4.5b). Considering the steep streamwise variation of $\omega_{0,r}$ around x^{ca}, the accuracy of the criterion may be affected by the strong non-parallelism of the base flow. The effect of numerical dissipation, as discussed in section 4.2.3, may also cause a slight shift of the transition station x^{ca} in the downstream direction, thereby lowering the effective value of ω_0^{ca}.

While the k^--nature of the front upstream of x^{ca} is apparent, the slope

of $\eta_1(x)$ does not decrease to the absolute spatial growth rate $-k_{0,i}^{ca}$ at x^{ca}, as might have been expected. The observed front shape fails to adjust to this sharp decrease over a distance much shorter than a single wavelength. Alternatively, the envelope slope may also be compared to the k^--branch corresponding to the observed global frequency ω_g instead of ω_0^{ca}: the branch $k^-(\omega_g, x)$, not displayed in figure 4.8(b), is then found to exhibit a slightly larger spatial growth rate and a smoother streamwise development than $k^-(\omega_0^{ca}, x)$, so that it reproduces more faithfully the observed envelope shape.

4.2.5 Nonlinear global modes in jets with absolutely unstable inlet

The configuration examined in the previous section, namely a pocket of absolute instability embedded within a convectively unstable flow, was designed by allowing for suitable streamwise variations of the ambient temperature T_∞. It is not typical of laboratory experiments such as those of Monkewitz *et al.* [82]. In this section, we examine the global dynamics of a family of hot jets with absolutely unstable inlet conditions, where T_∞ is kept constant along the stream. According to global mode theory in semi-infinite media (Chomaz [19]), the self-sustained oscillations are then expected to display a front which is pinned against the upstream boundary at $x = 0$, where the perturbation vorticity is imposed to be zero.

All base flows under consideration start from an initial momentum thickness such that $R/\theta = 10$, with temperature ratios S ranging from 0.1 to 1. In this range of parameters, a transition from upstream convective to downstream absolute instability within the jet is impossible: According to figure 4.9(a), the absolute growth rate is seen to decay monotonically with downstream distance. The streamwise variations of $\omega_{0,i}$ and $\omega_{i,max}$ are plotted for the least ($S = 0.3125$) and the most ($S = 0.1$) heated cases exhibiting self-sustained oscillations. All base flows in this range are seen to be absolutely unstable at the inlet. Corresponding curves for the absolute frequency $\omega_{0,r}(x)$ are given in figure 4.9(b).

The perturbation equations (4.16) are solved on a grid of 430×876 points in the radial and axial directions, respectively, the physical region extending over $0 \leq r \leq 46$ and $0 \leq x \leq 80$. Self-sustained oscillations induced by box size effects have been ruled out by conducting tests on shorter domains with physical regions $0 \leq x \leq 60$ and $0 \leq x \leq 40$. Grid independence has been demonstrated for $\Delta x = 0.05$ and $\Delta x = 0.1$, and the latter value has been retained for the present calculations.

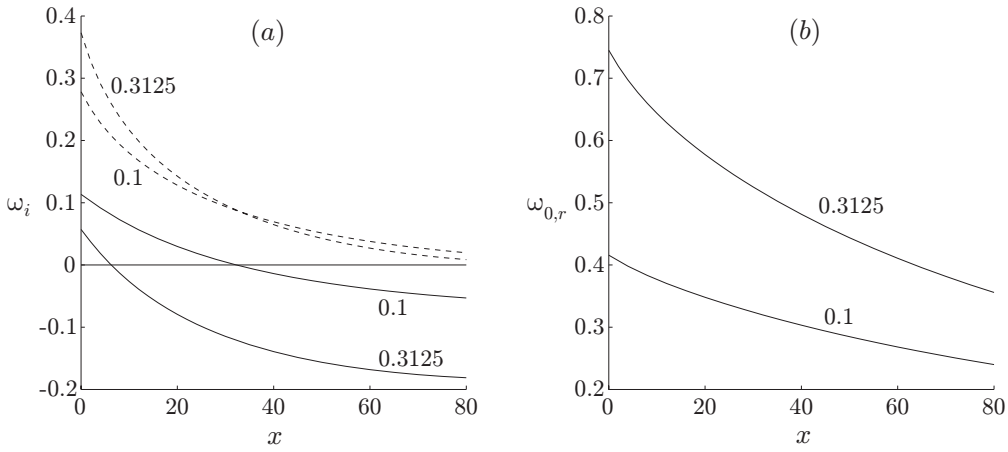

Figure 4.9: a) Local absolute and maximum growth rates $\omega_{0,i}$ (—), $\omega_{i,max}$ (---) as functions of streamwise distance for $S = 0.3125$ and $S = 0.1$. b) Corresponding absolute frequencies $\omega_{0,r}$.

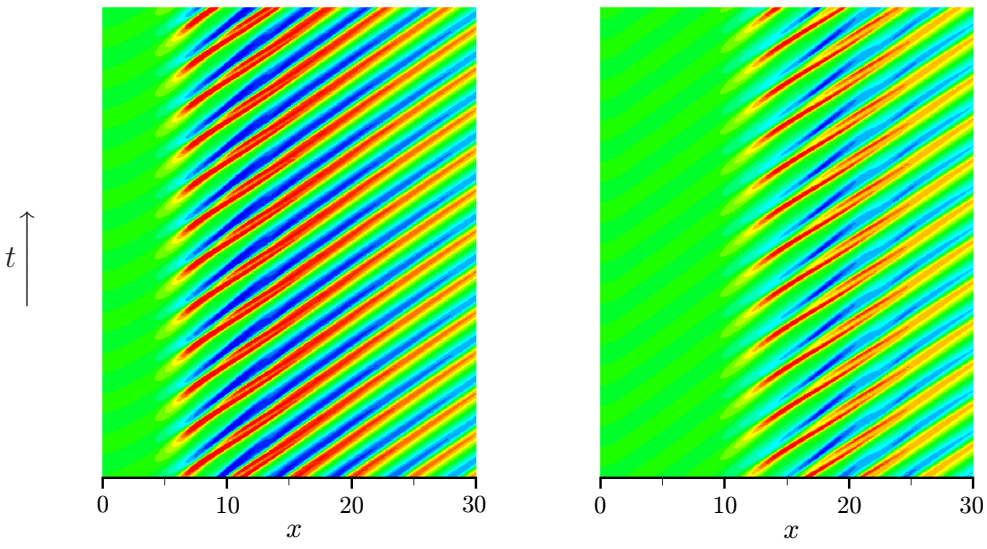

(a) mode 1 (b) mode 2

Figure 4.10: Spatio-temporal diagrams of $v'(r = 1, x, t)$ in the asymptotic régime over a time interval $\Delta t = 100$ for both modes observed at $S = 0.3$.

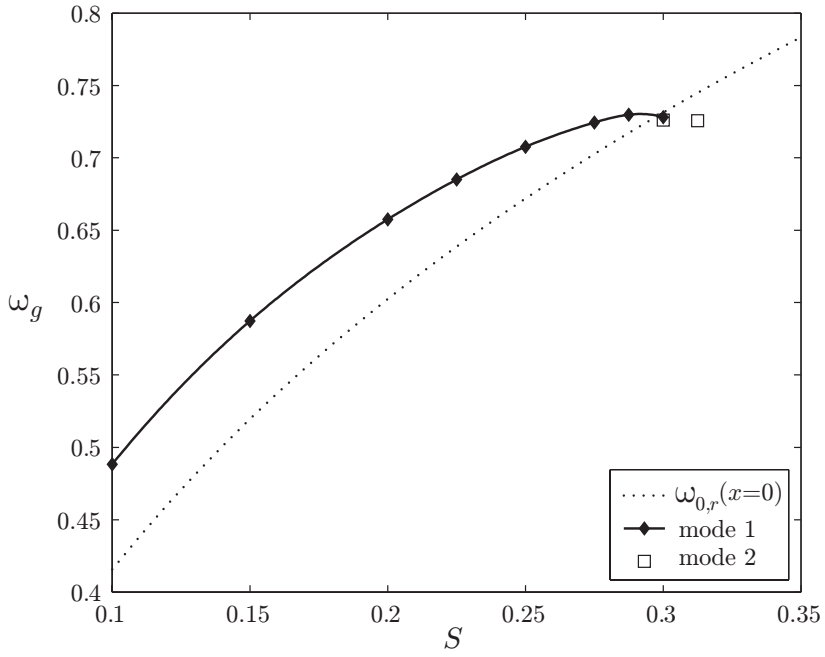

Figure 4.11: Global frequencies observed numerically at different values of S, compared to the absolute frequency at the inlet (dotted line).

Starting from an initial perturbation of the form (4.18) with $A = 0.01$, self-sustained oscillations are observed to develop for temperature ratios $S \leq 0.3$. The asymptotic states are characterized by the presence of ring vortices very similar to the ones displayed in figure 4.6. Typical spatio-temporal diagrams of the synchronized oscillations of the radial perturbation velocity v' at the center of the shear layer are presented in figure 4.10: The periodicity of the asymptotic states is clearly exhibited.

The global frequencies observed for different values of S are represented in figure 4.11. These numerical results should be compared to the theoretical prediction from global mode theory given by $\omega_{0,r}(x = 0)$ (dotted line in figure 4.11). While local absolute instability at the inlet sets in as soon as S decreases below the transition value $S_{ca} = 0.453$, synchronized oscillations are observed numerically to persist only below the value $S_g = 0.3125$. The jet must therefore exhibit a sufficiently wide region of absolute instability, which is found to be of the order of one instability wavelength, in order to sustain a nonlinear front. In the range $0.325 \leq S \leq 1$, the wavepacket produced by the initial pulse is advected downstream, ultimately leaving only low-level residual fluctuations within the physical domain.

The most prominent feature in figure 4.11 is the presence of a branch of global frequencies, denoted "mode 1" (solid line), covering the entire range $0.1 \leq S \leq 0.3$. At onset, the global frequency $\omega_g = 0.728$[2] of this mode coincides with the absolute frequency at the inlet $\omega_{0,r}(x = 0) = 0.731$ (dotted line). The global frequency selection criterion derived by Couairon & Chomaz [27], which predicts $\omega_g = \omega_{0,r}(x = 0)$ in the vicinity of the global instability threshold, is therefore recovered. As S decreases, *i.e.* in the highly supercritical régime, ω_g departs from the absolute frequency. The spatio-temporal structure of mode 1 is illustrated in figure 4.10(a) at $S = 0.3$. Around $x = 9$, the shear layer rolls up into vortices, which are convected downstream without pairing. As S decreases, the vortex roll-up location of mode 1 moves towards the inlet.

Choosing as initial condition a weaker pulse (4.18) with an amplitude $A = 10^{-4}$ reveals the existence of another self-sustained oscillatory state ("mode 2", empty squares in figure 4.11) for the specific values $S = 0.3$ and $S = 0.3125$. This mode is characterized by a vortex roll-up station located distinctly further downstream (compare figures 4.10a and b), outside the absolutely unstable region, while the global frequency stays within 3% of the absolute frequency at the inlet. As mode 2 is continued towards lower values of S, the front saturates within the absolutely unstable region, moves upstream, and mode 1 is recovered as the asymptotic state.

The simulation results are affected to some extent by the choice of the numerical upstream boundary conditions. Computations in which the first-order corrected conditions of Giles [46] are replaced by a zeroth-order formulation yield a qualitatively similar behaviour of both modes, but the deviation of the mode 1 frequency from $\omega_{0,r}(x = 0)$ is more pronounced for low values of S.

4.2.6 Concluding remarks

The occurrence of self-sustained synchronized oscillations in hot axisymmetric jets has been examined numerically for two distinct configurations, one displaying an absolutely unstable region embedded within a convectively unstable flow, the other starting from an absolutely unstable inlet. The results have demonstrated that in both cases these oscillations are the manifestation of a nonlinear global mode following the predictions from model analyses in

[2]In the nearly marginal case $S = 0.3$ the calculations converge very slowly, and the asymptotic value of ω_g has therefore been obtained from computations in a shorter domain, with a physical region stretching over $0 \leq x \leq 40$

infinite and semi-infinite domains, respectively.

In the case of an embedded pocket of absolute instability, the observed synchronized oscillations have been shown to be dominated by a steep nonlinear front, located at the convective/absolute transition station x^{ca} and decaying in the upstream direction as a k^-–wave. The global frequency matches within 10% accuracy the absolute frequency at x^{ca}. This discrepancy is attributed to the non-parallelism of the flow induced by the streamwise gradient of the ambient temperature T_∞, which is required in order to obtain a transition from convective to absolute instability within the flow. The location and the spatial structure of the front, as well as the global frequency, are in full agreement with the theoretical predictions pertaining to nonlinear global modes in an infinite domain (Pier *et al.* [96, 95]).

We note at this point that, according to Monkewitz & Sohn [85], an embedded pocket of absolute instability may also occur in jets with constant outside temperature for a narrow range of parameters. However, such a configuration is replete with numerical difficulties, as it necessitates a very thin initial shear layer (R/θ well above 50 at the inlet). As a result, the flow is then prone to spurious acoustic forcing that may contaminate the global mode oscillations.

The simulations of flow configurations with constant ambient temperature and absolutely unstable inlet conditions have revealed the existence of two distinct synchronized oscillatory states close to the onset of global instability. One of these modes is seen to be dominant throughout the supercritical range of S, the other being only observed close to the global instability threshold $S_g = 0.3125$. At onset, the frequency of mode 1 coincides, within 0.4% accuracy, with the absolute frequency at the inlet. For lower values of S, the global frequency gradually departs from $\omega_{0,r}(x = 0)$. This result is in agreement with the Ginzburg-Landau model analysis of Couairon & Chomaz [26], according to which the $\omega_{0,r}(x = 0)$ criterion only holds close to threshold, even in parallel flows. However, as soon as non-parallelism is present (Couairon & Chomaz [27]), a nonlinear front is only sustainable if its saturation takes place within the absolutely unstable region. In the present simulations, it has indeed been observed that the absolutely unstable region must be of sufficient streamwise extent in order to give rise to a nonlinear global mode. The non-parallelism of the base flow therefore accounts for the gap between local absolute instability onset at $S_{ca} = 0.453$ and global instability onset at $S_g = 0.3125$. As a result, the scaling law derived by Couairon & Chomaz [26] for parallel flows could not be recovered.

Self-sustained oscillations may also be present in the absence of absolute

instability, which *a priori* precludes the onset of a global mode (Chomaz, Huerre & Redekopp [20]). For instance, constant-density jets may, under carefully tuned conditions, experience synchronized oscillations associated with a feedback loop consisting of a downstream propagating instability wave and an upstream travelling acoustic wave, preferentially emanating from vortex roll-up and pairing events [64, 48]. This scenario has been observed, for instance, in the numerical simulations of convectively unstable, compressible jets carried out by Grinstein, Oran & Boris [47]. In our study, all calculations performed in the convectively unstable range $S > 0.453$ indicate that self-sustained oscillations induced by acoustic feedback do not arise for our parameter settings: vortex roll-up is observed not to give rise to synchronized oscillations, and vortex pairing never occurs in any of the asymptotic states presented. In the experiments of Monkewitz *et al.* [82], however, vortex pairing was systematically present. Their parameter régime, which involves thinner initial shear layers and higher Reynolds numbers, remains to be investigated numerically.

Acknowledgements

The authors warmly acknowledge fruitful discussions with Jean-Marc Chomaz and Carlo Cossu. Lutz Lesshafft has been supported by an ONERA PhD fellowship.

ERRATUM

A typographical error has been committed by the authors in equation (2.4*b*) of the published article. This error has been corrected in the corresponding equation (4.12) of the present manuscript.

Section 4.3

Frequency selection in globally unstable round jets

Lutz Lesshafft and Patrick Huerre

Laboratoire d'Hydrodynamique (LadHyX), CNRS – École Polytechnique, 91128 Palaiseau, France

Pierre Sagaut

D'Alembert Institute, Université Pierre et Marie Curie – Paris 6, 4 place Jussieu, 75252 Paris Cedex 05, France

accepted for publication in *Physics of Fluids*, volume 19, issue 4

Abstract

The self-sustained formation of synchronized ring vortices in globally unstable hot round jets is investigated by direct numerical simulation of the axisymmetric equations of motion. The onset of global instability and the global frequency of synchronized oscillations are examined as functions of the ambient-to-jet temperature ratio and the initial jet shear layer thickness. The numerical results are found to follow the predictions from nonlinear global instability theory: global instability sets in as the unperturbed flow is absolutely unstable over a region of finite streamwise extent at the inlet, and the global frequency near the global instability threshold corresponds to the absolute frequency of the inlet profile. In strongly supercritical *thin* shear layer jets, however, the simulations display global frequencies well above the absolute frequency, in agreement with experimental results. The inner structure of rolled-up vortices in hot jets displays fine layers of positive and negative vorticity that are produced and maintained by the action of the baroclinic torque.

4.3.1 Introduction

Axisymmetric jets have been experimentally observed to sustain self-excited large-scale vortices, synchronized at a well-defined frequency, if the jet is sufficiently heated with respect to the ambient air (Monkewitz *et al.* [82]). Such self-excited oscillations are the manifestation of a global instability of the unperturbed steady flow. Subjected to an arbitrary perturbation, a globally unstable steady flow will bifurcate and settle into a new organized régime of highly regular oscillations. This new state is termed a *global mode* of the underlying steady flow, and its oscillations are tuned to a well-defined *global frequency*. In a large variety of open shear flows, the occurrence of global instability has been shown to be closely connected to the local linear instability properties (see Huerre & Monkewitz [54] and Chomaz [19] for reviews): if the unperturbed flow is locally *convectively* unstable everywhere, externally induced perturbations are amplified, but the flow is globally stable. In the absence of continuous forcing, it will ultimately return to a steady state. In the presence of a locally *absolutely* unstable flow region, in contrast, the flow may bifurcate to a global mode. Prominent examples of flows exhibiting global instability triggered by local absolute instability include the cylinder wake [97, 27, 94, 93], counterflowing shear layers [53], swirling jets [44] and jets with counterflow [106, 56].

In the hot jet experiments of Monkewitz *et al.* [82], self-sustained synchronized oscillations were found to set in as the ambient-to-jet temperature ratio $S = T_\infty/T_c$ was lowered below a critical value of 0.73. The Strouhal number of these oscillations is given as $St \approx 0.3$, based on jet diameter and exit velocity. At temperature ratios below 0.63, a second oscillating state with $St \approx 0.45$ was observed to be dominant. Both of these modes were axisymmetric. Kyle & Sreenivasan [62] (see also Ref. [105]) investigated the stability of mixed helium/air jets in ambient air. The jet-to-ambient density ratio that served as a control parameter in these experiments is equivalent, under the perfect gas assumption, to the ambient-to-jet temperature ratio used in Ref. [82]. The experiments of Kyle & Sreenivasan [62] showed only one oscillating state, also axisymmetric, with Strouhal number and density ratio ranges in good agreement with the $St \approx 0.45$ mode of Monkewitz *et al.* [82]. More recent helium jet experiments [100, 116] confirm the results of Kyle & Sreenivasan [62].

The linear spatio-temporal instability analysis of Monkewitz & Sohn [85] revealed that hot axisymmetric jets display a region of absolute instability as the temperature ratio falls below a critical value. In the inviscid, zero-Mach-number limit, this critical value is $S = 0.72$, in striking agreement with

the first threshold value $S = 0.73$ at which global instability was observed experimentally [82].

Further theoretical studies by Jendoubi & Strykowski [56] demonstrated that two distinct axisymmetric spatio-temporal instability modes exist in round jets: a *shear layer* mode, similar to the Kelvin–Helmholtz instability mode in a plane shear layer, and a *jet column* mode, identical to the one discovered by Monkewitz & Sohn [85], with maximum pressure perturbations on the jet axis. In jets without counterflow, the absolute instability mode is of the jet column type. A recent linear analysis [67] has revealed that the transition from convective to absolute instability in variable-density jets, even in the absence of gravity, ensues from the action of the baroclinic torque.

Theoretical discussions of the experimental results on global instability in variable-density jets have so far essentially been restricted to a comparison of the temperature or density ratio threshold values for the observed onset of self-sustained oscillations with the predicted onset of absolute instability in inviscid, zero-Mach-number parallel flow. For the particular value $S = 0.48$, Kyle & Sreenivasan [62] also compared the measured global frequencies with theoretical values of the absolute frequency given in Ref. [85]. Rather good agreement was found as long as the jet shear layer at the nozzle exit was not too thin. For very thin shear layers however, as well as for lower values of S, the comparison was much less favorable. Furthermore, the shear layer thickness was determined from a measured boundary layer velocity profile at the nozzle exit in the experiments [62], and from an analytical free jet profile in the theoretical study of Monkewitz & Sohn [85].

Theoretical analyses of the frequency selection process in globally unstable semi-infinite flows, such as jets, have been carried out by Couairon & Chomaz [24, 25] on the basis of Ginzburg–Landau model equations. Their criterion for a semi-infinite *parallel* base flow states that nonlinear global instability coincides with the onset of linear absolute instability, and that the selected global frequency at this threshold is given by the absolute frequency of the base flow. In supercritical flows, the absolute frequency only provides a leading order prediction of the global frequency. However, the numerical simulations by Chomaz [18] have demonstrated that, in parallel wakes, this zero-order criterion yields highly accurate predictions far into the supercritical regime. The theoretical analysis has been extended to account for slow streamwise variations of the base flow [27]. In such cases, the global frequency at the global instability threshold is still given by the absolute frequency at the upstream boundary. However, global instability is expected to set in only if the region of absolute instability is sufficiently large to allow

for a nonlinear saturation of the oscillation amplitude.

The objective of the present study is to explore numerically the applicability of nonlinear global mode theory [24, 25, 26, 27] to the self-sustained synchronized oscillations in hot jets. A recent investigation [69] has established that the theoretical predictions of Couairon & Chomaz [27] accurately match numerical simulation results for a family of heated thick shear layer jets. The present study extends the investigated parameter range to approach the experimental settings of Monkewitz *et al.* [82] and of Sreenivasan *et al.* [105].

The paper is organized as follows. In Sec. II, the physical flow model is presented, and the different flow parameters are specified. Numerical aspects such as the computational grid, boundary and initial conditions are discussed in Sec. III. Further details on the employed flow solver can be found in Ref. [69]. Numerical results are presented in Sec. IV. A comparison with experiments [82] is included, and the rôle of acoustic feedback is discussed. Section V describes observations on the inner structure of rolled-up vortex billows in strongly heated jets. The main results are summarized in Sec. VI.

4.3.2 Problem formulation

Consider an axisymmetric subsonic jet of radius R issuing into a quiescent ambient medium. The flow is assumed to be governed by the axisymmetric compressible Navier–Stokes equations and the equation of state for a perfect gas, cast in cylindrical coordinates x and r. These equations are given explicitly in Lesshafft *et al.* [69]. The system is formulated in terms of conservative flow variables $\boldsymbol{q} = (\rho, \rho u, \rho v, \rho E)$, where ρ is density, u and v are the axial and radial velocity components, respectively, and E is the total energy.

The total quantities $\boldsymbol{q}$ are separated into a base flow $\boldsymbol{q}_b(x, r)$ and a perturbation component $\boldsymbol{q}'(x, r, t)$. By construction, any given base flow $\boldsymbol{q}_b$ is a steady state solution of the governing equations. As in Ref. [69], the streamwise development of the base flow is obtained as a numerical solution of the compressible boundary layer equations, starting at $x = 0$ from the analytical velocity profile (Michalke [77])

$$u_b(r) = \frac{1}{2} + \frac{1}{2} \tanh \left[\frac{R}{4\theta} \left(\frac{1}{r} - r \right) \right] \tag{4.21}$$

of momentum shear layer thickness θ. All quantities are made non-dimensional with respect to the jet radius R, velocity U_c, density ρ_c and temperature T_c,

where the subscript c denotes the value on the jet centerline in the inlet plane. The dynamic viscosity μ and the thermal conductivity κ are taken as constant throughout the flow, and gravity is neglected. A specific flow configuration is then defined by the following set of parameters: the Reynolds number $Re = \rho_c R U_c/\mu$, the Mach number $\mathrm{Ma} = U_c/c_c$ with respect to the speed of sound c_c on the jet centerline, the Prandtl number $Pr = \mu c_p/\kappa$, with c_p the specific heat at constant pressure, the ambient-to-jet temperature ratio $S = T_\infty/T_c$, the inlet velocity profile parameter R/θ, and the ratio of specific heats $\gamma = c_p/c_v$.

The flow parameters considered in the numerical study are chosen to closely correspond to settings of Monkewitz *et al.* [82]. The Reynolds number is taken as $Re = 3750$ ($Re_D = 7500$, based on jet diameter as in Ref. [82]) and the Mach number as $\mathrm{Ma} = 0.1$. Values of $Pr = 1$ and $\gamma = 1.4$ are retained throughout. The occurrence of global instability is then explored for combinations of the inlet profile parameter and the temperature ratio over the ranges $10 \leq R/\theta \leq 25$ and $0.3 \leq S \leq 1$.

4.3.3 Numerical method

The numerical procedure used in the simulations is identical to that of Lesshafft *et al.* [69]. An algorithm described by Lu & Lele [74] is used to obtain the base flow $\boldsymbol{q}_b$ by numerical integration of the boundary layer equations. The temporal evolution of perturbations $\boldsymbol{q}'$ within this base flow is then computed directly from the axisymmetric Navier–Stokes equations. Spatial derivatives are evaluated from a sixth-order accurate explicit centered finite-difference scheme, and the solution is advanced in time via a third-order Runge–Kutta algorithm. Numerical stability of the finite-difference formulation is achieved by applying a tenth-order explicit filter scheme at each time step [66, 113].

The orthogonal grid that has been used in all computations discretizes the physical domain $0 \leq x \leq 30$ and $0 < r \leq 30$ into 500×278 grid points. In the radial direction, these points are concentrated in the shear layer region around $r = 1$, with a minimum spacing $\Delta r_{min} = 0.01$. In the axial direction, Δx is kept at 0.05 for $x \leq 15$, and then is slowly increased up to $\Delta x = 0.1$ at $x = 25$. Sponge regions are introduced at the lateral and downstream boundaries of the physical domain, where grid stretching is gradually increased up to a rate of 4%. These sponge regions extend over $30 \leq r \leq 112$ and $30 \leq x \leq 125$, discretized with 37 radial and 200 axial grid points. A damping term $-\lambda(x, r)\boldsymbol{q}'$ is added to the Navier–Stokes

equations within the sponge regions. The value of the damping coefficient $\lambda(x, r)$ is smoothly ramped up from zero at the boundary of the physical domain to 0.3 at $x = 50$ and $r = 50$, according to a function given by Chomaz [18]. Convergence tests on finer grids (750×410 points) and on larger computational domains have confirmed that the results are grid independent and unaffected by box effects.

The theoretical model for global modes in a semi-infinite domain studied by Couairon & Chomaz [27], to which our numerical simulation results are to be compared, assumes a nonlinear wave front blocked at a Dirichlet-type upstream boundary that lies within an absolutely unstable flow region. Such a configuration precludes the implementation of an additional sponge region at the upstream boundary of the computational domain, which then would be penetrated by the upstream-traveling wave front up to the streamwise station where artificial damping induces a transition to convective instability. Instead, as in Ref. [69], the characteristic boundary conditions of Giles [46] are used at the inlet. These are designed to provide a first order correction for oblique incidence of upstream-traveling acoustic waves. Tests have shown that this correction significantly reduces the coupling of acoustic and vortical disturbances at the upstream boundary. Numerical instabilities due to these boundary conditions have been reported by Colonius *et al.* [23], but they have not been encountered in the present simulations.

A different set of characteristic upstream boundary conditions, without any correction for oblique incidence of acoustic waves, was employed in an earlier study [68]. The global dynamics observed in the simulations are quite sensitive to the quality of the upstream boundary conditions. It must be pointed out that the use of the term "first order" in the context of the boundary conditions given by Giles [46] is ambiguous in the literature. In compliance with Ref. [23], we will henceforth denote as "first order" boundary conditions those used in Ref. [69] as well as in the present study. The boundary conditions used in Ref. [68], which assume acoustic wave fronts to be parallel to the upstream boundary, will be denoted as being of "zero order".

All computations start from a divergence-free initial velocity perturbation

in the form of a vortex ring (Bogey *et al.* [10])

$$\begin{aligned} u'(r,x) &= -A\frac{r_0(r-r_0)}{rs}\,g(r,x)\ , \\ v'(r,x) &= A\frac{r_0(x-x_0)}{rs}\,g(r,x)\ , \\ g(r,x) &= \exp\left[-\ln 2\frac{(x-x_0)^2+(r-r_0)^2}{s^2}\right]\ , \end{aligned} \tag{4.22}$$

$$\text{with}\quad (r_0,x_0)=(1,2),\quad s=0.3\quad\text{and}\quad A=0.1\,.$$

We have found that the jet column mode, which alone may give rise to the growth of a nonlinear global mode induced by absolute instability, is most efficiently excited by a high-amplitude initial pulse that quickly leads to vortex roll-up. That way, a strong exponential temporal growth of shear layer modes is bypassed, and the jet-column mode grows to nonlinear saturation within a short time interval.

In section 4.3.4, the numerical results are compared to predictions drawn from a linear stability analysis of the underlying base flow. A detailed description of the numerical method used to solve the linear instability problem is given in Ref. [67].

4.3.4 Onset and frequency of self-sustained oscillations

Numerical observations and comparison with theoretical predictions

The long-time flow behavior, after the transient wave packet induced by the initial perturbation (4.22) has left the computational domain, is radically distinct for globally stable and globally unstable situations. For subcritical combinations of R/θ and S, only low-level broadband fluctuations persist near the inlet, followed by irregular vortex roll-up and pairing events. At sufficiently high values of R/θ and strong heating, the flow settles into a highly periodic oscillatory state. The jet shear layer in these cases rolls up at a fixed streamwise station, forming a street of regularly spaced ring vortices that are slowly attenuated as they travel downstream. Periodic states obtained in two typical configurations are visualized in figure 4.12. Note that the rolled-up vortices in the thin shear layer jet (figure 4.12b) undergo one pairing event around $x = 13$. In the present simulations, precisely one such stage of vortex pairing is observed in all globally unstable cases with inlet

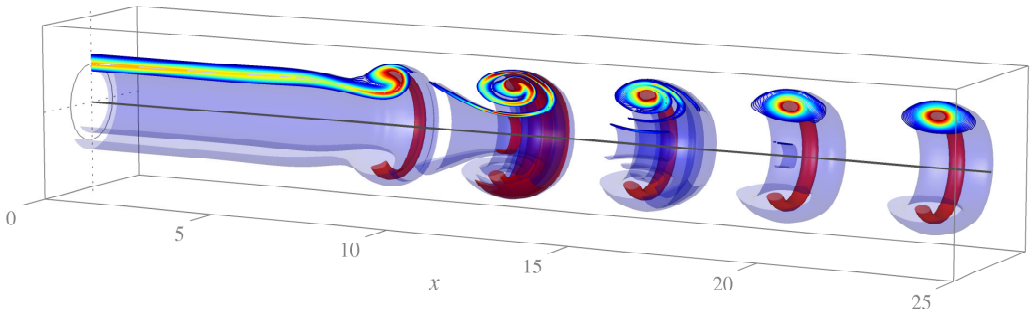

a) $R/\theta = 10$, $S = 0.4$

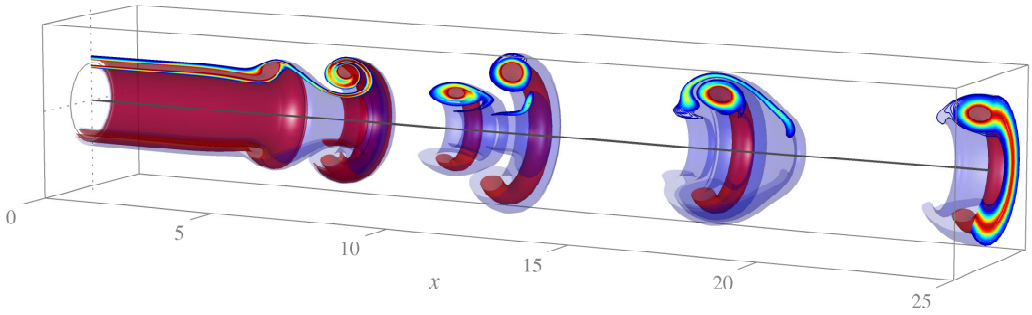

b) $R/\theta = 20$, $S = 0.6$

Figure 4.12: Snapshots of synchronized oscillations in two globally unstable jets. Vorticity isosurfaces $\Omega = 1$ (blue) and $\Omega = 3$ (red), isocontours $1 \leq \Omega \leq 3$. (a) Thick shear layer jet, no vortex pairing; (b) thin shear layer jet, with vortex pairing.

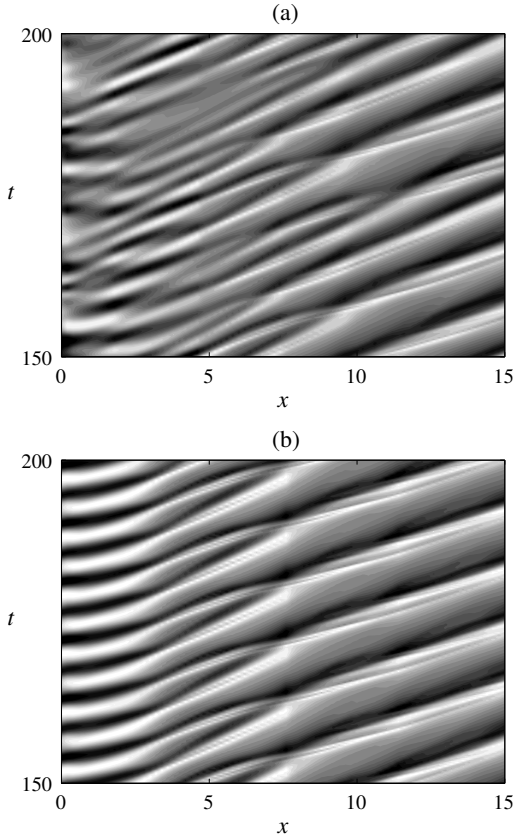

Figure 4.13: Spatio-temporal diagrams of the radial perturbation velocity $v'(r = 1, x, t)$ in the long-time régime. a) globally stable case $R/\theta = 25$, $S = 0.65$; b) globally unstable case $R/\theta = 25$, $S = 0.55$.

profiles $R/\theta > 10$. Vortex pairing in the asymptotic flow state shows the same high degree of repeatability as the initial vortex roll-up.

The qualitative difference between synchronized and non-synchronized asymptotic states is demonstrated in the spatio-temporal diagrams in figure 4.13. The thinnest shear layer jet considered in this study, with temperature ratios just above and below the critical value, is chosen as an example. The radial perturbation velocity $v'(r = 1, x, t)$ at the center of the shear layer is presented as a function of streamwise distance and time. In order to clearly visualize all flow regions, v' has been normalized independently at each streamwise station x with respect to its maximum amplitude over the displayed time interval in figure 4.13.

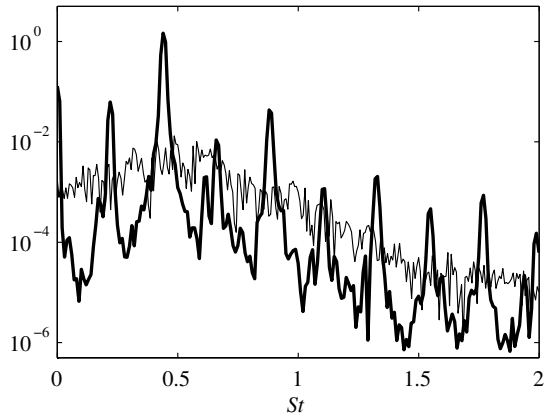

Figure 4.14: Spectral density of $v'(r = 1, x = 1, t)$ as a function of Strouhal number for the two configurations of figure 4.13. Thin line: globally stable case $R/\theta = 25$, $S = 0.65$; thick line: globally unstable case $R/\theta = 25$, $S = 0.55$.

The corresponding Strouhal number spectra, computed from $v'(r = 1, x = 1, t)$, are displayed in figure 4.14. As in Monkewitz *et al.* [82], the Strouhal number is defined as $St = 2fR/U_c$. In the globally stable configuration with $S = 0.65$ (thin line), the spectrum is broadband. As the base flow in this case is convectively unstable throughout the entire physical domain, persisting perturbations at long times can only arise from a continuous, spurious excitation at the numerical inlet boundary. This excitation is caused by upstream-travelling acoustic waves that in turn are emitted from the downstream vortices. The jet shear layer then acts as a band-pass filter, promoting the growth of the most amplified spatial instability modes. In contrast, the spectrum of the synchronized flow case (thick line in figure 4.14) is marked by sharp peaks, while the background noise level is significantly lowered. As the spectra are taken near the upstream boundary, the dominant peak corresponds to the fundamental global frequency St_g of vortex roll-up. A subharmonic peak in the spectrum of the synchronized case announces the occurrence of vortex pairing further downstream. Some peaks in the line-dominated spectrum in figure 4.14, *e.g.* at $St = 1.1$, are accompanied by small 'side peaks' on both sides. Whether these are the result of a *sideband instability* [81], or just an effect of the FFT algorithm (a Hanning windowing technique has been used), cannot be decided at present.

The globally unstable region of the S-R/θ parameter plane is identified in figure 4.15. Flow cases exhibiting self-sustained synchronized oscillations

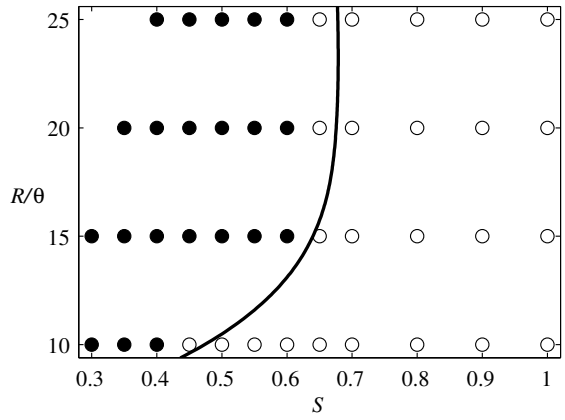

Figure 4.15: State diagram of hot jets: synchronized (•) and non-synchronized (∘) asymptotic states observed over the investigated ranges of temperature ratio S and inlet profile parameter R/θ; absolute/convective instability boundary of inlet profile (—).

are marked as solid circles, whereas open circles represent non-synchronized cases. The black line marks the absolute/convective instability boundary of the inlet profile, computed for Ma = 0.1 and Re = 3750. Base flows in the parameter region to the left of this boundary display absolute instability at the inlet, and they do so over an increasingly large streamwise interval for stronger heating and thinner initial shear layers. Figure 4.15 clearly demonstrates that global instability is detected only in base flows with an absolutely unstable inlet profile. The boundary of global instability in the S-R/θ plane closely follows that of local absolute instability, with a slight offset into the absolutely unstable parameter region. In full agreement with the theoretical predictions of Couairon & Chomaz [27] as well as with earlier numerical simulations [69], the present results confirm that global instability occurs only in the presence of a sufficiently large pocket of local absolute instability.

Due to the high quality of the flow synchronization, the global frequency can be determined by measuring the oscillation period τ directly from the temporal signal $v'(r = 1, x = 1, t)$ of the asymptotic state. The temporal development of $St = 2/\tau$ is shown in figure 4.16 for the three globally unstable cases encountered at $S = 0.5$. The asymptotic values St_g in these cases are converged to at least three significant digits. Corresponding FFT frequency spectra of the v' signal, similar to the thick line in figure 4.14, are

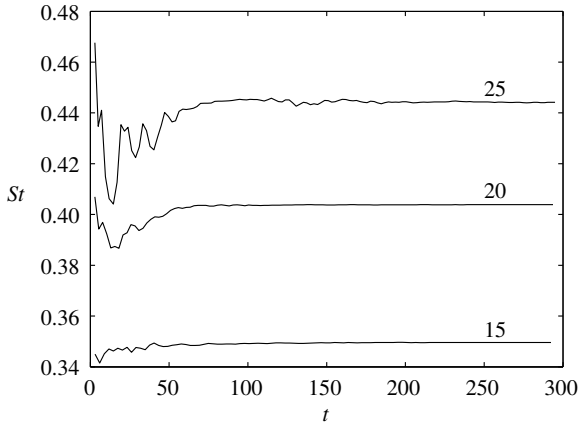

Figure 4.16: Temporal development of the oscillation Strouhal number in jets at $S = 0.5$. Labels indicate the value of R/θ.

fully consistent with the results obtained for St_g from figure 4.16, but they would require much larger signal samples of the asymptotic régime in order to give the same accuracy.

The model analysis of Couairon & Chomaz [27] predicts the frequency of a global mode in a semi-infinite domain to correspond to the absolute frequency at the upstream boundary in the limit of *marginal* global instability. As the base flow becomes increasingly supercritical, the global frequency may depart from this leading-order criterion. In figure 4.17, values of the global frequency St_g, observed in the numerical simulations, are compared to the Strouhal number St_0 of the absolute instability mode, obtained from a linear stability analysis of the inlet base flow profile. For each R/θ, values of St_0 are given over the absolutely unstable range of temperature ratios. Experimental measurements from Monkewitz *et al.* [82] are also shown and will be discussed in section 4.3.4.

The thickest shear layer jet with $R/\theta = 10$ synchronizes to the absolute frequency within 0.5% at its global instability threshold $S = 0.4$. At supercritical temperature ratios, St_g gradually shifts to values slightly higher than St_0. The same general trend is observed for jets with thinner initial shear layers, but as R/θ increases, the interval of S over which the frequency selection criterion $St_g = St_0(x = 0)$ may be regarded as valid is confined to an ever smaller vicinity of the global instability threshold. Note that the occurrence of vortex pairing, which distinguishes the configurations with $R/\theta \geq 15$ from those with $R/\theta = 10$, is not associated with any sudden change in the

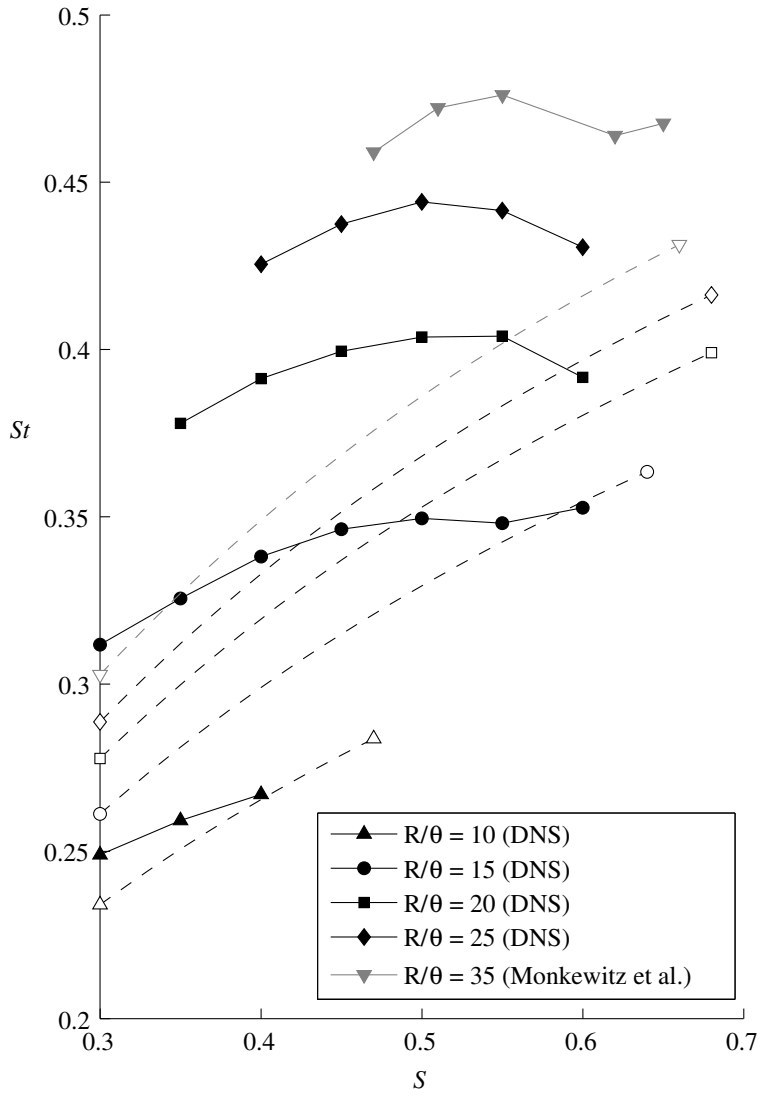

Figure 4.17: Global frequency compared to absolute frequency of the inlet profile, both as functions of the temperature ratio S for various values of the inlet profile parameter R/θ. Black solid lines: global frequencies observed in the present simulations; grey solid line: experimental values from Monkewitz *et al.* [82]; dashed lines and open symbols: corresponding absolute frequency of the inlet profile, shown over the absolutely unstable range of S.

global flow dynamics, in particular with respect to the frequency selection mechanism. The global frequencies close to onset in jets with $R/\theta = 15$ are also remarkably well predicted by the absolute frequency at the inlet. At the highest value of S for which synchronization is observed in an $R/\theta = 20$ jet, the selected frequency still falls within 3% of the expected value, but the frequency prediction degrades rapidly as S is lowered. For $R/\theta = 25$, only the 8% agreement between St_0 and St_g at $S = 0.6$ closest to threshold may still be considered satisfactory.

Tests have shown that the numerical values of St_g are quite sensitive to the choice of upstream boundary conditions. For instance, when the zero order characteristic boundary conditions (see section 4.3.3) were used in earlier simulations [68], the global frequency of an $R/\theta = 20$, $S = 0.5$ jet was measured as $St_g = 0.443$, whereas the first order formulation employed in the present study leads to $St_g = 0.404$.

It should be noted that the only difference between the $R/\theta = 10$ cases presented in figure 4.17 and those studied in section 4.2.5 lies in the choice of the Reynolds number (Re = 3750 here, Re = 1000 in section 4.2.5). The results are fully consistent: in the present study, global instability sets in at a slightly higher value of S, because the streamwise development of the base flow scales with Re, and the absolutely unstable region at a given temperature ratio is therefore 3.75 times as long as in the Re = 1000 case.

Limited parameter range in the DNS

In simulations of strongly heated thin shear layer jets, the pairing of large-scale vortices gives rise to an irregular ejection of free vortical structures into the outer flow. These structures visually resemble pictures of two-dimensional turbulence, and their generation is not a matter of numerical discretization, but seems to be a genuine feature of the axisymmetric equations of motion. Unsteady flow visualizations suggest that the formation of these structures results from a secondary instability due to the finely-spun layer structure of rolled-up vortices in strongly stratified shear layers, which is documented in section 4.3.5 below.

The pairing of two such layered vortices generates violent accelerations that easily lead to folding and ejection of the outer vorticity layers. These folded layers then tend to form vorticity dipoles that are propelled into the outer flow through their self-induced motion. The dipoles are only slowly dissipated by viscosity and therefore may accumulate in the vicinity of the vortex pairing location. Such structures certainly would be highly unstable

in a three-dimensional geometry, and their long-time dynamics observed in the axisymmetric simulations therefore should not be regarded as physical.

If the pairing takes place several jet diameters downstream of the inlet, the eventual ejection of free vorticity dipoles into the outer flow has no impact on the global flow dynamics. In cases of strong heating and thin initial shear layers, however, the location of vortex pairing moves further upstream. The free vorticity dipoles may then contaminate the upstream boundary region and induce high-amplitude perturbations that disrupt the global flow synchronization. This behavior has been observed in three base flow configurations (R/θ=20, S=0.3), (R/θ=25, S=0.3) and (R/θ=25, S=0.35), and these cases therefore have been excluded from the presentation of results in section 4.3.4. Throughout the present study, only such cases have been considered where the upstream region down to at least $x = 4$ is free of spurious vorticity structures in the outer flow. The accessible ranges of the inlet velocity profile parameter R/θ and temperature ratio S in the numerical simulation are limited due to this restriction.

Comparison with experiments

In figure 4.17, experimental values given by Monkewitz *et al.* [82] for the global frequency are included as grey symbols together with present numerical results. Only the "mode II" [82] oscillating state is considered. According to a relation given in Ref. [82], at a Reynolds number Re = 3750 based on the jet radius, the inlet conditions for these measurements should correspond to $R/\theta \sim 35$. The dimensional frequencies reported by Monkewitz *et al.* [82] are scaled in figure 4.17 with respect to jet exit velocities that had to be deduced from the Reynolds number. The Mach number in these experiments varies within the interval $0.025 < \mathrm{Ma} < 0.05$.

Numerical simulations at $R/\theta = 35$ were too much contaminated with free vortices in the outer flow to be presented here. However, the experimentally measured Strouhal numbers align very well with the extrapolated trend of the numerical values as R/θ increases. A comparison with the linear instability properties of the base flow displays the same behavior that has been found in the simulations. Global instability almost coincides with the onset of absolute instability at the nozzle. At threshold, the global frequency St_g sets in 9% above the absolute frequency St_0 (grey dashed line in figure 4.17), but while St_0 decreases with stronger heating, St_g remains nearly constant over the covered range of temperature ratio S.

Influence of acoustic feedback

In several convectively unstable flow configurations, such as flow over cavities [63] or jets impinging on an obstacle [49], self-sustained oscillations are known to arise from the synchronization of a feedback loop consisting of a downstream-travelling vortical branch and an upstream-travelling acoustic branch. In numerical simulations of compressible free jets, such a feedback loop may involve acoustic waves that are emitted from nonlinear vortex roll-up and pairing events [64, 48], but also spurious acoustic noise generated at the numerical outflow has been reported to potentially give rise to unphysical self-excitation in numerical simulations of mixing layers [16]. Grinstein *et al.* [47] observed self-sustained oscillations due to acoustic feedback from vortex pairing in their simulation of a convectively unstable jet.

In the present simulations, in the absence of a hard nozzle, such acoustic feedback may only arise from spurious coupling between outgoing acoustic and incoming vortical waves at the numerical upstream boundary. Certainly the irregular perturbations that are observed to persist in simulations of entirely convectively unstable base flows must be the result of such spurious acoustic forcing, and these configurations therefore can be used to characterize the quality of the numerical upstream boundary conditions. Measures of typical conversion rates from outgoing acoustic to incoming vortical waves in these globally stable cases may then serve as a criterion to examine whether or not the synchronized oscillations observed in the globally unstable regime, considering their amplitude levels near the inlet, are likely to be influenced by spurious acoustic forcing.

Pressure fluctuations p' outside the jet at the upstream boundary $x = 0$ are purely acoustic in nature, whereas v' fluctuations inside the shear layer are strongly dominated by vortical instability waves. An *ad hoc* measure of the acoustic-vorticity conversion at the inlet in a convectively unstable flow may be defined as the ratio

$$C_{av} = \frac{v'_{rms}(r = 1, x = 1)}{p'_{rms}(r = 2, x = 0)}\,, \tag{4.23}$$

evaluated in the asymptotic regime. Values of C_{av} for all flow cases are given in figure 4.18. In all globally stable configurations (open symbols in figure 4.18, compare to figure 4.15), C_{av} varies between 10^{-2} and 10^{-1}. This order of magnitude seems to be characteristic of situations where instabilities are driven by acoustic forcing at the inlet. Such forcing naturally is more efficient in thin shear layer jets, but for constant values of R/θ it is found to vary only slowly with S in the globally stable regime. In contrast, C_{av} takes

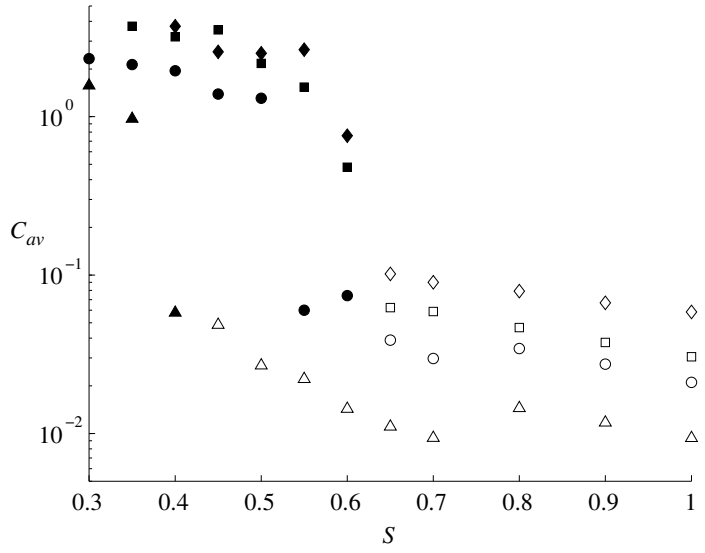

Figure 4.18: Values of the conversion ratio $C_{av} = v'_{rms}(1,1)/p'_{rms}(2,0)$, as defined in (4.23), as a function of S for different values of R/θ. Symbols as in figure 4.17: ▲, △ $R/\theta = 10$; ●, ○ $R/\theta = 15$; ■, □ $R/\theta = 20$; ♦, ◊ $R/\theta = 25$. Solid symbols denote synchronized cases, open symbols denote unsynchronized cases.

on significantly higher values in most configurations exhibiting synchronized oscillations. The v' fluctuations in these cases are too strong to be the result of acoustic forcing, and the noise-driven oscillations therefore appear to have been replaced by a global mode induced by absolute instability.

According to figure 4.18, one might wonder whether the cases ($R/\theta = 10$, $S = 0.4$) and ($R/\theta = 15$, $S = 0.55$) are likely to be dominated by acoustic feedback. We feel that these two marginal cases quite accurately mark the onset of a supercritical bifurcation. The configuration ($R/\theta = 15$, $S = 0.6$) is atypical: Although it marks the onset of self-sustained oscillations, this threshold does not coincide with a significant increase of C_{av}. This observation suggests that acoustic feedback is indeed involved in the self-excited behavior. However, the inlet profile in this case is already absolutely unstable, and the global frequency has been found to very accurately obey the selection criterion for a global mode (see figure 4.17). We therefore believe this flow configuration to exhibit the behavior of a *slightly damped oscillator*, in the sense of Huerre & Monkewitz [54]: in the absence of any upstream forcing, such a flow would be globally stable, but very close to threshold. The

low-level acoustic forcing introduced by the numerical boundary conditions seems to be sufficient to destabilize the otherwise slightly damped global mode. Note that the 'mode 2' oscillatory states reported in Ref. [69] bear the same characteristic features as the one observed here in the ($R/\theta = 15$, $S = 0.6$) base flow. It may be surmised that the occurrence of these 'mode 2' states [69] are also the manifestation of a slightly damped global mode destabilized by low-level acoustic feedback.

4.3.5 Inner structure of rolled-up stratified vortices

In an isothermal jet, vortex roll-up is a process involving only the redistribution and viscous dissipation of the vorticity initially contained in the unperturbed shear layer. Figure 4.19a shows a vortex rolling up in a perturbed isothermal jet with $R/\theta = 10$. The action of viscosity leads to a smooth vorticity distribution inside the vortex core, and to a preferred dissipation in the thin braids that connect neighboring vortices. No negative vorticity is produced. In contrast, in the regime of low S, where global instability is observed, the simulations display a more complex inner structure of the rolled-up vortex billows, as demonstrated in figure 4.19b for a typical newly-formed vortex in a jet with $R/\theta = 10$ and $S = 0.4$. Isocontours of the total vorticity $\Omega = \Omega_b + \Omega'$ are shown. The rolled-up sheets of positive vorticity from the initial shear layer are interlaced with regions of negative vorticity, and their absorption into the compact vortex core takes place on a slower time scale than in the isothermal jet.

In the context of non-isothermal planar shear layers, Klaassen & Peltier [59, 60] conclude that baroclinic production of vorticity in the vortex braids may dominate over viscous dissipation if the temperature gradient is sufficiently strong. Thin layers of high vorticity from the braids are then successively wrapped around the vortex core, forming a more pronounced spiral sheet structure than is found in isothermal shear layers. In Refs. [59, 60], the braid regions are identified as the prevalent site of baroclinic vorticity production.

A closer investigation of the vortex roll-up process in the heated jet confirms that the baroclinic torque is responsible for the formation of the layered vorticity structure. Figure 4.20a displays the total density distribution corresponding to figure 4.19b. The vortex billow is composed of two entwined spiraling fingers of high and low density fluid. Mixing between these two densities only occurs in the very core of the vortex. The vorticity layers displayed in figure 4.19b are located on the interfaces between regions of high

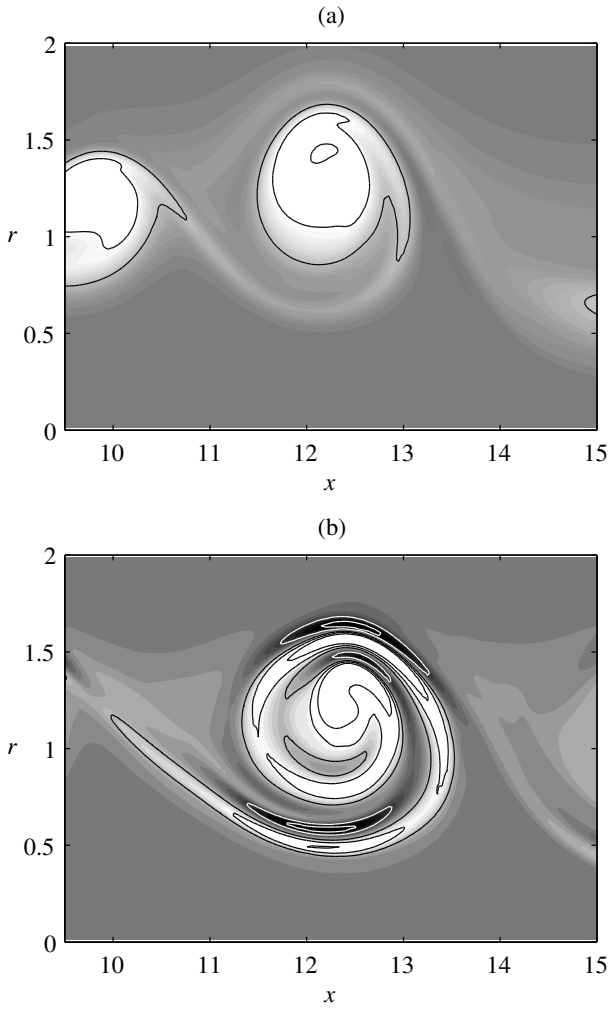

Figure 4.19: Vortex roll-up in jets with parameters (*a*) $R/\theta = 10$, $S = 1$ (isothermal), (*b*) $R/\theta = 10$, $S = 0.5$ (heated). Vorticity isocontours: Light shading and black lines are positive, dark shading and white lines are negative.

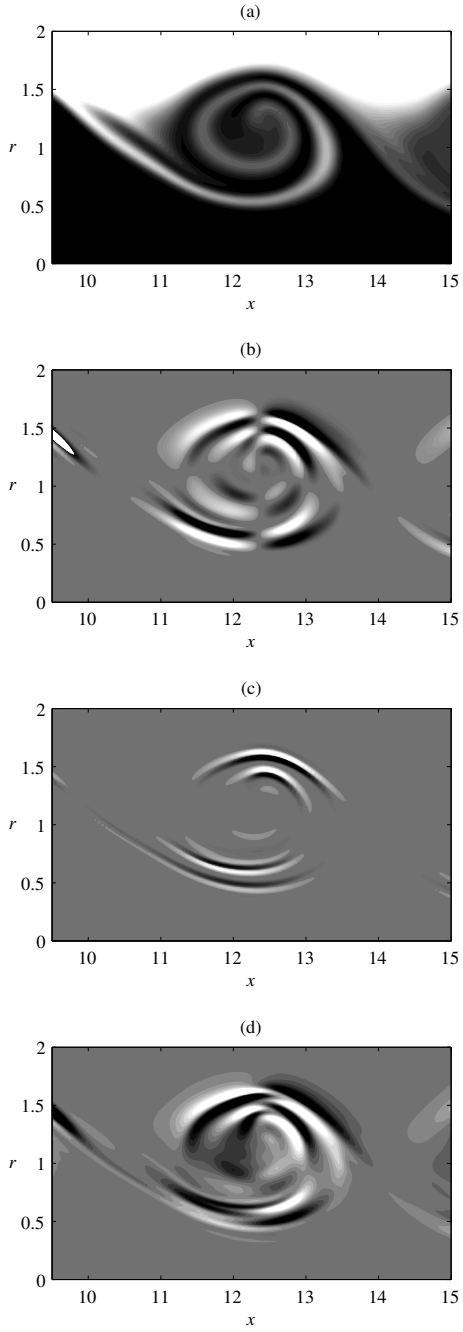

Figure 4.20: (*a*) Total density: black is light fluid, white is heavy fluid. (*b*) Baroclinic torque, (*c*) viscous vorticity dissipation, (*d*) total vorticity production $D_t\Omega$. Greyscale values are identical in (*b–d*): light is positive, dark is negative. All snapshots are taken at the same time as in figure 4.19b.

and low density. The density and pressure gradients are misaligned, and therefore exert a baroclinic torque $(\nabla\rho \times \nabla p)/\rho^2$, mapped in figure 4.20b. A fluid particle on an anti-clockwise trajectory around the center of the vortex successively passes through alternating regions of positive and negative baroclinic torque. Such alternating regions in figure 4.20b are perfectly aligned with the outer vorticity layers displayed in figure 4.20a. Written in total flow quantities, the vorticity equation reads

$$D_t\Omega = -\Omega\left(\partial_x u + \partial_r v\right) + \frac{\nabla\rho \times \nabla p}{\rho^2} + \mathrm{curl}\left(\frac{\mathrm{div}\tau}{\rho}\right). \qquad (4.24)$$

The distribution of the viscous dissipation term is displayed in figure 4.20c. Dissipation is concentrated in layers that align with those of 4.19b. The material derivative $D_t\Omega = \partial_t\Omega + \nabla\Omega\cdot\mathbf{u}$ is presented in figure 4.20d. Comparison with figure 4.20b clearly demonstrates that the dominant contribution to $D_t\Omega$ in the outer layers of the vortex is provided by the baroclinic torque. However, in contrast to the study of Klaassen & Peltier [59, 60], the vorticity production does not take place in the braids between neighboring vortices, but inside the vortex billow.

4.3.6 Conclusion

The global stability of hot round jets has been examined via direct numerical simulation of the axisymmetric equations of motion. The shear layer thickness of the inlet profile and the ambient-to-jet temperature ratio have been systematically varied over the ranges $10 \leq R/\theta \leq 25$ and $0.3 \leq S \leq 1$. Globally unstable situations are characterized by the onset of self-sustained synchronized oscillations that give rise to highly regular ring vortices.

The numerical results have clearly demonstrated that global instability, over the investigated parameter range, is associated with the presence of a finite region of local absolute instability. No synchronized oscillations have been found to persist in flow configurations that are convectively unstable everywhere. At any fixed value of R/θ, global instability has been observed to set in at a temperature ratio just slightly below the critical value at which local absolute instability starts to develop at the upstream boundary of the flow domain. As S is lowered further beyond the global instability threshold, and the streamwise extent of the absolutely unstable flow region consequently grows larger, the flow never returns to a globally stable behavior. These numerical observations are in excellent agreement with the theoretical model of nonlinear global modes in a semi-infinite domain described by Couairon

& Chomaz [27]. Spurious excitation from upstream-travelling acoustic waves does not qualify as the driving mechanism of the flow synchronization. Its influence seems to be limited to a possible slight destabilization of flows on the brink of global instability.

It has further been shown that the frequencies of globally unstable jets obey the theoretical predictions [27]: at threshold, the global frequency of the thickest shear layer jet ($R/\theta = 10$) matches the absolute frequency at the inlet within 0.5% accuracy. An agreement of 8% is found in the thinnest shear layer jet considered ($R/\theta = 25$). The conclusions drawn in Ref. [69] from the investigation of jets with $R/\theta = 10$ and over a range of temperature ratios $0.1 \leq S \leq 1$ are found to hold true also in jets with thinner initial shear layers. However, the numerical results indicate that in thin shear layer jets the validity of the theoretical frequency selection criterion [27] is restricted to the immediate vicinity of the global instability threshold.

The numerical observations pertaining to the onset of global instability and the selection of the global frequency seem to be consistent with the 'mode II' oscillations reported in the experiments of Monkewitz *et al.* [82]. In agreement with Kyle & Sreenivasan [62], no oscillating states have been detected that would correspond to 'mode I' of Ref. [82]. The comparison remains qualitative, because the experimentally investigated range $R/\theta \geq 35$ [82, 62] could not be attained in the present study. Above the upper limit $R/\theta = 25$, free vortical structures in the outer flow quickly contaminate the numerical inflow region.

The inner structure of the rolled-up ring vortices in hot jets has been documented. It is characterized by thin vorticity layers of alternating sign, wrapped around a compact core. This layer structure has been shown to arise from vorticity production due to the baroclinic torque.

It may be concluded that the nonlinear global mode model of Couairon & Chomaz [27] accurately describes the physical mechanism that causes the onset of global instability in hot jets: a nonlinear wave front moves upstream in an absolutely unstable environment, until it is blocked at the upstream boundary. In the asymptotic state, the front then imparts its linearly selected frequency to the entire flow. In supercritical flow situations, the model [27] foresees a departure of the global frequency from the absolute frequency, as the spatial envelope of the oscillations must satisfy a matching condition between a region of exponential growth and the upstream boundary conditions. Whether this mechanism alone accounts for the numerically observed discrepancy between absolute and global frequencies in highly supercritical thin shear layer jets remains to be clarified.

Acknowledgments

The authors gratefully acknowledge the advice and support of Marc Terracol in the development of the numerical code. Many valuable discussions with Jean-Marc Chomaz have greatly contributed to this study. Computational ressources were provided by ONERA. Lutz Lesshafft has been supported by a PhD fellowship from the EADS Foundation.

4.4 Further remarks

4.4.1 Influence of inflow boundary conditions

The crucial importance of clean numerical boundary conditions, in particular with regard to the frequency selection, has been stressed in section 4.3.4. An earlier published study [68], where zero order boundary conditions have been used at the inlet, is included as an appendix to this manuscript for quantitative comparison.

Laufer & Monkewitz [64] have proposed a scenario for the influence of boundary conditions on the possible global instability of a class of isothermal jets: these authors assume that synchronized oscillations may arise from a resonance between the vortex pairing station, as a source of sound generation, and the jet inlet, where acoustic waves are partially converted to downstream traveling instability waves. Such an *acoustic feedback* would constitute a mechanism for the occurrence of synchronized states radically different from the global modes investigated in this chapter. From the results presented here, it can be safely concluded that the global instability observed in the direct numerical simulations is due to the presence of an absolutely unstable region in the baseflow, as opposed to acoustic resonance. The investigation presented in the appendix confirms this conclusion: the frequency selection criterion derived by Laufer & Monkewitz [64] for an acoustically driven synchronization fails to predict the observed global frequencies.

Yet, if the present study has allowed to identify the physical mechanism by which hot jets become globally unstable, it has at the same time demonstrated that the underlying theoretical model falls short of providing a reliable quantitative prediction of the global frequency in hot jets far from threshold. In the simulations, the inlet boundary conditions play a determining rôle in the frequency selection process. The same must be expected to hold true in experimental settings. If numerical simulations are to be used as a tool for the prediction of global jet dynamics in real life situations, the quality of the results will largely depend on a faithful numerical reproduction of nozzle effects. Including the quantitative influence of non-trivial boundary conditions into the theoretical model promises to be a very challenging task. A simplified model of the unsteady Kutta condition at the trailing edge of a splitter plate in compressible flow has been proposed by Bechert *et al.*[5]. The complexity of the issue in convectively unstable shear flows alone is discussed in a review article by Crighton [30].

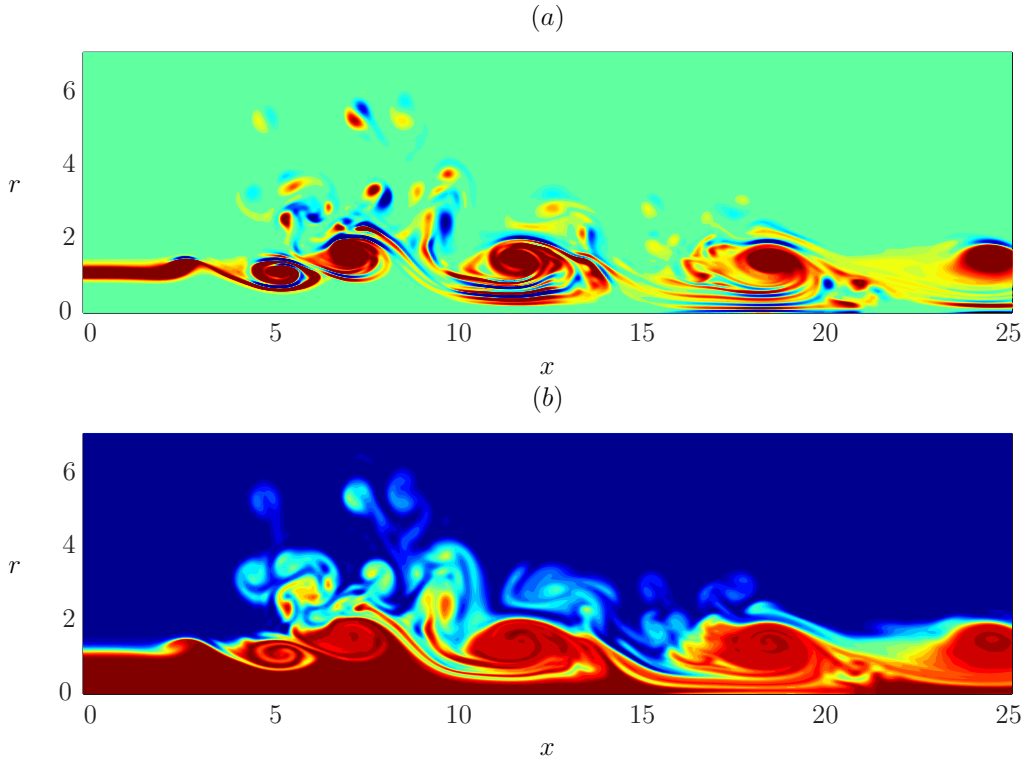

Figure 4.21: Pseudo-turbulent structures in the simulation of a jet with $R/\theta = 15$, $S = 0.3$. (a) Total azimuthal vorticity; blue: $\Omega \leq -1.5$, red: $\Omega \geq 1.5$. True range: $-4.8 \leq \Omega \leq 8.0$. (b) Total density; red: $\rho \leq 1$, blue: $\rho \geq 3.3$. True range: $0.98 \leq \rho \leq 3.63$.

4.4.2 Pseudo-turbulent states in thin shear layer jets

As briefly described in section 4.3.4, numerical simulations of strongly heated thin shear layer jets display vortical structures in the outer flow, reminiscent of two-dimensional turbulence as observed, for instance, in the soap film experiments of Couder, Chomaz & Rabaud [28]. Pictures of the resulting vorticity and density distributions are displayed in figure 4.21 for a rather extreme situation.

Due to their visual resemblence, it is tempting to seek a connection between the ejection of free vorticity dipoles in the present axisymmetric simulations and the experimentally observed formation of *side jets* (Monkewitz *et al.*[82]). Yet, the studies of Monkewitz & Pfizenmaier [84] and of Brancher *et al.*[12] have clearly demonstrated that these side jets are the result of three-dimensional effects. Whether the axisymmetric instability that leads to the

chaotic structures in figure 4.21 may be involved in early stages of side jet formation, or whether it may provide a route to turbulence, cannot be decided from our present understanding.

Chapter 5

Acoustic field of a global mode

Objective

The aim of the following investigation is to characterize the acoustic field associated with the global mode in a hot jet, as observed in the direct numerical simulations discussed in the previous chapter. The directivity pattern of the sound radiated at the global frequency will be described for a suitable globally unstable flow configuration, and the simulation data will be compared to results obtained from the acoustic analogy due to Lighthill [71]. An analysis of the contributions of individual source terms in the Lighthill equation leads to identify the dominant noise generation mechanisms. Strategies for the use of the Lighthill equation in the analysis of jet noise are explored, and some difficulties related to the analogy's capabilities as a predictive tool are exposed.

5.1 Integration of the Lighthill equation

Lighthill [71] obtained an inhomogeneous wave equation for acoustic fluctuation quantities from a simple algebraic manipulation of the exact continuity and momentum equations. In Cartesian coordinates x_i, and with the physical assumptions made in sections 4.2 and 4.3, the complete Lighthill equation for pressure fluctuations reads (see Crighton [29] and Dowling [37])

$$\frac{1}{c_\infty^2}\frac{\partial^2 p'}{\partial t^2} - \frac{\partial^2 p'}{\partial x_i^2} = \frac{\partial^2 T_{ij}}{\partial x_i \partial x_j} - \frac{\partial^2 \rho_e}{\partial t^2}\,, \tag{5.1}$$

where c_∞ denotes the speed of sound in the far field. The Lighthill stress tensor

$$T_{ij} = \rho_b u_{b,i} u'_j + (\rho u_i)' u_{b,j} + (\rho u_i)' u'_j - \tau'_{ij} \tag{5.2}$$

is composed of Reynolds stresses and viscous terms, while the 'excess density'

$$\rho_e = \rho' - p'/c_\infty^2 \tag{5.3}$$

is related to entropy fluctuations. Expressed as (5.1), the Lighthill equation is exact.

One possible way to proceed is to solve for p' via numerical time integration of equation (5.1), simultaneously with a DNS of the near field, from which the right hand side terms are determined at each time step. Contributions to the acoustic far field due to individual source terms can then be examined separately. This strategy has been applied, for instance, by Freund [42] and by Boersma [9].

The more classical approach, known as the Lighthill acoustic analogy, is pursued in the present investigation: the left hand side of equation (5.1) is regarded as the acoustic wave propagation operator, and a solution for the acoustic pressure is sought in terms of a Green function that is to be evaluated for the the right hand side source terms of (5.1). The derivation below follows the analysis of Crighton [29].

A first approximation is introduced by choosing the free space Green function

$$G(\boldsymbol{x}, \boldsymbol{\xi}, t', t) = \frac{\delta(t - t' - |\boldsymbol{x} - \boldsymbol{\xi}|/c_\infty)}{4\pi|\boldsymbol{x} - \boldsymbol{\xi}|} \tag{5.4}$$

to describe the acoustic signal observed at the far field position $\boldsymbol{\xi}$ at time t, radiated from the source position $\boldsymbol{x}$ at time t'. This approximation neglects the influence of density and velocity inhomogenities within the jet on acoustic waves, and it is valid only if the propagation distance through the jet region is small compared to the acoustic wavelength. With (5.4), a first formal solution to (5.1) is found as

$$p'(\boldsymbol{\xi}, t) = \frac{\partial^2}{\partial x_i \partial x_j} \int \big[T_{ij}\big] \frac{\mathrm{d}^3\boldsymbol{x}}{4\pi|\boldsymbol{x} - \boldsymbol{\xi}|} - \frac{\partial^2}{\partial t^2} \int \big[\rho_e\big] \frac{\mathrm{d}^3\boldsymbol{x}}{4\pi|\boldsymbol{x} - \boldsymbol{\xi}|} \,. \tag{5.5}$$

The integrands $\big[T_{ij}\big]$, $\big[\rho_e\big]$ are to be evaluated at the retarded time $t - |\boldsymbol{x} - \boldsymbol{\xi}|/c_\infty$.

With the Fraunhofer far field approximation

$$\begin{aligned} t - \frac{|\boldsymbol{x}-\boldsymbol{\xi}|}{c_\infty} &\rightarrow t - \frac{\xi}{c_\infty} + \frac{\boldsymbol{x}\cdot\boldsymbol{\xi}}{\xi\, c_\infty} \\ |\boldsymbol{x}-\boldsymbol{\xi}|^{-1} &\rightarrow \xi^{-1} \\ \frac{\partial}{\partial x_i} &\rightarrow -\frac{\xi_i}{\xi\, c_\infty}\frac{\partial}{\partial t}\,, \end{aligned}$$

where ξ is written for $|\boldsymbol{\xi}|$, the solution (5.5) becomes

$$p'(\boldsymbol{\xi},t) = \frac{\xi_i\xi_j}{4\pi\xi^3 c_\infty^2}\frac{\partial^2}{\partial t^2}\int \left[T_{ij}\right] \mathrm{d}^3\boldsymbol{x} - \frac{1}{4\pi\xi}\frac{\partial^2}{\partial t^2}\int \left[\rho_e\right] \mathrm{d}^3\boldsymbol{x}\,. \tag{5.6}$$

Finally, with the temporal and spatio-temporal Fourier transformations defined as

$$\hat{f}(\boldsymbol{x},\omega) = \int f(\boldsymbol{x},t)\, e^{i\omega t}\mathrm{d}t \tag{5.7}$$

$$\tilde{f}(\boldsymbol{k},\omega) = \iint f(\boldsymbol{x},t)\, e^{i(\omega t - \boldsymbol{k}\cdot\boldsymbol{x})}\mathrm{d}^3\boldsymbol{x}\,\mathrm{d}t\,, \tag{5.8}$$

the temporal Fourier-transformed acoustic pressure reads

$$\begin{aligned} \hat{p}(\boldsymbol{\xi},\omega) &= -\frac{k_a^2}{4\pi\xi}\, e^{ik_a\xi}\,\frac{\xi_i\xi_j}{\xi^2}\int \hat{T}_{ij}(\boldsymbol{x},\omega) e^{-i\boldsymbol{k}_a\cdot\boldsymbol{x}}\,\mathrm{d}^3\boldsymbol{x} \\ &\quad + \frac{\omega^2}{4\pi\xi}\, e^{ik_a\xi}\int \hat{\rho}_e(\boldsymbol{x},\omega) e^{-i\boldsymbol{k}_a\cdot\boldsymbol{x}}\,\mathrm{d}^3\boldsymbol{x} \\ &= -\frac{k_a^2}{4\pi\xi}\, e^{ik_a\xi}\,\frac{\xi_i\xi_j}{\xi^2}\,\tilde{T}_{ij}(\boldsymbol{k}_a,\omega) + \frac{\omega^2}{4\pi\xi}\, e^{ik_a\xi}\,\tilde{\rho}_e(\boldsymbol{k}_a,\omega), \end{aligned} \tag{5.9}$$

where the acoustic wave number is taken as

$$\boldsymbol{k}_a = \frac{\omega}{c_\infty}\,\mathbf{e}_\xi\,. \tag{5.10}$$

As pointed out by Crighton [29], the acoustic radiation observed at a far field location $\boldsymbol{\xi}$ is caused by a single spectral component of the Lighthill source terms: a plane wave of wavenumber k_a, travelling in the radiation direction. Bastin, Lafon & Candel [3] compared numerical results obtained from various formulations of the Lighthill solution. In particular, it has been shown that for a numerical treatment the Fourier-transformed formulation (5.9) must be preferred over a formulation that relies on retarded times, like expression (5.6).

5.1.1 Axisymmetric source terms

Under the assumption of an axisymmetric source term distribution, the three-dimensional equation (5.9) was rewritten by Huerre & Crighton [52] for the particular case of a Gaussian envelope function $T_{ij}(r,x) \propto \exp(-x^2/\sigma^2)$, and in a more general form by Fleury [39]. The formulation of Fleury is extended here to include viscous and entropy-related source terms.

Source locations in equation (5.9) are expressed in cylindrical coordinates (x,r,φ), while the observer location $\boldsymbol{\xi}$ in the axisymmetric far field is characterized by its spherical coordinates (ξ,ϑ). The observation angle ϑ is taken relative to the downstream jet axis. The resulting source term integral can be solved numerically in all three (x,r,φ) directions (see Mitchell *et al.*[80]), yet Huerre & Crighton [52] have demonstrated that the circumferential integration admits closed-form solutions. After integration in φ, equation (5.9) becomes

$$\hat{p}(\xi,\vartheta,\omega) = -\frac{k_a^2}{2\xi}\, e^{ik_a\xi} \iint (I_{xx} + I_{rx} + I_{rr} + I_{\varphi\varphi} - c_\infty^2 I_e)\, r \,\mathrm{d}r\,\mathrm{d}x, \qquad (5.11)$$

with the integrand given by

$$\begin{aligned}
I_{xx} &= J_0(\alpha)\, \cos^2\vartheta\, e^{-ik_a x\cos\vartheta}\, \hat{T}_{xx}(x,r,\omega) && (5.12)\\
I_{rx} &= i2J_1(\alpha)\, \sin\vartheta\, \cos\vartheta\, e^{-ik_a x\cos\vartheta}\, \hat{T}_{rx}(x,r,\omega) && (5.13)\\
I_{rr} &= \frac{1}{2}\,[J_0(\alpha) - J_2(\alpha)]\, \sin^2\vartheta\, e^{-ik_a x\cos\vartheta}\, \hat{T}_{rr}(x,r,\omega) && (5.14)\\
I_{\varphi\varphi} &= \frac{1}{2}\,[J_0(\alpha) + J_2(\alpha)]\, \sin^2\vartheta\, e^{-ik_a x\cos\vartheta}\, \hat{T}_{\varphi\varphi}(x,r,\omega) && (5.15)\\
I_e &= J_0(\alpha)\, e^{-ik_a x\cos\vartheta}\, \hat{\rho}_e(x,r,\omega). && (5.16)
\end{aligned}$$

The argument of the Bessel functions is $\alpha = -k_a r \sin\vartheta$. Expression (5.11) explicitly gives the far field pressure amplitude in terms of a spatial phase, a radial decay $\propto \xi^{-1}$, and a ϑ-dependent far field directivity function:

$$\hat{p}(\xi,\vartheta,\omega) = \frac{e^{ik_a\xi}}{\xi}\, D(\vartheta) \quad \rightarrow \quad D(\vartheta) = \xi\,|\hat{p}(\xi,\vartheta,\omega)|\,. \qquad (5.17)$$

The Bessel functions $J_i(\alpha)$ represent the effect of azimuthal interference, whereas the $\cos^2\vartheta$, $\sin^2\vartheta$ and $\cos\vartheta\sin\vartheta$ factors produce the well-known quadrupole directivity of sources related to the viscous and Reynolds stresses. Note that the entropy-related term I_e *a priori* takes the form of a monopole source.

The source distributions $\hat{T}_{ij}(r,x,\omega)$, $\hat{\rho}_e(r,x,\omega)$ are available from the DNS. The associated far field pressure $\hat{p}(\xi,\vartheta,\omega)$ according to the Lighthill equation can then be evaluated by numerically solving the integration over r and x in equation (5.11).

Radially compact source terms

Following the approach of Huerre & Crighton [52], the aeroacoustic source distributions in a jet can be assumed to be compact in the radial direction, whereas their axial distribution may strongly influence the far field directivity pattern. As in the analysis of Fleury [39], the source terms are modelled as being concentrated in the center of the shear layer at $r = 1$ such that

$$\hat{T}_{ij}(x,r,\omega) = \hat{T}^x_{ij}(x,\omega)\,\delta(r-1), \tag{5.18}$$

and therefore

$$\hat{T}^x_{ij}(x,\omega) = \int_0^\infty \hat{T}_{ij}(x,r,\omega)\,r\,\mathrm{d}r\,. \tag{5.19}$$

A radially compact entropy source term $\hat{\rho}^x_e(x,\omega)$ is obtained accordingly.

Under this assumption, equation (5.11) simplifies to

$$\hat{p}(\xi,\vartheta,\omega) = -\frac{k_a^2}{2\xi}\,e^{ik_a\xi}\left(I^x_{xx} + I^x_{rx} + I^x_{rr} + I^x_{\varphi\varphi} - c_\infty^2 I^x_e\right), \tag{5.20}$$

with

$$\begin{aligned}
I^x_{xx} &= J_0(\alpha)\,\cos^2\vartheta\,\tilde{T}^x_{xx}(k_a\cos\vartheta,\omega) && (5.21)\\
I^x_{rx} &= i2J_1(\alpha)\,\sin\vartheta\,\cos\vartheta\,\tilde{T}^x_{rx}(k_a\cos\vartheta,\omega) && (5.22)\\
I^x_{rr} &= \frac{1}{2}\left[J_0(\alpha) - J_2(\alpha)\right]\sin^2\vartheta\,\tilde{T}^x_{rr}(k_a\cos\vartheta,\omega) && (5.23)\\
I^x_{\varphi\varphi} &= \frac{1}{2}\left[J_0(\alpha) + J_2(\alpha)\right]\sin^2\vartheta\,\tilde{T}^x_{\varphi\varphi}(k_a\cos\vartheta,\omega) && (5.24)\\
I^x_e &= J_0(\alpha)\,\tilde{\rho}^x_e(k_a\cos\vartheta,\omega). && (5.25)
\end{aligned}$$

The Bessel functions now take the argument $\alpha = -k_a\sin\vartheta$.

This formulation, if the assumption of radial compactness holds, is particularly convenient for an analysis of aeroacoustic sound generation, as the influence of the spatial source term distribution on the directivity pattern of the radiated sound is explicitly expressed in terms of the one-dimensional Fourier transform along x. For long wavelengths, $k_a \ll 1$, the variations of the Bessel functions are negligible. The directivity of the acoustic field

is then given as the superposition of viscous and Reynolds stress related quadrupoles and one entropy-related monopole, each term modulated along ϑ by an "antenna factor" [52], according to the variation of the spatial Fourier spectrum $\tilde{T}^x_{ij}(k_a \cos\vartheta, \omega)$, $\tilde{\rho}^x_e(k_a \cos\vartheta, \omega)$ of the corresponding source term over the interval $-k_a \leq k \leq k_a$. As a general rule, a source distribution of large streamwise extent in physical space displays strong variations along k in Fourier space, and therefore may radiate a highly directional sound field. The Fourier spectrum of a more localized sound source, by contrast, varies slowly in k. In the limit of *fully compact source distributions*

$$\hat{T}_{ij}(x, r, \omega) = \hat{T}^\delta_{ij}(\omega)\, \delta(x)\, \delta(r-1) \tag{5.26}$$

$$\Rightarrow \hat{T}^\delta_{ij}(\omega) = \iint \hat{T}_{ij}(x, r, \omega)\, r \, \mathrm{d}r \, \mathrm{d}x \,, \tag{5.27}$$

the antenna factors vanish, and the contributions of the individual source terms in equation (5.20) simplify further to

$$\begin{aligned}
I^\delta_{xx} &= J_0(\alpha)\, \cos^2\vartheta\, \hat{T}^\delta_{xx}(\omega) && (5.28)\\
I^\delta_{rx} &= i2J_1(\alpha)\, \sin\vartheta\, \cos\vartheta\, \hat{T}^\delta_{rx}(\omega) && (5.29)\\
I^\delta_{rr} &= \frac{1}{2}\left[J_0(\alpha) - J_2(\alpha)\right] \sin^2\vartheta\, \hat{T}^\delta_{rr}(\omega) && (5.30)\\
I^\delta_{\varphi\varphi} &= \frac{1}{2}\left[J_0(\alpha) + J_2(\alpha)\right] \sin^2\vartheta\, \hat{T}^\delta_{\varphi\varphi}(\omega) && (5.31)\\
I^\delta_e &= J_0(\alpha)\, \hat{\rho}^\delta_e(\omega). && (5.32)
\end{aligned}$$

5.2 Test: a linearly diverging forced jet

5.2.1 Baseflow

A test case is designed to correspond closely to the assumptions made about the hydrodynamic field in the study of Huerre & Crighton [52]. A linearly diverging jet of momentum thickness $\theta(x) \propto x$ is forced at a frequency which is locally unstable near the inlet, but becomes stable at some downstream distance. Assuming that $k_i \propto \theta$, local linear stability theory predicts a Gaussian variation of the perturbation amplitude along x [52]. The aim of this test case is to produce such a Gaussian instability wave packet as a nominally compact acoustic source, i.e. with a half-width much smaller than the acoustic wavelength λ_a. The streamwise variation of θ must therefore be sufficiently fast to yield a narrow envelope width, and at the same time

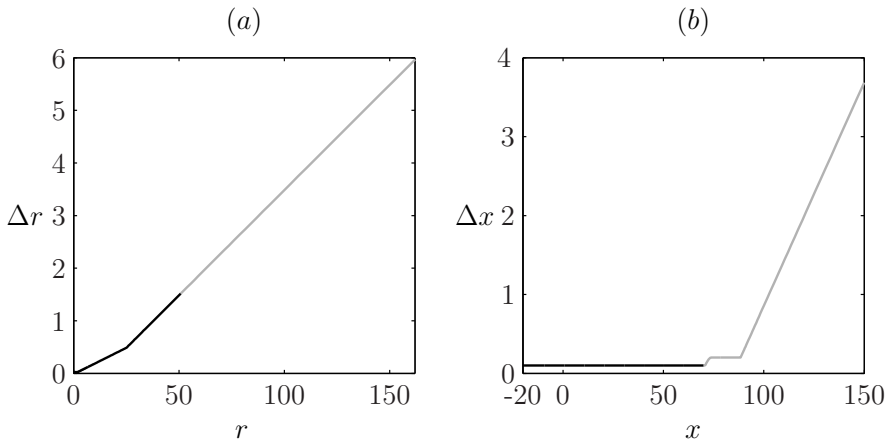

Figure 5.1: Grid point distribution used in the direct numerical simulation of a linearly diverging jet; sponge zones in grey.

should respect the assumption of a locally parallel baseflow in order for the local instability analysis to hold.

The chosen baseflow starts out with a momentum thickness $\theta = 0.1$ and grows to $\theta = 0.5$ between $x = 0$ and $x = 40$. Throughout the rest of the physical region down to $x = 70$ and in the adjacent sponge region $70 < x \leq 150$, the baseflow remains parallel. Near $x = 0$, the spreading rate $\partial_x \theta$ changes smoothly from zero to 0.1 and smoothly back to zero near $x = 40$. If the flow is forced with appropriate instability eigenfunctions at $x = 0$, test calculations with various forcing frequencies have shown that the instability wave packet develops cleanly, but the acoustic far field is dominated by direct sound emitted from the forcing at the upstream boundary. In order to minimize this spurious radiation, a parallel flow region with $\theta = 0.1$ is added upstream of the spreading jet. Instability waves grow exponentially within the parallel flow, and the amplitude of the upstream forcing can therefore be significantly lowered. The length of the parallel flow region must be calibrated such that the forcing amplitude is several orders of magnitude below the peak amplitude of the instability wave packet, but at the same time the explicitly applied forcing must remain dominant over spurious fluctuations at the numerical inlet, that may be provoked by upstream traveling acoustic waves. A length of $-20 \leq x < 0$ has been found to be optimal. A shorter length of 15 yields the same results for the near field development, a length of 30 gives rise to a contamination from spurious acoustic forcing at the inlet boundary conditions.

The baseflow profiles are not computed from an analytical model, but

from a numerical solution of the boundary layer equations (see section 3.3). The x-axis is then mapped in such a way as to give the linear $\theta(x)$ distribution, and the resulting $u_b(x,r)$ field is interpolated on the grid point distribution shown in figure 5.1. Finally, v_b is recalculated from $\operatorname{div}\vec{u}_b = 0$ using second-order finite differences. Pressure, temperature and density of the baseflow are uniform throughout the domain.

5.2.2 Forcing

A Gaussian envelope function of the instability wave packet amplitude evolves if the spatial growth rate $-k_i$ decreases linearly with x (Huerre & Crighton [52]). A spatial instability analysis of the baseflow described above shows that this assumption is adequate if $\omega_f > \omega_{max}$, with ω_{max} the spatially most amplified frequency of the inlet profile. For an optimal amplification of the forcing frequency within this zone, ω_f should in practice be chosen close to ω_{max}. The spatial growth rate $-k_i$ as a function of forcing frequency ω is given in figure 5.3a for the inlet profile ($R/\theta = 10$). A value of $\omega_f = 2$ is used in these calculations. At a Mach number $Ma = 0.1$, this choice results in an acoustic wavelength $\lambda_{ac} = 10\pi$. The precise eigenfunctions of velocity, density and pressure perturbations for $\omega_f = 2$ are used for the inflow forcing.

5.2.3 Near field results

The temporal evolution of the forced flow is computed directly according to the *linear* equations of motion. The Reynolds number is chosen as $\mathrm{Re} = 1000$. As the inflow forcing sets in abruptly at the start of the computation, with an initially unperturbed baseflow, a transitional wavepacket forms. Once this wavepacket is convected out of the computational domain, a periodic flow state is reached, highly synchronized at $\omega_f = 2$ at all streamwise stations. The amplitude envelope function of the pressure perturbation at $r = 1$ along x, displayed in figure 5.2, grows exponentially over the parallel flow region $x < 0$ and is close to a Gauß distribution for $x > 0$. The envelope width, defined as the streamwise distance between the two stations where $|p| = |p|_{max}\, e^{-1}$, is $2\sigma = 12.5 \approx 0.4\,\lambda_{ac}$. The ratio of the maximum and the forcing amplitude is 4.6×10^5. Downstream of the maximum location, down to $x = 40$, the perturbation amplitude decreases to approximately the level of the forcing applied at the inflow. A slower decay of what appears to be residual fluctuations, probably a stable k^+ wave, is observed downstream of $x = 40$, also highly synchronized at $\omega_f = 2$. It has been verified by

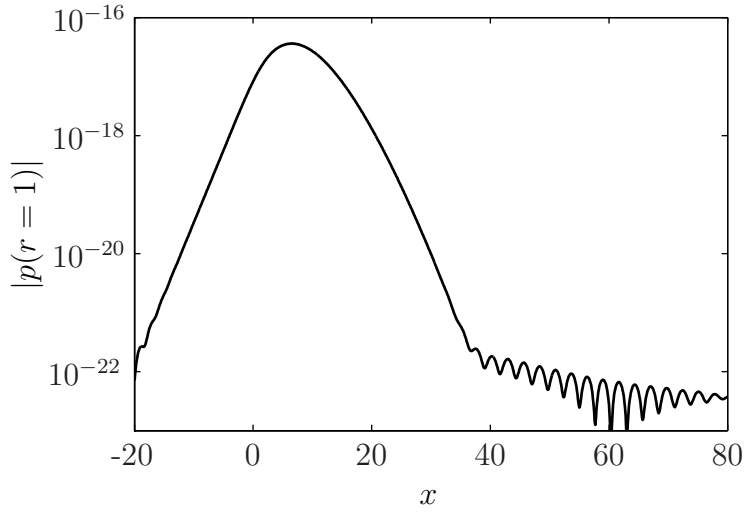

Figure 5.2: Amplitude envelope of near field pressure oscillations at $r = 1$ as a function of downstream distance.

comparison with further spreading baseflows that these fluctuations are not due to the re-parallelization of the baseflow at $x = 40$.

The local spatial growth rate in the non-parallel flow, obtained from the simulation as $-k_i^{num} = \partial(\ln|p|)/\partial x$, is compared to the results of the strictly parallel local stability analysis in figure 5.3b: the instability wavepacket is well described under the assumption of a locally parallel baseflow. Note that the theoretical curve in figure 5.3b ends at $x = 15$; the k^+ branch could not be retrieved beyond this point due to numerical difficulties with the dispersion relation for very thick shear layers.

5.2.4 Acoustic field in the DNS

The acoustic far field from the numerical simulation is investigated in terms of the temporal Fourier coefficient of the pressure $\hat{p}(r, x, \omega_f)$. In the synchronized flow regime, the real pressure is given by $p(r, x, t) = \hat{p}(r, x, \omega_f)\, e^{i\omega_f t}$+c.c. The Fourier coefficient at each computational grid point is computed during the simulation, once the periodic state has been reached, over one cycle period as

$$\hat{p}(r, x, \omega_f) = \frac{1}{N} \sum_{j=1}^{N} p(r, x, t_j)\, (\cos \omega_f t_j + i\, \sin \omega_f t_j) \tag{5.33}$$

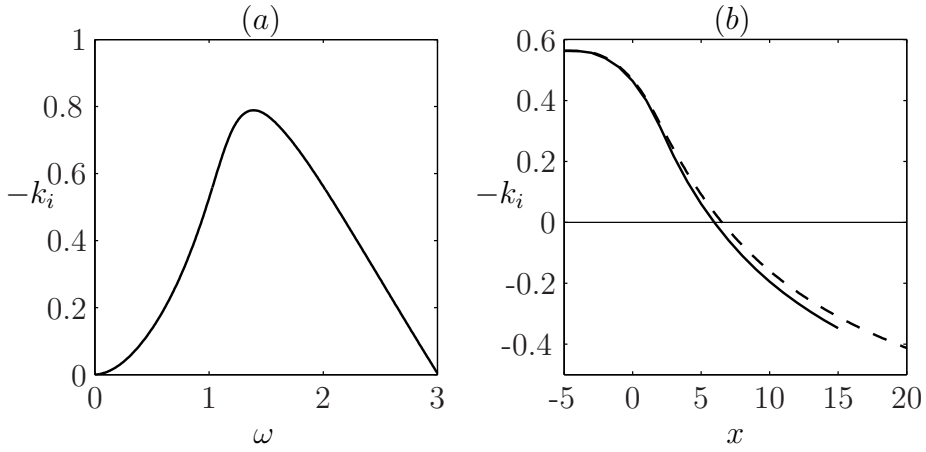

Figure 5.3: (a) Spatial growth rate as a function of frequency for the $R/\theta = 10$ profile in the upstream parallel region; (b) spatial growth rate as a function of x for $\omega_f = 2$. Solid: local instability analysis, dashed: $-k_i^{num}$ obtained from the pressure amplitude envelope in the DNS.

$$\text{with} \quad t_j = t_0 + j\Delta t, \quad N = \frac{2\pi}{\omega_f \, \Delta t} \, .$$

Absolute values of the resulting $\hat{p}(x, r, \omega_f)$ distribution are shown in figure 5.4. Only isocontours in the acoustic field are represented. Three acoustic lobes are visible in the (r, x) half-plane, separated by extinction lines at angles of 62 and 126 degrees from the jet axis. Both lines cross the axis at $x = 2$, which is taken as the apparent source location. The directivity factor $D(\theta)$ (as defined in equation 5.17) is evaluated by interpolating the values $\xi \, |\hat{p}|$ in equidistant points on an arc of radius ξ around the apparent source location. The results obtained for radii $\xi = 20$, 30 and 40 are compared in figure 5.5. It is found that the directivity is almost independent of the radius ξ already at $\xi = 20$. The sound pressure level in figure 5.5 is given in decibels according to

$$\text{SPL} = 20 \, \log_{10} \left(\frac{D(\vartheta)}{p_{\text{ref}}} \right) \, . \tag{5.34}$$

The transition from the hydrodynamic field to the acoustic field is explored in figure 5.6: Along the ray $(x = 2, r)$, the pressure amplitude decays exponentially for $r < 5$. Beyond this point, the decay is algebraic. Within the acoustic near field, stretching over approximately one wavelength $\lambda_a = 10\pi$, the slope adjusts to the asymptotic decay $|\hat{p}| \propto \xi^{-1}$. The acoustic pressure amplitude at $r = 20$ and the maximum near field pressure amplitude are separated by seven orders of magnitude.

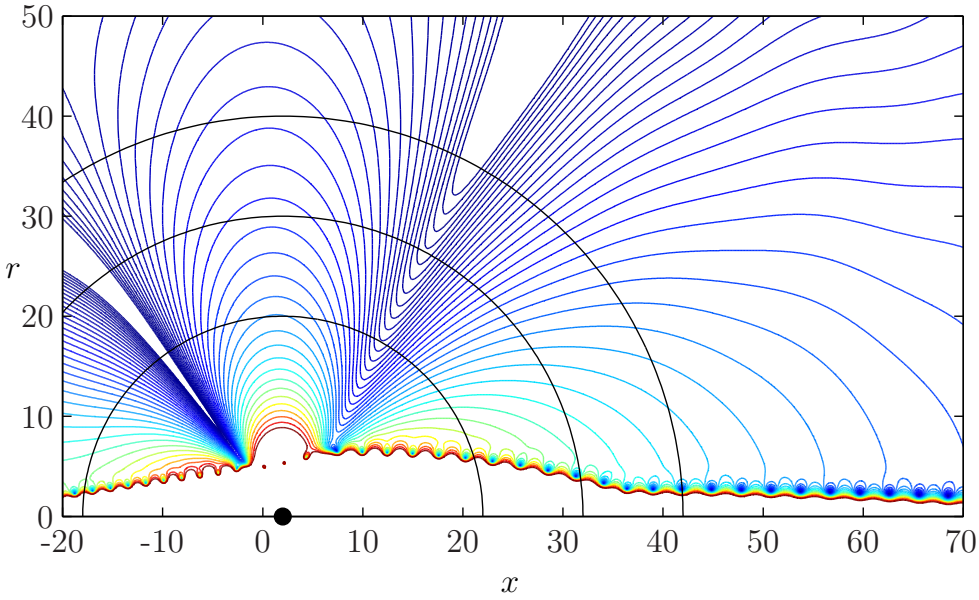

Figure 5.4: Pressure amplitude $|\hat{p}(r, x, \omega_f)|$ in the acoustic far field, exponentially spaced isocontours. Apparent sound source on the jet axis at $x = 2$, three arcs of radius 20, 30 and 40.

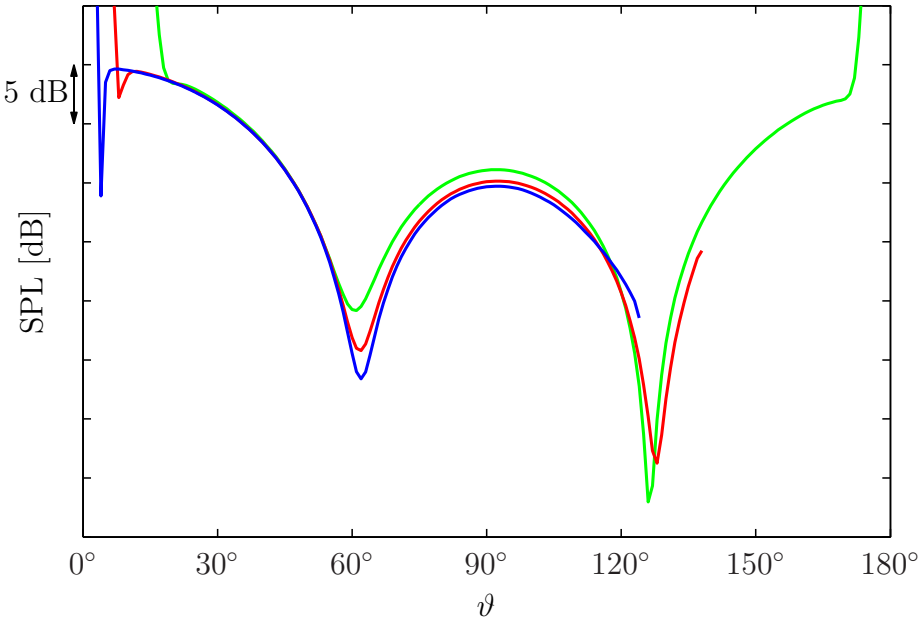

Figure 5.5: Far field directivity $D(\vartheta)$ from the DNS along three arcs of radius $\xi = 20$ (green), $\xi = 30$ (red), $\xi = 40$ (blue).

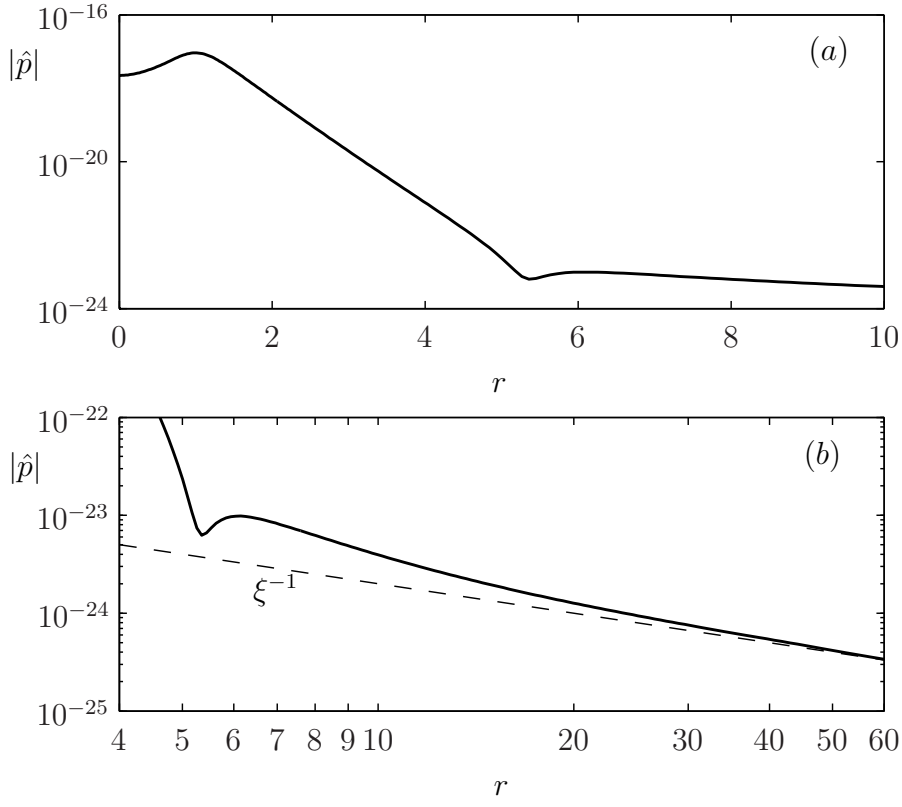

Figure 5.6: Radial variation of the pressure amplitude $|\hat{p}(r, x = 2)|$. (a) Exponential decay in the near field; (b) algebraic decay in the far field.

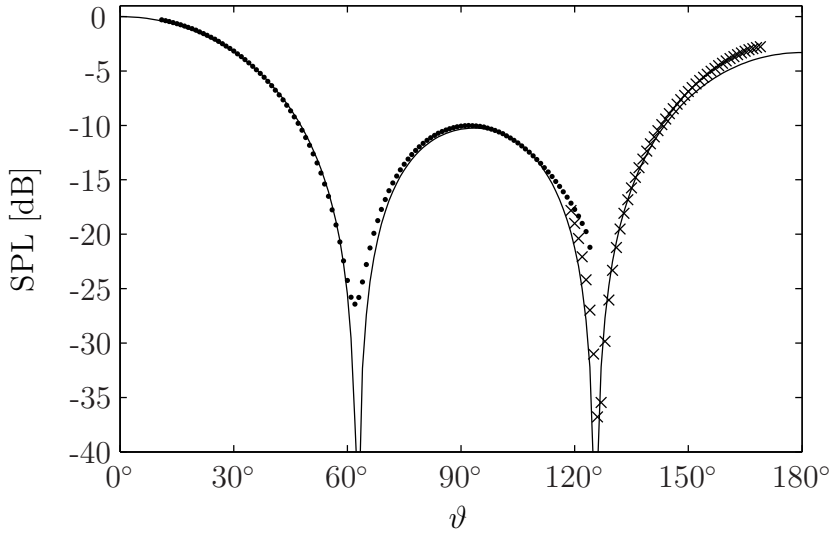

Figure 5.7: Directivity of the acoustic far field according to the DNS at $\xi = 40$ (•) and $\xi = 20$ (×); and according to the Lighthill equation (—) without compactness assumption.

5.2.5 Acoustic field according to the Lighthill equation

No compactness assumption

For comparison with the DNS solution, the acoustic far field according to the Lighthill equation is first computed from (5.11) without any assumption about the compactness of the source region. The source distributions $T_{ij}(x, r, t)$ and $\rho_e(x, r, t)$ are directly available from the DNS, and their temporal Fourier coefficients are computed in the same way as $\hat{p}(x, r, \omega_f)$ from equation (5.33) over one period during the simulation. The integrands specified in equations (5.21–5.25) can then be evaluated for any observer angle ϑ, and the spatial integration in equation (5.11) is performed numerically first along r, then along x, using the trapezoidal rule. The directivity factor $D(\vartheta)$ of the acoustic far field obtained from the Lighthill equation is compared to the direct Navier–Stokes solution in figure 5.7. DNS values along arcs of $\xi = 20$ (×) and $\xi = 40$ (•) are combined in this figure.

Agreement between DNS results and those obtained from the Lighthill equation (5.11) is excellent. The pressure level of the Lighthill solution at $\vartheta = 0$ has been used as reference value p_{ref} in the dB-scaling (5.34) for both the simulation and the Lighthill results. The extinction angles $\vartheta = 62°$ and $\vartheta = 126°$ observed in the simulation are retrieved within 1° accuracy

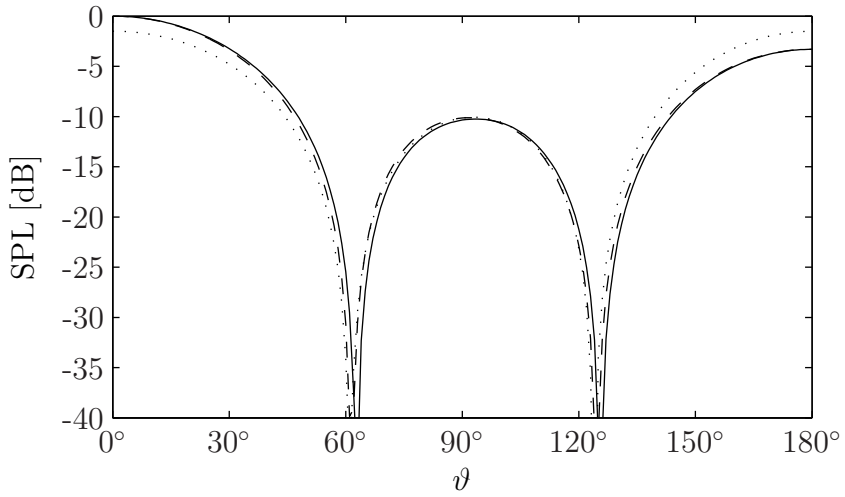

Figure 5.8: Prediction of the far field directivity according to the Lighthill equation: (—) without compactness assumption, (---) sources compact in r, $(\cdots)$ sources compact in r and x.

in the Lighthill solution. In the interior of the lobes, both solutions match within less than 0.5 dB, except very near the upstream boundary of the computational domain.

Figure 5.7 also clearly demonstrates that the sound field computed in the direct numerical simulation is barely affected by the numerical boundary conditions. A slight deformation of the directivity curve is observed along the $\xi = 40$ arc (bullet symbols) at angles $115° < \vartheta < 125°$, i.e. less than five jet radii away from the upstream boundary. The numerical treatment at all computational boundaries is seen to yield highly accurate results for the acoustic field in the interior of the domain.

Compact sources

Assuming that the source distributions are acoustically compact in r, the sound field in the present flow example is computed from the simplified Lighthill solution (5.20). The resulting far field directivity is compared to the solution obtained from the non-compact source terms in figure 5.8: the dashed and solid curves are nearly identical. Acoustic interference from radial source variations has indeed a negligible impact on the far field in the present flow case.

Also shown in figure 5.8 is the directivity pattern obtained under the as-

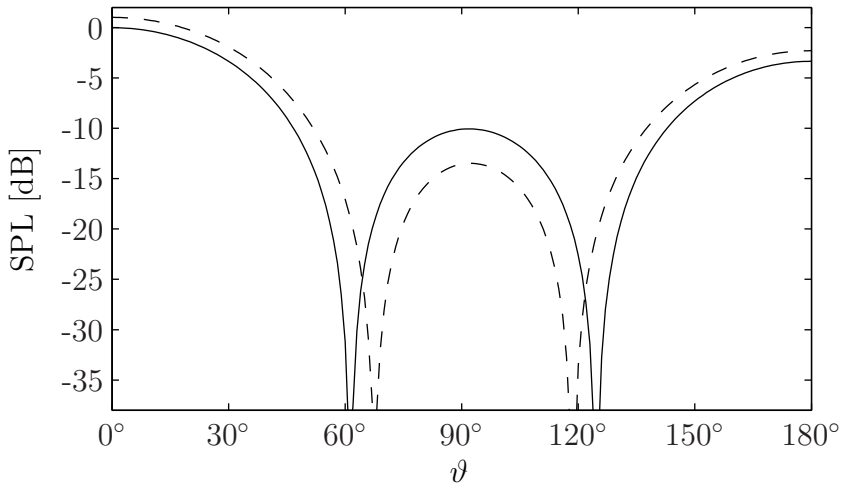

Figure 5.9: Acoustic directivity pattern according to equation (5.20) with (solid) and without (dashed) the entropy-related source term $\hat{\rho}_e^x$.

sumption of fully compact sources (5.20). The lobe structure of the acoustic field is very well predicted from just the superposition of compact multipoles. The upstream and downstream lobes are of equal amplitude in this approximation, but the omitted antenna factor in the present example only causes a 3 dB difference between the $\vartheta = 0°$ and 180° directions.

The entropy-related source term ρ_e is often neglected in calculations of the Lighthill equation for isothermal flows. However, in agreement with the results of Mitchell, Lele & Moin [79], the entropy term is found to be important for an accurate predicition of the acoustic field in the present case. Figure 5.9 compares the solutions of equation (5.20) with and without the influence of ρ_e^x. While the overall lobe pattern is due to the T_{ij}^x terms, the positions of the extinction angles as well as the amplitude of the lobe around $\vartheta = 90°$ are noticably altered by the contribution of entropy sound.

5.3 Acoustic radiation from a globally unstable jet

5.3.1 Acoustic field in the DNS

The typical characteristics of the acoustic field associated with the global mode of a hot jet are investigated for the case studied in section 4.2.5 with

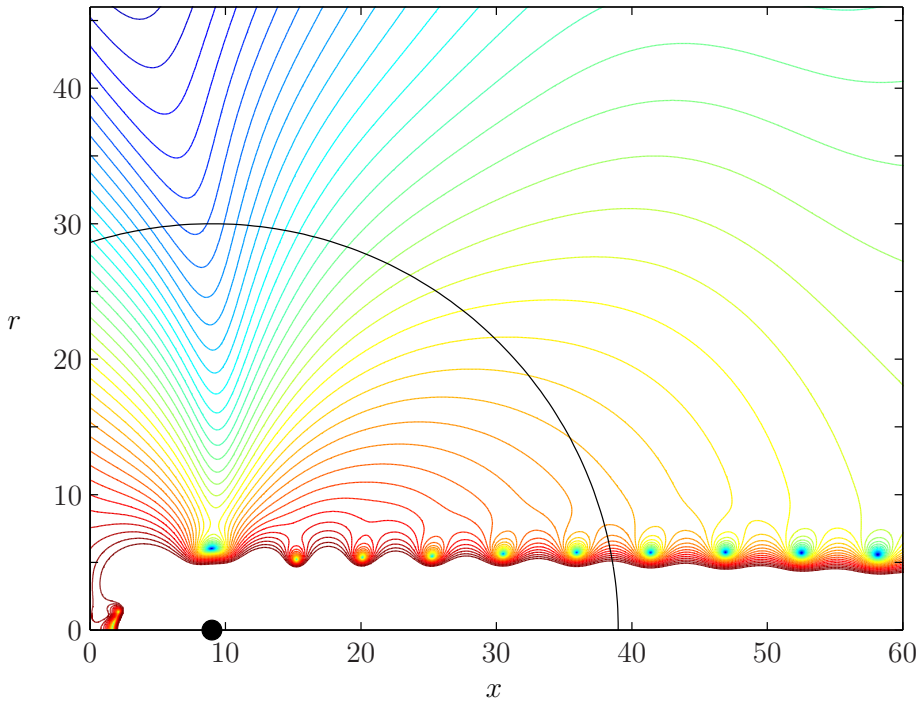

Figure 5.10: Pressure amplitude $|\hat{p}(r, x, \omega_g)|$ in the acoustic far field, exponentially spaced isocontours. Apparent sound source on the jet axis at $x = 9$, arc of radius 30.

parameters $R/\theta = 10$, $S = 0.3$, $M = 0.1$ and $Re = 1000$. No vortex pairing occurs in this flow configuration, the radiated sound therefore is monochromatic, tuned to the synchronization frequency $\omega_g = 0.728$. The acoustic wavelength is then $\lambda_a = 2\pi c_\infty/\omega_g = 47.3$. The physical region of the computational domain was chosen rather large ($0 \le x \le 80$, $0 \le r \le 46$), and the acoustic far field therefore can be expected to be accurately resolved. Isocontours of the acoustic amplitude $|\hat{p}(x, r, \omega_g)|$ are shown in figure 5.10. The acoustic field is composed of two lobes, with an extinction angle at about 90°. The apparent source location is $x = 9$. Values of $|\hat{p}|$ are interpolated along an arc of radius $\xi = 30$ for a quantitative examination. Figure 5.11 reveals that the directivity pattern is that of a dipole.

5.3.2 Acoustic field according to the Lighthill equation

Evaluation of the Lighthill solution (5.11) with all source terms obtained from the DNS, integrated over the whole physical domain without any com-

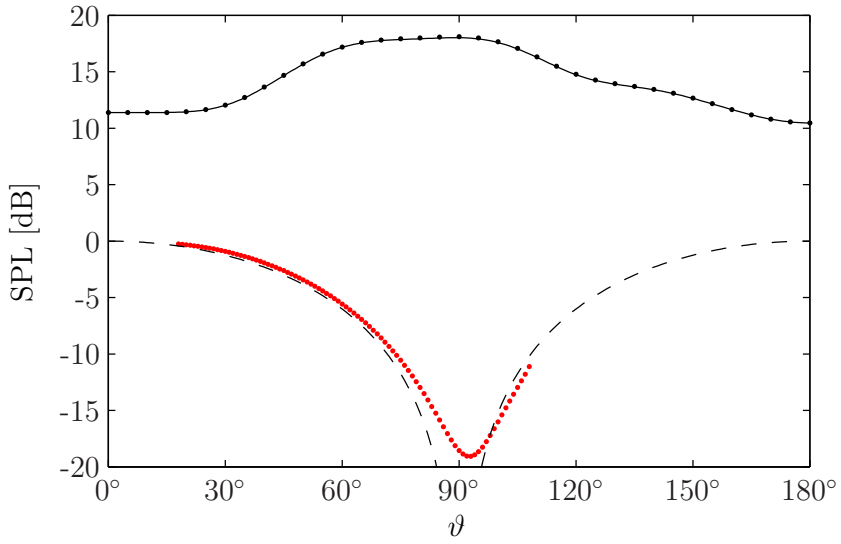

Figure 5.11: Acoustic directivity $D(\vartheta)$ as found from the DNS (•), compared to a dipole $D(\vartheta) \propto \cos\vartheta$ (dashed line). Prediction from the Lighthill equation with (•) and without (—) assumption of radially compact sources.

pactness assumption, yields the directivity pattern displayed in figure 5.11 (solid line). The Lighthill solution at this point fails completely to predict the directly computed acoustic field. Also included in figure 5.11 are the results found under the assumption of radial compactness from equation (5.20). As in the test case described in the previous section, the acoustic sources seem to be well approximated as being compact in the radial direction. For convenience, the further investigation will focus on the radially compact source terms $\hat{T}^x_{ij}$, $\hat{\rho}^x_e$. All viscous terms have been retained, although their effect on the acoustic field is indeed found to be negligible.

The axial variations of the radially compact source distributions are presented in figure 5.12 in terms of their absolute values and phase. The phase is only shown for $\hat{\rho}^x_e$, but the picture is very similar for all other source terms. The amplitude functions in figure 5.12*a* all display a sharp front near $x = 0$, and a slow decay downstream of the vortex roll-up location around $x = 10$. So slow indeed that $|\hat{\rho}^x_e|$ only decreases by a factor of 35 between the position of its maximum and the end of the physical domain. The truncation of the integration interval at $x = 80$ in equation (5.20) therefore is likely to produce significant errors in the spatial Fourier spectrum.

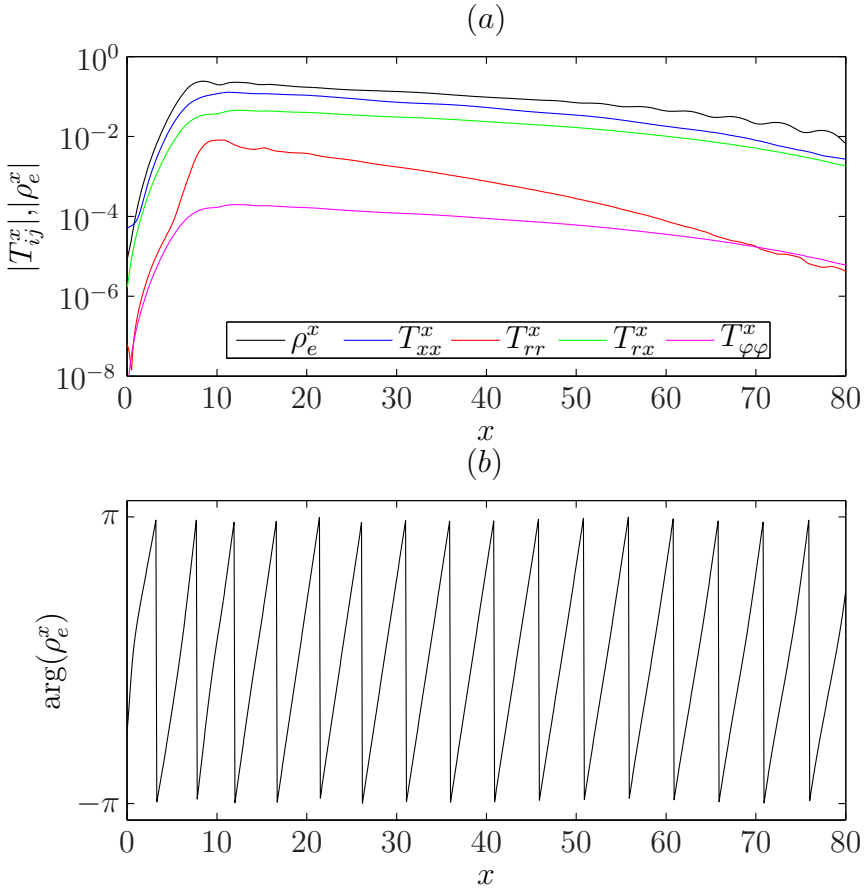

Figure 5.12: (a) Absolute values of $\hat{T}^x_{ij}$, $\hat{\rho}^x_e$ as functions of x; (b) Phase of $\hat{\rho}^x_e$ as function of x.

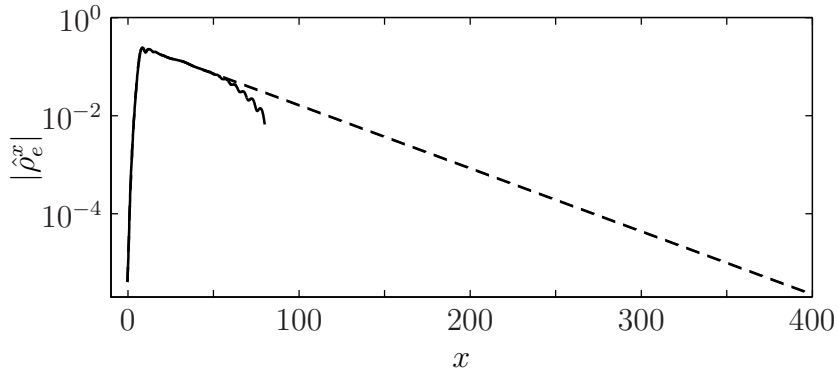

Figure 5.13: Original (solid) and extrapolated (dashed) streamwise variation of $\hat{\rho}^x_e$.

Extrapolated source distributions

Mitchell *et al.*[79, 80] faced the same problem in their computations of the acoustic field of forced isothermal round jets. These authors propose to extrapolate the source term distributions from the end of the computational domain over a sufficiently long downstream region prior to the evaluation of the Lighthill solution. The results obtained from this procedure are in good agreement with the directly computed acoustic fields of Mitchell *et al.*[80]. For the hot jet case investigated here, figure 5.12*a* indicates indeed that the downstream decay of the source term amplitudes is nearly exponential, and that the axial wavenumber is nearly constant. Following the procedure of Mitchell *et al.*[80], the source terms $\hat{T}_{ij}^x$, $\hat{\rho}_e^x$ downstream of $x_0 = 40$ are taken to develop as

$$f(x) = f(x_0)\, e^{ik_x(x-x_0)} \quad \text{with } k_x = -i\frac{f'(x_0)}{f(x_0)} \tag{5.35}$$

down to $x = 400$. The shape of the extrapolated $|\hat{\rho}_e^x|$ distribution is shown in figure 5.13.

The Lighthill prediction obtained from the extrapolated source terms, according to (5.20), is compared to the DNS results in figure 5.14: The solid line represents the total sound emitted by all source terms, the dashed line shows the contribution of the entropy-related term $\hat{\rho}_e^x$ alone. Both curves are nearly identical. The dB scaling takes the Lighthill solution at $\vartheta = 0°$ as reference value for all curves. The amplitude at low angles ϑ is very accurately predicted, and the overall dipole character is satisfactorily recovered. However, the extinction angle in the Lighthill solution is shifted by 15° with respect to the DNS data. In spite of this imperfect match, it seems safe to conclude from figure 5.14 that the entropy source is dominant in this flow configuration, whereas contributions from the Reynolds stresses to the acoustic field are negligible.

Since the entropy-related term in (5.20) appears in the explicit form of a monopole source, the dipole-like radiation observed in the hot jet example under investigation must result from subtle phase cancellation effects due to the spatial modulation of $\hat{\rho}_e^x$. In the formulation (5.20), these effects are contained in the Fourier transform $\tilde{\rho}_e^x(k_a \cos\vartheta, \omega)$. These spectral distributions are examined in figure 5.15. FFT-spectra of the original source distribution, defined over $0 \le x \le 80$, and of the extrapolated source are compared in figures 5.15*a*, *b*: over a range of the dominant wavenumbers, say $1 < k < 4$, both spectra are essentially identical. By contrast, the spectral components in the vicinity of $k = 0$ are strongly affected by the truncation of the domain

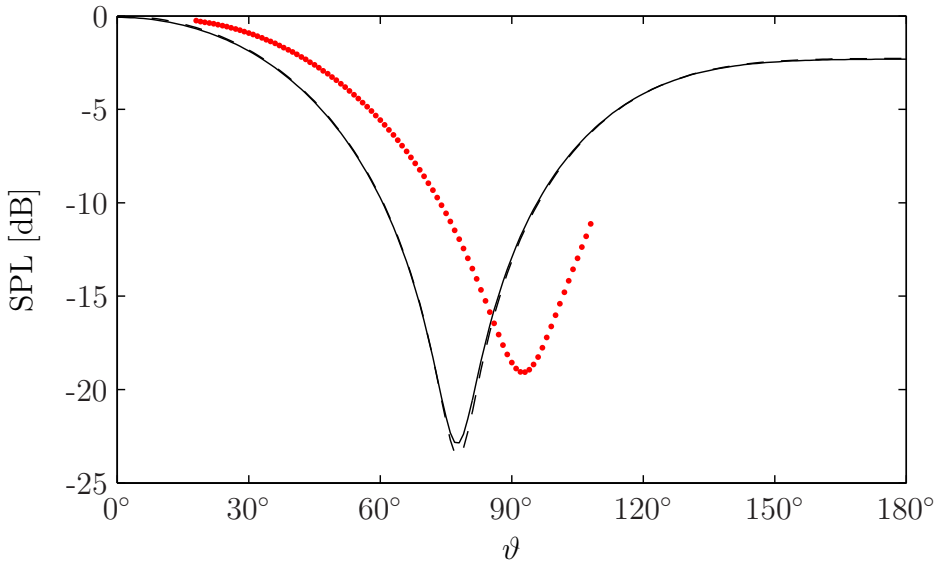

Figure 5.14: Directivity computed from the Lighthill equation (5.20) with extrapolated source terms, compared to DNS data (●). Solid line: total acoustic field from all source terms, dashed line: acoustic field of the entropy term alone.

at $x = 80$, visible in figure 5.15*c*. The dashed line shows the spectrum of the truncated source distribution, the solid line is obtained from the extrapolated source. The acoustically relevant portion of the Fourier transform, $-k_a \leq k \leq k_a$ with $k_a = 0.132$, is indicated by dotted lines. Comparison of this small interval of low spectral density to the full spectrum gives an idea of the precision that is required if a reliable prediction of the acoustic field is sought based on the spatial source term distribution. In particular, the sensitivity of the position of the dip in the solid line near $k = 0$, which determines the extinction angle in the Lighthill solution, does not seem surprising. Figure 5.15*d* shows the real (solid) and imaginary (dashed) part of $\tilde{\rho}_e^x(k, \omega)$, obtained from the extrapolated source. If both were zero at $k = 0$, the predicted extinction angle would be found at $\vartheta = 90°$, in agreement with the DNS results.

It is clear from the discussion of figure 5.15 that the axial non-compactness of the entropy-related acoustic source is essential when a dipole field is caused by a nominally monopole-type source. The data available from the present simulations is sufficiently accurate to allow for such an analysis. Yet, for a precise prediction of the extinction angles, similar to the test case of section 5.2, it is necessary to use source terms in the Lighthill formulation that are

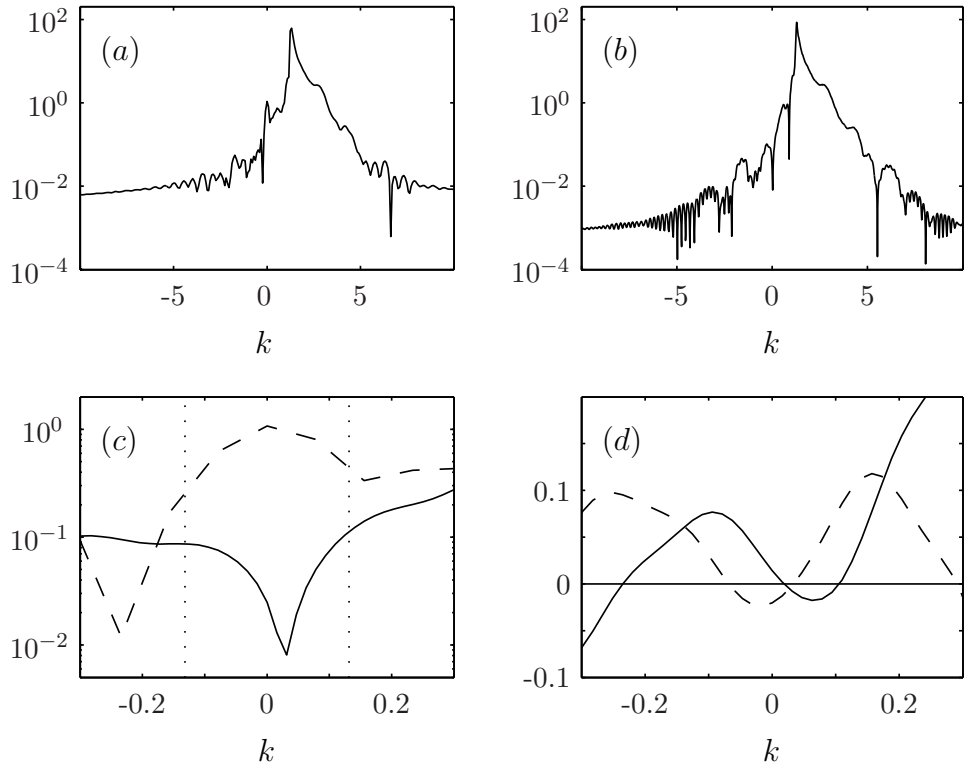

Figure 5.15: Fourier transform $\tilde{\rho}_e^x(k, \omega_g)$. (a) FFT spectrum $|\tilde{\rho}_e^x(k, \omega_g)|$ of the original source distribution; (b) FFT spectrum $|\tilde{\rho}_e^x(k, \omega_g)|$ of the extrapolated source distribution; (c) Zoom of the spectra in (a, b) around $k = 0$, solid: extrapolated source, dashed: original source, dotted: $\pm k_a$; (d) Real (solid) and imaginary (dashed) parts of $\tilde{\rho}_e^x(k, \omega_g)$ computed from the extrapolated source.

explicitly of the appropriate multipole type. The following section attempts to identify explicit acoustic dipole sources due to entropy effects.

5.3.3 Decomposition of the entropy-related source term

According to Dowling [37], the entropy-related source term in dimensional quantities can be decomposed in the following way:

$$\begin{aligned}\frac{\partial^2 \rho_e}{\partial t^2} &= \frac{\partial}{\partial t}\frac{\rho_\infty}{c_p \rho T}\left(\kappa \Delta T' - \frac{\partial u_i}{\partial x_j}\tau_{ij}\right) \\ &\quad -\frac{1}{c_\infty^2}\frac{\partial}{\partial t}\left[\left(1-\frac{\rho_\infty c_\infty^2}{\rho c^2}\right)\frac{Dp}{Dt} - \frac{p'}{\rho}\frac{D\rho}{Dt}\right] - \frac{\partial^2 (u_i \rho_e)}{\partial t\, \partial x_i}\,,\end{aligned} \tag{5.36}$$

where all unprimed symbols represent total flow variables. Only the last term is explicitly of a dipole type. It describes the effect of momentum changes of density inhomogenities, which may indeed be expected to be appreciable in an oscillating hot jet. For shorter writing, let

$$m_x = (u_{xb} + u_x')\rho_e\,, \quad m_r = (u_{rb} + u_r')\rho_e. \tag{5.37}$$

In a similar way as in (5.11), the contribution $\hat{p}_{e,di}$ of this term to the acoustic far field is expressed as

$$\begin{aligned}\hat{p}_{e,di}(\xi,\theta,\omega) &= \frac{\omega^2}{2c_\infty}\frac{e^{ik_a\xi}}{\xi}\iint \Big[J_0(\alpha)\,\cos\vartheta\,\hat{m}_x(x,r,\omega) \\ &\quad + i\,J_1(\alpha)\,\sin\vartheta\,\hat{m}_r(x,r,\omega)\Big]\,e^{-ik_a x\cos\vartheta}\,r\,\mathrm{d}r\,\mathrm{d}x.\end{aligned} \tag{5.38}$$

Under the assumption of radial compactness, the explicit dipole component of the entropy sound can be computed as

$$\hat{p}_{e,di}(\xi,\theta,\omega) = \frac{\omega^2}{2c_\infty}\frac{e^{ik_a\xi}}{\xi}\,I^x_{e,di}\,, \tag{5.39}$$

with

$$I^x_{e,di} = J_0(\alpha)\,\cos\vartheta\,\tilde{m}^x_x(k_a\cos\vartheta,\omega) + iJ_1(\alpha)\,\sin\vartheta\,\tilde{m}^x_r(k_a\cos\vartheta,\omega)\,, \tag{5.40}$$

$$\tilde{m}^x_{[x,r]}(k,\omega) = \iint \hat{m}_{[x,r]}(r,x,\omega)\,e^{-ikx}\,r\,\mathrm{d}r\,\mathrm{d}x. \tag{5.41}$$

The acoustic field $\hat{p}_{e,di}$ computed from equation (5.39) with the physical region $0 \le x \le 80$ as integration interval is compared to the directly computed solution in figure 5.16 (blue line). The extinction angle is very well

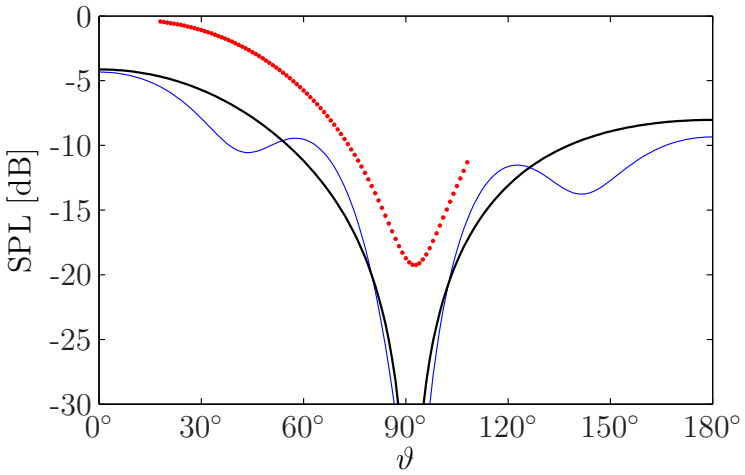

Figure 5.16: Acoustic directivity of entropy dipole sources $\hat{m}_r^x$, $\hat{m}_x^x$ compared to the DNS results (•): Direct evaluation of equation (5.39) (— blue); Evaluation of $\tilde{m}_x^x$, $\tilde{m}_r^x$ from interpolation of the FFT spectrum (— black), as displayed in figure 5.17*b*.

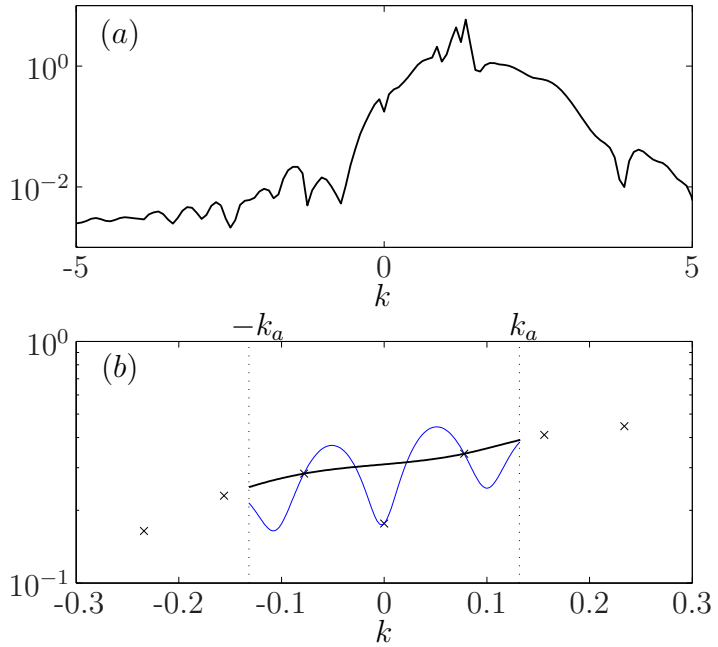

Figure 5.17: Fourier transform of $\hat{m}_r^x$. (*a*) FFT spectrum; (*b*) spectrum around $k = 0$: points from FFT (×); numerical Fourier integration as in equation (5.41) (— blue); interpolation of the FFT spectrum (— black), excluding $k = 0$.

retrieved, but the amplitude level at small angles is underpredicted by 4dB, which corresponds to a factor 1.6 in the pressure amplitude. The truncation of the integration domain at $x = 80$ causes an undulation of the predicted directivity curve. As before, the source terms could be extrapolated in x. Depending on the parameters used in the extrapolation, this procedure can yield some improvement (not shown). However, a cleaner method can be employed here.

Means to improve the Lighthill solution should first be sought from an examination of the spectral distributions $\tilde{m}_x^x$, $\tilde{m}_r^x$. The $\tilde{m}_x^x(k)$ variation as obtained from an FFT algorithm is displayed in figure 5.17*a*. As a result of the long acoustic wavelength, the relevant interval $-k_{ac} \leq k \leq k_{ac}$, magnified in figure 5.17*b*, is resolved by only three points, and the value at $k = 0$ is clearly affected by the domain truncation. Direct evaluation of the Fourier integral (5.41) therefore yields a strongly oscillating solution (blue line).Given the available data, the most accurate way to proceed seems to consist in an interpolation of $\tilde{m}_x^x(k)$ over $-k_{ac} \leq k \leq k_{ac}$, excluding the value at $k = 0$ which is contaminated by domain truncation. A spline interpolation curve for $\ln(\tilde{m}_x^x)$ seems to follow well the global trend of the spectral distribution (black line).

The acoustic directivity computed according to (5.39) from these interpolated values is presented in figure 5.16 as a black line. The relative dipole directivity pattern is very well retrieved, and the extinction angle is predicted within about 2° accuracy. However, the absolute sound pressure level is still underpredicted by 4dB. The $\tilde{m}_x^x$-related cosine dipole is clearly dominant over the sine dipole. Yet it seems that the relevant entropy-related dipole sound sources in this flow are not given by the $\tilde{m}$ terms alone.

5.4 Conclusion

Based on the studies of Huerre & Crighton [52] and Fleury [39], the far-field solution of the Lighthill equation in an axisymmetric geometry has been formulated for non-compact, radially compact and fully compact source distributions. In full agreement with the discussion of Huerre & Crighton [52], axial non-compactness of the Lighthill sources has been found to result in an antenna factor that modulates the quadrupole radiation pattern of Reynolds stress-related sources and the monopole pattern of entropy-related sources. Under the assumption of radially compact sources, this antenna factor is given explicitly by the spatio-temporal Fourier transform of the axial source

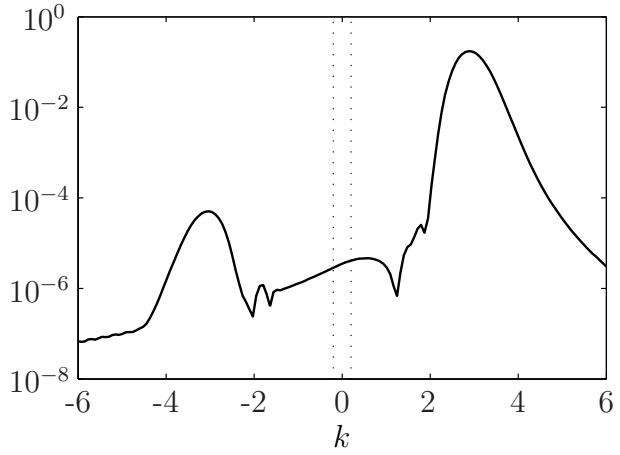

Figure 5.18: Fourier transform $|\tilde{T}^x_{xx}(k)|$ of the source distribution from the test case of section 5.2. Dotted lines: $\pm k_a$.

distributions, according to equation (5.20).

Investigations of a forced isothermal jet have demonstrated that the chosen formulation of the Lighthill solution yields highly accurate predictions of the acoustic far field, as compared to direct numerical simulations, in a case where the near field wave packet is given over its entire streamwise extent. In the present example, the extinction angles in the acoustic field according to DNS and Lighthill solutions match within 1°, and the maximum amplitudes of the individual acoustic lobes agree within 0.5 dB accuracy. Although the baseflow is isothermal, entropy-related acoustic radiation is found to noticeably influence the position of the extinction angles. These results demonstrate the high quality of the DNS results in the acoustic field, and at the same time they confirm the validity of the Lighthill far field solution.

According to the predictions of Huerre & Crighton [52], the test case of section 5.2 should display a *superdirective* acoustic field, *i.e.* an antenna factor of the form

$$\tilde{T}^x_{ij}(k_a \cos\vartheta) = e^{-A(1-\mathrm{Ma}\,\cos\vartheta)^2}, \tag{5.42}$$

where A can be estimated as being of the order of 10 for the present configuration. The observed antenna factor only yields a 3 dB difference between $\vartheta = 0°$ and 180°, significantly less than expected from (5.42): 3 dB approximately corresponds to $A = 0.86$. The prediction in the theoretical model has been derived for an ideal, perfectly Gauß-shaped source term envelope in an infinite jet. In this case, its Fourier transform $\tilde{T}^x_{ij}(k)$ is also of Gaussian shape. While the numerical test case presented in section 5.2 has been designed to mimic these conditions as closely as possible, figure 5.18 clearly

shows that the acoustically relevant interval $-0.2 \leq k \leq 0.2$ of the Fourier transform $\tilde{T}^x_{xx}(k)$ is dominated by non-Gaussian portions of the spatial envelope. Indeed, from the slope of the quasi-Gaussian peaks around $k = \pm 3$ in figure 5.18 it can be estimated that their spectral in the vicinity of $k = 0$ could not even be resolved with 64-bit precision. The sound pressure level emitted from the quasi-Gaussian part of the source envelope is unobservably low in this example.

Nonetheless, the validation study of section 5.2 has demonstrated that the proposed Lighthill formulation may be used as an efficient tool for the analysis of acoustic radiation from instability structures in axisymmetric jets. With the insight gained from the test calculation, strategies for further investigation of superdirective sound radiation can be proposed: In order to observe the superdirective component of the acoustic field in direct numerical simulations, one will probably have to resort to Mach numbers in the transsonic or supersonic régime, such that k_a is comparable to the wavenumber of the instability carrier wave. A very narrow envelope width of the instability wave packet in physical space results in a wider Gauß distribution in Fourier space. Superdirective decline of the acoustic amplitude with the observation angle ϑ in this case will be slower, but observable over a larger range of ϑ. Finally, the physical envelope shape of the Lighthill source terms must be of Gaussian form over a large streamwise interval in both directions from the maximum amplitude location. With the approach of section 5.2, *i.e.* low-level forcing at the inlet of an unstable baseflow, the generation of such a wave packet in a numerical simulation is restricted by considerable numerical difficulties. Such a scenario may first be investigated in calculations where ideal near field oscillations are prescribed directly at all streamwise stations.

The acoustic field radiated by a global mode in a hot jet has been investigated in section 5.3 for a thick shear layer configuration, with an inlet profile parameter $R/\theta = 10$ and heating ratio $S = 0.3$. No vortex pairing arises in this example, the spatial global mode structure therefore is not altered by secondary instabilities. The direct numerical simulation displays the acoustic field of a pure dipole, with maximum amplitude along the jet axis. Due to the slow streamwise amplitude decay of the acoustic source terms, the Lighthill solution for the acoustic far field has been found to be strongly contaminated by the truncation of the computational domain at $x = 80$. Good results have been recovered once the source distributions were extrapolated over a large streamwise interval down to $x = 400$, under the assumption of their radial compactness: At observation angles $\vartheta < 30°$, the acoustic far field amplitudes obtained from the numerical simulation and from the Lighthill prediction agree within 1 dB, and the dipole pattern observed in

the simulation is well retrieved. However, the extinction angle is predicted at $\vartheta = 77°$, as opposed to $\vartheta = 92°$ in the direct simulation.

The global mode acoustic field is strongly dominated by radiation due to the *entropy-related* source term. In the Lighthill solution (5.20), this term appears as a monopole source. The observed dipole pattern results from amplitude modulations via the antenna factor, and the prediction of the extinction angle position therefore is highly sensitive to subtle details of the spatial envelope shape. An explicit dipole-type entropy source component has been extracted via a decomposition of the full entropy source term given by Dowling [37]. The predicted acoustic field due to this isolated component accurately reproduces the relative directivity pattern of the direct solution, but the absolute amplitude is underpredicted by 4 dB. It is concluded that other components of the entropy source term must also contribute to the total acoustic dipole field. According to Dowling [37], although only the source component investigated in section 5.3.3 explicitly displays a dipole directivity in its general analytical form, dipole-type radiation may indeed be caused by various entropy source components in physical situations.

In the global mode case, Lighthill predictions of the acoustic field suffered from errors due to the finite size of the computational domain. Two procedures have been successfully applied to manipulate the source term distribution either in physical space or in Fourier space. For an *a posteriori* analysis of the directly computed acoustic field, the proposed Lighthill formalism has provided valuable insights on the dominant sound generation mechanisms. By contrast, for the purpose of reliable *a priori* predictions, the presented spectral formulation requires a detailed knowledge of the source term distributions throughout a domain that includes the entire amplitude envelope down to very low values. In addition, the correct prediction of extinction angles depends crucially on the appropriate formulation of the source terms. An interesting topic for future investigations would be how these restrictions of a *spectral* representation of the Lighthill solution translate to the *physical* sound generation mechanisms. In other words, to what extent does the spatial structure of the very low-amplitude wings of an instability wave packet influence the acoustic directivity in a physical setting? In particular, the answer to this question may lead to a criterion for the observability of superdirective sound radiation in numerical and experimental configurations.

Chapter 6

Épilogue

6.1 Conclusions

The main objective of this dissertation has been to establish whether intrinsic synchronized oscillations in hot jets may be described as nonlinear global modes, according to the theoretical framework recently developed in the context of Ginzburg–Landau model equations. The main conclusion to be drawn from the results presented herein is affirmative: nonlinear global mode theory has indeed proven to successfully predict the features of these oscillations.

Linear local instability. Theory predicts that the *nonlinear global* flow dynamics are determined by *linear local* mechanisms. A numerical method for the linear instability analysis of parallel baseflows has been implemented. Parametric studies have elucidated the competition of *jet column* and *shear layer* modes in the linear impulse response of axisymmetric jets. The dominant absolute mode of zero group velocity is always of the jet column type and axisymmetric; its temporal growth rate is positive if the jet is sufficiently hot with respect to the ambient medium. However, in jet profiles typical of the potential core, the most unstable convected shear layer modes display much larger temporal growth rates than the jet-column-type absolute mode.

The transition from convective to absolute instability in hot jets has been demonstrated to arise from the action of the baroclinic torque. In its absence, heating has no effect on the instability of a jet. Inspection of the absolute mode eigenfunction has yielded a physical argument for the destabilizing effect of the baroclinic torque.

Nonlinear global instability. Global jet dynamics have been investigated via direct numerical simulation. A suitable numerical method for this purpose has been conceived, relying on highly accurate discretization schemes and boundary conditions. Simulations of strongly heated jets display self-sustained oscillations, in qualitative agreement with the experiments of Monkewitz *et al.* [82] and Sreenivasan *et al.* [105].

Numerical results have been quantitatively compared with predictions drawn from nonlinear global mode theory . A first study was performed for an idealized infinite baseflow featuring a finite pocket of absolute instability. The emerging oscillatory state displayed all the features of a global mode according to the model of Pier *et al.* [96, 94]. The investigations of realistic hot jet baseflows in a semi-infinite domain have then been compared to the theory of Couairon & Chomaz [26, 27]: as predicted, global instability has been observed to set in at heating ratios slightly below the onset of absolute instability. A finite minimum length of the absolutely unstable region is necessary to sustain synchronized oscillations. At different values of the inlet shear layer thickness, the global frequency near onset has been found to correspond to the absolute frequency at the inlet.

The simulations have shown that the global frequency shifts to values above ω_0 as the heating exceeds the global threshold value. This trend is increasingly strong in thin shear layer jets. The measurements of Monkewitz *et al.* [82] (see figure 4.17) appear to display the same behavior. Although this result is not in contradiction with the theory, which only provides a leading-order frequency prediction near threshold, it contrasts with the behavior of wakes: the simulations of Chomaz [18] display perfect agreement between global and absolute frequency in parallel wakes even for highly supercritical parameter settings. A parallel jet example given in section 3.5.4 indicates that non-parallelism in the present simulations is not alone responsible for this difference, but that the numerical boundary conditions have an appreciable impact on the frequency selection.

Sound radiation. A method has been presented to obtain predictions of the far field sound from Lighthill's acoustic analogy, based on the knowledge of the near field oscillations from the DNS. These predictions allow for a detailed analysis of the contribution of individual source terms to the total radiated sound.

Excellent agreement between Lighthill predictions and directly computed sound has been demonstrated in test calculations for a forced isothermal jet. The acoustic field in this case is dominated by quadrupole source terms

related to Reynolds stresses. Yet, similar to the findings of Mitchell *et al.* [79], entropy-related sound noticeably influences the position of the extinction angles. The nearly Gaussian wave packet in this example had been *a priori* expected to emit a *superdirective* acoustic field. An analysis of the Fourier transform of the spatial source distribution revealed that the observation of superdirective sound fields in numerical simulations at low Mach numbers is extremely delicate, as it requires almost perfectly Gaussian tails of the wave envelope.

The acoustic field of nonlinear global modes in hot jets has been determined to be that of a dipole. Its radiation is due to *entropy-related* source terms, whereas Reynolds stress sources are negligible. An extrapolation of the source distribution far beyond the exit boundary of the DNS domain had to be performed in order to reproduce the directly computed far field directivity from the Lighthill analogy. Since the nonlinear global mode envelope is far from being a simple Gaussian wave, superdirectivity of the sound field has not been observed.

The analysis of the global mode acoustic field has once more confirmed that the Lighthill analogy represents a very useful tool for analytical purposes, if the nature of the sound field is known *a priori*. For a reliable *prediction* of the sound field, the near field wave packet must be resolved over its entire streamwise extent, including the very low-amplitude regions. This requirement appears to be a weakness of the formulation of the Lighthill solution in Fourier space. The directly computed acoustic field of the global mode is unaffected by the downstream truncation of the computational domain, the acoustically active region in physical space is apparently localized around the station of vortex roll-up.

6.2 Suggestions for future work

The insights gained from the investigation of axisymmetric global instability in hot jets immediately lead on to the question: how do the intrinsic dynamics persist in a three-dimensional setting? For instance, the experiments of Monkewitz *et al.* [82] have indicated that synchronized oscillations may be accompanied by the formation of spectacular *side jets*, later interpreted by Brancher *et al.* [12] as the result of a three-dimensional secondary instability of the axisymmetric vortex street. Helical secondary instabilities of rolled-up vortex rings in hot jet simulations have been reported by Nichols [86]. Also, vortex pairing as an axisymmetric secondary instability of the nonlinear wave

train has been observed in the present simulations, as well as in the reference experiments, but a theoretical analysis remains to be conducted.

Vortex streets in bluff body wakes may be observed in any bathtub, whereas global modes in hot jets so far appear as a *rara avis in terris*, only studied under highly controlled conditions. Whether this phenomenon is of practical importance, especially in the context of jet engine exhaust, remains to be determined by investigating larger parameter ranges, including unfavorable conditions like high Mach numbers, turbulent régimes and co-flow.

Numerical results have exposed the sensitivity of global jet dynamics to the inlet boundary conditions, discussed in sections 3.5.4 and 4.3.4. In order to predict the global frequency in a jet of practical interest on the basis of global mode theory, the quantitative influence of nozzle effects will have to be included into the theoretical model. Such an extension of the theory would probably have to start again from studies of the Ginzburg–Landau equation, which could be coupled with a wave equation in order to account for sound radiation.

The aeroacoustic results of chapter 5 have demonstrated the capacity of the proposed Lighthill formulation for further jet noise analysis. In particular, the method may prove useful in the investigation of *superdirective* sound radiation, both in the subsonic and supersonic régimes. A strategy for such an investigation has been outlined in section 5.4. Finally, the study of global mode sound presented herein has been restricted to a case without vortex pairing, but the analysis can be extended with relative ease to situations where vortex pairing occurs.

Appendix

Global modes in hot jets, absolute/convective instabilities and acoustic feedback

Lutz Lesshafft, Patrick Huerre, Pierre Sagaut & Marc Terracol

presented as *AIAA Paper 2005-3040*
at the 11th AIAA/CEAS Aeroacoustics Conference
23 - 25 May 2005, Monterey, California

Abstract

The occurrence of self–sustained synchronized oscillations in a family of hot axisymmetric jets is investigated in direct numerical simulations. With parameter settings close to those used in the experiments of Monkewitz, Bechert, Barsikow & Lehmann [82], such synchronized states are found numerically to arise when the ambient–to–jet temperature ratio S falls below a critical value. At a Reynolds number $Re = 3750$, based on the jet radius, global oscillations of Strouhal number $St \approx 0.45$ occur for $S \leq 0.6$, which corresponds well to the 'mode II' state of Monkewitz *et al.*[82]. The distinct 'mode I' oscillations of $St \approx 0.3$ reported in the experiments [82] are assumed to correspond to the subharmonic of a synchronized state that is numerically observed only to arise at a higher Reynolds number $Re = 7500$. Both modes are compared to theoretical predictions pertaining to nonlinear global modes which may exist due to the presence of absolute instability, as well as to the subharmonic acoustic resonance model of Laufer & Monkewitz [64]. It is found that the synchronization of the 'mode I' state sets in at temperature ratios for which the entire flow is convectively unstable. A nonlinear global mode therefore cannot exist in these cases. The onset of the 'mode II' state occurs in the presence of an absolutely unstable flow region of finite streamwise extent; however, even near the global instability threshold, the 'mode II' frequency does not match the absolute frequency at the inlet, as should be expected from global mode theory. The subharmonic acoustic resonance model [64], which assumes a feedback loop between the inlet and the station of vortex pairing, is found not to apply in any of the observed cases of self–sustained synchronized oscillations.

A.1 Introduction

The spontaneous formation of regular large–scale vortical structures in the absence of external forcing is a commonly observed phenomenon in jet flows over wide ranges of Reynolds and Mach numbers. In particular, the experiments of Sreenivasan, Raghu & Kyle [105] and Monkewitz *et al.*[82] have firmly established that self–excitation leads to perfectly synchronized oscillations in low-density jets if the jet–to–ambient density ratio falls below a critical value. Studies of the underlying mechanisms that are responsible for such behavior in hot jets are largely motivated by aeroacoustic problems related to jet engine exhaust. Specifically, synchronized vortex structures have been observed to give rise to a superdirective acoustic radiation pattern (Laufer & Yen [65], Freund [42]).

In the hot air jet experiments of Monkewitz *et al.*[82], the threshold value of the ambient–to–jet temperature ratio S for the appearance of self–sustained synchronized oscillations was found to coincide with the value at which local absolute instability first occurs (Monkewitz & Sohn [85]). This result strongly supports the idea that the observed oscillations are the manifestation of a *global mode* of the base flow, the existence of which is due to a region of absolute instability. Vorticity perturbations within this region can, by definition, grow faster in time than they are advected, thereby extracting energy from the base flow without being forced externally. According to global mode theory (see the review of Chomaz [19]), a nonlinear front may be sustained within the absolutely unstable region, which then generates instability waves into the downstream convectively unstable flow. The von Kármán vortex street in the cylinder wake is the paradigm for such a nonlinear global mode (Pier & Huerre [94]). Just recently, the authors have demonstrated in a numerical investigation of hot jets at $Re = 1000$, based on the jet radius, and with moderately steep velocity profiles, that the observed self–sustained oscillations in such jets display all the characteristics of a nonlinear global mode due to local absolute instability (Lesshafft, Huerre, Sagaut & Terracol [69]).

Another possibility for the occurrence of self–sustained synchronized oscillations may arise from the presence of a feedback loop consisting of downstream traveling vortical instability waves and upstream traveling acoustic waves that are suitably synchronized. These acoustic waves may be generated at a downstream obstacle, as in the case of cavities or impinging jets, or they can be induced by dynamical events within the jet, such as vortex roll–up and pairing. Laufer & Monkewitz [64] first proposed a feedback

model for acoustically driven self–excitation in jets, which assumes that the upstream propagating acoustic branch originates from vortex pairing events taking place at fixed streamwise stations. The frequency selection criterion deduced from this model has been shown to be in good agreement with the experimental data of Kibens [58]. In an early numerical simulation of a low-density jet, Grinstein, Oran & Boris[47] also found that the position of vortex pairings obeys the acoustic resonance criterion of Laufer & Monkewitz [64].

In the light of recent advances in the theoretical description of fully nonlinear global modes (Chomaz [19]), one of the goals of the present investigation is to determine if one of the two competing interpretations for the occurrence of self–excitation in jets can be proven to be consistent with the results of direct numerical simulations. The test case under consideration is chosen to correspond to the parameter settings of the Monkewitz *et al.*[82] experiments. At a Reynolds number of $Re_D = 7500$ based on jet diameter, two axisymmetric modes have been experimentally observed to exist over different ranges of the ambient–to–jet temperature ratio S: The first ('mode I' in Monkewitz *et al.*[82]), with a Strouhal number $St \approx 0.3$, is seen to be dominant in the range $0.62 < S < 0.73$. The second ('mode II'), with $St \approx 0.45$, is observed throughout the highly supercritical régime $0.47 \leq S < 0.63$ that has been investigated. Despite the striking agreement of the threshold value $S = 0.73$ for the onset of first global instability with the value $S_{ca} = 0.72$ at which local absolute instability first occurs in the inviscid, incompressible limit (Monkewitz & Sohn [85]), several open questions remain to be elucidated: First, a theoretical interpretation for the co-existence of two distinct global modes is not obvious. Second, in order to ascertain the character of the observed oscillations, their frequencies need to be compared to the respective theoretical frequency selection criteria pertaining to global modes and acoustic feedback modes. These two questions are addressed in the present study.

A.2 Governing equations and numerical method

According to experimental observations [105, 82], self-sustained oscillations in round jets appear in the form of axisymmetric ring vortices. The present numerical simulation is therefore restricted to an axisymmetric geometry, and the compressible, viscous conservation equations of mass, momentum and energy are cast in two-dimensional (r, x) coordinates. These equations are formulated in conservative flow variables $\vec{q} = (\rho, \rho u, \rho v, \rho E)$, where ρ denotes density, u and v are the axial and radial components of the flow velocity $\vec{u}$, and E is the total energy. The total flow variables are written as

a superposition $\vec{q} = \vec{q_b} + \vec{q'}$ of a steady base flow $\vec{q_b}(r,x)$ and perturbation components $\vec{q'}(r,x,t)$. The equations that govern the evolution of $\vec{q'}$ are obtained by subtracting the conservation equations written in terms of $\vec{q_b}$ from the same equations written out in terms of total variables. The perturbation equations are then readily found to be

$$\frac{\partial \rho'}{\partial t} = -\text{div}\,(\rho\vec{u})' \tag{A.1}$$

$$\frac{\partial}{\partial t}(\rho\vec{u})' = -\text{div}\,[\rho_b\vec{u}_b \otimes \vec{u}' + (\rho\vec{u})' \otimes \vec{u}_b + (\rho\vec{u})' \otimes \vec{u}'] - \text{grad}\; p' + \text{div}\;\underline{\underline{\tau}}(\vec{u}') \tag{A.2}$$

$$\frac{\partial}{\partial t}(\rho E)' = \text{div}\Big\{ -[(\rho E)' + p']\,\vec{u}_b - [\rho_b E_b + p_b]\,\vec{u}' - [(\rho E)' + p']\,\vec{u}' + \underline{\underline{\tau}}(\vec{u}_b)\cdot\vec{u}' + \underline{\underline{\tau}}(\vec{u}')\cdot\vec{u}_b + \underline{\underline{\tau}}(\vec{u}')\cdot\vec{u}' + \frac{1}{RePr}\frac{\text{grad}\; T'}{(\gamma-1)M^2}\Big\} \tag{A.3}$$

with

$$\underline{\underline{\tau}}(\vec{u}) = -\frac{2}{3Re}(\text{div}\;\vec{u})\underline{\underline{I}} + \frac{1}{Re}\left(\text{grad}\;\vec{u} + \text{grad}^T\vec{u}\right) \tag{A.4}$$

being the viscous stress tensor for a Newtonian fluid, and p, T denoting pressure and temperature. All quantities have been made nondimensional with respect to the jet radius R, the jet exit velocity U_c, density ρ_c and temperature T_c. The viscosity μ and the thermal conductivity κ are assumed to be constant throughout the flow. The flow parameters defined in terms of dimensional quantities are: the Reynolds, Mach and Prandtl numbers $Re = \rho_c U_c R/\mu$, $M = U_c/c_c$ (with c_c the speed of sound on the centerline), $Pr = \mu c_p/\kappa$ (with c_p the specific heat at constant pressure), the ratio of ambient–to–jet temperature $S = T_\infty/T_c$, and the ratio of specific heats $\gamma = c_p/c_v$. Values of $M = 0.1$, $Pr = 1$ and $\gamma = 1.4$ are used throughout the present study.

We consider base flows that slowly develop in the streamwise direction, and which are therefore sought as solutions of the compressible boundary layer equations

$$\frac{\partial \rho_b u_b}{\partial x} + \frac{1}{r}\frac{\partial}{\partial r}(r\rho_b v_b) = 0 \tag{A.5}$$

$$\rho_b u_b \frac{\partial u_b}{\partial x} + \rho_b v_b \frac{\partial u_b}{\partial r} = -\frac{1}{Re}\frac{\partial}{\partial r}\left(r\frac{\partial u_b}{\partial r}\right) \tag{A.6}$$

$$T_b = S + (1-S)u_b + \frac{\gamma-1}{2}M^2 u_b(1-u_b) \tag{A.7}$$

$$\rho_b = T_b^{-1}\ . \tag{A.8}$$

Note that for $Pr = 1$ and zero pressure gradient the temperature is given explicitly by the Crocco–Busemann relation (A.7). This set of equations is

integrated numerically using an algorithm adapted from Lu & Lele [74]. As the system is parabolic, radial profiles can be obtained stepping forward in x. An analytic hyperbolic tangent profile, taken from Michalke [78] (his profile 2), is prescribed as boundary condition for u_b at $x = 0$.

For the perturbation equations (A.1–A.3), spatial derivatives in r and x are discretized by a classical sixth–order–accurate explicit centered finite difference scheme, which uses a six–point stencil. The solution is advanced in time using a third–order Runge–Kutta algorithm. As centered finite differences are known to give rise to spurious oscillations of under–resolved wavelength, a selective tenth–order explicit filter scheme is applied in both spatial directions at each time step (Visbal & Gaitonde [113]). This technique, which consists of recalculating the flow variables as a weighted average of the non-filtered solution on an eleven–point stencil, dissipates all oscillations on the scale of the grid spacing, while it leaves well–resolved wavelengths unaffected. The numerical schemes have been extensively tested in aerodynamic and aeroacoustic computations by Terracol, Manoha, Herrero, Labourasse, Redonnet & Sagaut [108]. A validation case for the implementation used in the present study is given in Lesshafft, Huerre, Sagaut & Terracol [69].

The simulations presented in this paper have been performed on an orthogonal grid composed of 355×706 points in the radial and axial directions, respectively. The computational domain consists of a 'physical region', spanning over $0 \leq x \leq 30$ and $0 < r \leq 30$, where the perturbation equations are solved in the form (A.1–A.3). Great care was taken to prevent reflection of acoustic waves at the boundaries, as these are known to potentially give rise to non-physical self-excited states (Buell & Huerre [16]). Tests on larger meshes have confirmed that the self–excited states that are documented below are not due to such numerical box resonances. At the lateral and outflow boundaries of the physical domain, 'sponge regions' are added, in which all perturbations are gradually attenuated before they reach the actual boundaries of the computational box. Inside these sponge regions, strong artificial dissipation is achieved by adding a damping term $-\lambda\vec{q'}$ to the right–hand side of Eqs. (A.1–A.3), while the grid is significantly stretched (Colonius [22]). The damping coefficient λ increases smoothly from 0 to 0.3 over a distance $l_x = 20$ in the axial direction within the outflow region, and from 0 to 1 over a distance $l_r = 70$ in the radial direction within the lateral sponge region. Axial symmetry is imposed at $r = 0$ by appropriately copying the values of $\vec{q'}$ onto five virtual points across the axis. The first physical radial grid point is placed at half the local step size away from the axis, in order to avoid the coordinate singularity at $r = 0$. Near the other three boundaries of the computational domain, the stencil size of the spatial differentiation

and filter schemes is successively reduced, while centered formulations are retained. All fluctuations are set to zero at r_{max} and x_{max}. At the inlet, the first–order formulation of the non–reflecting characteristic boundary conditions developed by Giles [46] and further discussed by Colonius, Lele & Moin [23] is applied.

In the radial direction, grid points are clustered in the shear layer region, with a minimum spacing of $\Delta r = 0.01$ at $r = 1$. The radial distribution of physical grid points r_i is computed from equidistant computational points η_i via a mapping function $r_i = f(\eta_i)$ which is composed of piecewise fifth–order polynomials with continuous first– and second–order derivatives at the junction points. Thus the metric Jacobian $\partial r/\partial \eta$ can be computed to high accuracy with the implemented differentiation scheme. In the axial direction, the grid spacing is kept constant at $\Delta x = 0.05$ between the inlet and $x = 15$, from whereon it smoothly increases over 100 points to $\Delta x = 0.1$. In the sponge regions, grid stretching is gradually brought up to a rate of 4% from one point to the next, placing the outermost points at $r_{max} = 100$ and $x_{max} = 125$. Numerical grid convergence has been verified in test calculations on finer meshes.

A.3 Linear stability analysis

The results of the numerical simulation are to be compared with the linear stability properties of the underlying base flow. These features are analyzed by solving the linearized compressible Navier–Stokes equations around parallel base flow profiles prevailing at frozen streamwise stations, and seeking solutions for perturbations in normal mode form (Huerre & Monkewitz [54]). The dispersion relation, relating a complex frequency ω to its associated complex streamwise wavenumbers k, takes the form of a generalized eigenvalue problem, which is discretized by Chebyshev collocation and solved numerically (Khorrami, Malik & Ash [57]). The numerical implementation has been adapted from a code developed by Olendraru & Sellier [89]. If ω is given real, values for k^+ and k^- are obtained, which respectively correspond to downstream and upstream traveling instability waves, thereby providing a prediction for the local flow response to external forcing. By allowing complex values for ω and varying its imaginary part, the stability code also serves to determine the complex absolute frequency ω_0: An iterative search algorithm (Monkewitz & Sohn[85]) identifies the point k_0 in the complex k–plane where a k^+– and a k^-–branch pinch. The sign of the imaginary part $\omega_{0,i}$ of the absolute frequency determines the absolute ($\omega_{0,i} > 0$) or convective

($\omega_{0,i} < 0$) nature of the local instability.

A.4 Numerical results

Direct numerical simulations are performed for a family of jet profiles at $Re = 3750$ (based on the jet radius) and $M = 0.1$, with temperature ratios S ranging from 0.4 to 1. The steepness parameter of the inlet velocity profile is chosen to be $R/\theta_0 = 20$, where θ_0 is the initial shear layer momentum thickness. These settings closely match the parameter range for which most experimental data are available from Monkewitz *et al.*[82] ($Re_D = 7500$ in their nomenclature). Some calculations have also been carried out for a Reynolds number $Re = 7500$.

In order to trigger instabilities, an initial perturbation in the form of a ring vortex

$$u'(r,x) = -A\frac{r_0(r-r_0)}{r\sigma}\exp\left[-\ln 2\frac{(x-x_0)^2+(r-r_0)^2}{\sigma^2}\right] \quad \text{(A.9)}$$

$$v'(r,x) = A\frac{r_0(x-x_0)}{r\sigma}\exp\left[-\ln 2\frac{(x-x_0)^2+(r-r_0)^2}{\sigma^2}\right] \quad \text{(A.10)}$$

$$\text{with} \qquad (r_0,x_0) = (1,2) \quad \text{and} \quad A = 0.1 \quad \text{(A.11)}$$

is introduced into the shear layer, and the flow is allowed to evolve without further forcing. If the base flow is globally unstable, its intrinsic oscillations should develop regardless of the precise form of the initial perturbation.

Strouhal number spectra of the long–time flow response at $Re = 3750$ and various S are shown in figure A.1a. These spectra are calculated from the time signal of the radial perturbation velocity $v'(r = 1, x = 2, t)$ over the interval $200 \leq t \leq 600$, after initial transients have died out. In the unheated and slightly heated cases $0.65 \leq S \leq 1$, only low-level broadband oscillations persist. The behavior changes drastically as S falls below 0.65: In this range, the spectra are clearly dominated by pronounced peaks, while the background noise level is lowered. The flow in these cases synchronizes to a fundamental frequency of Strouhal number $St \approx 0.45$, which remains approximately constant over $0.4 \leq S \leq 0.6$. In the presence of strong heating, the level of background noise rises again, and the quality of the dominant peaks gradually deteriorates.

The qualitative difference between synchronized and non-synchronized states is clearly visualized in the spatio–temporal diagrams of figure A.2,

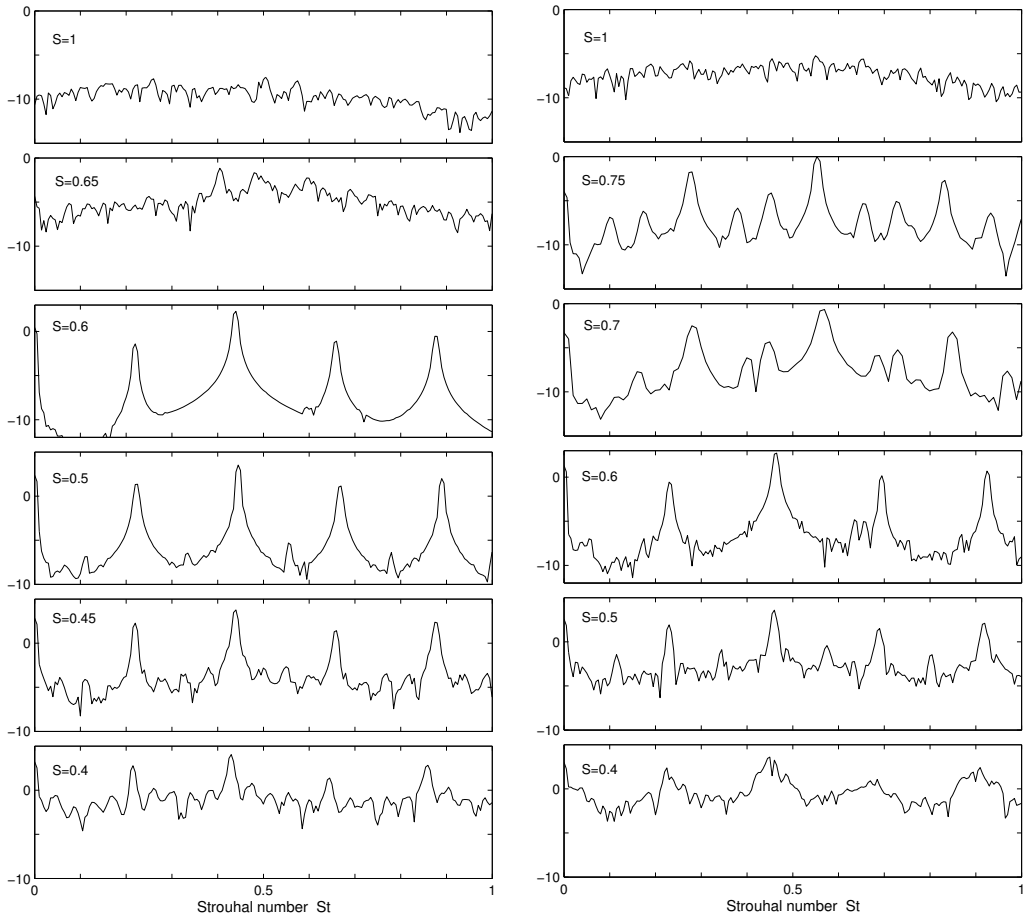

(a) $Re = 3750$ (b) $Re = 7500$

Figure A.1: Strouhal number spectra of the radial perturbation velocity signal $v'(r = 1, x = 2, t)$ for temperature ratios $0.4 \leq S \leq 1$ and two different Reynolds numbers; all abscissae are scaled to the same logarithmic units.

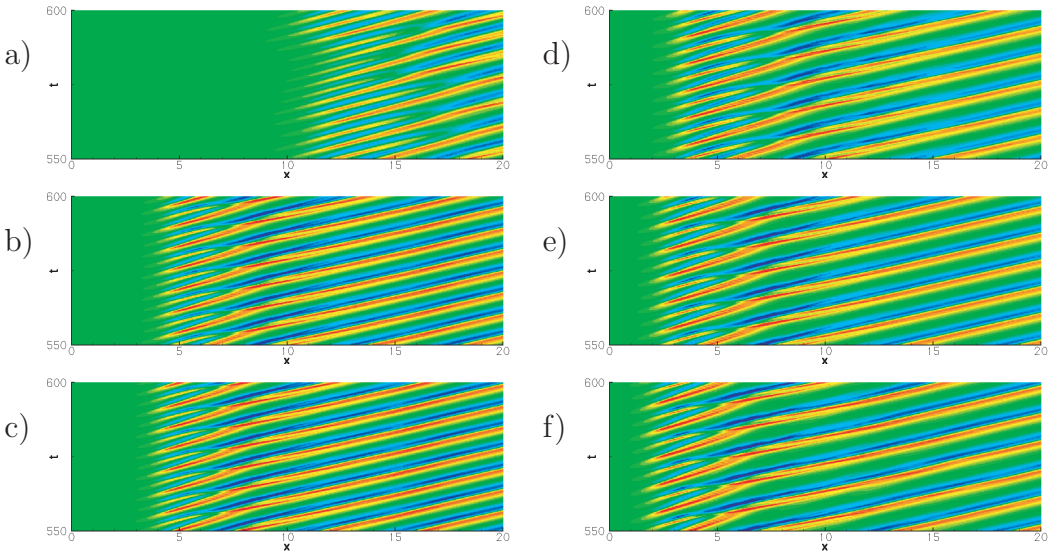

Figure A.2: Spatio–temporal diagrams of the radial perturbation velocity at $r = 1$ as a function of x and t. Red: positive, blue: negative. a) $S = 1$, $Re = 3750$, b) $S = 0.75$, $Re = 7500$, c) $S = 0.7$, $Re = 7500$ d) $S = 0.6$, $Re = 3750$, e) $S = 0.5$, $Re = 3750$, f) $S = 0.4$, $Re = 3750$

which display the fluctuations of the radial velocity at the center of the shear layer ($r = 1$) as a function of time and streamwise distance for typical values of S. For all cases at $Re = 3750$ and $S \leq 0.6$ (figures A.2d,e,f), the flow settles into a limit cycle, displaying perfectly periodic oscillations at each streamwise station. Note that in the non–synchronized cases, relatively regular structures evolve far downstream, after the merging of typically two rolled-up vortices (figure A.2a). We point out that any eventual organization of the flow in this region may not correspond to observations from experiments, where the downstream dynamics are altered by the onset of turbulence. From flow visualizations presented in Monkewitz *et al.*[82], the transition to turbulence at this Reynolds number can be estimated to take place between $x = 6$ and $x = 8$.

As the global frequencies of the synchronized states are to be compared to results of a *local* linear stability analysis, which assumes a slow streamwise development of the base flow, the influence of the non-parallelism of the base flow on the global frequency selection should be assessed. For this purpose, calculations have been performed at a Reynolds number $Re = 7500$, while all other parameters are retained from the cases presented above. The Strouhal number spectra for typical values of S are shown in figure A.1b. For $S \leq 0.6$ and $S \geq 0.8$, the spectra display the same behavior as those obtained at

$Re = 3750$: Below $S = 0.6$, self–sustained oscillations synchronize at a fundamental Strouhal number $St \approx 0.45$. In the cases $S = 0.75$ and $S = 0.7$, however, new synchronized states arise, that were not observed at the lower Re setting. These states are characterized by a dominant spectral peak at $St \approx 0.55$ and a strong subharmonic associated with downstream vortex pairing. The additional low–amplitude peaks that appear in these two spectra will not be further discussed. Although these peaks occur to some extent independently of the various windowing techniques that have been tested (a Hanning window function has been used to generate all spectra presented in this study), we do not rule out that they may be aliasing artefacts of the FFT.

Whereas the global oscillations at $St \approx 0.45$ develop very quickly during only a few oscillation periods after the initial perturbation, a satisfactory synchronization of the $St \approx 0.55$ mode does not take place before the much longer time $t = 300$. The spectra presented in figure A.1b for $S = 0.7$ and $S = 0.75$ are therefore calculated from a time signal $v'(r = 1, x = 2, t)$ over the time interval $300 \leq t \leq 600$.

A.5 Comparison with the experiment

The numerical results presented above agree very well with the experimental observations of Monkewitz *et al.*[82]: The self–sustained synchronized oscillations of Strouhal number $St \approx 0.45$ that arise at temperature ratios $S \leq 0.6$ in the simulations are easily identified with the 'mode II' state reported from the experiments, which displays the same frequency and sets in at $S = 0.63$. Both the numerical and the experimental data show that the frequency, beyond onset, is nearly independent of S, and that the rolled–up vortices experience one pairing event.

A second synchronized state of Strouhal number $St \approx 0.3$, found experimentally to set in at $S = 0.73$ ('mode I' in Monkewitz *et al.*[82]), does not arise in the numerical simulations at $Re = 3750$. However, it seems likely that the distinct synchronized oscillations in the cases $S = 0.7$ and $S = 0.75$ at $Re = 7500$ (figures A.1b and A.2b,c) are indeed identical with 'mode I' of Monkewitz *et al.*[82] The subharmonic component of this mode is seen to be very close to $St = 0.3$. We speculate that this subharmonic appeared as the dominant spectral peak in the experimental measurements, due to the non-local sensitivity of the microphone probe that was used. The fact that this mode is only observed in calculations at a higher Reynolds num-

ber may well be ascribed to differences in the numerical and experimental flow configurations. In support of our numerical results, only one single self-sustained synchronized state was identified in the helium jet experiments of Sreenivasan *et al.*[105], and as Monkewitz *et al.*[82] point out, this state most likely corresponds to their 'mode II' of $St \approx 0.45$.

An important point that calls for discussion is the choice of the momentum thickness of the inlet velocity profile. Monkewitz *et al.*[82] provide a semi–empirical formula from measurements in a cold jet, which gives the vorticity thickness θ_ω at the nozzle as $\theta_\omega/D = 4.9Re_D^{-0.5}$. In our nomenclature, this corresponds to a profile parameter $R/\theta_0 = 35$ for $Re = 3750$. Numerous calculations have been carried out for base flows with an inlet velocity profile of $R/\theta_0 = 30$, but no satisfactory synchronization was achieved in any of these cases. The frequency spectra, not presented here, show only broad peaks of rather low amplitude even at $S \leq 0.6$, more reminiscent of the behavior displayed in figure A.1 for high (globally stable) values of S. Steeper profiles exhibit larger growth rates for shear–layer–type instability modes of short wavelength. The range of parameters R/θ_0 that is accessible to the numerical study of intrinsic jet dynamics is therefore limited by the capacity of the numerical upstream boundary conditions to prevent the generation of vortical disturbances by incident acoustic waves. Note that the same qualitative behavior is observed in the experiments (figure 13 of Monkewitz *et al.*[82]), where in cases of very thin initial shear layers the dominance of short–wavelength modes prevents the formation of synchronized structures. The experimental value of R/θ_0 in the heated jet cases at $Re = 3750$ is not precisely known. However, the Strouhal numbers of the numerically obtained spectral peaks, as well as their very narrow shape (compare with figure 4 of Monkewitz *et al.*[82]), seem to indicate that the chosen value of $R/\theta_0 = 20$ adequately represents the effective experimental conditions in the numerical simulation.

A.6 Comparison to theoretical predictions

In this section, the simulation results are compared to criteria that can be drawn from theoretical models of acoustic feedback versus nonlinear global modes linked to absolute instability.

Acoustic feedback The possibility of an acoustic feedback loop between the inlet and the vortex pairing location is considered first. The criterion

given by Laufer & Monkewitz [64] states that *subharmonic resonance* takes place if the fundamental frequency and its subharmonic are in phase, which means that the period of the subharmonic must match the time that it takes for one vortical instability wave to travel from the inlet at $x = 0$ to the vortex pairing location x_p, and for the acoustic disturbance generated at x_p to propagate back to the inlet. In a low Mach number approximation, the propagation time of the acoustic signal can be neglected (Ho & Huerre [48]), and the resonance criterion simply relates the first pairing location and the fundamental Strouhal number as

$$x_p = 4N\frac{c_{ph}}{St}, \tag{A.12}$$

where N is an integer and c_{ph} the phase velocity of the instability wave. Over the entire range of S, the phase velocity is measured from the numerical results to always lie within the interval $0.55 < c_{ph} < 0.65$. The mean value $c_{ph} = 0.6$ can be chosen for the discussion without significant loss of precision. For Strouhal numbers $St = 0.44 \pm 0.01$, the criterion (A.12) with $N = 1$ then predicts vortex pairing to take place at $x_p = 5.46 \pm 0.12$. From the calculations at $Re = 3750$ and temperature ratios S of 0.4, 0.5 and 0.6 however, the respective pairing locations x_p are determined to be 5.5, 6.5 and 8.5, defined as the streamwise stations at which the vortex cores are vertically aligned (Grinstein *et al.*[47]). Granted that the precise location of vortex pairing is somewhat ambiguous, the measured differences between the three cases are much less so (compare figures A.2d,e,f). Within the simplifying assumptions made in Eq. (A.12), the almost identical global frequencies that are obtained for $S \leq 0.6$ should correspond, if their synchronization is due to an acoustic feedback loop, to identical vortex pairing locations. But even if the finite speed of sound and the small differences in the measured phase velocities are taken into account, the quality of the predictions for x_p does not improve. The subharmonic resonance model clearly does not describe the numerical observations.

Only two cases of the states that synchronize at Strouhal numbers around $St \approx 0.55$ are available from the simulations, associated earlier with 'mode I' of Monkewitz *et al.*[82]. This will not be sufficient for a definite interpretation. With $c_{ph} = 0.64$, identical in both cases, and with $St(S = 0.75) = 0.55$ and $St(S = 0.7) = 0.565$, the criterion (A.12) yields $x_p(S = 0.75) = 4.65$ and $x_p(S = 0.7) = 4.53$. These values do not at all match the positions of vortex pairing, which are found to lie between $x = 7$ and $x = 8$(figures A.2b,c). However, they correspond remarkably well to the streamwise stations where vortex *roll–up* is seen to take place. Vortex roll–up events in the simulations are indeed observed to radiate sound. If in future calculations a sufficient

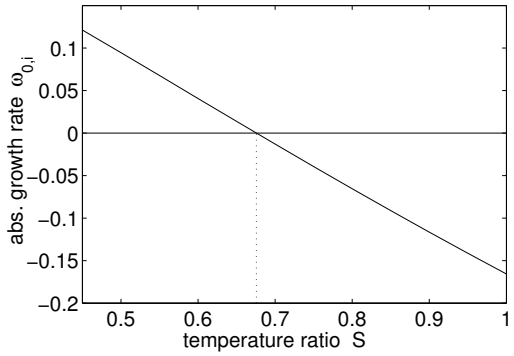

Figure A.3: Absolute growth rate $\omega_{0,i}$ of the inlet profiles at $R/\theta_0 = 20$ and $Re = 3750$ as a function of ambient–to–jet temperature ratio S. Absolute instability occurs below $S_{ca} = 0.676$.

number of cases of this mode can be generated, a feedback loop between the inlet and the vortex roll–up station might be found to provide a satisfying explanation for its synchronization.

Nonlinear global mode The characteristics of nonlinear global modes that arise from local absolute instability have been extensively studied in the context of Ginzburg–Landau model equations and, in some instances, these characteristics have been demonstrated to describe very well the behavior of real flows (see Chomaz [19] for a review). In particular, it has been shown in the numerical investigation of Lesshafft *et al.*[69] that in similar hot jet cases as those considered here (but at $Re = 1000$ and $R/\theta_0 = 10$), global instability sets in at a value of S for which the streamwise extent of the absolutely unstable region is sufficiently large to sustain a nonlinear front. Close to onset, the global frequency is then given by the absolute frequency $\omega_{0,r}$ at the inlet, whereas for highly supercritical values of S it gradually shifts away from this value. These results are in full agreement with the predictions deduced from the Ginzburg–Landau model. If the dominant synchronized states of $St \approx 0.45$ presented above are indeed the manifestation of a nonlinear global mode, as conjectured by Monkewitz *et al.*[82], the same criteria should be expected to apply.

From figure A.3, which displays the absolute growth rate $\omega_{0,i}(x = 0)$ as a function of S for $Re = 3750$, the flow is seen to exhibit absolute instability for values of S below $S_{ca} = 0.676$. Note that in the range of parameters used in the present study, absolute instability always appears first at the inlet. We also point out that the absolute frequencies for both Reynolds numbers

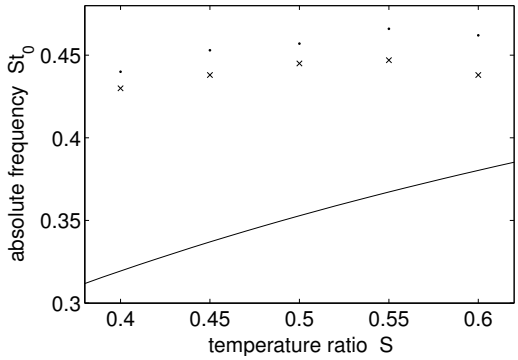

Figure A.4: Comparison of global frequencies ($\times$ $Re = 3750$, $\bullet$ $Re = 7500$) and absolute frequency of the inlet profiles at $Re = 3750$ (—), expressed as Strouhal numbers, as functions of S.

used in the simulations coincide within about 1% accuracy. The fact that the synchronization at Strouhal numbers $St \approx 0.45$ sets in below S_{ca} at $S = 0.6$ seems to strongly indicate the global mode nature of these oscillations.

The mode of $St \approx 0.55$ appears in a range of temperature ratios where the entire flow is still convectively unstable, which *a priori* precludes the existence of a global mode. Monkewitz *et al.*[82], who compare the critical S for the onset of this mode to the absolute instability threshold $S_{ca} = 0.72$ obtained in the incompressible, inviscid limit for a near–top–hat velocity profile (Monkewitz & Sohn [85]), already express their doubts about whether a global mode can be expected to exist in this range of S. The present results obtained from a compressible, viscous instability analysis applied to the precise base flow profiles used in the simulation (figure A.3) confirm that absolute instability is not responsible for the occurrence of this synchronized state.

Figure A.4 compares the observed global frequencies in the absolutely unstable range of S with the real part of the absolute frequency at $x = 0$, both expressed as Strouhal number. Surprisingly, even near the onset of global instability, at $S = 0.6$, the agreement is seen to be quite unsatisfactory. This discrepancy cannot be attributed to the non-parallelism of the base flow, since the agreement between global and absolute frequency does not improve with higher Reynolds number.

A.7 Conclusion

Direct numerical simulations of hot axisymmetric jets have been carried out at parameter settings close to the experimental configuration of Monkewitz *et al.*[82]. The experimental results have been reproduced to good accuracy: At temperature ratios $S \leq 0.6$, the simulated flow exhibits self–sustained synchronized oscillations of fundamental Strouhal number $St \approx 0.45$, precisely as observed experimentally. A different mode of Strouhal number $St \approx 0.55$ has been numerically observed at a higher Reynolds number over a narrow range $0.75 \leq S \leq 0.7$. Its subharmonic appears to coincide with the experimentally reported 'mode I' state at $St \approx 0.3$ of Monkewitz *et al.*[82].

The latter mode occurs at temperature ratios for which the flow is still convectively unstable everywhere, and the existence of a nonlinear global mode due to absolute instability therefore is readily dismissed in these cases. The synchronization of this mode must then be due to an acoustic feedback mechanism, although the subharmonic resonance criterion given by Laufer & Monkewitz [64] could not be recovered. Indeed, the streamwise station of vortex pairing appears to be uncorrelated with the global frequency in all cases for which self–sustained oscillations are observed. Vortex pairing then only occurs as a secondary instability of the nonlinear wavetrain, but it does not seem to be involved in the synchronization process.

The dominant mode, with Strouhal numbers around $St \approx 0.45$, sets in shortly after absolute instability first develops at the inlet, which seems to identify these oscillations as being due to the presence of a nonlinear global mode. However, even close to the global instability threshold value of S, the selected global frequency does not correspond to the absolute frequency at the inlet. This result is in contrast with the theoretical model of nonlinear global modes (Chomaz [19]), as well as with the behavior found in jets at lower Reynolds numbers and R/θ_0, as documented in Lesshafft *et al.*[69]. In the context of the linear impulse response, the observed global frequencies correspond to linear modes of non-zero group velocity that would be advected for long times in the absence of forcing at the inlet. It seems plausible to assume that upstream traveling acoustic waves are involved in the destabilization of this mode, even though the resulting frequency selection process is not adequately described by the subharmonic resonance model of Laufer & Monkewitz [64]. Such effects involving the interaction of acoustic and vortical modes are not accounted for in the framework of global mode theory. From our ongoing investigations of the influence of the various flow parameters on the frequency selection, we hope to report on further insights

into these mechanisms.

Acknowledgments

The authors are grateful to Jean-Marc Chomaz and Carlo Cossu for enlightening discussions and helpful suggestions. Lutz Lesshafft has been supported by an ONERA PhD fellowship, and all calculations have been performed on the ONERA supercomputing facilities.

Bibliography

[1] D.A. Anderson, J.C. Tannehill & R.H. Pletcher, 1984.
Computational Fluid Mechanics and Heat Transfer.
Hemisphere Publishing Co., New York.

[2] R.L. Ash & M.R. Khorrami, 1995.
Vortex stability. In S.I. Green, editor, *Fluid Vortices*, pages 317–372.
Kluwer.

[3] S. Bastin, P. Lafon & S. Candel, 1997.
Computation of jet mixing noise due to coherent structures: the plane jet case. *J. Fluid Mech.* **335**, 261–304.

[4] G.K. Batchelor & A.E. Gill, 1962.
Analysis of the stability of axisymmetric jets.
J. Fluid Mech. **14**, 529–551.

[5] D.W. Bechert & E. Pfizenmaier, 1975.
Optical compensation measurements on the unsteady exit condition at a nozzle discharge edge. *J. Fluid Mech.* **71**, 123–144.

[6] H. Bénard, 1908.
Formation de centres de giration à l'arrière d'un obstacle en mouvement. *Comptes rendus hebdomadaires des séances de l'Académie des sciences* **147**, 839–842.

[7] A. Bers, 1983.
Space-time evolution of plasma instabilities – absolute and convective.
In M.N. Rosenbluth & R.Z. Sagdeev, editors, *Handbook of Plasma Physics 1.* North-Holland, Amsterdam.

[8] W. Blumen, P.G. Drazin & D.F. Billings, 1975.
Shear layer instability of an inviscid compressible fluid. part2.
J. Fluid Mech. **71**, 305–316.

[9] B.J. Boersma, 2005.
Large eddy simulation of the sound field of a round turbulent jet.
Theoret. Comput. Fluid Dynamics **19**, 161–170.

[10] C. Bogey, C. Bailly & D. Juvé, 2003.
Noise investigation of a high subsonic, moderate Reynolds number jet using a compressible large eddy simulation.
Theoret. Comput. Fluid Dynamics **16**, 273–297.

[11] S. Boujemaa, M. Amielh & M.P. Chauve, 2004.
Analyse spatio-temporelle de jets axisymétriques d'air et d'hélium.
C. R. Mecanique **332**, 933–939.

[12] P. Brancher, J.-M. Chomaz & P. Huerre, 1994.
Direct numerical simulations of round jets: vortex induction and side jets. *Phys. Fluids* **6**(5), 1768–1774.

[13] J.E. Bridges & F. Hussain, 1992.
Direct evaluation of aeroacoustic theory in a jet.
J. Fluid Mech. **240**, 469–501.

[14] R.J. Briggs, 1964.
Electron-stream interaction with plasmas. Research Monograph 29. MIT Press, Cambridge, MA.

[15] L.G. Brown & A. Roshko, 1974.
On density effects and large structure in turbulent mixing layers.
J. Fluid Mech. **64**, 775–816.

[16] J.C. Buell & P. Huerre, 1988.
Inflow/outflow boundary conditions and global dynamics of spatial mixing layers. In *Proc. 2nd Summer Prog.*, pages 19–27. Stanford Univ. Cent. Turbul. Res.

[17] J.-M. Chomaz, 1992.
Absolute and convective instabilities in nonlinear systems.
Phys. Rev. Lett. **69**, 1931–1934.

[18] J.-M. Chomaz, 2003.
Fully nonlinear dynamics of parallel wakes. *J. Fluid Mech.* **495**, 57–75.

[19] J.-M. Chomaz, 2005.
Global instabilities in spatially developing flows: Non-normality and nonlinearity. *Annu. Rev. Fluid Mech.* **37**, 357–392.

[20] J.-M. Chomaz, P. Huerre & L.G. Redekopp, 1988.
Bifurcations to local and global modes in spatially developing flows. *Phys. Rev. Lett.* **60**, 25–28.

[21] J.-M. Chomaz, P. Huerre & L.G. Redekopp, 1991.
A frequency selection criterion in spatially developing flows. *Stud. Appl. Math.* **84**, 119–144.

[22] T. Colonius, 2004.
Modeling artificial boundary conditions for compressible flow. *Annu. Rev. Fluid Mech.* **36**, 315–345.

[23] T. Colonius, S.K. Lele & P. Moin, 1993.
Boundary conditions for direct computation of aerodynamic sound generation. *AIAA J.* **31**, 1574–1582.

[24] A. Couairon & J.-M. Chomaz, 1996.
Global instability in fully nonlinear systems. *Phys. Rev. Lett.* **77**, 4015–4018.

[25] A. Couairon & J.-M. Chomaz, 1997.
Absolute and convective instabilities, front velocities and global modes in nonlinear systems. *Physica D* **108**, 236–276.

[26] A. Couairon & J.-M. Chomaz, 1997.
Pattern selection in the presence of a cross flow. *Phys. Rev. Lett.* **79**, 2666–2669.

[27] A. Couairon & J.-M. Chomaz, 1999.
Fully nonlinear global modes in slowly varying flows. *Phys. Fluids* **11**, 3688–3703.

[28] Y. Couder, J.-M. Chomaz & M. Rabaud, 1989.
On the hydrodynamics of soap films. *Physica D* **37**, 384–405.

[29] D.G. Crighton, 1975.
Basic principles of aerodynamic noise generation. *Prog. Aerospace Sci.* **16**, 31–96.

[30] D.G. Crighton, 1985.
The Kutta condition in unsteady flow. *Annu. Rev. Fluid Mech.* **17**, 411–445.

[31] D.G. Crighton & M. Gaster, 1965.
Stability of slowly diverging jet flow. *J. Fluid Mech.* **77**, 397–413.

[32] D.G. Crighton & P. Huerre, 1990.
Shear-layer pressure fluctuations and superdirective acoustic sources. *J. Fluid Mech.* **220**, 355–368.

[33] S.C. Crow & F.H. Champagne, 1971.
Orderly structure in jet turbulence. *J. Fluid Mech.* **48**, 547–591.

[34] G. Dee & J. Langer, 1983.
Propagating pattern selection. *Phys. Rev. Lett.* **50**, 383–386.

[35] I. Delbende, J.-M. Chomaz & P. Huerre, 1998.
Absolute/convective instabilities in the batchelor vortex: a numerical study of the linear impulse response. *J. Fluid Mech.* **355**, 229–254.

[36] G. Desquesnes, M. Terracol, E. Manoha & P. Sagaut, 2006.
On the use of a high order overlapping grid method for coupling in CFD/CAA. *J. Comput. Phys.* **220**(1), 355–382.

[37] A.P. Dowling, 1992.
Thermoacoustic sources and instabilities. In *Modern Methods in Analytical Acoustics*, pages 378–405. Springer.

[38] F. Falissard, 2005.
Schémas numériques préservant la vorticité en aérodynamique compressible. PhD thesis, ENSAM, Paris, France.

[39] V. Fleury, 2006.
Superdirectivité, bruit d'appariement et autres contributions au bruit de jet subsonique. PhD thesis, École Centrale de Lyon, France.

[40] V. Fleury, C. Bailly & D. Juvé, 2005.
Shear-layer acoustic radiation in an excited subsonic jet: experimental study. *C. R. Mecanique* **333**, 746–753.

[41] V. Fleury, C. Bailly & D. Juvé, 2005.
Shear-layer acoustic radiation in an excited subsonic jet: models for vortex pairing and superdirective noise.
C. R. Mecanique **333**, 754–761.

[42] J.B. Freund, 2001.
Noise sources in a low-Reynolds-number turbulent jet at Mach 0.9.
J. Fluid Mech. **438**, 277–305.

[43] F. Gallaire & J.-M. Chomaz, 2003.
Mode selection in swirling jet experiments: a linear stability analysis. *J. Fluid Mech.* **494**, 223–253.

[44] F. Gallaire, M. Ruith, E. Meiburg, J.-M. Chomaz & P. Huerre, 2006.
Spiral vortex breakdown as a global mode. *J. Fluid Mech.* **549**, 71–80.

[45] M. Gaster, E. Kit & I. Wygnanski, 1985.
Large scale structures in a forced turbulent mixing layer.
J. Fluid Mech. **150**, 23–39.

[46] M.B. Giles, 1990.
Nonreflecting boundary conditions for Euler equation calculations. *AIAA J.* **28**, 2050–2058.

[47] F.F. Grinstein, E.S. Oran & J.P. Boris, 1987.
Direct numerical simulation of axisymmetric jets. *AIAA J.* **25**, 92–98.

[48] C.-M. Ho & P. Huerre, 1984.
Perturbed free shear layers. *Annu. Rev. Fluid Mech.* **16**, 365–424.

[49] C.-M. Ho & N.S. Nosseir, 1981.
Dynamics of an impinging jet. part 1. the feedback phenomenon.
J. Fluid Mech. **105**, 119–142.

[50] C.M. Ho & L.S. Huang, 1982.
Subharmonics and vortex merging in mixing layers.
J. Fluid Mech. **119**, 443–473.

[51] P. Huerre, 2000.
Open shear flow instabilities. In G.K. Batchelor, H.K. Moffatt & M.G. Worster, editors, *Perspectives in Fluid Dynamics*, pages 159–229. Cambridge University Press.

[52] P. Huerre & D.G. Crighton, 1983.
Sound generation by instability waves in a low mach number flow. *AIAA Paper* 83-0661.

[53] P. Huerre & P.A. Monkewitz, 1985.
Absolute and convective instabilities in free shear layers.
J. Fluid Mech. **159**, 151.

[54] P. Huerre & P.A. Monkewitz, 1990.
Local and global instabilities in spatially developing flows. *Annu. Rev. Fluid Mech.* **22**, 473–537.

[55] P. Huerre & M. Rossi, 1998.
Hydrodynamic instabilities in open flows. In C. Godreche & P. Manneville, editors, *Hydrodynamics and Nonlinear Instabilities*, pages 81–294. Cambridge University Press.

[56] S. Jendoubi & P.J. Strykowski, 1994.
Absolute and convective instability of axisymmetric jets with external flow. *Phys. Fluids* **6**, 3000–3009.

[57] M.R. Khorrami, M.R. Malik & R.L. Ash, 1989.
Applications of spectral collocation techniques to the stability of swirling flows. *J. Comput. Phys.* **81**, 206–229.

[58] V. Kibens, 1980.
Discrete noise spectrum generated by an acoustically excited jet. *AIAA J.* **18**, 434–441.

[59] G.P. Klaassen & W.R. Peltier, 1985.
Evolution of finite amplitude Kelvin–Helmholtz billows in two spatial dimensions. *J. Atmos. Sci.* **42**, 1321–1339.

[60] G.P. Klaassen & W.R. Peltier, 1991.
The influence of stratification on secondary instability in free shear layers. *J. Fluid Mech.* **227**, 71–106.

[61] A.N. Kolmogorov, I.G. Petrovsky & N.S. Piskunov, 1937.
Investigation of a diffusion equation connected to the growth of materials, and application to a problem in biology.
Bull. Univ. Moscow, Ser. Int. Sec. A **1**, 1–25.

[62] D. Kyle & K.R. Sreenivasan, 1993.
The instability and breakdown of a round variable-density jet. *J. Fluid Mech.* **249**, 619–664.

[63] L. Larchevêque, P. Sagaut, T.-H. Lê & P. Comte, 2004.
Large-eddy simulation of a compressible flow in a three-dimensional open cavity at high reynolds number. *J. Fluid Mech.* **516**, 265–301.

[64] J. Laufer & P.A. Monkewitz, 1980.
On turbulent jet flows: a new perspective. *AIAA Paper* 80-0962.

[65] J. Laufer & T.-C. Yen, 1983.
Noise generation by a low-Mach-number jet. *J. Fluid Mech.* **134**, 1–31.

[66] S.K. Lele, 1992.
Compact finite difference schemes with spectral-like resolution.
J. Comput. Phys **103**, 16–42.

[67] L. Lesshafft & P. Huerre, 2007.
Linear impulse response in hot round jets. *Phys. Fluids* **19**(2), 024102.

[68] L. Lesshafft, P. Huerre, P. Sagaut & M. Terracol, 2005.
Global modes in hot jets, absolute/convective instabilities and acoustic feedback. *AIAA Paper* 2005-3040.

[69] L. Lesshafft, P. Huerre, P. Sagaut & M. Terracol, 2006.
Nonlinear global modes in hot jets. *J. Fluid Mech.* **554**, 393–409.

[70] J.H. Lienhard, 2001. *The Engines of Our Ingenuity*, episode 1670.
Radio broadcast from KUHF-FM Houston.
available at `http://www.uh.edu/engines/engines.htm`.

[71] M.J. Lighthill, 1952.
On sound generated aerodynamically – I. General theory.
Proc. Roy. Soc. London, Series A **201**(1107), 564–587.

[72] T. Loiseleux, J.-M. Chomaz & P. Huerre, 1998.
The effect of swirl on jets and wakes: linear instability of the Rankine vortex with axial flow. *Phys. Fluids* **10**(5), 1120–1134.

[73] P.S. Lowery & W.C. Reynolds, 1988.
Numerical simulation of a spatially developing forced plane mixing layer. Technical Report TF-26, Department of Mechanical Engineering, Stanford University, Stanford, CA.

[74] G. Lu & S.K. Lele, 1996.
A numerical investigation of skewed mixing layers. Technical Report TF-67, Department of Mechanical Engineering, Stanford University, Stanford, CA.

[75] J. Le Conte, 1858.
On the influence of musical sounds on the flame of a jet of coal-gas.
Philos. Mag. **15**, 235–239.

[76] A. Michalke, 1965.
On spatially growing disturbances in an inviscid shear layer.
J. Fluid Mech. **23**, 521–544.

[77] A. Michalke, 1971.
Instabilität eines kompressiblen runden Freistrahls unter Berücksichtigung des Einflusses der Strahlgrenzschichtdicke.
Z. Flugwiss. **19**, 319–328.
English translation: NASA Tech. Memo 75190 (1977).

[78] A. Michalke, 1984.
Survey on jet instability theory. *Prog. Aerospace Sci.* **21**, 159–199.

[79] B.E. Mitchell, S.K. Lele & P. Moin, 1995.
Direct computation of the sound generated by subsonic and supersonic axisymmetric jets. Technical Report TF-66, Department of Mechanical Engineering, Stanford University, Stanford, CA.

[80] B.E. Mitchell, S.K. Lele & P. Moin, 1999.
Direct computation of the sound generated by vortex pairing in an axisymmetric jet. *J. Fluid Mech.* **383**, 113–142.

[81] P.A. Monkewitz, 1983.
On the nature of the amplitude modulation of jet shear layer instability waves. *Phys. Fluids* **26**(11), 3180–3184.

[82] P.A. Monkewitz, D.W. Bechert, B. Barsikow & B. Lehmann, 1990. Self-excited oscillations and mixing in a heated round jet.
J. Fluid Mech. **213**, 611–639.

[83] P.A. Monkewitz, P. Huerre & J.-M. Chomaz, 1993.
Global linear stability analysis of weakly non-parallel shear flow.
J. Fluid Mech. **251**, 1–20.

[84] P.A. Monkewitz & E. Pfizenmaier, 1991.
Mixing by "side jets" in strongly forced and self-excited round jets.
Phys. Fluids A **3**(5), 1356–1361.

[85] P.A. Monkewitz & K. Sohn, 1988.
Absolute instability in hot jets. *AIAA J.* **26**, 911–916.

[86] J.W. Nichols, 2005.
Simulation and stability analysis of jet diffusion flames. PhD thesis, University of Washington.

[87] J.W. Nichols, P.J. Schmid & J.J. Riley, 2004.
Self-sustained oscillations in variable-density jets. *Bulletin of the American Physical Society* **49**(9), 53.

[88] J.W. Nichols, P.J. Schmid & J.J. Riley, 2007.
Self-sustained oscillations in variable-density round jets.
J. Fluid Mech., in press.

[89] C. Olendraru & A. Sellier, 2002.
Viscous effects in the absolute-convective instability of the Batchelor vortex. *J. Fluid Mech.* **459**, 371–396.

[90] D.C. Pack, 1954.
Laminar flow in an axially symmetrical jet of compressible fluid, far from the orifice. *Proc. Camb. Phil. Soc.* **50**, 98–104.

[91] D. Parekh, A. Leonard & W.C. Reynolds, 1988.
Bifurcating jets at high Reynolds numbers. Technical Report TF-35, Department of Mechanical Engineering, Stanford University, Stanford, CA.

[92] S. Pavithran & L.G. Redekopp, 1989.
The absolute-convective transition in subsonic mixing layers.
Phys. Fluids A **1**, 1736.

[93] B. Pier, 2002.
On the frequency selection of finite-amplitude vortex shedding in the cylinder wake. *J. Fluid Mech.* **458**, 407–417.

[94] B. Pier & P. Huerre, 2001.
Nonlinear self-sustained structures and fronts in spatially developing wake flows. *J. Fluid Mech.* **435**, 145–174.

[95] B. Pier, P. Huerre & J.-M. Chomaz, 2001.
Bifurcation to fully nonlinear synchronized structures in slowly varying media. *Physica D* **148**, 49–96.

[96] B. Pier, P. Huerre, J.-M. Chomaz & A. Couairon, 1998.
Steep nonlinear global modes in spatially developing media.
Phys. Fluids **10**, 2433–2435.

[97] M. Provansal, C. Mathis & L. Boyer, 1987.
Bénard-von Kármán instability: transient and forced regimes.
J. Fluid Mech. **182**, 1–22.

[98] Lord Rayleigh, 1879.
On the instability of jets. *Proc. London Math. Soc.* **10**, 4–13.

[99] S. Redonnet, 2001.
Simulation de la propagation acoustique en présence d'écoulements quelconques et de structures solides par résolution numérique des équations d'Euler. PhD thesis, ONERA, Châtillon, France.

[100] C. Richards, B. Breuel, R. Clark & T. Troutt, 1996.
Concentration measurements in a self-excited jet.
Exp. Fluids **21**, 103–109.

[101] H. Schlichting, 1933.
Laminare Strahlausbreitung. *Z. angew. Math. Mech.* **13**, 260.

[102] D.S. Shin & J.H. Ferziger, 1992.
Stability of the compressible reacting mixing layer. Technical Report TF-53, Department of Mechanical Engineering, Stanford University, Stanford, CA.

[103] M.C. Soteriou & A.F. Ghoniem, 1995.
Effects of the free-stream density ratio on free and forced spatially developing shear layers. *Phys. Fluids* **7**(8), 2036–2051.

[104] E. Spenser, 1596.
The Faerie Queene. Book II, Canto III. Printed for William Ponsonbie, London.

[105] K.R. Sreenivasan, S. Raghu & D. Kyle, 1989.
Absolute instability in variable density round jets.
Exp. Fluids **7**, 309–317.

[106] P.J. Strykowski & D.L. Niccum, 1991.
The stability of countercurrent mixing layers in circular jets.
J. Fluid Mech. **227**, 309–343.

[107] C. Tam & P. Morris, 1980.
The radiation of sound by the instability waves of a compressible plane turbulent shear layer. *J. Fluid Mech.* **98**, 349–381.

[108] M. Terracol, E. Manoha, C. Herrero, E. Labourasse, S. Redonnet & P. Sagaut, 2005.
Hybrid methods for airframe noise numerical prediction.
Theoret. Comput. Fluid Dyn. **19**(3), 197–227.

[109] J. Tyndall, 1867.
Sound – A Course of Eight Lectures Delivered at the Royal Institution of Great Britain. Longmans, Green and Co., London.

[110] M. van Dyke, 1982.
An Album of Fluid Motion. Parabolic Press, Stanford, CA.

[111] W. van Saarlos, 1988.
Front propagation into unstable states: marginal stability as dynamical mechanism for velocity selection. *Phys. Rev. A* **37**, 211–229.

[112] W. van Saarlos, 1989.
Front propagation into unstable states: II. linear versus nonlinear marginal stability and rate of convergence.
Phys. Rev. A **39**, 6367–6390.

[113] M.R. Visbal & D.V. Gaitonde, 2002.
On the use of higher-order finite-difference schemes on curvilinear and deforming meshes. *J. Comput. Phys.* **181**, 155–185.

[114] J.E. Wesfreid, S. Goujon-Durand & B.J. Zielinska, 1996.
Global mode behavior of the streamwise velocity in wakes.
J. Phys. II France **6**, 1343–1357.

[115] C.D. Winant & F.K. Browand, 1974.
Vortex pairing, the mechanism of turbulent mixing-layer growth at moderate Reynolds number. *J. Fluid Mech.* **63**, 237–255.

[116] B.S. Yildirim & A.K. Agrawal, 2005.
Full-field measurements of self-excited oscillations in momentum-dominated helium jets. *Exp. Fluids* **38**, 161–173.

[117] B.J. Zielinska & J.E. Wesfreid, 1995.
On the spatial structure of global modes in wake flow.
Phys. Fluids **7**, 1418–1424.